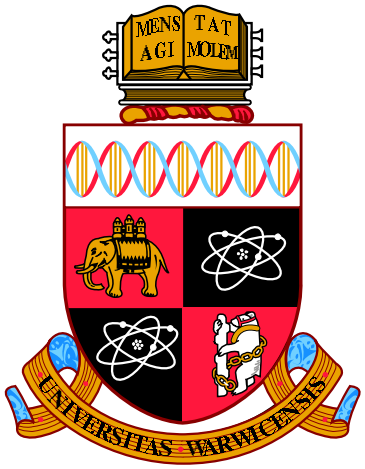

Measurement of the angular distribution of the $B^+ \to \pi^+\mu^-\mu^+$ decay and R&D towards a future upgrade of the particle identification system of the LHCb experiment

by

Maria Flavia Cicala

Thesis

Submitted to the University of Warwick

for the degree of

Doctor of Philosophy in Physics

Department of Physics

September 2022

THE UNIVERSITY OF WARWICK

Contents

List of Tables

List of Figures

Acknowledgments

I am extremely grateful to my supervisor, Tom Blake, without whom the completion of this Thesis would not have been possible, for guiding me in this endeavour with infinite patience. This feeling extends to Michal Kreps, Fernando Abudinen, and Tim Gershon for their constant valuable advice throughout my PhD program. I am deeply indebted to Thierry Gys, for his help and guidance in the TORCH lab. His teachings and constructive criticism were instrumental in the success of the characterisation of the TORCH detector hardware that I performed. I'm deeply indebted to Tom Latham for always being available when help was needed, and for doing his utmost best to teach me correct coding rules and guidelines. Whether his efforts were successful remains to be seen.

A special thank you for the support and camaraderie of my fellow PhD students, Andy Morris, Ross Hunter, Bryn Roberts and Eleanor Jones. Being part of this cohort of students gave me the strength to keep going when things got tough. I'm grateful to Ed Millard for being extremely welcoming and for taking on the role of a PhD student mentor for me. Furthermore, a heartfelt thanks to past and present office mates and group members, Tom Jones, Bhagyashree Pagare, Anja Beck, Alex Ward, Lorenzo Paolucci, Luismi Martin, working with and alongside you has been a pleasure.

A heartfelt thanks goes to my family. Mamma, Papà, non avrei raggiunto questo traguardo se non fosse stato per voi, che mi avete sempre spronato a seguire i miei sogni. Grazie!

Finally, I would like to thank my amazing husband Andrea from the bottom of my heart for being a constant source of unwavering support through the ups and downs of the Ph.D. course, and of life more broadly.

Declarations

The work presented in this thesis is all of my own work, unless it is specifically referenced to the contrary. This thesis has not been submitted, in any form, to this or any other university for another qualification.

Maria Flavia Cicala September 2022

Abstract

This thesis presents two complementary research studies, linked by the LHCb experiment. A first analysis of the angular distribution of the $B^+ \to \pi^+\mu^+\mu^-$ decay with LHCb Run 1 and 2 data is presented, using the Feldman-Cousins approach to ensure correct coverage of the angular observables measured, $A_{\rm FB}$ and $F_{\rm H}$. This decay is a rare $b \to d$ quark flavour changing neutral current process. The analysis is at an advanced stage and blind at the time of writing of this work. The analysis strategy is tested on control modes and pseudo-experiments. Sources of systematic uncertainties are identified and their effects evaluated.

In addition, studies for the R&D effort for the development of a new time-of-flight Cherenkov detector, TORCH, proposed for the next LHCb upgrade are presented. The proposed design uses MCP-PMTs to measure single photon time. The TORCH MCP-PMT is characterised with studies of uniformity and gain. The single photon time resolution of the TORCH MCP-PMT coupled to readout electronics has been measured, resulting in (47.5 ± 0.7) ps, meeting the TORCH design requirement.

Chapter 1

Introduction

The study of particle physics aims to shed light on the nature of the particles that make up the Universe, their origin and the laws regulating their interactions. While this discipline has always existed in various forms throughout the development of civilisation, it has emerged in its modern nature, regulated by equations describing quantum fields, during the first half of the twentieth century. The culmination of the description of the Universe in terms of particle physics takes form in the Standard Model. The Standard Model has been tested by the particle physics community since its conception by performing numerous experiments. While most observations confirm that the Standard Model is an excellent description of Nature, a small number have hinted that the Universe might include other particles or forces beyond what is described by the Standard Model. The phenomena and particles that might exist and that are not currently described by the Standard Model fall under the umbrella term "New Physics". The observed deviations from the Standard Model are modest. While they should not be ignored, they are not enough to claim discovery of New Physics. The current status of the observations motivates new studies that could result in experimental deviations from Standard Model predictions of greater significance. The work undertaken in this project aims to look for New Physics by measuring the angular structure in rare semileptonic decays.

This thesis includes two research topics: the analysis of the angular distribution of the $B^+ \to \pi^+\mu^+\mu^-$ decay; and characterization studies of the photon multiplier tubes for the TORCH detector. The connection between the two is the LHCb experiment. The angular analysis is performed with LHCb data, and the TORCH detector is proposed for the next LHCb upgrade to

improve its particle identification performance. The need for excellent particle identification is evident in most LHCb analysis, including the one performed in this work. Indeed, the $B^+ \to K^+\mu^+\mu^-$ decay where the kaon is mis-identified as a pion is a relevant background for the $B^+ \to \pi^+\mu^+\mu^-$ angular analysis.

The motivation for the $B^+ \to \pi^+\mu^+\mu^-$ angular analysis is supplied in Chapter 2 by exploring the recent results in flavour physics. In particular, the LHCb Collaboration measured a branching fraction of $(18.3 \pm 2.0 \pm 0.5) \times 10^{-9}$ for this decay using data collected during 2011 and 2012 [1]. In that occasion, the signal yield was too low to perform an angular analysis as well. The angular analysis sheds light on the possibility of any new physics entering this decay mode by looking for deviations from the Standard Model predictions for the angular observables and their measurements. This work uses LHCb data from 2011, 2012, 2015-2018 and is the first angular analysis of the $B^+ \to \pi^+\mu^+\mu^-$ decay. The LHC machine and the LHCb detector are described in detail in Chapter 3, while the data, the analysis strategy and the analysis results are described in Chapter 4.

The TORCH detector is the object of the second piece of research in this work. The detector is described in Chapter 5, which goes on to illustrate the characterization studies of the photon multiplier tubes. These comprise time resolution studies and measurements of the gain the device.

Finally, conclusions are drawn in Chapter 6.

Chapter 2

Theory

2.1 The Standard Model of Particle Physics

The Standard Model (SM) is a theory that describes the elementary particles and their interactions. Originating from work in the 1970s, it comprised all the then known particles and, with tools from quantum field theory (QFT), it predicted the existence of particles that had yet to be detected. These were the Z and W bosons (confirmed in 1983), the top quark (confirmed in 1995), the tau neutrino (ν_τ) (confirmed in 2000) and the Higgs boson (confirmed in 2012). Currently it encompasses all seventeen known particles, visible in figure 2.1.

The SM includes three of the four known forces of nature: the strong force, the electromagnetic force and the weak force. Gravity is not described by the SM mainly because it has not been quantized yet. How the forces act on the SM particles is determined by the properties of the particles. The SM particles present common traits that automatically separate them by family, generation, species. The biggest separating trait is whether a particle in question is a fundamental building block of matter or if it is a force mediator, called respectively fermions and bosons. The SM includes twelve fermions and five bosons. Fermions have half-integer spin and follow the Pauli exclusion principle, which states that no two fermions can occupy the same quantum state at the same time [3]. Bosons have whole-integer spin and do not obey the Pauli exclusion principle, so they may be described by the same quantum numbers. Each fermion has a corresponding antiparticle, which is an identical fermion with the same mass but opposite charge. Elementary fermions can be of two types: those that can exist independently, called leptons, and

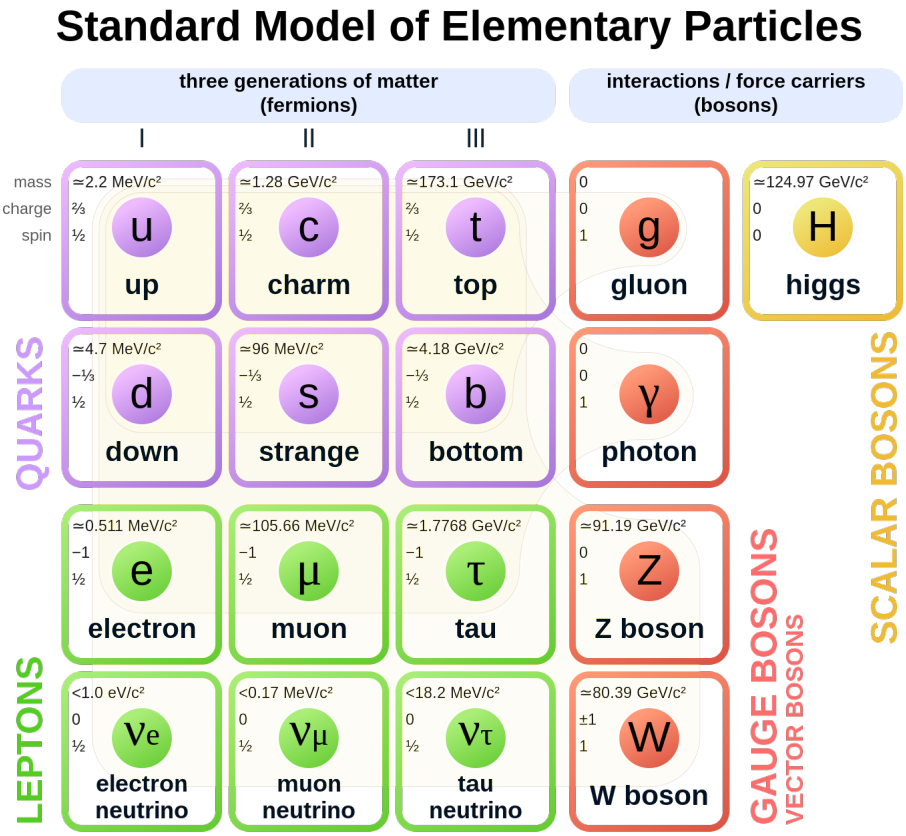

Figure 2.1: The elementary particles composing the Standard Model grouped by family, species, generation and interaction types. This graphical representation of the SM particles was sourced from Ref. [2].

those that must form a bound state, called quarks. Quarks carry colour and flavour charges and can experience the strong nuclear force and the weak force, respectively, because of this.

A particle resulting from the bound state of two or more quarks via the strong interaction is called a hadron. Hadrons have no overall colour charge. Furthermore, when two quarks, specifically a quark and an antiquark, are in a bound state, this is called a meson. Mesons can only have integer spin. The bound state of three quarks is called a baryon, and can only have half-integer spin values, therefore baryons are a subset of fermions. States comprising four or more quarks have recently been observed [4, 5] and there is a need for more thorough study to fully understand these states. Elementary fermions are also further divided into generations. The first generation of fermions is

composed of the up and down quarks and the electron and electron neutrino. While stable hadrons are combinations of first generation quarks, the latter can also combine to create unstable hadrons such as the pion. The second generation consists of the charm and strange quarks and the muon and muonic neutrino leptons. Hadrons composed of at least one second generation quark are unstable and will decay into stable final states. The third generation comprises the top and bottom quarks, the tau and the tauonic neutrino. The top quark is sufficiently heavy that it decays before forming a bound state. It is only studied though its decay products [6].

With respect to the electron electric charge equalling -1, the up-type quarks (up, charm and top) and the down-type quarks (down, strange, bottom) have electric charge $+\frac{2}{3}$ and $-\frac{1}{3}$ respectively. The leptons (electron, muon, tau) have electric charge -1 and the neutrinos (ν_e, ν_μ, ν_τ) are not electrically charged. All fundamental fermions have a corresponding anti-particle, with the same mass but opposite electric charge.

Elementary bosons are force carrying particles. Photons are the force carriers of the electromagnetic field. They are massless and have spin 1 as they correspond to a vector field, and have no electric charge. Gluons are massless vector gauge bosons, mediators of the strong interaction which binds quarks together. Gluons carry colour charge, which can take any of the following values: red, green, blue, anti-red, anti-green, anti-blue. The colour states can be mixed, with a total of nine linearly independent combinations which result in nine linearly independent states: a colour singlet and a colour octet. The colour singlet is $(r\bar{r} + b\bar{b} + g\bar{g})/\sqrt{3}$, and it is colour neutral.

The $W^{\pm}$ and Z bosons are the mediators of the weak force. They are massive. The final particle of the SM is the Higgs boson. It's existence was predicted in the theory to explain the fact that the $W^{\pm}$ and Z bosons are not massless. More detail on this is given in section 2.1.1. The Higgs boson is also massive. All the elementary bosons are electrically neutral with the exception of the $W^{\pm}$ bosons, which have electrical charge of ± 1.

2.1.1 The symmetries of the Standard Model

The SM is built by combining quantum theory with the principles of Lorenz invariance to obtain a renormalizable quantum field theory. One begins by postulating the SM's symmetry group $G_{\mathrm{SM}} = SU(3)_C \times SU(2)_L \times U(1)_Y$, where the combined eletromagnetic and weak (electroweak) interactions, unified via the Glashow-Weinberg-Salam (GWS) theory [7–9], are represented by the

invariance under $SU(2)_L \times U(1)_Y$. The strong interaction is governed by $SU(3)_C$. The SU(3) group conserves the colour charge. The Gell-Mann matrices can generate unitary matrix group elements of the SU(3) group, and produce the combinations in the colour octet of the colour states mentioned previously. The Gell-Mann matrices are:

$$\lambda_1 = \begin{pmatrix} 0 & 1 & 0 \\ 1 & 0 & 0 \\ 0 & 0 & 0 \end{pmatrix}, \qquad \lambda_2 = \begin{pmatrix} 0 & -i & 0 \\ i & 0 & 0 \\ 0 & 0 & 0 \end{pmatrix}, \qquad \lambda_3 = \begin{pmatrix} 1 & 0 & 0 \\ 0 & -1 & 0 \\ 0 & 0 & 0 \end{pmatrix},$$

$$\lambda_4 = \begin{pmatrix} 0 & 0 & 1 \\ 0 & 0 & 0 \\ 1 & 0 & 0 \end{pmatrix}, \qquad \lambda_5 = \begin{pmatrix} 0 & 0 & i \\ 0 & 0 & 0 \\ -i & 0 & 0 \end{pmatrix}, \qquad \lambda_6 = \begin{pmatrix} 0 & 0 & 0 \\ 0 & 0 & 1 \\ 0 & 1 & 0 \end{pmatrix},$$

$$\lambda_7 = \begin{pmatrix} 0 & 0 & 0 \\ 0 & 0 & -i \\ 0 & i & 0 \end{pmatrix}, \qquad \lambda_8 = \frac{1}{\sqrt{3}} \begin{pmatrix} 1 & 0 & 0 \\ 0 & 1 & 0 \\ 0 & 0 & -2 \end{pmatrix} \quad .$$

The SU(2) group conserves the weak isospin and the U(1) term conserves the so-called weak hypercharge. The particles introduced in section 2.1 are excitations of the quantum fields that make up the SM. In electroweak theory, the SU(2) left handed fermion fields are represented by the following doublets:

$$\begin{pmatrix} u \\ d \end{pmatrix}_L, \quad \begin{pmatrix} c \\ s \end{pmatrix}_L, \quad \begin{pmatrix} t \\ b \end{pmatrix}_L, \quad \begin{pmatrix} \nu_e \\ e^- \end{pmatrix}_L, \quad \begin{pmatrix} \nu_\mu \\ \mu^- \end{pmatrix}_L, \quad \begin{pmatrix} \nu_\tau \\ \tau^- \end{pmatrix}_L . \tag{2.1}$$

The SU(2) right handed fermion fields are represented by the singlets $u_{Rj} = u_R$ or c_R or t_R, and $d_{Rj} = d_R$ or s_R or b_R. Only the left handed fields interact weakly via one of the $W^{\pm}$ bosons.

Each of the equivalent right hand components correspond to a weak isospin singlet. This framework shapes the possible interactions. The $W^{\pm}$ bosons mediate the charged-current weak interactions between left handed fermions only. The Z^0 boson mediates neutral weak interactions. The photon mediates the purely electromagnetic interactions, which conserve parity. Experimental evidence suggests that QFT is an SU(3) gauge symmetry rather than a U(3) gauge symmetry. It acts on the colour triples of the quark fields. The eight gluons mediate the strong force by interacting with quarks or by

self-interaction.

The theoretical prediction of the Higgs boson stems from two inconsistencies between the SM and experimental observations. The gauge symmetry at the heart of the SM forbids the existence of massive bosons, but experimentally the masses of the electroweak bosons are not zero. Furthermore, the fermion mass terms of the SM Lagrangian are not gauge invariant because the weak force violates parity, allowing for left handed interaction only. The Higgs mechanism was proposed to solve this discrepancy between the model and experimental observation. It is based on the idea that particles at energies greater than the electroweak scale are massless. They acquire mass below the unification energy ($\sim$ 240 Gev) through the spontaneous breaking of the electroweak symmetry, U(1)$\times$ SU(2) [10–12]. Applying the Higgs mechanism to the non-abelian SU(2)$\times$U(1) gauge theory generates the three electroweak interaction massive bosons, $W^{\pm}$ and Z, and a massless boson, which corresponds to the photon, for the electromagnetic interaction [13].

2.1.2 Discrete symmetries in the Standard Model

Three discrete symmetries are present in the SM in addition to the gauge symmetries. These are parity inversion (P), charge conjugation (C) and time reversal (T). The parity operator inverts the spatial coordinates of a given vector. The charge conjugation operator inverts the sign of all of a particle's quantum numbers, transforming the particle into its antiparticle. The time reversal operator maps the variable t into $-t$: $t \mapsto -t$. A Lorentz invariant relativistic quantum field theory, such as the SM, is also invariant under the CPT combined operators. Experimental studies have shown that the individual C, P and T symmetries are not always conserved in the SM. The weak interaction violates both C and P symmetries individually and their combination, CP. The lack of observations of left handed anti-neutrinos and their absence form the SM is evidence of charge conjugation symmetry violation by the weak interaction. Wu's study of the beta decay of cobalt-60 was the first observation of parity violation by the weak force [14]. The CP symmetry broken by the weak interaction was shown experimentally by Christenson, Cronin, Fitch and Turlay, who observed the decay of a neutral kaon with long lifetime meson into two pions [15]. In this particular case there are two physical states, named K^1 and K^2, which are CP eigenstates. They superpose to make the mass eigenstates K^0_S, also known as short-lived, and K^0_L, also known as long-lived. These are a superposition of the particle K^0

and its antiparticle, $\overline{K}^0$

$$\begin{aligned} |K_S^0\rangle &= \tfrac{1}{\sqrt{2}}(|K^0\rangle + |\overline{K}^0\rangle), \\ |K_L^0\rangle &= \tfrac{1}{\sqrt{2}}(|K^0\rangle - |\overline{K}^0\rangle). \end{aligned} \tag{2.2}$$

The CP operators acting on the physical states

$$CP|K_S^0\rangle = +|K_S^0\rangle, \tag{2.3}$$

$$CP|K_L^0\rangle = -|K_L^0\rangle. \tag{2.4}$$

with states having eigenvalues ± 1. The decay products are 3π and 2π and have a CP of -1 and $+1$, respectively. It follows that for CP to be conserved $K_S^0 \to 2\pi$ only and $K_L^0 \to 3\pi$ only. This was not observed to be the case and CP is violated. The observation of CP violation motivated the need to extend the SM to 3 generations. CP violation was then observed in particle-antiparticle oscillation, also referred to as mixing. CP violation was observed in decays of B^+ [16, 17] systems; and in the interference of mixing and decay for B^0 [18, 19], B_s^0 systems [16, 17]. This was also observed by LHCb in charm decays [20].

Finally, some of the SM symmetries are accidental as they do not correspond to properties of the Lagrangian. One example is the symmetry caused by the SM's massless neutrinos. Massless neutrinos are described by a diagonal mixing matrix relating neutrino mass and flavour eigenstates. Since the off-diagonal terms are zero, there are no SM Lagrangian terms that couple to different generations of leptons. This results in the quantum numbers $\mathcal{L}_e$, $\mathcal{L}_\mu$, $\mathcal{L}_\tau$ being conserved in the SM. The process $\mu^+ \to e^- e^+ e^+$ is forbidden in the SM because it does not conserve lepton quantum numbers. Experimentally, the rate of this decay has an upper limit of 10^{-12} at 90% confidence level [21].

Lepton Flavour Universality (LFU) is an accidental symmetry of the SM. It results in leptons with different flavours coupling in the same way to the vector bosons γ, $W^\pm$, Z^0 and not coupling at all to gluons. Experimentally LFU holds for $W^\pm$ and Z^0 decays [22, 23], for decays of light mesons [24, 25] and for charmonium resonances [26].

2.1.3 Spontaneous symmetry breaking

The electroweak and electromagnetic gauge symmetry predicts massless fermions and bosons in the SM. If one takes a fermion field, this has a Lagrangian mass term, $m^2\bar{\psi}\psi$, which can be factorised into left handed and

right handed chiral fields, as:

$$m^2(\bar{\psi}_L\bar{\psi}_R)(\psi_L\psi_R) = m^2(\bar{\psi}_L\psi_L + \bar{\psi}_R\psi_R + \bar{\psi}_L\psi_R + \bar{\psi}_R\psi_L). \tag{2.5}$$

If this mass term were non-zero, it would allow left-handed and right-handed fermion fields to couple together. Experimental observation shows that left handed and right handed fermion fields transform differently under the weak force, fixing the value of these terms to 0. A similar problem is observed for mass terms related to bosons.

The Higgs mechanism [11, 27–29] reconciles theory and observation by breaking the electroweak symmetry and introducing mass terms allowed by the gauge theory. Another effect of the Higgs mechanism is that it provides flavour change in the quark sector. Spontaneous symmetry breaking (SSB),

$$\mathrm{SU}(2)_L \times \mathrm{U}(1)_Y \rightarrow \mathrm{U}(1)_{\mathrm{em}}, \tag{2.6}$$

is achieved by adding a Higgs Lagrangian term to the initial SM Lagrangian comprising the electroweak and QCD terms. The additional Lagrangian component is:

$$\mathcal{L}_{\mathrm{Higgs}} = (D^\mu\Phi^\dagger)(D^\mu\Phi) - V(\Phi), \tag{2.7}$$

where Φ is the new scalar field

$$\Phi = \begin{pmatrix} \phi^+ \\ \phi^0 \end{pmatrix}, \tag{2.8}$$

the Higgs potential $V(\Phi)$ is given by

$$V(\Phi) = -\mu^2\Phi^\dagger\Phi + \lambda(\Phi^\dagger\Phi), \quad \mu, \lambda > 0, \tag{2.9}$$

and D_μ is the covariant derivative defined as

$$D_\mu = \delta_\mu + igTW_\mu^i + ig'\frac{1}{2}B_\mu. \tag{2.10}$$

The three $\mathrm{SU}(2)_L$ gauge bosons, W_μ^i, and the single $\mathrm{U}(1)_Y$ gauge boson, B_μ are included in the covariant derivative definition. The coupling terms are g and g', and T^i are the Pauli matrices. The Higgs potential introduces a new mass term, $-\mu^2$, and a new coupling term, λ. Minimising the Higgs potential results in the energy vacuum expectation value (vev) $v = \sqrt{\frac{\mu^2}{\lambda}}$, which has an infinite number of solutions for positive values of μ^2. The Higgs potential has

a so-called Mexican Hat shape, as shown in figure 2.2.

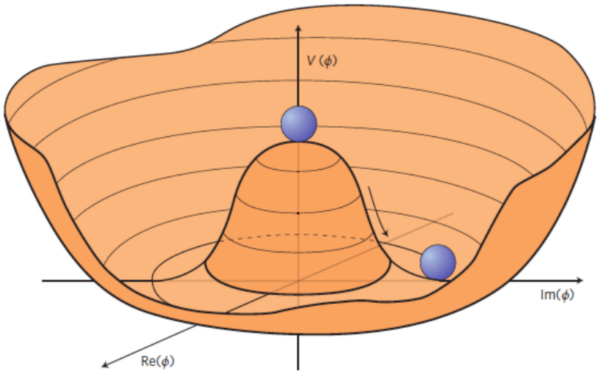

Figure 2.2: Higgs potential of the vacuum. It has an infinite number of minima arranged in a circle [30].

One chooses $\langle \Psi \rangle = \frac{1}{\sqrt{2}} \begin{pmatrix} 0 \\ v \end{pmatrix}$, so that solely the electroweak gauge symmetry $\mathrm{SU}(2)_L \times \mathrm{U}(1)_Y$ is broken and the electromagnetic gauge symmetry $\mathrm{U}(1)_Y$ is not. Oscillations from the potential minima are included by considering the perturbative substitution: $v \to v + h$, which produces quadratic terms from the kinetic term of the Higgs Lagrangian in equation 2.7. These terms are quadratic in h and in combinations of the pairs $W^{1\mu}$ and $W^{2\mu}$, and $W^{3\mu}$ and B^{μ}. These oscillations in the Higgs kinematic term produce a new massive scalar boson, the Higgs boson, mass terms for the $W^{\pm}$ bosons from the mixing of $W^{1,2\mu}$, and a mass term for the Z^0 boson from the mixing of $W^{3\mu}$ and B^{μ}. The SSB triggers the transition from having a gluon, the $W^{1,2,3}$ bosons and the B boson respectively from the $\mathrm{SU}(3)_{\mathrm{colour}}$, $\mathrm{SU}(2)_L$ and $\mathrm{U}(1)_{\mathrm{weakhypercharge}}$ symmetries, to having a gluon, the $W^{\pm}$ bosons, the Z^0 boson and the massless photon.

A consequence of the spontaneous symmetry breaking is that flavour and mass eigenstates do not coincide. This is the reason for flavour transitions in the SM. The theory postulates the existence of a new additional SM Lagrangian term, known as the Yukawa term:

$$\mathcal{L}_Y = -Y^d_{ij}\overline{Q_{Li}}\epsilon\Phi d_{Rj} - Y^u_{ij}\overline{Q_{Li}}\epsilon\Phi^* u_{Rj}, \tag{2.11}$$

where $Y^{u,d}$ are the Yukawa matrices, ϵ is the anti-symmetric Levi-Civita tensor and Φ is the Higgs field.

Mass terms can be extracted from equation 2.12 by substituting in the vacuum expectation value defined previously. These take the form $\frac{v}{\sqrt{2}}Y^d_{ij}\overline{q_L}q_R$, where q is for any of the six quarks. The Yukawa matrices are in the basis of the flavour eigenstates, so they must be transformed to a version in the basis of the mass eigenstates. The transformation occurs via the diagonalization of the Yukawa matrices, which generates terms which include unitary matrices of the form $V_{qL,R}$. The mass and quark terms then transform as following.

$$\begin{aligned} \frac{v}{\sqrt{2}}Y^d \rightarrow \frac{v}{\sqrt{2}}V_{qL}Y^d v^\dagger_{qR}, \\ q_{iL} \rightarrow V_{qL}q_{iL}. \end{aligned} \tag{2.12}$$

The matrix $(V^u_L)^\dagger V^d_L$ is the Cabibbo-Kobayashi-Maskawa (CKM) matrix, which regulates the transition between flavour and mass eigenstates:

$$\begin{pmatrix} d'_L \\ s'_L \\ b'_L \end{pmatrix} = \begin{pmatrix} V_{ud} & V_{us} & V_{ub} \\ V_{cd} & V_{cs} & V_{cb} \\ V_{td} & V_{ts} & V_{tb} \end{pmatrix} \begin{pmatrix} d_L \\ s_L \\ b_L \end{pmatrix}. \tag{2.13}$$

Further details regarding the SM's flavour structure follow in paragraph 2.2.

2.1.4 The Limitations of the Standard Model

The SM is an extremely successful theory which has been confirmed by experimental findings time and time again. Unfortunately, it is not yet complete. It has several limitations that motivate the particle physics community to look for physics beyond the SM. Firstly, the SM only unifies three of the four fundamental forces of nature. As gravity has not been quantised yet, a Grand Unified Theory of Physics has not been formulated yet. The different coupling strengths of the four forces of physics is also a puzzle.

Astronomical observations of galaxy and galaxy cluster rotation curves [31], gravitational lensing [32] and of the cosmic microwave background all imply the existence of Dark Matter and Dark Energy. These comprise about 95% of the total energy density of the Universe, and the SM does not account for them or give any insight into their nature.

In the SM's mass mechanism, all three generations of neutrinos are massless. Experimental observations of neutrino flavour oscillation [33] imply that neutrinos must have a non-zero mass and that mass and flavour eigenstates must be different. A description of the neutrino mixing is given by the

Pontecorvo-Maki-Nakagawa-Sakata matrix (PMNS), which also allows for CP violation to occur in the neutrino sector [34]. The SM does not include neutrino oscillations.

Another unsolved puzzle is the difference in the amount of matter and anti-matter observed in the Universe. The Big Bang Theory assumes that baryonic and antibaryonic matter was produced in statistical equilibrium during the hot stages of the early Universe. Assuming that the initial state of the Universe was symmetric in terms of matter and antimatter, a process must exist for the Universe to have transitioned from this initial state to the matter-antimatter asymmetry observed today. The transition process must respect the Sakharov conditions [35], which can be deduced when postulating a process which describes different rates of matter and antimatter production. The first condition states that a Baryon number violating mechanism must exist. The second condition states that for the Universe to evolve, interactions must have taken place outside of thermal equilibrium. Finally, a mechanism which violates both C and CP symmetries must exists. The known CP violating processes are not sufficient to account for the magnitude of CP violating processes required to explain the observed matter-antimatter asymmetry of the Universe [36].

Further conceptual issues in particle physics include why no strong CP violation has been observed experimentally despite the presence of a CP violating term in QCD [37]; why are there fermion generations and why are there three in particular; why does the SM have so many free parameters; why do the existing quantum loop contributions point to a higher Higgs mass that that found experimentally at 125 GeV [38].

As an answer to these questions, many different theories have been put forward. Amongst the most interesting and promising ones, is the proposal of the existence of new physics at the TeV energy scale [39]. Experimentally, a great global effort is under way to measure as many SM quantities as possible, to test the theory and detect any signatures of beyond the SM physics. A number of results in measurements related to rare decays of beauty hadrons are in tension with SM predictions, as described in detail in section 2.2.3. The discrepancy between the theory and experimental results is below the 5σ mark, but encourages the community to persevere in testing the SM in rare decay processes of beauty quarks to find signatures of New Physics. Despite the physics community's efforts to answer the above questions, and the numerous experimental Dark Matter searches, there is no evidence for new particles.

2.2 Flavour physics in rare decays of beauty hadrons

The only flavour changing process allowed by the SM occurs via the weak charged current. The transitions between different flavours of quarks depend on the corresponding matrix element of the Cabibbo-Kobayashi-Maskawa (CKM) quark-mixing matrix introduced in paragraph 2.1.3. The CKM matrix is a complex, unitary, 3×3 matrix with four degrees of freedom, one phase, δ_{13}, and three Euler angles, $\theta_{12}, \theta_{23}, \theta_{13}$ [40, 41]. It can be explicitly written as

$$V_{CKM} = \begin{pmatrix} V_{ud} & V_{us} & V_{ub} \\ V_{cd} & V_{cs} & V_{cb} \\ V_{td} & V_{ts} & V_{tb} \end{pmatrix} \tag{2.14}$$

$$= \begin{pmatrix} c_{12}c_{13} & s_{12}c_{13} & s_{13}e^{-i\delta_{13}} \\ -s_{12}c_{23} - c_{12}s_{23}s_{13}e^{i\delta_{13}} & c_{12}c_{23} - s_{12}s_{23}s_{13}e^{i\delta_{13}} & s_{23}c_{13} \\ s_{12}s_{23} - c_{12}c_{23}s_{13}e^{i\delta_{13}} & -c_{12}s_{23} - s_{12}c_{23}s_{13}e^{i\delta_{13}} & c_{23}c_{13} \end{pmatrix}, \tag{2.15}$$

where c_{jk} and s_{jk} are defined as the cosine and sine of the angle θ_{jk} respectively, where $j = 1, 2, 3$ and $k = 1, 2, 3$ [42, 43]. The terms of the CKM matrix are not predictions of the SM and are based on experimental measurements [44] and can be written in terms of the Wolfenstein parameters as

$$V_{CKM} \approx \begin{pmatrix} 1 - \frac{\lambda^2}{2} & \lambda & A\lambda^3(\rho - i\eta) \\ -\lambda & 1 - \frac{\lambda^2}{2} & A\lambda^2 \\ A\lambda^3(1 - \rho - i\eta) & A\lambda^2 & 1 \end{pmatrix} + \mathcal{O}(\lambda^4), \tag{2.16}$$

where $\lambda \sim 0.23$, $A \sim 0.83$, $\rho \sim 0.16$ and $\eta \sim 0.35$ [45]. Transitions between particles of the same generation are of $\mathcal{O}(1)$ and are represented by the diagonal elements of the CKM matrix, V_{ud}, V_{cs}, V_{tb}. Transitions between different generations are instead suppressed by powers of λ. In the SM, CP violation is associated with the single complex phase of the CKM matrix.

One example of rare decays in flavour physics is the process at the heart of this thesis: the $b \to dl^+l^-$ transition. It consists in a b quark decaying into a d quark and a lepton-antilepton pair. The initial and final states quarks have the same charge, but differ in flavour. This transition is also an example of a Flavour Changing Neutral Current (FCNC). Because of the structure of the Lagrangin and the unitarity of the CKM matrix, no FCNC can occur

at tree level in the SM. This is defined in the GIM mechanism, after the physicists Glashow, Iliopoulos and Maiani, who concluded this result [46]. The GIM mechanism also suppresses some loop level processes that would occur in the SM via penguin diagrams [43]. In an effort to go through all the SM process mediators (gluons, photons, Higgs, Z and $W^{\pm}$) one by one, one observes that the charge conservation forbids the $W^{\pm}$ as mediators at tree level. FCNC cannot be mediated by the massless gauge bosons (photons and gluons) either at tree level because the three down-type quarks share the same gauge interactions since they have the same gauge representations. The Higgs boson cannot mediate FCNC at tree level because its Yukawa coupling to fermions is aligned to the mass matrix. Finally, FCNC cannot proceed via the Z^0 boson at tree level because the boson's universal couplings are diagonal. This results in the SM not allowing FCNC at tree level. With tree level FCNCs forbidden in the SM, these processes are only allowed at loop level. A Feynman diagram of a FCNC $b \to dl^+l^-$ transition is illustrated in figure 2.3. This adds further electroweak couplings which reduce the processes' rate. Moreover, FCNC are doubly suppressed, because the GIM mechanism [47] adds a suppression factor of the order of

$$\sim \sum_i \frac{m_i^2}{m_W^2} V_{ib} V_{id}, \tag{2.17}$$

where V_{ib} and V_{id} are elements of the CKM matrix, and the index $i \in [u, c, t]$. The $b \to dl^+l^-$ transition is conceptually similar to the more studied $b \to sl^+l^-$ transition, which drives the $B^+ \to K^+l^+l^-$ decay. The latter transition has a branching fraction $\mathcal{O}(10^{-6})$ [21]. In both cases, the loop process is dominated by the top quark since it is the only quark with a mass greater than the m_W and since both products $V_{ib}V_{id}$, $V_{ib}V_{is}$ are maximised by $i = t$. The difference in suppression factors causes the $b \to dl^+l^-$ transition to occur 1/25 times compared to the frequency of the occurrence of $b \to sl^+l^-$ transition because $|V_{td}|/|V_{ts}| = 0.266 \pm 0.035$ (stat.) ± 0.003 (syst.) [48].

2.2.1 Effective Field Theory

The rare decays involving $b \to ql^+l^-$ processes, where $q = s, d$, have been object of numerous studies. These decays are regulated by two different processes: the electroweak force of the $b \to ql^+l^-$ transition, and the strong force acting between the quarks of the parent B^+ and child K^+, K^0, $\pi^{\pm}$ or π^0 hadrons.

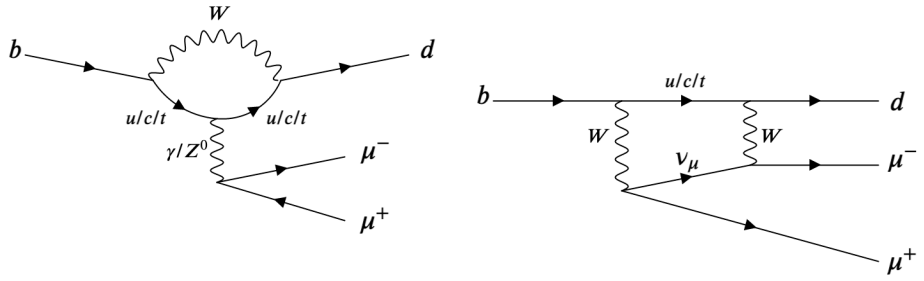

Figure 2.3: Leading order Feynman diagrams allowed in the SM for the $b \to dl^+l^-$ transition. This process is forbidden at tree level so these diagrams contain loops. On the left, a penguin diagram, and on the right, a box diagram. The quark in the penguin diagram's loop can be any of the three up-type SM quarks, and the dominant contribution to this loop is from the top quark.

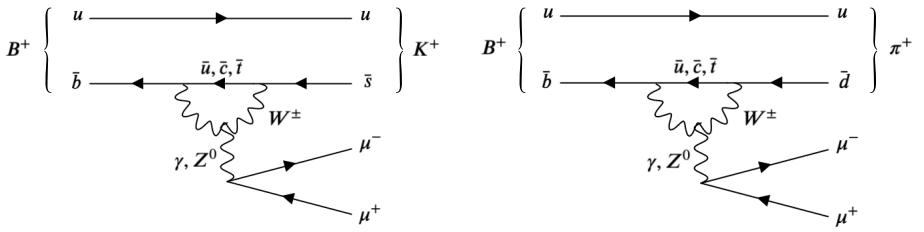

Figure 2.4: Penguin diagrams for the $B^+ \to K^+\mu^+\mu^-$ (left) and $B^+ \to \pi^+\mu^+\mu^-$ (right) decays.

These two processes can be factorised because they are characterised by very different energy scales, the electroweak effects occurring at $m_W \sim 80$GeV, the mass of the beauty quark, ~ 4.18GeV [49], and the strong interaction occurring at $\Lambda \sim 0.1$GeV. These effects can be treated separately via an Effective Field Theory (EFT), where the short distance processes that occur in loops are integrated out and one works with the remaining four local fermion operators. This is equivalent to modelling the decay as a four-body point-like interaction [50]. The difference between the magnitudes of m_b and m_W allows for the construction of an EFT that computes the loop perturbatively and separately from the hadronic process. For this reason, observables which are intrinsically robust against theoretical uncertainties are constructed. The

effective Hamiltonian for this system at a given mass scale μ_s is:

$$\mathcal{H}_{\text{eff}} = -\frac{4G_F}{\sqrt{2}} V_{tb} V_{tq}^* \frac{\alpha_e}{4\pi} \sum_i C_i(\mu_s) \mathcal{O}_i(\mu_s), \tag{2.18}$$

where G_F is the Fermi constant, V_{ij} are elements of the CKM matrix, α_e is the fine structure constant, $C_i(\mu_s)$ are Wilson coefficients and $\mathcal{O}_i(\mu_s)$ are local operators with different Lorentz structures.

Electroweak and strong interactions are separated into the Wilson coefficents or Wilson operators. Those with a scale below μ_s contribute to the local operators $\mathcal{O}_i$, where the i index runs over a complete basis of operators. Those interactions with energy scales above μ_s are encompassed by the Wilson coefficients $C_i(\mu_s)$. The Wilson coefficients and the local operators related to them are evaluated at the renormalization scale of the b quark mass. In equation 2.18 the doubly Cabibbo-suppressed contributions proportional to $V_{ub}V_{uq}^*$ have been neglected [51]. Because $|V_{ud}| >> |V_{us}|$, the $b \to dl^+l^-$ transition is rarer than the $b \to sl^+l^-$ transition. This means that the doubly Cabibbo-suppressed $V_{ub}V_{ud}^*$ terms might be more interesting than the doubly Cabibbo-suppressed $V_{ub}V_{us}^*$ terms if there are non-SM CP violating effects in the electroweak loop. The most important local operators for semi-leptonic decays are the following:

$$\mathcal{O}_7 = \frac{m_b}{e}(\overline{q}\sigma^{\mu\nu}P_{\text{R}}b)(F_{\mu\nu}), \quad \mathcal{O}_{7'} = \frac{m_b}{e}(\overline{q}\sigma^{\mu\nu}P_{\text{L}}b)(F_{\mu\nu}), \tag{2.19}$$

$$\mathcal{O}_9 = (\overline{q}\gamma_\mu P_L b)(\bar{l}\gamma^\mu l), \quad \mathcal{O}_{9'} = (\overline{s}\gamma_\mu P_R b)(\bar{l}\gamma^\mu l), \tag{2.20}$$

$$\mathcal{O}_{10} = (\overline{q}\gamma_\mu P_L b)(\bar{l}\gamma^5 l), \quad \mathcal{O}_{10'} = (\overline{s}\gamma_\mu P_R b)(\bar{l}\gamma^5 l), \tag{2.21}$$

where $P_{L/R} = (1 \mp \gamma_5)/2$ is a left/right handed chiral projection and $F_{\mu\nu}$ is the electromagnetic field strength tensor, m_b is the mass of the beauty quark, $\sigma^{\mu\nu} = \frac{i}{2[\gamma^\mu,\gamma^\nu]}$, and γ^μ and γ_5 are the Dirac matrices. The primed operators are chirally flipped and correspond to right-handed couplings, therefore they are obtained by flipping the chiral projection of the $\mathcal{O}_i$ operators. The operators $\mathcal{O}_9$ and $\mathcal{O}_{10}$ correspond to a vector current and an axialvector current in the dilepton system respectively. The $W^\pm$ boson's charged current interaction has a left-handed chirality. This causes the Wilson coefficient corresponding to the primed operators to be suppressed in the SM by m_q/m_b. The corresponding Wilson coefficients from $b \to sll$ processes have the following values at $\mu_s = m_b$

assuming SM dynamics [51]:

$$C_7^{SM} = -0.3, \qquad C_9^{SM} = +4.2, \qquad C_{10}^{SM} = -4.2. \tag{2.22}$$

Beyond SM theories contemplate the existence of the scalar ($\mathcal{O}_S$, $\mathcal{O}_{S'}$), pseudoscalar ($\mathcal{O}_P$, $\mathcal{O}_{P'}$) and tensor ($\mathcal{O}_T$, $\mathcal{O}_{T5}$) operators defined as:

$$\mathcal{O}_S = \bar{s}P_R b\bar{l}l, \quad \mathcal{O}_{S'} = \bar{s}P_L b\bar{l}l, \tag{2.23}$$

$$\mathcal{O}_P = \bar{s}P_R b\bar{l}\gamma_5 l, \quad \mathcal{O}_{P'} = \bar{s}P_L b\bar{l}\gamma_5 l, \tag{2.24}$$

$$\mathcal{O}_T = \bar{s}\sigma_{\mu\nu} b\bar{l}\sigma^{\mu\nu} l, \quad \mathcal{O}_{T5} = \bar{s}b\bar{l}\sigma^{\mu\nu}\gamma_5 l. \tag{2.25}$$

These are vanishingly small in the SM and would modify the Wilson coefficients such that $C_{i^{(\prime)}} = C_{i^{(\prime)}}^{SM} + C_{i^{(\prime)}}^{NP}$. It is possible for new physics to not couple universally to leptons, in this case some operators will be affected by it and others will not, according to different lepton flavours involved. For this reason operators are most often studied individually, assuming that the remaining operators in the set have SM contributions only. Some beyond SM theories propose the existence of new physics that respects the SM Lagrangian $\mathrm{SU}(2)_L$ gauge symmetry at high mass scales. To test these theories it is useful to rewrite the semileptonic operators in a basis made from left and right projections of the leptons [52, 53]:

$$\mathcal{O}_{\mathrm{LL}} = (\mathcal{O}_9 - \mathcal{O}_{10})/2, \quad \mathcal{O}_{\mathrm{LR}} = (\mathcal{O}_9 + \mathcal{O}_{10})/2, \tag{2.26}$$

$$\mathcal{O}_{\mathrm{RL}} = (\mathcal{O}_9' - \mathcal{O}_{10}')/2, \quad \mathcal{O}_{\mathrm{RR}} = (\mathcal{O}_9' + \mathcal{O}_{10}')/2, \tag{2.27}$$

where the corresponding Wilson coefficients are:

$$C_{\mathrm{LL}} = C_9 - C_{10}, \quad C_{\mathrm{LR}} = C_9 + C_{10}, \tag{2.28}$$

$$C_{\mathrm{RL}} = C_9' - C_{10}', \quad C_{\mathrm{RR}} = C_9' + C_{10}'. \tag{2.29}$$

This basis is sensitive to new physics which only contributes to one of the operators defined in 2.27, and constraints can be imposed on the Wilson coefficients corresponding to the remaining operators. From this basis one can also derive $\mathrm{SU}(2)_L$ relations between top physics and b-decays [54].

The decay amplitude of a B meson decaying to a final state, f, is a function of the form factor:

$$\langle f|Q_i(\mu_b)|B\rangle = \langle \bar{l}lV|Q_i|B\rangle = \mathrm{F}(q^2)\langle \bar{l}l|Q_i|0\rangle. \tag{2.30}$$

The form factor factorises into two parts, one of which depends on the value of the dilepton mass squared. Electroweak decays involving $b \to q l^+ l^-$ transitions are sensitive to new physics in two different kinematic regimes. The first is characterised by the emitted hadron being energetic, with an energy $E \gg \Lambda_{\rm QCD}$ and a low invariant dilepton mass-squared (q^2) in the $[1.0 - 6.0]{\rm GeV}^2/c^4$ interval. In this frame, QCD factorisation is allowed [55]. This involves factorising the decay amplitude of a hadronic B meson decay into a hard-scattering part and a process independent part which contains hadronic quantities including form factors, meson decay constants and light-cone wave functions. The former factor is process dependent and perturbatively calculable, the latter component is non perturbative and composed of universal hadronic quantities. The second kinematic regime corresponds to the region of low hadronic recoil, where q^2 is higher and $\mathcal{O}(m_b^2)$. In this regime the q^2 varies in the $[15.0 - 22.0]{\rm GeV}^2/c^4$ interval and an operator product expansion in $1/m_b$ is applicable [56]. The differential decay rate of the $B^0 \to K^* \mu^+ \mu^-$ decay as a function of q^2 is shown as an example in figure 2.5. Tools to predict the decays involving $b \to q l^+ l^-$ transitions systematically exists. At low q^2 parametric uncertainties from the hadronic transition form-factors, which consist in $1/m_b$ power corrections, are the dominant systematic uncertainty for the theoretical prediction. Conversely, at high q^2 the dominant theoretical systematic uncertainty is caused by the backgrounds from the $c\bar{c}$ resonances that occur beyond the open charm threshold. The two interesting kinematic regimes (low and high q^2) must be investigated separately because of this difference in the theoretical prediction. It must be noted that the amplitude of decay studied in this work also receives contributions from b hadons decaying to charmonia via the process $b \to c\bar{c}s$, which happens at tree level via the charged current. The $c\bar{c}$ resonance then decays to lepton pairs. The biggest effect these resonances have on the study undertaken in this work is the presence of peaks at $q^2 = m^2_{J/\psi}, m^2_{\psi(2S)}$ visible in figure 2.5. Broader resonances are present at high q^2 values, beyond 15.0GeV. [51]. The kinematics limit the q^2 range such that $q^2 < 22.0{\rm GeV}$. These are the reasons behind the chosen q^2 ranges.

The Wilson coefficients can be extrapolated from measurements of observables in different b-hadron decay channels. Some interesting results are presented in section 2.2.3.

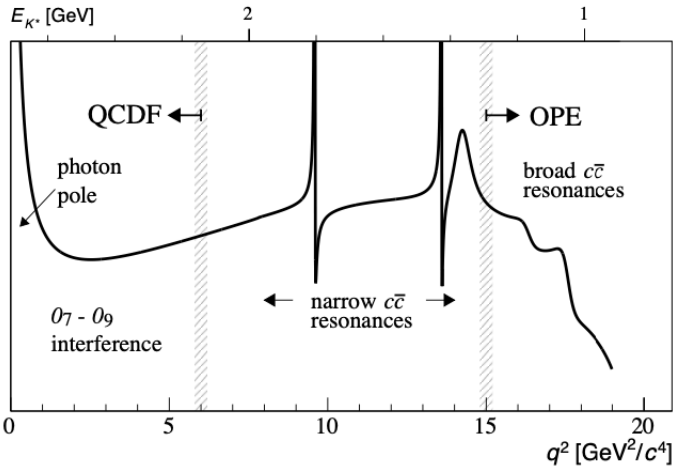

Figure 2.5: Sketch of the differential decay rate of the $B^0 \to K^*\mu^+\mu^-$ decay across the whole kinematic regime. Between 0 and 1GeV$^2/c^4$ the virtual photon contribution, which is accounted for by the $C_{7^{(\prime)}}$ Wilson coefficient, dominates. In the low q^2 region, between 1.0GeV$^2/c^4$ and 6.0GeV$^2/c^4$, the interference between the operators $\mathcal{O}_7$ and $\mathcal{O}_9$ gives sensitivity to the $C_{9^{(\prime)}}$ Wilson coefficient. For central q^2 values, the kinematic region is dominated by the J/ψ and $\psi(2S)$ resonances and therefore not suitable to study the Wilson coefficients. Finally, in the high q^2 region, the contributions from broad charmonium resonances can be described by a local operator product expansion, making this a good regime for Wilson coefficient measurements [51].

2.2.2 Angular observables in processes involving $b \to ql^+l^-$ transitions

The angular distribution of the particles produced from semileptonic decays with $b \to ql^+l^-$ transitions allows to access a set of good angular observables to probe the SM and the presence of signatures of new physics. To understand these observables one must start from the equations for the invariant amplitudes of these decays. The invariant amplitude for $B^+ \to \pi^+\mu^+\mu^-$ is

$$\mathcal{M} = i\frac{G_F\alpha_e}{\sqrt{2\pi}}V_{tb}V_{td}^* f_+(q^2)(F_V p_B^\mu[\bar{l}\gamma_\mu l] + F_A p_B^\mu[\bar{l}\gamma_\mu\gamma_5 l] + \tag{2.31}$$

$$(F_S + \cos\theta_l F_T)[\bar{l}l] + (F_P + \cos\theta_l F_{T5})[\bar{l}\gamma_5 l]), \tag{2.32}$$

where p_B^μ is the 4-momentum of the B^+, $f_+(q^2)$ is the dominant form factor, θ_l is the angle between the direction of the μ^+ and the direction opposite to

the π^+ in the dimuon rest frame, defined as

$$\cos\theta_l = -\frac{\vec{p}_{\pi}^{\,\mu\mu} \cdot \vec{p}_{\mu^+}^{\,\mu\mu}}{|\vec{p}_{\pi}^{\,\mu\mu}||\vec{p}_{\mu^+}^{\,\mu\mu}|} \tag{2.33}$$

$$= +\frac{\vec{p}_{\mu\mu}^{\,B} \cdot \vec{p}_{\mu^+}^{\,\mu\mu}}{|\vec{p}_{\mu\mu}^{\,B}||\vec{p}_{\mu^+}^{\,\mu\mu}|}. \tag{2.34}$$

The vector, axialvector, scalar, pseudoscalar, tensor and axialtensor contributions are represented by the labels V, A, S, P, T and $T5$ respectively. In the SM, only terms F_V and F_A receive sizeable contributions from the Wilson coefficients C_7 and C_9, and C_{10} respectively. All the other contributions are vanishingly small in the SM [57, 58]. In equation 2.33, after boosting from the lab-frame to the B^+ rest-frame and then from the B^+ rest-frame to the dimuon rest-frame, $\vec{p}_X^{\,\mu\mu}$ is the momentum of particle X in the rest-frame of the dimuon system. This also justifies the equality between the two expressions of $\cos\theta_l$. In the second expression, $\vec{p}_{\mu\mu}^{\,B}$ is the momentum of the dimuon system in the rest-frame of the B^+ meson, defining θ_l as a Helicity angle.

The differential decay rate of the $B^+ \to \pi^+\mu^+\mu^-$ decay is

$$\frac{\mathrm{d}^2\Gamma}{\mathrm{d}q^2\,\mathrm{d}\cos\theta_l} = a(q^2) + b(q^2)\cos\theta_l + c(q^2)\cos^2\theta_l \ , \tag{2.35}$$

where

$$\begin{aligned} a(q^2) \propto\ & q^2(\beta^2|F_S|^2 + |F_P|^2) + \tfrac{\lambda}{4}(|F_A|^2 + |F_V|^2) \\ & + 2m_l(m_B^2 - m_K^2 + q^2)\mathrm{Re}(F_P F_A^*) + 4m_l^2 m_B^2 |F_A|^2 \ , \end{aligned} \tag{2.36}$$

$$\begin{aligned} b(q^2) \propto\ & 2q^2(\beta^2\mathrm{Re}(F_S F_T^*) + \mathrm{Re}(F_P F_{T5}^*)) \\ & + 2m_l(\sqrt{\lambda}\beta\mathrm{Re}(F_S F_V^*) + (m_B^2 - m_K^2 + q^2)\mathrm{Re}(F_{T5} F_A^*)) \ , \end{aligned} \tag{2.37}$$

$$c(q^2) \propto q^2(\beta^2|F_T|^2 + |F_{T5}|^2) - \tfrac{1}{4}\beta^2(|F_A|^2 + |F_V|^2) + 2m_l\sqrt{\lambda}\beta\mathrm{Re}(F_T F_V^*) \ . \tag{2.38}$$

Here, $\beta = \sqrt{1 - 4m_l^2/q^2}$ and λ is the Källen function,

$$\lambda \equiv m_B^4 + m_K^4 + q^4 - 2m_B^2 m_K^2 - 2m_K^2 q^2 - 2m_B^2 q^2 \ . \tag{2.39}$$

One of the most relevant angular observable is the forward-backward asymmetry of the dilepton system, which is proportional to the term $b(q^2)$, introduced in equation 2.37 [57]. The interference between the local operators $\mathcal{O}_{7^{(\prime)}}$ and $\mathcal{O}_{9^{(\prime)}}$, respectively photon and vector operators, causes the forward-backward asymmetry to change sign at $q^2 \sim 4\mathrm{GeV}^2/c^4$ [55, 59, 60]. The forward-backward asymmetry can be expressed as a function of the terms $\mathrm{Re}(F_S F_T^*)$ and $\mathrm{Re}(F_P F_T 5^*)$, but $F_{S,P,T,T5} \approx 0$ in the SM, so the SM prediction for the forward-backward asymmetry is zero.

Angular analyses of electroweak penguin decays involving $b \to q l^+ l^-$ transitions use the fact that the angular distribution can be described by the following relationship:

$$\frac{1}{\Gamma}\frac{\mathrm{d}\Gamma(B \to \pi l^+ l^-)}{\mathrm{d}\cos\theta_l} = \frac{3}{4}(1 - F_H)(1 - \cos^2\theta_l) + \frac{1}{2}F_H + A_{FB}\cos\theta_l, \quad (2.40)$$

where F_H is the fractional contribution of (pseudo)scalar and tensor amplitudes, which is zero in the SM operator basis. In particular, A_{FB} is sensitive to the interference of tensor and scalar couplings, and F_{H} is sensitive to tensor couplings [61]. Angular analyses are a way of measuring the A_{FB} and therefore a good probe for New Physics.

Another prominent angular observable is $P_5^{'}$, a bilinear combination of amplitudes that causes the corresponding QCD form-factors to cancel at leading order in a $1/m_b$ expansion [62]. $P_5^{'}$ is part of a set of clean observables called $P^{'}$-family, and it is defined as:

$$P_5^{'} = \sqrt{2}\frac{\mathrm{Re}(\mathrm{A_0^L A_\perp^{L*}} - \mathrm{A_0^R A_\perp^{R*}})}{\sqrt{(|A_0^{\mathrm{L}}|^2 + |A_0^{\mathrm{R}}|^2)(|A_{||}^{\mathrm{L}}|^2 + |A_{||}^{\mathrm{R}}|^2 + |A_\perp^{\mathrm{L}}|^2 + A_\perp^{\mathrm{R}}|^2)}} \quad (2.41)$$

$$\approx \sqrt{2}\frac{\mathrm{Re}(\mathrm{C_0^L C_\perp^L} - \mathrm{C_0^R C_\perp^R})}{\sqrt{(|C_0^{\mathrm{L}}|^2 + |C_0^{\mathrm{L}}|^2)(|C_\perp^{\mathrm{L}}|^2 + C_\perp^{\mathrm{L}}|^2 + |C_{||}^{\mathrm{L}}|^2 + |C_{||}^{\mathrm{L}}|^2)}}, \quad (2.42)$$

where A_0, $A_\perp$ and $A_{||}$ are leading transversity amplitudes contributions that can be factorised in a transversity form factor and C_0 or $C_\perp$ or $C_{||}$, respectively. The form factors contain long-distance QCD information, and the C_i factors are short-term and sensitive to electro-weak effects only.

The advantage of measuring $P_5^{'}$ is that the theoretical uncertainties coming from the predictions of QCD form-factors also cancel at leading order in $1/m_b$, so this observable is sensitive to new physics not included in the SM.

2.2.3 The Flavour anomalies

By definition, rare decays processes are predicted to have very low branching fractions in the SM. As illustrated in previous sections, those that involve $b \to sl^+l^-$ electroweak penguin transitions have good observables to probe the SM and detect any new physics that could be contributing negatively or positively to these processes. A negative contribution would result in an effect being less present than expected, and a positive contribution would result in an effect being more prevalent than expected in the experimental results. The LHCb collaboration has performed some of the most precise measurements to date of the branching fractions and CP asymmetries of processes involving the $b \to sl^+l^-$ and $b \to dl^+l^-$ transitions. Furthermore, LHCb leads in precision on measurements of angular observables from $b \to sl^+l^-$ decays (see below). The findings of these studies fuel the motivation to perform the angular analysis of $B^+ \to \pi^+\mu^+\mu^-$ as a coherent pattern away from SM predictions seems to be present in $b \to sll$ decays.

Branching fractions and asymmetry measurements in $b \to sl^+l^-$ and $b \to dl^+l^-$ decays

Branching fraction measurements of purely leptonic FCNC decays are theoretically clean observables since the uncertainty from the theoretical prediction is small. For example, this uncertainty for the $B^0 \to \mu^+\mu^-$ decay is $\mathcal{O}(1\%)$, an order of magnitude smaller than the uncertainty on the form factor uncertainties which is $\mathcal{O}(10\%)$ [63]. Upper limits on this measurement have been set by LHCb, ATLAS and CMS. The branching fraction measurement of the $B^0 \to \mu^+\mu^-$ can be combined with that of the $B_s^0 \to \mu^+\mu^-$, which was also measured by various collaborations [64–66], to probe the possibility of non-zero BSM scalar and pseudoscalar operators in the $b \to dl^+l^-$ and $b \to sl^+l^-$ processes. The average of the experimental results for each decay has been combined and compared the combination of the averages of the SM predictions in figure 2.6. There is a 2.1σ tension between the SM and this experimental average [67]. Since the CMS, LHCb, and ATLAS average measurement was published, the LHCb collaboration has released a new measurement which is in compatible with previous experimental results and with the SM prediction [68, 69].

The CDF, LHCb and CMS collaborations have measured the branching fractions of the following decay channels in bins of q^2: $B^+ \to \pi^+\mu^+\mu^-$,

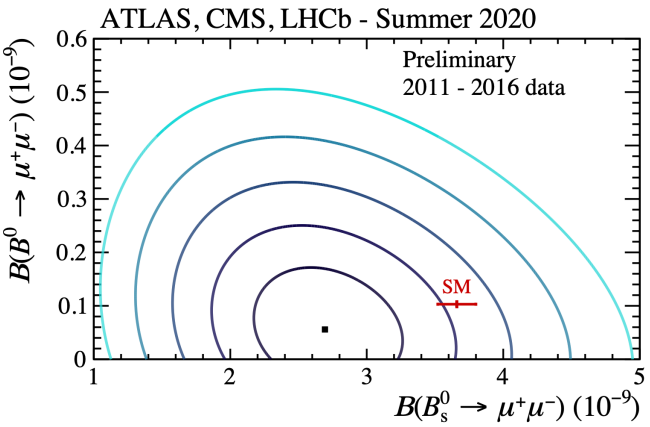

Figure 2.6: Average of the branching fractions of the $B^0 \to \mu^+\mu^-$ and $B_s^0 \to \mu^+\mu^-$ decays measured by the LHCb, CMS and ATLAS experiments. The contours correspond to different likelihood levels. From darkest to lightest shade, the values of $-2\Delta\ln\mathcal{L}$ of 2.3, 6.2, 11.8 19.2 and 30.2 are drawn. The SM prediction is represented by the red point [67].

$B^+ \to K^+\mu^+\mu^-$, $B^0 \to K^{*0}\mu^+\mu^-$, $B_s^0 \to \phi\mu^+\mu^-$ and $\Lambda_b^0 \to \Lambda\mu^+\mu^-$ [1, 70–75].

The differential branching fraction measured by LHCb in bins of q^2 of the $B^+ \to K^+\mu^+\mu^-$ decay is shown in figure 2.7. The measured values are consistently below the SM theoretical prediction [70]. This suggest that some process not present in the SM could be suppressing this particular decay.

Experimental uncertainties in the $B^+ \to \pi^+\mu^+\mu^-$, $B^+ \to K^+\mu^+\mu^-$ and $B^0 \to K^{*0}\mu^+\mu^-$ decays are much smaller than the theoretical uncertainties on their predictions, which is currently the limiting factor and corresponds to $\mathcal{O}(30\%)$ [51]. This limit is caused by the large uncertainties on the hadronic form factors which go into the calculation of the theoretical predictions. For this reason, the CP asymmetry ($\mathcal{A}_{CP}$) between B and $\overline{B}$ decays is a better probe. The CP asymmetry has a SM prediction of $\mathcal{O}(10^{-3})$, but some models which include new physics predict greater values of $\mathcal{A}_{CP}$. All results have $\mathcal{A}_{CP}$ measurements compatible with zero [51].

The branching fractions of the $B^+ \to \pi^+\mu^+\mu^-$ and $B^+ \to K^+\mu^+\mu^-$ decays and the CP asymmetry of the first decay were measured by the LHCb experiment [1]

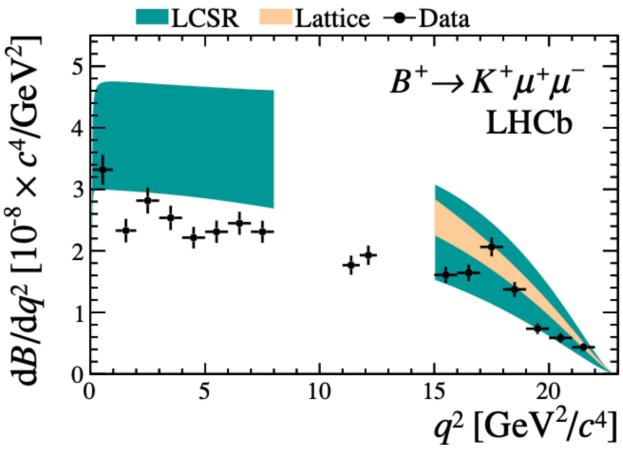

Figure 2.7: Differential branching fraction in bins of q^2 of the $B \to K^+\mu^+\mu^-$ by the LHCb collaboration. Especially at low q^2, the measured value is consistently below the SM prediction. [70].

$$B(B^+ \to \pi^+\mu^+\mu^-) = (18.337 \pm 2.270 \pm 0.435) \times 10^{-9}, \tag{2.43}$$

$$B(B^+ \to K^+\mu^+\mu^-) = (457.576 \pm 9.370 \pm 8.802) \times 10^{-9}, \tag{2.44}$$

$$\mathcal{A}_{CP} = -0.107 \pm 0.124 \pm 0.007. \tag{2.45}$$

The results obtained so far in this area motivate further studies of the $b \to dl^+l^-$ process. Any BSM CP-violating effect caused by scalar and pseudoscalar operators will be more visible in $b \to dl^+l^-$ transitions than in $b \to sl^+l^-$ transitions because of how much more suppressed the former ones are in the SM.

Lepton flavour universality ratios

An intelligent trick to extract information from the branching fraction measurements consists in pairing them up and taking their ratio. Such ratios are known as lepton flavour universality (LFU) ratios. This way the form-factors common to both decays in the pair cancel out, reducing the theoretical hadronic uncertainty on the ratio significantly. For this trick to work, the pairs

must be chosen so that the only difference between them is the non hadronic part of the FCNC process. This was done with the decays $B^0 \to K^{*0} l^+ l^-$, where the leptons in the final state are electrons in one case and muons in the other. The ratio $R_{K^{*0}}$ is then defined as:

$$R_{K^{*0}} = \frac{\int_{q^2_{\min}}^{q^2_{\max}} \frac{d\mathcal{B}(B^0 \to K^{*0}\mu^+\mu^-)}{dq^2}\, dq^2}{\int_{q^2_{\min}}^{q^2_{\max}} \frac{d\mathcal{B}(B^0 \to K^{*0}e^+e^-)}{dq^2}\, dq^2}. \tag{2.46}$$

LHCb found a tension with the SM prediction of $R_{K^{*0}}$ grater than 2σ [76–81]. Similarly, the R_{K^+} LFU ratio shows a SM deviation of about 3.1σ [82]. These results are shown in figures 2.8, 2.9.

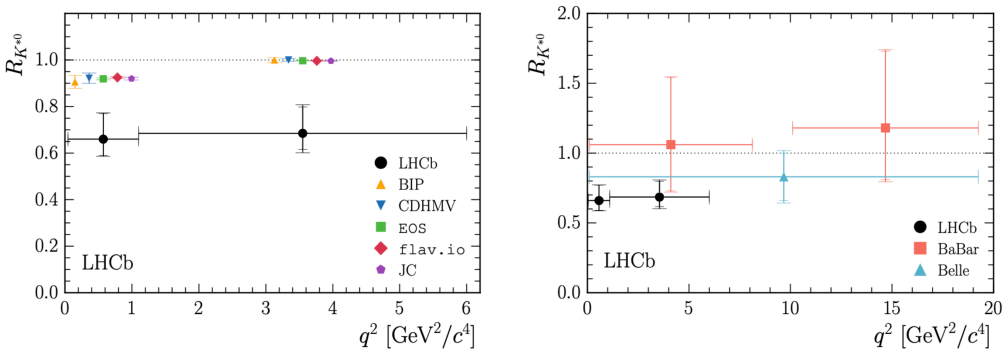

Figure 2.8: LHCb measurement of $R_{K^{*0}}$ compared to various SM predictions on the left, and to experimental measurements from the B factories to the right [83].

Angular observables from processes mediated by $b \to s l^+ l^-$ transitions

Angular observables measured by LHCb in the $B \to K^* \mu^+ \mu^-$ decay are in tension with their SM predictions [86]. This is most evident for the P_5' observable, as shown in figure 2.10. The measured value of P_5' in the

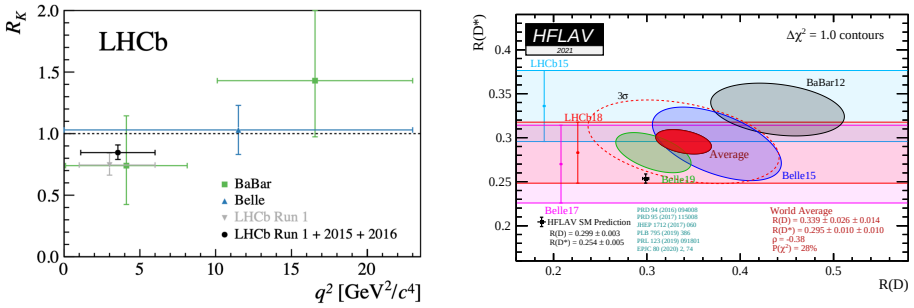

Figure 2.9: On the left, LHCb, Belle and BarBar measurements of R_{K^+} compared to the nominal SM value [84]. On the right, the HFLAV average of the measured and predicted R_D and R_{D^*} values. The SM prediction is in black and the measured average is in dotted red at 3σ and in filled in red at 1σ confidence levels [85].

$(3-10)\text{GeV}^2/c^4$ bins of dilepton mass squared is incompatible and consistently above the SM prediction.

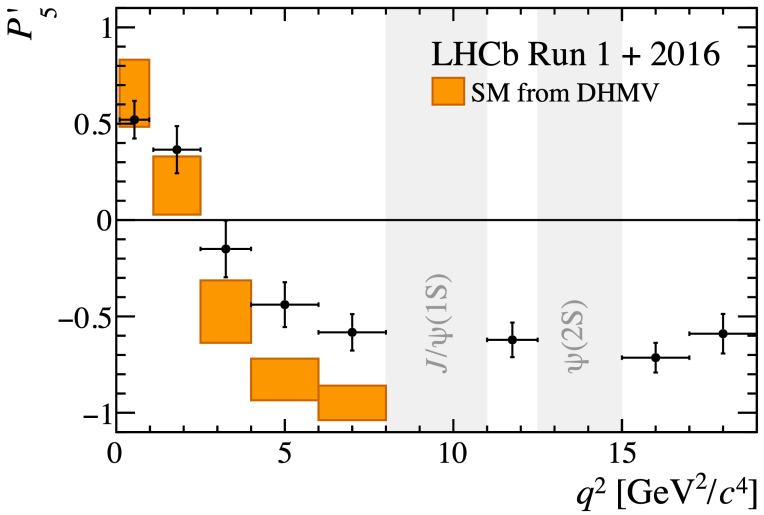

Figure 2.10: The P_5' result from the full set of CP-averaged observables in bins of q^2 for the $B \to K^* \mu^+ \mu^-$ decay. The measurement is compared to a theoretical SM prediction [86].

2.3 New Physics in $b \to s\ell^+\ell^-$ and $b \to d\ell^+\ell^-$ decays

To further understand the contributions to the $b \to s\mu\mu$ transition, the information from the studies of $B_s^0 \to \mu\mu$, R_K, R_{K^*} and other $b \to s\mu\mu$ processes was used to evaluate relevant Wilson coefficients. From the full set of Wilson coefficients, the $C_{10}^{bs\mu\mu}$ and $C_9^{bs\mu\mu}$ coefficients are allowed to differ from the SM predicted value, allowing non-SM-like processes, while the remaining Wilson coefficients are fixed to their SM predictions. Plots of this are shown in figures 2.11, 2.12. The SM predicts both $C_{10}^{bs\mu\mu}$ and $C_9^{bs\mu\mu}$ at 0. The combined experimental results in the 2D parameter space introduce a tension greater than 2σ, strengthening the case for new physics. Global fits of these observables show a strong preference for $C_9^{bs\mu\mu} = -C_{10}^{bs\mu\mu} \cong 0.39$ [87]. Ongoing $b \to s\mu\mu$ and $b \to d\mu\mu$ studies, including this work, are probing this tension.

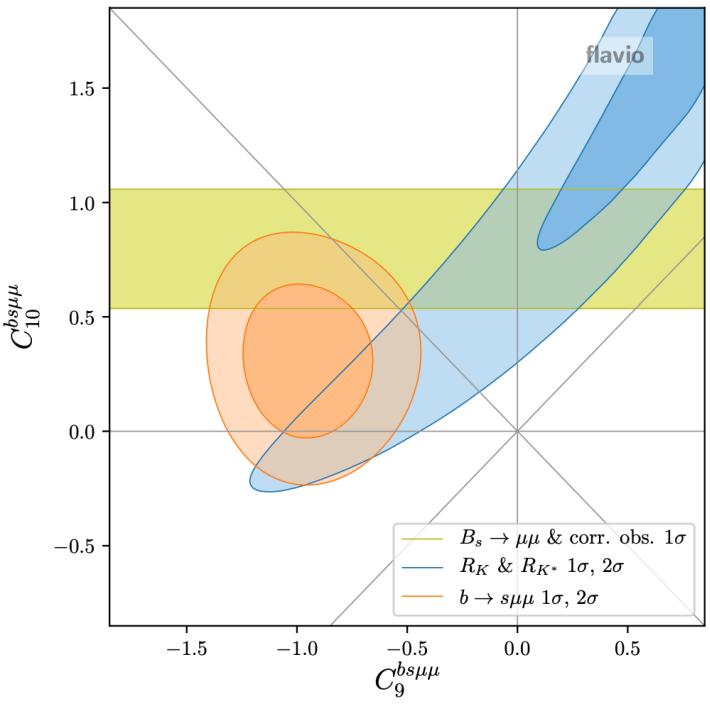

Figure 2.11: New physics contribution to $C_{10}^{bs\mu\mu}$ and $C_9^{bs\mu\mu}$ with all other Wilson coefficients being SM-like. These regions are computed from studies of $B_s^0 \to \mu\mu$, R_K, R_{K^*} and $b \to s\mu\mu$ processes. The SM prediction is at $(0, 0)$. The regions of less intense colour correspond to a confidence level of 2σ, and those of more intense colour correspond to a confidence level of 1σ [87].

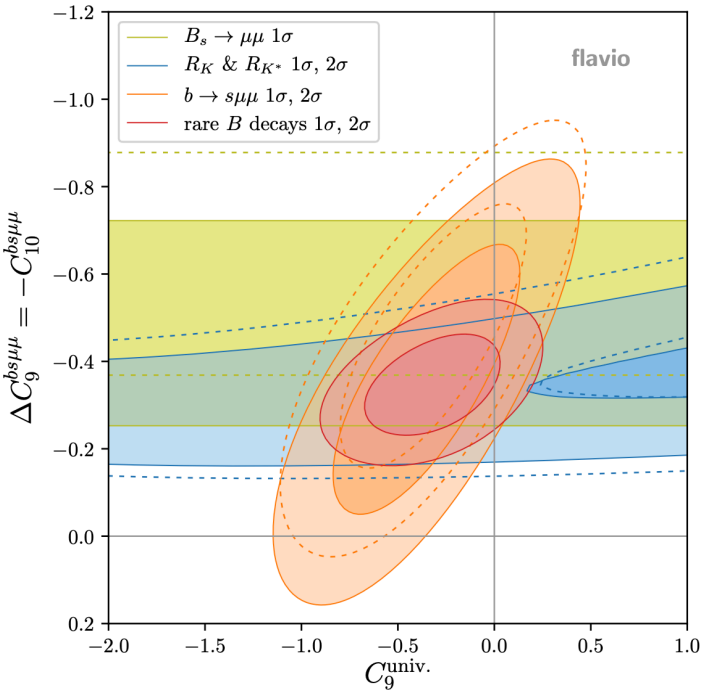

Figure 2.12: Global likelihood fits to the flavour anomalies where it is assumed that the C_9 coefficients of the three lepton flavours is shifted from the SM by the same amount. Furthermore, the assumption that the C_9 and C_{10} muon coefficients are subjected to a further shift of the same magnitude but with opposite sign. In this hypothesis, all other Wilson coefficients are SM-like. These regions are computed from studies of $B_s^0 \to \mu\mu$, R_K, R_{K^*} and $b \to s\mu\mu$ processes. The regions of less intense colour correspond to a confidence level of 2σ, and those of more intense colour correspond to a confidence level of 1σ [87].

The big question in the community is: can the Flavour Anomalies be explained by the SM or are they an observation of beyond SM physics? As anticipated in section 2.2.3, global likelihood fits in the space of the Wilson coefficients have been performed to find an answer [87–96]. In general, these global fits show that the experimental data supports the hypothesis that New Physics is present, i.e. that some of the Wilson coefficients have a non-zero contribution by the $C_i^{(\prime)NP}$ introduced in section 2.2.1, with a tension greater than 5σ from the SM prediction [87]. One example of a global fit is shown in figure 2.11, another interesting global fits is reported in figure 2.12. These fits consider different behaviours of NP. The first one only allows NP contributions to the C_9 and C_{10} coefficients of the muon sector, the second fit assumes the same NP contribution to all lepton flavours, and assumes a further shift from the SM prediction in the muon sector which is of the

same magnitude but opposite sign for the C_9 and C_{10} coefficients. These fits together present a picture where the two NP hypothesis are well constrained since they allow complementary areas of the parameter space. This contributes to the motivation of studying the angular distribution of the $B^+ \to \pi^+\mu^+\mu^-$ as presented in this thesis.

Many theoretical models have been proposed to address the limitations of the SM and to explain the flavour anomalies. In particular, some postulate the existence of New Physics in the $b \to s\ell^+\ell^-$ and $b \to d\ell^+\ell^-$ transitions which might also explain the Flavour Anomalies. A set of models consist in NP particles mediating these transitions at tree level. A NP tree level mediator could in principle explain the Flavour Anomalies. Figure 2.13 is a Feynman diagram of a $b \to s\ell^+\ell^-$ process mediated by a Lepto-Quark (LQ), a new boson that mediates an interaction between quarks and leptons. The signature for the LQ would be a significant deviation from SM predictions of some Wilson coefficients, as illustrated in section 2.2.1. The presence of the LQ translates in baryon and lepton numbers not being conserved individually, while conserving their difference. Another beyond the SM particle proposed to explain experimental anomalies is the Z' boson, which would contribute to the B decays discussed so far as shown in figure 2.13. Direct searches, which consist in looking for the decay products of NP particles, have found no trace of the Z' boson so far [97, 98]. This means that the Z' boson can only be characterised by energy scales greater than the ones we can access with the current accelerator technologies. The advantage of indirect searches is that they rely on loop processes, which can include heavier virtual particles in the loop part of the process. This is the reason for probing the SM via the $B^+ \to \pi^+\mu^+\mu^-$ electroweak penguin decay.

The measured F_{H} value and branching fraction from $B^+ \to K^+\mu^+\mu^-$ and $B^+ \to K^{*0}\mu^+\mu^-$ decays can be used to constrain the values of C_T, as can be seen in figure 2.14. The angular parameter F_{H} is proportional to terms which feature scalar couplings of the form $|C_i + C_{i'}|$, where $i = S$, S', P, P'. The dual terms $|C_i - C_{i'}|$ can be extrapolated from measurements of the time-integrated branching fraction of $B_s^0 \to \mu^+\mu^-$. The combination of this information can constrain the real and imaginary parts of the scalar coefficients. This is done and the constraints on $\mathrm{Re}(C_i \pm C_{i'})$ are illustrated in figure 2.15. The constraints on $\mathrm{Im}(C_i \pm C_{i'})$ are very similar to those in figure 2.15 so they are not shown [61]. Vector couplings contribute to F_{H} via the term $(C_{10} + C_{10'})$. The effects of a non-zero $C_{10,10'}^{NP}$ on the constraints on C_S

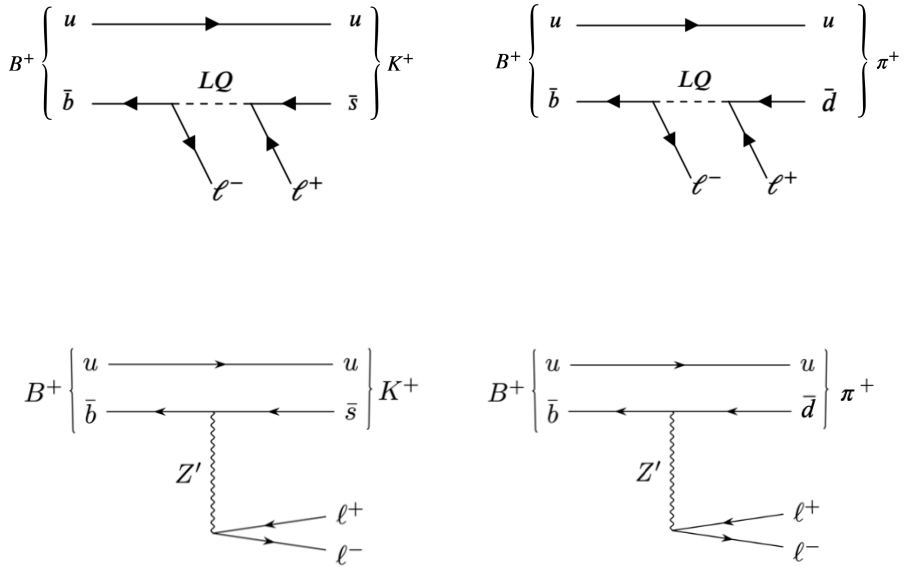

Figure 2.13: Proposed New Physics processes for the $B^+ \to K^+\mu^+\mu^-$ and $B^+ \to \pi^+\mu^+\mu^-$ decays. On top: B decays proceed at tree level via the production of a NP particle called the lepto-quark. On the bottom: The decays proceed via the production of a beyond SM particle, the Z' boson, at loop level.

are visible in figure 2.16. With the current measurements, these constraints do not exclude nor confirm the presence of NP. Future measurements, including this work, and improvements on theoretical uncertainties could clarify the picture.

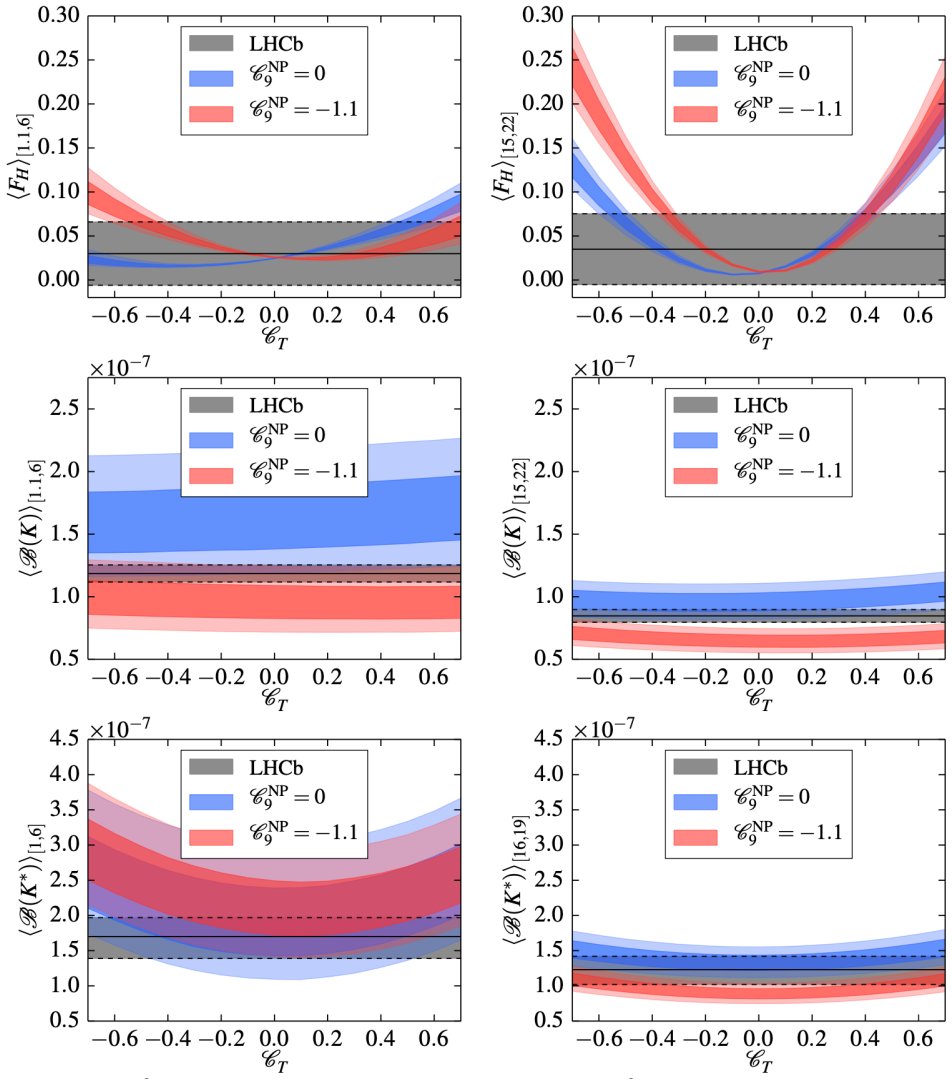

Figure 2.14: Constraints on the Wilson coefficient C_T by the measured branching fraction of the $B^+ \to K^+\mu^+\mu^-$ and $B^+ \to K^{*0}\mu^+\mu^-$ decays and by the measured $F_{\rm H}$ from the same decay. The constraints differ in different q^2 bins. The gray band corresponds to the constraints from the LHCb measurements. The blue and red bands respectively represent the constraint on C_T for the specific cases of $C_9^{NP} = 0$ and $C_9^{NP} = -1.1$. The shades on each band show the theoretical uncertainty at 68% and 95% probability of the prior predictive [61].

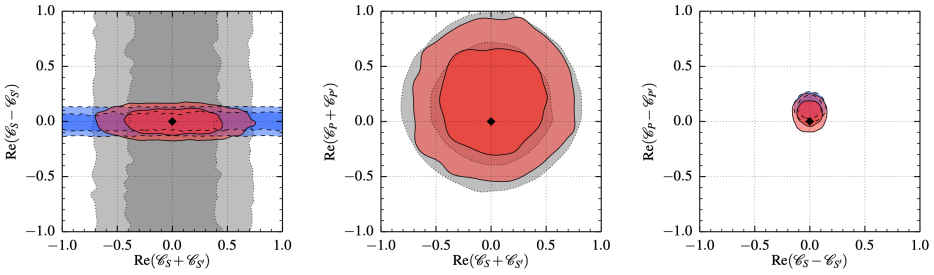

Figure 2.15: Constraints on the coefficient $C_{S,S',P,P'}$ from $F_{\rm H}$ only, in dotted gray, from the time-integrated branching fraction measurement of the $B_s^0 \to \mu^+\mu^-$, in dashed blue, and from a combination of measurements which includes non-zero $C_{9,9',10,10'}$, in solid red. The darker and lighter shades of red correspond respectively to the 68% and 95% probability. The combination constraints receive contributions from the decay channels $B_s^0 \to \overline{\mu}\mu$, $B^+ \to K^+\mu^+\mu^-$, $B0 \to K^{*0}\mu^+\mu^-$ and from the form factors for the $B \to K$ and $B \to K^*$ processes. The SM prediction is indicated by the black diamond [61].

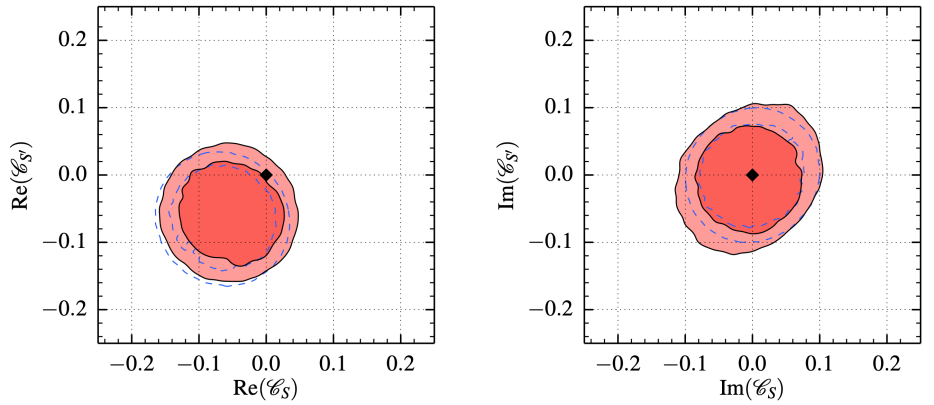

Figure 2.16: Constraint to the scalar couplings $C_{S,S'}$ in a SM effective field theory scenario, where $C_{10,10'}^{NP}$ is non-zero, and the constraints are results of combining contributions from the decay channels $B_s^0 \to \mu^+\mu^-$, $B^+ \to K^+\mu^+\mu^-$, $B0 \to K^{*0}\mu^+\mu^-$ and from the form factors for the $B \to K$ and $B \to K^*$ processes. The darker and lighter shades of red correspond respectively to the 68% and 95% probability. The constraints from the combination of the time-integrated branching fraction measurement of the $B_s^0 \to \mu^+\mu^-$ and all the $B \to K\mu^+\mu^-$ processes produce the constraint in dashed blue. The SM prediction is indicated by the black diamond [61].

Chapter 3

The LHCb Detector

The angular analysis of the $B^+ \to \pi^+\mu^+\mu^-$, described in chapter 4, was performed using data collected by the Large Hadron Collider beauty experiment (LHCb), positioned along the LHC (Large Hardon Collider), at CERN. The work done for the development of the TORCH detector, described in chapter 5, was done on site, at CERN. This chapter provides a brief explanation of the LHC accelerator and describes the LHCb detector.

3.1 The CERN organisation and the Large Hadron Collider

CERN is an intergovernmental organisation which has developed many different accelerators and accelerator-based facilities on its site along the border between Switzerland and France, on the outskirts of Geneva. The accelerators and colliders present at CERN are illustrated in figure 3.1. The Large Hadron Collider (LHC) [99] is a proton accelerator and collider. The LHC machine sits underground, inside the tunnel originally built for the LEP collider [100]. It is composed of two 26.7km long rings, which can be filled with counter-rotating beams, and which intersect four times along their circumference to allow for proton-proton collisions to take place. The experiments ATLAS, CMS, ALICE and LHCb, placed at the collision points, take data to study particle interaction at high energies.

The protons colliding in the LHC begin their journey in a hydrogen gas canister. The hydrogen is ionised to isolate the protons, which are accelerated by a linear accelerator called LINAC2. The resulting 50 MeV beam is accelerated by increasingly larger circular accelerators, namely the

Proton Synchrotron Booster (PSB), the Proton Synchrotron (PS) and the Super Proton Synchrotron (SPS), to raise its energy to 450 GeV. The proton bunches that make up the beam are injected into the two LHC beam-pipes in opposite directions, as is shown in figure 3.2. Each bunch has $\mathcal{O}(10^{11})$ protons and there are about 5600 bunches in total in the beam. The LHC accelerates both beams to the desired collision energy, which in 2011, 2012, and 2015-2018 corresponded respectively to 3.5 TeV, 4 TeV and 6.5 TeV per beam.

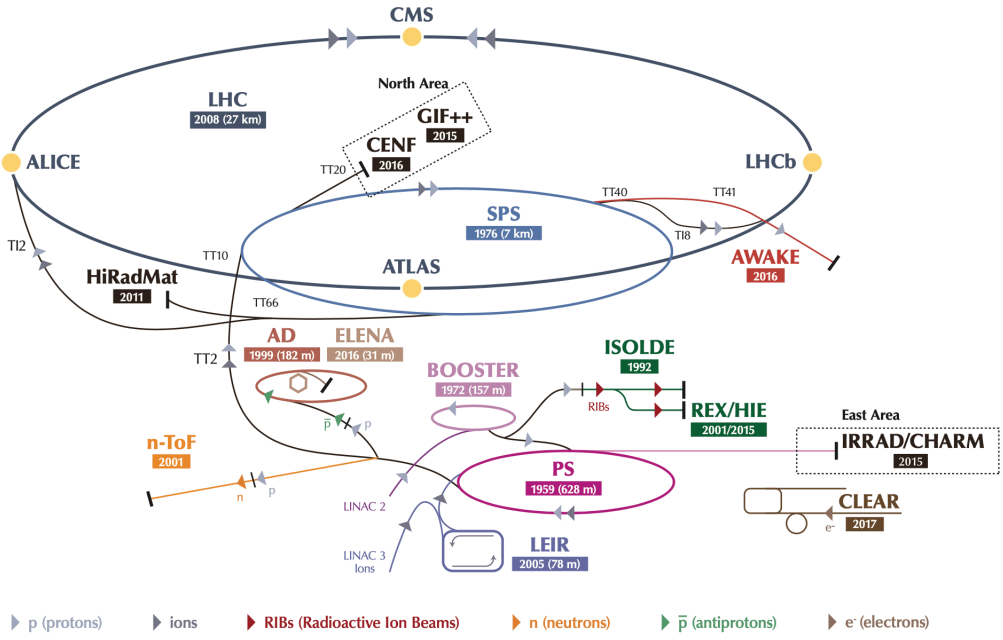

Figure 3.1: A schematic of the CERN accelerator complex [101]. The colour scheme in the legend at the bottom shows which particles are used in each accelerator. This work uses data collected by the LHCb experiment situated at Point 8 of the LHC.

The beams are accelerated with the use of radio-frequency cavities (RF cavities) operating in the straight sections of the LHC. 1232 superconducting dipole magnets are used to bend the beams in the arced LHC sections. The beam is collimated and kept stable with the use of quadrupole, sextuple, octupole and decapole magnets [102]. The different magnets and RF cavities are arranged in the LHC tunnel between the LHC sections containing the CMS, ATLAS, ALICE and LHCb experiments, and between the sections dedicated to beam injection and beam dumps, with the goal of maximising collisions at the beam crossing points. The beam-pipe is evacuated using cryogenic vacuum techniques.

The beams cross at four different interaction points, where the ATLAS,

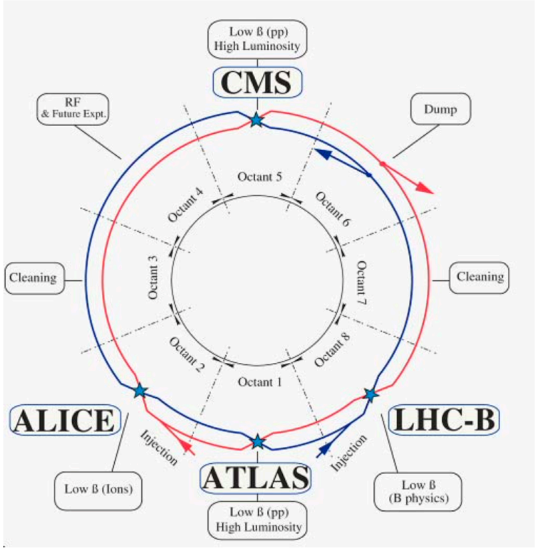

Figure 3.2: A schematic of the LHC beams [102].

CMS, ALICE and LHCb detectors take data. Besides providing proton proton collisions, the LHC also performs proton-ion and ion-ion collisions. These kinds of processes will not be discussed here as they are outside the scope of this work.

The proton beams inside the LHC are not continuous. The protons are accelerated and grouped in bunches. For every LHC proton fill there is a maximum of 2808 bunches per beam, with a minimum time difference between each bunch of 25 ns. This corresponds to a bunch crossing frequency of 40 MHz [102].

The quantity used to describes the beam intensity in accelerators is instantaneous luminosity. It is defined as

$$\mathcal{L} = \frac{1}{\sigma}\frac{dN}{dt} = \frac{N_B(N_p^2 f)}{4\pi\delta^2}S, \tag{3.1}$$

where σ is the cross section of a given process, $\frac{dN}{dt}$ is the number of given processes generated per second, N_B is the number of bunches in the beam, N_p is the number of protons per bunch, δ is the transverse size of the beam at the beam crossing point, f is the revolution frequency and S is a geometrical factor that depends on the beam crossing angle [103].

While the LHC's design maximum instantaneous luminosity is $1 \times 10^{34}\text{cm}^{-2}\,\text{s}^{-1}$, the LHCb detector was designed to operate at a maximum

instantaneous luminosity of $2 \times 10^{32} \mathrm{cm}^{-2}\,\mathrm{s}^{-1}$ to maximise the probability of a one and only proton-proton interaction per bunch crossing. The LHCb detector has exceeded its instantaneous luminosity goal for most of the data-taking campaigns, usually operating at double the maximum design instantaneous luminosity. The LHCb detector operated at a lower instantaneous luminosity than that of the LHC to minimise the number of tracks that populate each event, and to extend the lifetime of its sub-detectors. Figure 3.3 shows the instantaneous luminosities of the ATLAS, CMS and LHCb detectors over a fill. It also illustrates the integrated luminosity at the LHCb detector over the course of the data-taking campaigns. The LHCb instantaneous luminosity is kept constant using the "luminosity levelling" method. This consists in varying the beam overlap to compensate for changes in the number of protons per bunch, which decrease over time in a fill. A constant instantaneous luminosity allows the LHCb collaboration to have a uniform detector condition and to use the same trigger configuration for a given fill.

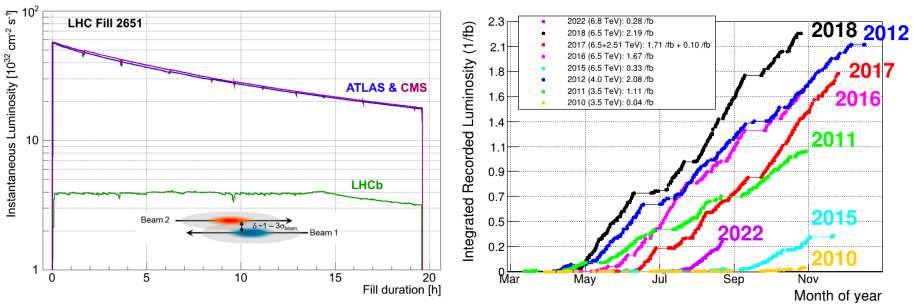

Figure 3.3: Left: The instantaneous luminosity at the ATLAS, CMS and LHCb detectors over the course of a fill. The LHCb instantaneous luminosity is constant at $4 \times 10^{32} cm^{-2} s^{-1}$, with 5% fluctuations, for about 15 hours. [104].
Right: Integrated luminosity recorded by the LHCb experiment over the years belonging to Runs 1, 2 and 3 [105].

The LHCb detector has completed two data-taking campaigns known as LHC Run 1 and LHC Run 2. The former began in 2011, with $0.98\,\mathrm{fb}^{-1}$ integrated luminosity and 7 TeV collision energy, and ended in 2012, with $1.92\,\mathrm{fb}^{-1}$ integrated luminosity and 8 TeV collision energy. Run 2 lasted from 2015 to 2018 with a collision energy of 13 TeV and an integrated luminosity of $0.28\,\mathrm{fb}^{-1}$, $1.62\,\mathrm{fb}^{-1}$, $1.69\,\mathrm{fb}^{-1}$, $2.16\,\mathrm{fb}^{-1}$ for the four years respectively. A new data-taking campaign, known as LHC Run 3 has begun in the second half of 2022 and will terminate in 2025. The LHC is currently the only proton-proton machine which allows to perform the angular analysis of the $B \to \pi\mu\mu$. This

is because its collision energy is large enough for a statistically significant number of signal events to be produced over the data-taking period.

Great part of the physics program of the LHCb experiment is based on b and c decays. This makes the LHC's $b\bar{b}$ and $c\bar{c}$ production from proton-proton collisions essential to the physics results of the experiment. The main production modes for both sets of quarks are gluon interaction processes. A minority is produced via valence quark scattering [106, 107]. The relevance of each production process is a function of the energy of the interaction and on the energy of the LHC collision. At the LHC production energies, the next to leading order contributions are the most abundant ones in $b\bar{b}$ and $c\bar{c}$ production. These consist of flavour excitation processes, with gluon splitting processes being close seconds. The $b\bar{b}$ production mechanisms are illustrated via their Feynman diagrams in figure 3.4, and Feynman diagrams 2 and 3 show the processes which dominate the total $b\bar{b}$ production cross-section. The $b\bar{b}$ production at LHCb results in both beauty quarks flying off in the same direction (see fig 3.5).

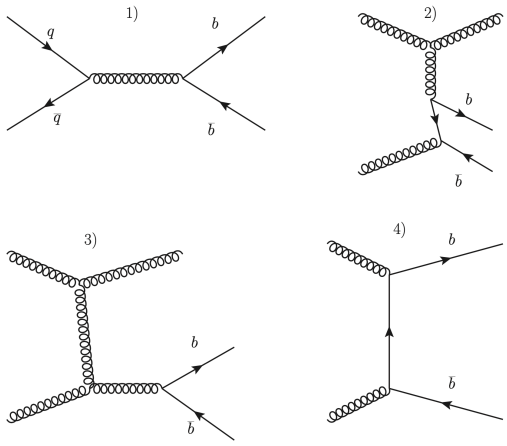

Figure 3.4: Allowed $b\bar{b}$ production mechanisms. Channel 1 corresponds to quark-antiquark annihilation, channel 2 is flavour excitation, Feynman diagram 3 illustrates gluon splitting, and mechanism 4 is gluon-gluon fusion. Figure taken from [108].

3.2 The LHCb experiment

The LHCb experiment is a single-arm forward spectrometer designed to study the production and decay of beauty and charm hadrons. This work focuses on the version of the LHCb detector operated between the years 2011 - 2018, collecting the data runs referred to as Run 1 and Run 2. The large centre of mass energy of the LHC beams provides a large $b\bar{b}$ production cross-section of 500 µb at $\sqrt{s} = 13\,\text{TeV}$. This corresponds to about $10^{11} - 10^{12}$ $b-$hadrons produced in a normal data taking year [109]. The LHCb experiment differs from ATLAS and CMS in that its geometry is optimised to cover the region in which the b and $\bar{b}$ production is largest. The experiment covers the pseudo-rapidity region of $2 < \eta < 5$, and 49% of the total produced $\bar{b}$ or b quarks are produced in the LHCb detector's acceptance (fig.3.5), as these are mainly either produced in the forwards direction or in the backward direction.

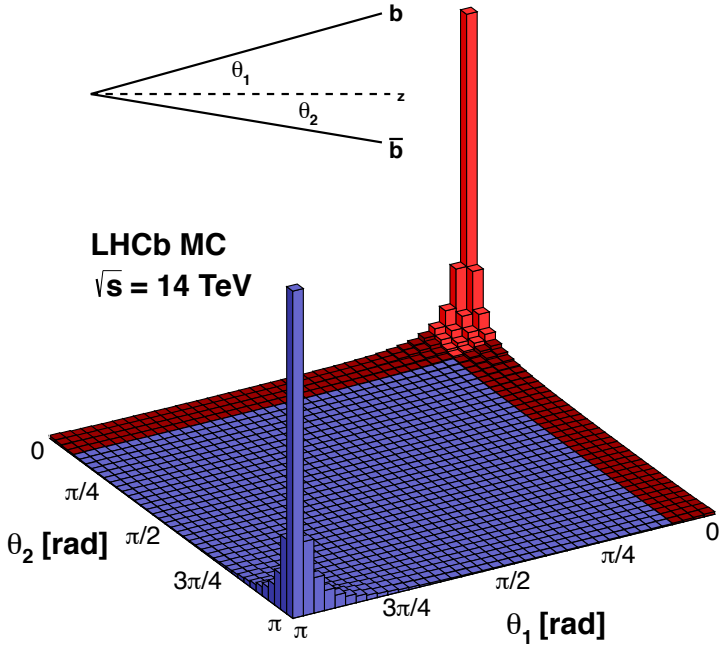

Figure 3.5: Angular distribution of b and $\bar{b}$ quarks in the LHCb simulation [110]. The LHCb detector is a single-arm forward spectrometer, so it can only detect one $b\bar{b}$ peak

The LHCb detector is placed at intersection point 8 of the LHC and is comprised of several sub-detectors arranged in a line along the beam-line which track and identify particles produced in the proton-proton collisions. A view of the experimental set-up can be seen in figure 3.6. This is a side view of the LHCb detector, in the $y - z$ plane. The x axis develops into the view, with its origin point positioned at the centre of the Vertex Locator subdetector. A detailed overview of the LHCb detector is given in [111]. Its performance is described in [104]. The following sections will describe the LHCb sub-detectors and systems.

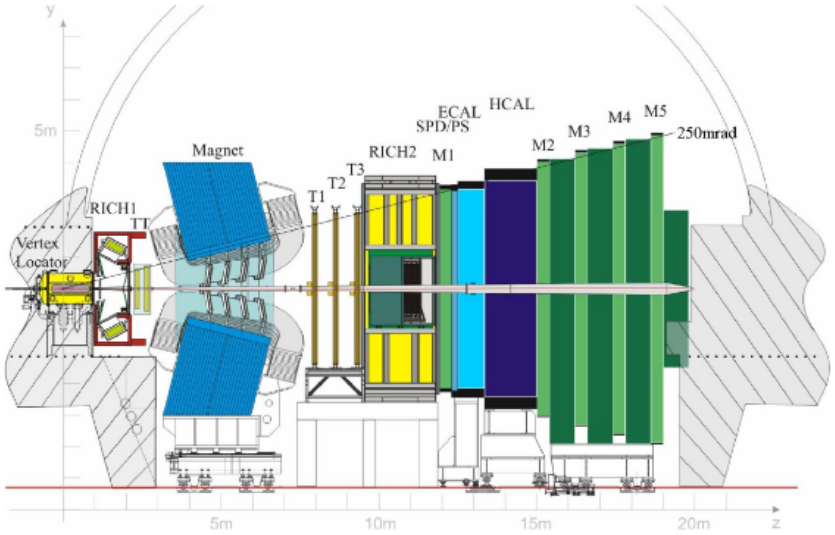

Figure 3.6: Side view of the LHCb detector. The individual sub-detectors are labelled. Figure taken from Ref. [111]

3.3 Particle tracking in LHCb

The LHCb tracking system comprises the Vertex Locator (VELO), and the following tracking stations: Tracker Turicensis (TT), T1, T2 and T3. The VELO and the TT are silicon microstrip detectors placed upstream of a dipole magnet. The T1-T3 stations are set-up downstream of the magnet and each consists of a central silicon detector (Inner Tracker, IT) and an outer, straw-tube-based detector (Outer Tracker, OT). The TT and the IT make up the Silicone Tracker (ST) and were developed together. Sections 3.3.1, 3.3.2, 3.3.3, 3.3.4 respectively describe the VELO, the TT, the IT and the OT. Section 3.3.6 gives an overview of the vertexing and tracking performance

at LHCb. Figure 3.7 provides a sketch of the tracking system and of the reconstructed track categories at LHCb. LHCb tracks can be assigned to a category according to where the hits composing each track are registered. Tracks with hits registered in the VELO are called VELO tracks. VELO tracks have no momentum information. Tracks that comprise hits in the VELO and in the TT tracker are categorised as Upstream tracks. Tracks made of hits from the TT and T1-3 stations are Downstream tracks. T tracks are formed of hits coming from the T1-3 station only, and tracks that pass through all the tracking stations are labelled as Long tracks. T tracks are the least useful for physics studies since they lack information regarding momentum.

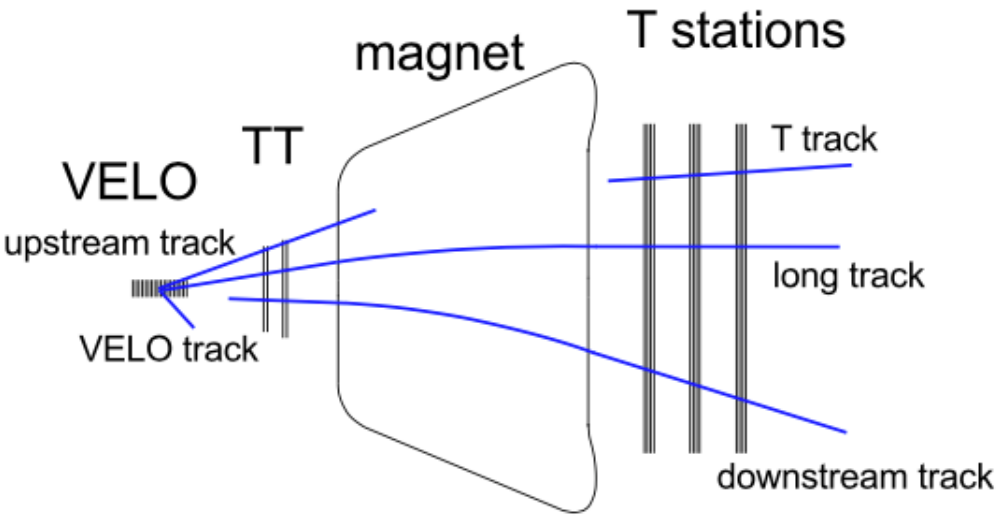

Figure 3.7: Tracking system and track types at LHCb in the x-z plane [112].

3.3.1 The Vertex Locator

Collisions occur in the region surrounded by the Vertex Locator (VELO), so this is the first of the LHCb sub-detectors encountered by any particle produced from pp collisions. The VELO provides precise measurements of the initial track coordinates. These are then used to reconstruct the primary vertices and the displaced secondary vertices, a distinctive feature of b and c hadron decays [113]. The distance between the primary and secondary vertices in the case of b and c hadron decays corresponds to a few millimetres. The VELO consists of two halves, each made of 21 semi-circular silicon strip modules placed with an r-ϕ geometry along the beam, which constitutes the z

axis. One half of the VELO is shown in figure 3.8.

Each VELO module is composed of an r-sensor and a ϕ-sensor, and corresponds to a position along the z coordinate. The r-sensor measures the radial distance of a hit from the beam axis. The ϕ-sensor measures the azimuthal position of a hit. Combined they give a 2D position in the $x - y$ plane. For the VELO acceptance to cover the full azimuthal range, the two VELO halves overlap. This overlap causes a 1.5 cm displacement along the z-axis between the two halves.

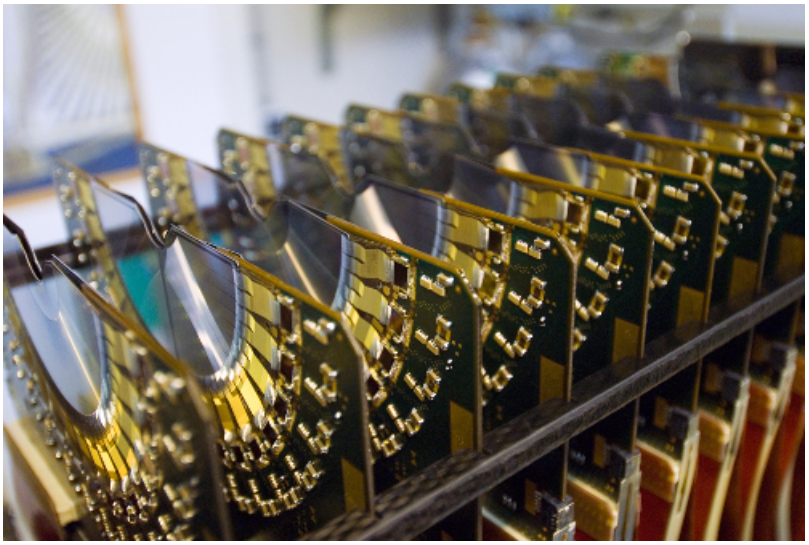

Figure 3.8: Close-up photograph of the VELO halves [114].

Each r-sensor is divided into sections spanning 45° to minimize the occupancy and reduce strip capacitance. The silicon strips are arranged in concentric semi-circles, with the pitch varying linearly from 38 µm at the inner radius to 101.6 µm at the outer radius, resulting in track measurements at different radii contributing to the impact parameter with approximately equal weights. The ϕ-axis is orthogonal to the r-sensor strips. The ϕ-sensor is divided into two concentric regions, an inner and an outer region, to better control strip pitch and occupancy, the interface between the regions is at a radius of 17.25 mm. The strip pitch of the inner (outer) region varies from 38 µm(39 µm) to 79 µm (97 µm). The strips are positioned with a skew of 20° (10°) away from to the orthogonal direction to the radial axis. The modules are arranged so that adjacent ones have opposite skews, improving the pattern recognition of tracks. The distance between the VELO modules closest to the interaction point is of 3.5 cm, and increases for modules downstream of the

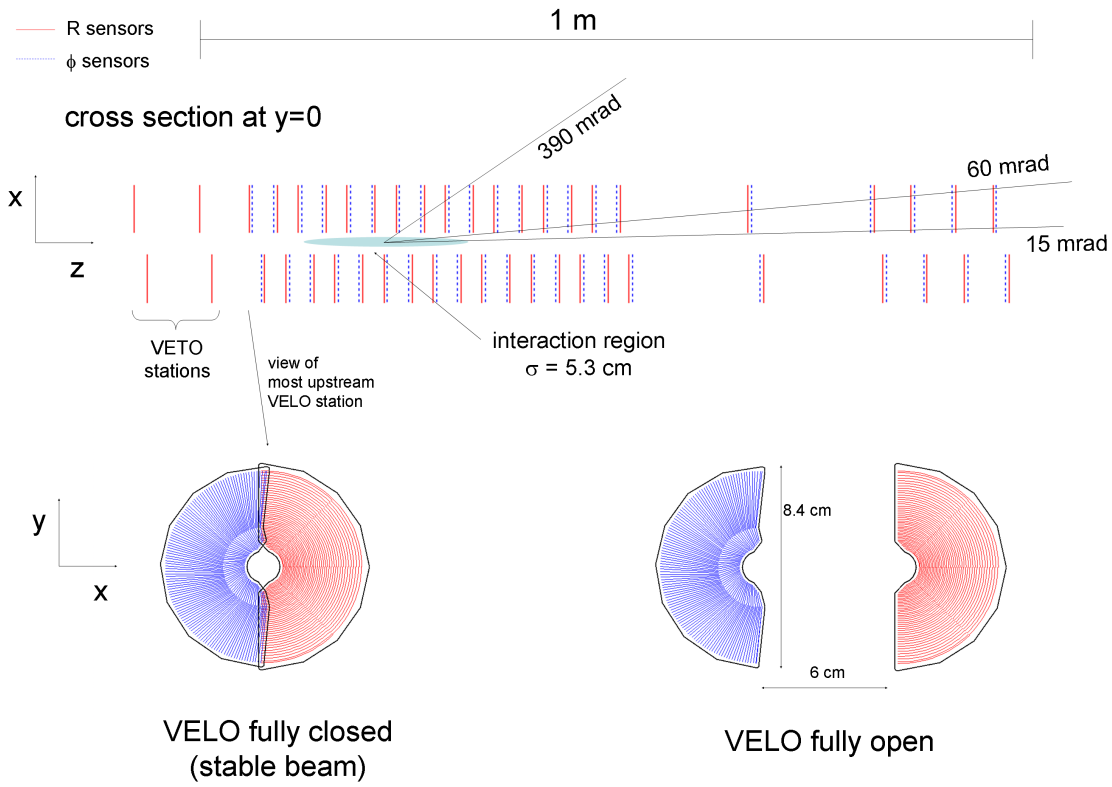

Figure 3.9: Top: Sketch of the assembled VELO modules. Bottom: Sketch of a VELO module with the r-ϕ geometry. [111]

interaction point. The position of each module results from the requirement that a track which falls in LHCb's acceptance must traverse at least four VELO modules. The VELO r-ϕ geometry and the velo module placement is illustrated in figure 3.9. The VELO modules are designed to be at a distance of 8.2 mm from the beamline when taking data. As the LHC prepares the beam for data-taking, during beam injection and ramping up phases, the beam is larger, and the detector-safe distance from it increases. For this reason, the VELO is a retractable sub-detector. When LHCb is not taking data, the VELO is retracted by 30 mm. The final position of the VELO halves during data-taking runs is recentred after every fill, to allow for shifts in the beam position.

3.3.2 The Tracker Turicensis

The TT is placed downstream of the RICH1 sub-detector and upstream of LHCb's dipole magnet and covers the whole LHCb acceptance. It serves two purposes: to reconstruct long-lived particles that decay outside the VELO, such as Λ and K^0_S; and to reconstruct tracks of soft particles whose low momentum causes them to be deflected out of the acceptance of the tracking stations downstream of the magnet. The TT detector is a planar station and comprises four layers of silicon microstrips arranged in a so called *(x-u-v-x)* geometry. The first and last layer have vertical strips, while the two inner layers have strips rotated by -5° and 5° from the vertical axis to improve the overall resolution of the TT. An inner layer is visible in the $x-y$ plane in figure 3.10, which highlights components of the layer. These are explained in detail in the following paragraph. The arrangement of the layers introduces a stereo angle, a practice similar to that employed in the design of the VELO modules. There is a 27 cm separation between the second and the third layers introduced to improve tracking reconstruction.

Each TT layer is fashioned out of half-modules. There are seven silicon sensors to a half-module, arranged in a column. For the first and third layer (second and fourth), one half-module sits directly above and below the beampipe, while seven (eight) full, 14 silicone sensor long modules, are positioned to either side of the beampipe. Three stacked readout electronic units are placed at the extremity of each half-module. To account for the difference in particle density along the length of the half-module, each half-module is split into smaller regions, labelled L,M and K. The L region covers the four silicon sensors furthest from the beam. The sensors in the L region have the lowest occupancy and are connected to one of the three stacked readout unit. The M sector consists of the next three silicon sensors along the half-module towards the beamline. The sensors in this region are connected to the second readout unit. Lastly, the K sector is the silicon sensor closest to the beam. This sensor is connected to the third readout unit.

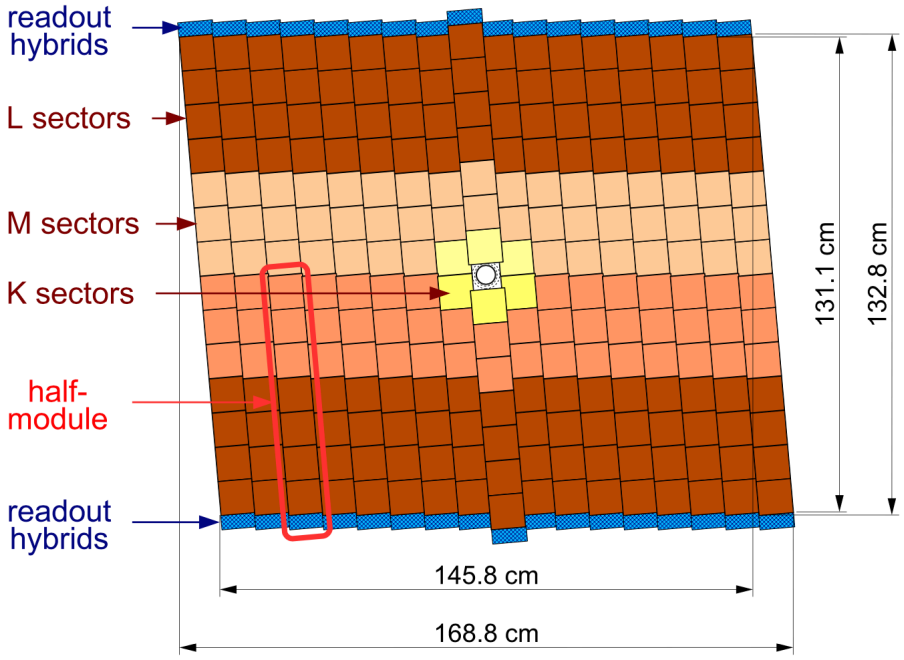

Figure 3.10: Illustration of the layout of the third layer of the TT [111].

3.3.3 The Inner Tracker

The inner tracker consists of the inner regions of each of the tracking stations downstream of the LHCb magnet, T1-3. Figure 3.11 is a sketch of one of these inner regions. The area covered by the IT has a high track multiplicity, being traversed by $\sim 20\%$ of all the particles in LHCb's acceptance, because it is so close to the beampipe. This is the reason for the different design of the IT and the OT. The position of the boundary between IT and OT was determined by the latter's maximum occupancy limit. The IT shares the TT's conceptual design, comprising of four layers of silicon sensors arranged in the *(x-u-v-x)* configuration. A view in the $x - y$ plane of the first layer of the IT in shown in figure 3.11. The IT differs from the TT because its building blocks are a single silicon sensor module and two silicon sensor module. A row of seven single sensor modules sits above and below the beampipe. Seven rows of two silicon sensor modules are positioned to either side of the beamline.

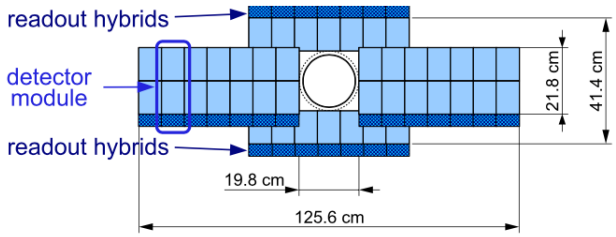

Figure 3.11: Illustration of the x layer in one of the IT stations in the $x-y$ plane [111]. The single silicon and two silicon detector modules as well as the position of the readout electronics are visible. The circle at the centre of the image is the beampipe.

3.3.4 The Outer Tracker

The OT is a drift-time detector which relies on a gas straw-tube design. The base concept is a long tube, filled with ionizable gas, with a wire going down the middle of the tube. A potential difference is applied to the wire and the tube. Particles traversing the tube ionise the gas, resulting in moving charges. The current produced in this manner indicates that a particle has passed through the detector. The OT is the outer planar region of the three tracking stations downstream of the LHCb magnet. Measuring the track trajectory after the LHCb magnet, which is needed to reconstruct the track momentum, is the purpose of this detector. The choice of design results in a maximum occupancy of 10% at a luminosity of $2 \times 10^{32}\,\mathrm{cm}^{-2}s^{-1}$.

Modules comprising two staggered layers of 64 drift tubes (inner diameter of 4.9 mm), containing a mixture of Argon and CO_2 in a 70% : 30% proportion respectively, are arranged in four layers to create a tracking station. The four layers are arranged in the *(x-u-v-x)* formation already described in section 3.3.2. The modules are 4850 mm long to either side of the beampipe, and 2425 mm long if they are directly above and below the beampipe. The readout electronics is connected to the far end of the modules. The gas mixture employed in the OT was chosen because of the fast drift time (less than 50 ns) and low material budget. Figure 3.12 shows some tracking stations of the ST and OT detectors.

3.3.5 The LHCb Magnet

The magnetic field is generated by a warm dipole magnet inserted between the TT and the T1 station. The field is vertical, along the y direction, and it is small in the VELO and in the tracking stations. The LHCb magnet (fig.3.13)

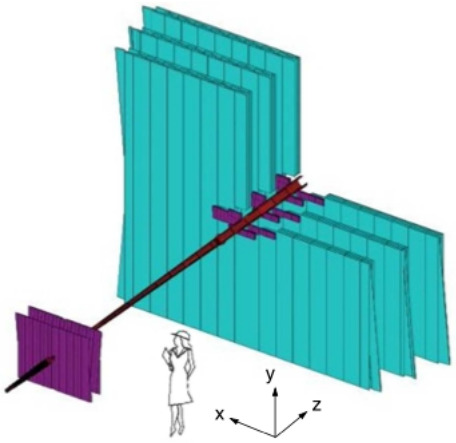

Figure 3.12: Sketch of the tracking stations. ST in purple and OT in turquoise [111].

comprises two saddle shaped coils, placed symmetrically around the z axis, enclosed in an iron yoke. The coils are made of aluminium and are separated into 15 layers.

The magnet covers the full LHCb forward acceptance, ± 250 mrad vertically and ± 300 mrad horizontally, and produces a 4 T m integrated magnetic field over a 10 m distance. The polarity of the magnet is inverted during data-taking runs to account for any charge asymmetry introduced by the hardware of the detector. This is beneficial for *CP* violation studies as it allows for more control over the systematic effects of the detector.

The magnetic field is well understood in the 10 m between the interaction point and the RICH2 sub-detector thanks to the use of an array of Hall probes, which confirmed a relative precision of $\sim 10^{-4}$. This level of understanding of the field is necessary for the tracking system to achieve the momentum precision of $\delta p/p < 5 \times 10^{-3}$, required for particles with momentum lower than 100GeV/c. The magnetic field generated further from the magnet is low enough that the trajectory of the tracks is not significantly affected, nor does it interfere with any sub-detectors. This is not the case for the RICH detector system. The photon detectors used in the RICH are at high risk of failure even in such a small magnetic field. The solution is to protect the delicate equipment with an iron case that shields the sensors from the magnetic field.

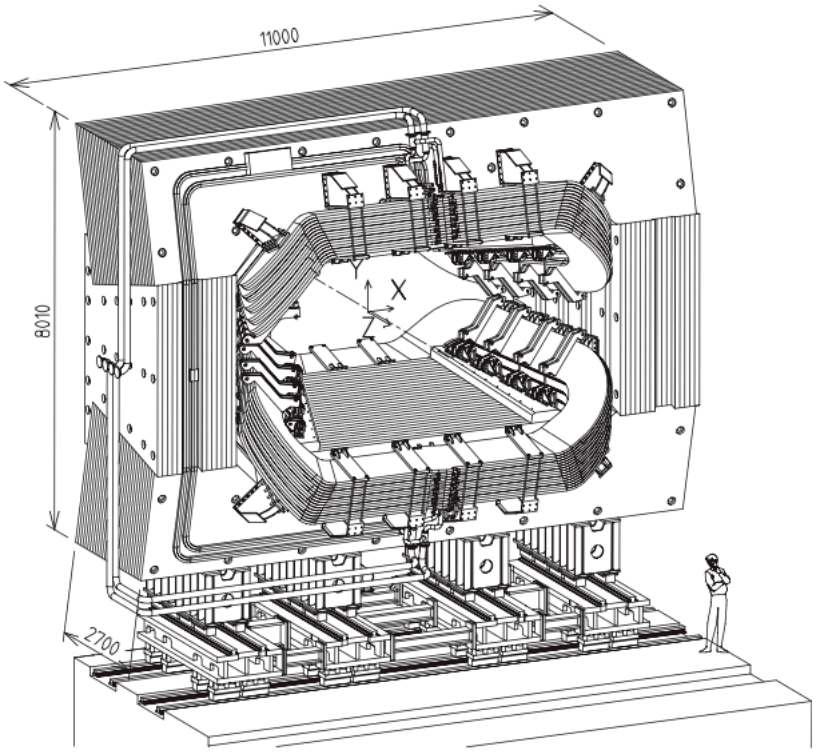

Figure 3.13: Sketch of the LHCb magnet. This point of view is from downstream of the magnet. Dimensions stated in the sketch are in mm [111].

3.3.6 Vertexing and Tracking Performance

The lifetime of the B mesons leads to a decay topology comprising a primary vertex (PV) and a secondary vertex (SV) which mark in time and space the production point and decay point of the B. These are well separated by $\sim 1\,\text{cm}$ at LHCb. The LHCb experiment successfully identifies PVs and SVs, correctly traces particles as they traverse the LHCb detector and interact with the sub-detectors; and identifies the particles involved in an event. The exact location of primary and secondary vertices in any LHCb event is crucial to achieve the experiment's research goals of studying b and c quark processes. The vertex position is determined using all the tracks that originate from that vertex. The vertex resolution can be measured by dividing these associated tracks into two random groups. Then each group of tracks is used to reconstruct the location of the vertex. A typical PV is characterised by 25 reconstructed tracks, which result in a vertex resolution of $13 \times 13 \times 71\,\mu\text{m}$ in the $x - y - z$ direction.

Each track is assigned a value for its impact parameter (IP). The IP is the distance of closest approach of a track to its PV. B meson decays are characterised by tracks with large IP values as the meson flight length is in the order of several mm, displacing secondary vertices significantly. As this work details the analysis of a B meson decay, these tracks are particularly relevant. The IP can also be used to reject background which could otherwise contaminate the signal population. The IP track resolution is measured by fitting a PV with N tracks to measure its IP. One track is removed randomly from the fit, which is performed again. The variation between the IP values is the IP resolution. This depends on the transverse momentum of the tracks involved, as can be seen in figure 3.14. The best IP resolution achieved was $(10.8 \pm 23.2)\mu\text{m}/p_{\text{T}}$, which equates to $< 2\mu$m for high momentum tracks and $< 9\mu$m for low momentum tracks [115]. The average IP in B decays is $\mathcal{O}(1.5\text{cm})$.

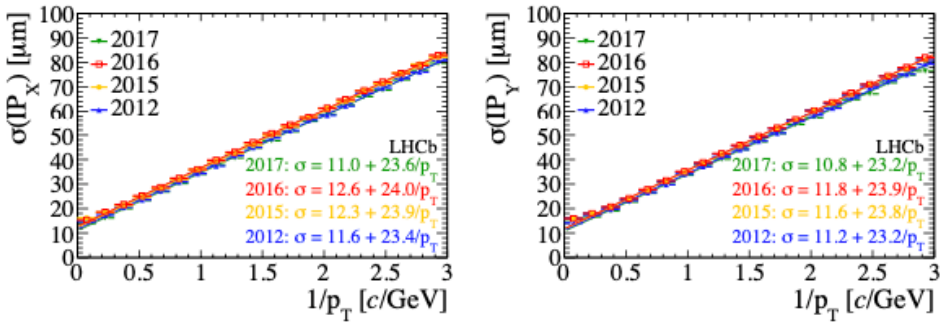

Figure 3.14: Impact parameter resolution as a function of p_T, along the x axis on the left and along the y axis on the right [115].

3.4 Particle Identification at LHCb

The physics studies performed at the LHCb experiment rely on correctly identifying the final-state products of the pp collisions. These can be charged hadrons (pions, kaons, protons), muons, electrons and photons. The former are identified using two Ring Imaging Cherenkov (RICH) detectors. Electrons and photons are identified by the calorimetry system, which measures their energies as well as those of hadrons. As described in paragraph 3.4.2, electrons and photons are identified by their different signatures in the calorimetry system. The muon detector system detects muons. This system comprises five muon stations, of which four are placed at the furthest distances from the

interaction point. Amongst all the particles produced in pp collisions, muons travel farthest because of their minimal interaction quality. For this reason, muons are the only products of pp collisions to reach the four muon stations mentioned previously. More detail regarding muon identification is given in sec. 3.4.3. The position the Particle Identification (PID) detectors take in LHCb is shown in figure 3.6.

3.4.1 The RICH Detectors

Two RICH detectors perform charged hadron ID in the momentum range 2–100 GeV/c [111]. The comprehension of the decay channel studied in this work relies vitally on correct pion/kaon separation to distinguish signal from background.

The RICH detectors exploit the phenomenon of Cherenkov radiation. Cherenkov radiation occurs when a charged particle traverses an optically transparent, dielectric medium at a speed greater than the phase velocity of light in the medium. When this happens, the medium emits coherent radiation in a cone at an angle θ along the path of the particle. The angle θ is given by the speed of the particle, v_p, the refractive index of the material, n, and the speed of light in vacuum, c as

$$\cos\theta = \frac{c}{nv_p}. \tag{3.2}$$

By measuring the Cherenkov angle and momentum of a particle, one can infer the mass and therefore the species. The Cherenkov angle as a function of momentum for final state particles are shown in figure 3.15.

In both sub-detectors, Cherenkov light is focused and reflected out of the instrument's acceptance region with the use of spherical and flat mirrors. The emitted Chrenkov radiation is cone-shaped, so as it reflects off the spherical mirrors it is focused into an image of a ring. The photons are then detected using Hybrid Photon Detectors (HPDs). HPDs are sensors that collect photons via photocathodes, which then emit photoelectrons that are accelerated towards inversely polarised silicon anodes via the use of an electric field. The anodes absorb the photoelectrons, producing electon-hole pairs, which are detected, producing an electric signal that identifies the detection of photons. The spatial resolution of the HPDs is 0.72 mm, limited by the finite pixel size of the silicon pixel array. The RICH detectors are partially shielded from the magnetic field generated by the LHCb magnet to protect

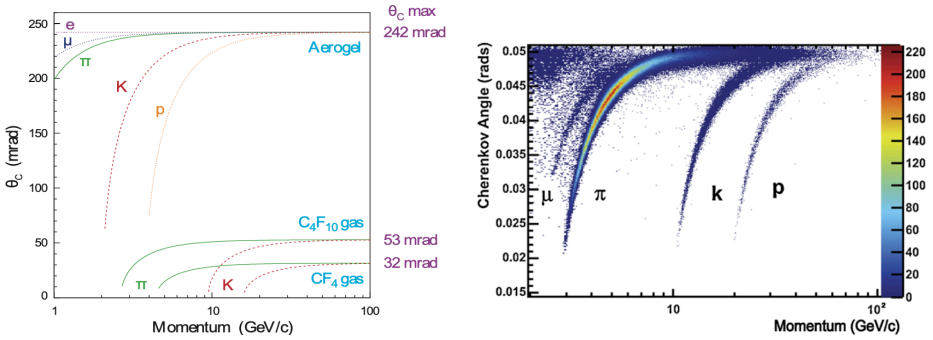

Figure 3.15: Left: Cherenkov angle as a function of momentum for different particles and different media used in the LHCb RICH detectors [111]. Aerogel was originally selected, but was eventually removed from RICH. Right: Reconstructed Cherenkov angle as a function of track momentum in RICH1 instrumented with C_4F_{10} radiators only [116].

the HPDs, whose performance would otherwise be negatively affected because the field would distort the trajectories of the photoelectrons.

RICH1 is located upstream of the magnet and has an acceptance from ±25 mrad to ±300 mrad horizontally and ±250 mrad vertically. It is designed to observe low momentum particles, in the 2–60 GeV/c range. It was originally designed to use C_4F_{10} based radiators to cover the 10–60 GeV/c range and an aerogel radiator for the 2–10 GeV/c range. Because of the higher occupancy in Run 2, the aerogel radiator's performance was degraded and the radiator was removed after Run1 [117]. The angular resolution of RICH1 is shown in figure 3.15.

RICH2 is located downstream of the magnet, designed to observe particles in the $\sim$ 15–100 GeV/c range, and has an angular acceptance from ±15 mrad to ±120 mrad horizontally and ±100 mrad vertically. The placement downstream of the magnet, and the higher momentum range allow for the choice of a smaller acceptance since the magnet sweeps away low-momentum particles. RICH2 uses a CF_4 radiator, chosen for its suitable momentum range and low chromatic dispersion (refractive index $n \sim 1.0005$ [116]). The TORCH detector discussed in chapter 5 aims to complement the current RICH detectors to improve the LHCb PID performance during data-taking Runs 5 and 6.

Particles are identified by the RICH system based on a likelihood ratio test with an algorithm called the global pattern-recognition. The measured pattern of hit pixels in the RICH photon sensors across all RICH radiators is

compared to the patterns generated by a set of known particles hypotheses. These are electron, muon, pion, kaon and proton hypotheses. The maximum likelihood when varying the particle's hypothesis is identified. The hypothesis that maximises the likelihood is assigned as the identity of the particle [118].

3.4.2 The Calorimeter system

The calorimeter system comprises an Electromagnetic Calorimeter (ECAL), a Hadronic Calorimeter (HCAL), a Scintillating Pad Detector (SPD) and a Preshower Detector (PS), whose position in LHCb can be seen in figure 3.6. To improve LHCb's PID performance, energy of electrons and photons is measured by the ECAL, while that of hadrons is measured by both the HCAL and the ECAL [104]. Furthermore, the calorimetry system plays an important role in the hardware trigger, which is described in section 3.5.

The four subdetectors alternate pads of organic scintillators made of doped polystyrene as active medium and absorber layers. Particles traversing the medium interact electromagnetically or hadronically and cause cascading particle showers. The processes occurring in electromagnetic interactions are Compton scattering, pair production and bremsstrahlung radiation. Hadronic interactions consist of inelastic processes and result in pion production and cascading electromagnetic processes which create further showers. Layers of lead, an absorbing material, are placed between the layers of pads to prompt the showers from particles traversing the detectors. The PS and SPD pads projectively match the ECAL. These three subdetectors work in conjunction to discriminate electrons, photons and pions. Photons do not scintillate as they pass though the scintillators, but they cause showers in the lead. Specifically, photons traversing the SPD will only interact with the lead, initiating a shower whose particles then traverse and trigger the PS. This combination of a lack of signal in the SPD and a signal in the PS is a signature sign of a photon. Electrons are identified by the fact that they do produce scintillation. Electrically charged particles are more likely to interact and shower in the SPD and neutral particles tend to deposit energy in the ECAL. Because of the material and thickness of the absorber layer, optimised to 15 mm, electrons predominantly shower in the PS, while pions do not. The cause of this is that lead's radiation length is much shorter than its interaction length. The PS and ECAL performance combined with tracking information provides a pion-rejection rate of $\sim 99\%$ with an electron acceptance rate of 95% [119].

The ECAL consists of layers of scintillator tiles interspersed with 2 mm

thick absorber material, both arranged transversal to the beam axis. With depths of 25 radiation lengths, it is designed to fully contain electromagnetic showers triggered by highly energetic photons and electrons. The energy resolution of the ECAL is $\sigma_E/E = (8.5 - 9.5)\%/\sqrt{E} \bigoplus 1\%$, while its π^0 mass resolution is $\sim 8\,\mathrm{MeV}/c^{\,2}$ [119].

The HCAL's purpose is to contribute to the hardware trigger. It is composed of layers of absorber material and scintillator tiles arranged parallel to the beam axis. The absorber material is iron. This subdetector is not designed to fully contain the hadronic showers produced in it, partially because this is not necessary to contribute to the hardware trigger, and partially because of the limited space available in the LHCb cavern. The HCAL is 1.65 m deep, which equates to 5.6 interaction lengths. The HCAL's energy resolution is $\sigma_E/E = 69\%/\sqrt{E} \bigoplus 0.9\%$ [119].

3.4.3 The Muon system

The muon system is a fundamental aid to triggering in LHCb as it provides fast information for the high-p_{T} muon trigger at the earliest level, in the hardware trigger (L0), as well as muon identification for the high-level trigger (HLT) and offline analysis [118]. The LHCb muon identification system is composed of five stations, M1-M5, which can be seen in figure 3.6 and in figure 3.16.

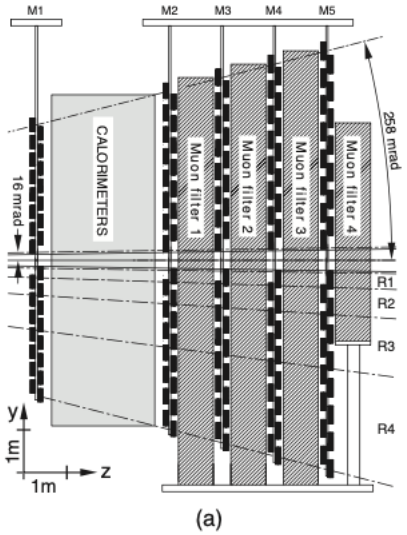

Figure 3.16: Sideview of the Muon System stations M1-M5 [118].

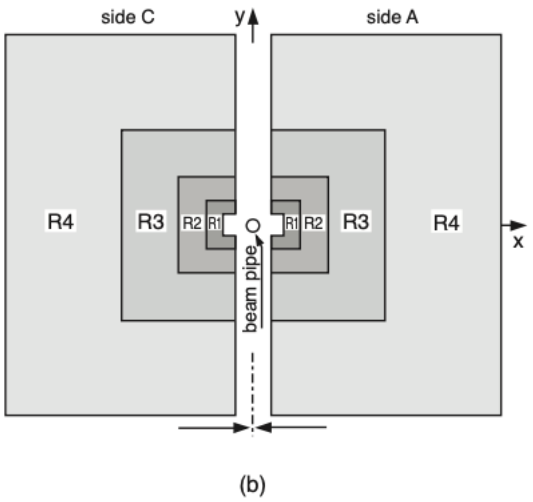

Figure 3.17: A muon station from the beam's point of view divided into the four sections of approximately the same flux [120].

Layers of iron, used as absorber material, are interlaced with the muon stations to exploit the penetrative nature of the muons and stop other particles from entering the muon stations. The layers of iron are referred to as "muon filters". The muon stations are rectangular projections to cover the whole acceptance of the LHCb detector [118]. The first station, M1, is positioned upstream of the calorimeters to improve the p_{T} measurement of the trigger and to provide muon track segments to the tracking system. Each station is divided into four concentric areas (R1-R4) in such a way that each area has approximately the same amount of particle flux. The regions are visible in figure 3.17. The muon system stations, with the exception of Region1 of M1 (M1R1), make use of Multi-Wire Proportional Chambers (MWPC) to detect muons. The wires are filled with a gaseous mixture of CO_2, Ar and CF_4 at a $40 : 55 : 5$ ratio. M1R1, the region with the highest particle flux, is composed of Gas Electron Multiplier (GEM) Chambers instead of MWPCs. The chambers in the M1 station are arranged in 2 layers, while those in the M2-M-5 stations are arranged in four layers. The stations M1-M3 provide information on the direction of the muon track. M1 is positioned upstream of the calorimeter system to measure a more accurate p_{T} since the muons have not traversed the densely packed SPD, PS nad HCAL. This measurement is provided to the trigger. The cumulative p_{T} resolution of the M1-M3 stations is of 20% in the bending plane. The remaining stations, M4

and M5, have a smaller granularity and provide information on penetrative particles. The spatial resolution varies across the five muon stations and across the regions within each station. Region 1 of M1, closest to the interaction point and close to the beam, has the best resolution, at $\sigma_x \times \sigma_y = 4 \times 10\,\mathrm{mm}^2$. The poorest resolution is that of the R4 region of the M5 station, where $\sigma_x \times \sigma_y = 150 \times 180\,\mathrm{mm}^2$ [120]. The minimum momentum needed for a muon to cross all five stations is $6\,\mathrm{GeV}/c$. The MWPC regions of the muon system have a measured efficiency greater or equal to 99.3%. The M1R1 region's efficiency is of 98.7%. The muon system efficiency benefits from the redundancy introduced by layering the chambers in each station.

3.4.4 The PID performance

The information gathered by the LHCb's PID detectors can be combined to construct a hypothesis of a track or final-state particle's nature. This is done using two alternative methods. The first method was LHCb's original PID algorithm and consists in constructing an overall likelihood value for a track to be a specific particle, relative to its likelihood of being a pion. The overall likelihoods are calculated by combining results from the sub-detectors' reconstruction algorithms. The second PID method is more recent and feeds the subdetector data to a neural network. This allows it to assign an ID to a track by using the correlations between the hits in the various PID detectors, which is not possible with the first method [118]. In this work, PID was performed using the first method for all the Run 1 samples and some of the Run II samples, and using the second method for the remaining Run II samples. In the case of each sample, the PID performance is calibrated using a data-driven approach to correct for any difference present in using two PID methods. Well known decay processes, such as $D^{*+} \to (D^0 \to K^-\pi^+)\pi^+$ decay, are used to perform data-driven calibration of the PID performance. The reason behind this is that $K^-\pi^+$ can be identified using only kinematic information. Specifically, pion-kaon PID efficiencies are calculated by tagging the final-state pion that does not originate from the decay of the D^0 meson, and inferring the hadron species of the children of the intermediate particle from the aforementioned final-state pion's charge. Figure 3.18 shows the kaon identification and pion mis-identification efficiency of the RICH detector system based on LHCb data. Similarly, protons are reconstructed based on data samples from the $\Lambda_c^+ \to pK^-\pi^+$ and $\Lambda \to p\pi$ decays. The efficiency of proton PID and pion mis-identification are illustrated in figure 3.19.

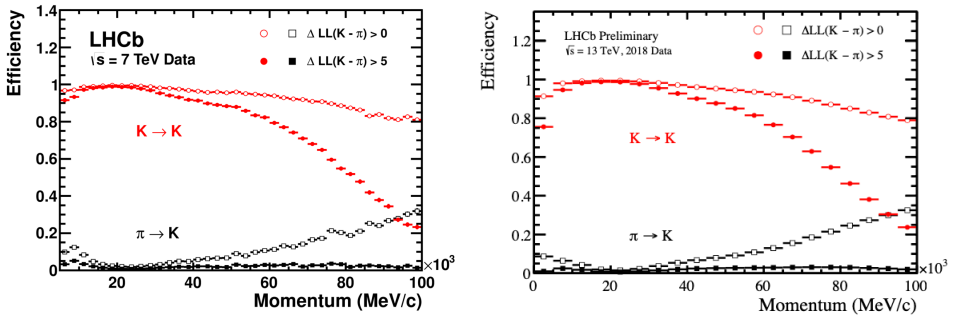

Figure 3.18: Efficiency of kaon identification in red and pion mis-identification in black based on data samples. Two different $\Delta\log\mathcal{L}(\mathrm{p}-\pi)$ requirements applied to the data sample are presented using open and filled markers. Run 1 data is used for the plot on the left [121] and Run 2 data is used for the plot on the right [122].

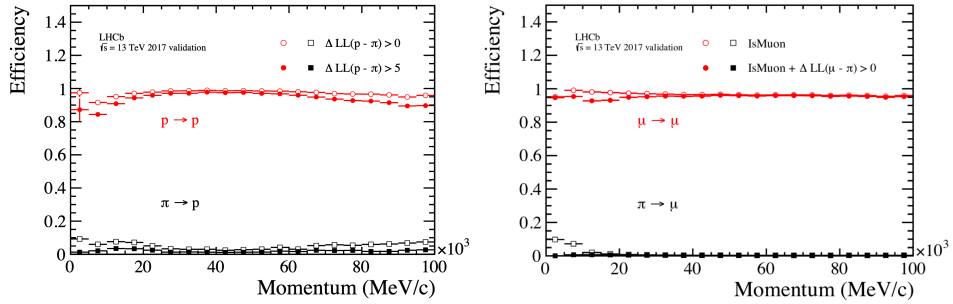

Figure 3.19: Left: Efficiency of proton identification in red and pion mis-identification in black based on Run 2 data samples. Two different $\Delta\log\mathcal{L}(\mathrm{K}-\pi)$ requirements applied to the data sample are presented using open and filled markers.
Right: Efficiency of muon identification in red and pion mis-identification in black based on Run 2 data samples. Two different requirements are applied to the data sample, IsMuon and IsMuon + $\Delta\log\mathcal{L}(\mu-\pi)$, are presented using open and filled markers respectively [123].

The muon identification procedure consist of three steps. First those candidates that penetrate to the muon stations beyond the calorimeters and muon filters are selected loosely as muons and labelled "IsMuon". This reduces the probability of misidentifying a hadron as a muon to $\mathcal{O}(1\%)$, while maintaining a high muon identification efficiency. A closer scrutiny of the loosely selected muon candidates is achieved by computing a likelihood for the muon and non-muon hypotheses. This is based on the hits registered in the muon stations combined with the tracking information. The difference between the logarithms of the likelihoods of the two hypotheses is used when applying selection cuts on the muon candidate samples and is refereed to

as muDLL. A plot of the muDLL variable for different candidates is shown in figure 3.20. The final step in the muon identification process consists in calculating a combined likelihood using information from the RICH and calorimeters systems, for each particle hypotheses, as already described in the previous paragraph [124].

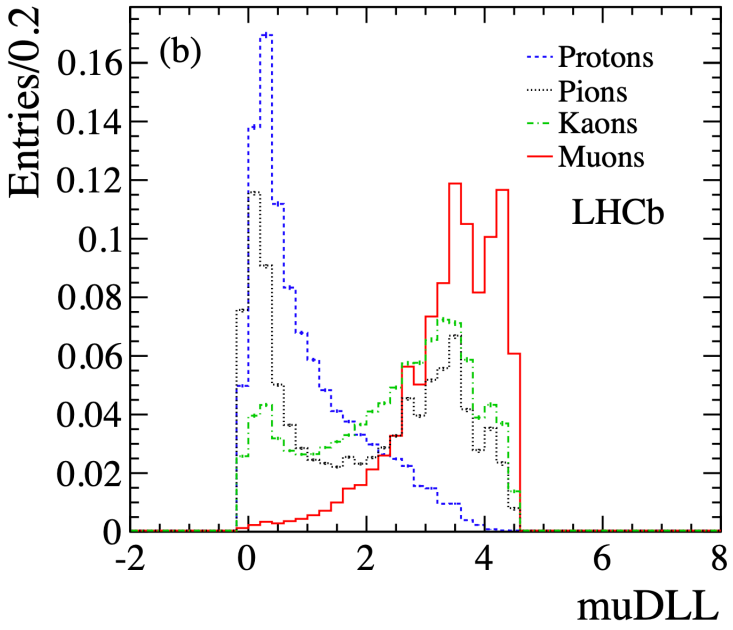

Figure 3.20: muDLL for proton, pion, kaon and muon candidates reconstructed by LHCb. Muon candidates ate clearly separated from protons and pions, albeit to a lesser extent in the case of the latter. This variable alone is not sufficient to solidly discriminate muons from kaons. [124].

The muon tagging efficiency is measured on the $J/\psi \to \mu^+\mu^-$ decay. This decay is abundant at LHCb and high quality data samples for this decay can be obtained. This is done by selecting only those events with a high primary vertex impact parameter, a large reconstructed J/ψ flight distance and a good decay vertex quality. The efficiency measurement is based on the *tag and probe* method. This consists in requiring that one of the products in the $J/\psi \to \mu^+\mu^-$ decay is identified as a muon, and labelled "tag" muon. The remaining muon candidate is labelled "probe" muon. The efficiency is calculated using "probe" muon candidates only. The proton misidentification probability is also calculated in this manner. The computation of the kaon and pion misidentification probabilities is similar and relies on the $D^0 \to K^-\pi^+$ decay [124]. The muon tagging efficiency across the momentum range for Run

2 is shown as an example in figure 3.19.

3.5 The LHCb Trigger

The LHC bunch crossing rate is 40 MHz, but some bunches are not filled, resulting in an actual crossing rate of 30 MHz. The maximum rate at which all LHCb's sub-detectors can readout data is 1.1 MHz. This limit depends on the sub-detectors' readout electronics frequency and bandwidth. It is crucial for the trigger system to identify and store events of interest, and discard the remaining events to reduce the rate. The trigger system consists of two stages, the Level 0 Trigger (L0) and the High Level Trigger (HLT). L0 is hardware based and operates online. Data are stored in front-end electronics temporarily, while being processed by L0. The data read out rate is reduced to 1.1 MHz. HLT is software based and can occur off line to further reduce the rate.

While the Run 1 trigger system allowed to perform most of LHCb's physics program studies, it had some important limitations. These include the lack of information regarding low-momentum charged particles in L0 and the lack of full particle identification in HLT, which are both important to perform c-hadron physics studies. For these reasons, the HLT was redesigned, and 800 computing nodes were added, for LHC's Run 2 data-taking campaign [115]. The HLT redesign includes its separation into different processes, allowing for the possibility to run some parts of HLT asynchronously to optimise disk space use. Furthermore, the use of real time alignment and calibration for intermediate stages of the output of HLT was introduced to improve the quality of event reconstruction [115].

3.5.1 The L0 Trigger

The L0 trigger selects events within 5 µs based on information from the calorimeter and muon systems [115]. As already mentioned in section 3.4.2, the energy deposited in the ECAL and HCAL is used to make an initial hardware level trigger decision. The SPD and PS sub-detectors gather information to classify candidates into hadrons, electrons and photons. L0 trigger selects tracks that traverse at least five muon stations in a straight line. In a given event, the two tracks with the highest p_{T} are labelled by the L0 trigger as muon candidates. If at least one of the muon candidates has a p_{T} greater than the set muon p_{T} threshold the event passes the L0 trigger. Alternatively,

if the product of the two muon candidate p_{T} is greater than the muon p_{T} threshold, the event passes the L0 trigger. The L0 muon p_{T} threshold varies for the data-taking campaigns. In Run 1 this corresponds to $1.3\mathrm{GeV}^2$ for a single muon candidate and to $1.5\mathrm{GeV}^2$ for the product of the two muon candidates [125]. The Run 2 muon and dimuon thresholds correspond to $2.8\mathrm{GeV}^2$ and $1.69\mathrm{GeV}^2$ for 2015, $1.8\mathrm{GeV}^2$ and $2.25\mathrm{GeV}^2$ for 2016, $1.35\mathrm{GeV}^2$ and $1.69\mathrm{GeV}^2$ for 2017 [126].

3.5.2 The HLT Trigger

Events that pass the L0 trigger are moved to the Event Filter Farm (EFF). Here they are combined with complementary information collected by the other LHCb sub-detectors. The EFF is a computing system made from 900 (1700) nodes for Run 1 (Run 2) which runs the HLT software. The HLT trigger is divided into two processes: HLT1 and HLT2. HLT1 performs a partial reconstruction of the events that pass the L0 trigger and runs synchronously to it. First it uses VELO information to reconstruct PVs and tracks. A minimum of five VELO tracks are necessary to reconstruct a PV, and this has to be within 300 µm of the average pp interaction position in the $x - y$ plane [127]. Hits in the sub-detectors are used to extrapolate tracks from the PV down the LHCb detector. Finally, the IP of each track in a given event is calculated. Events pass the HLT1 trigger if at least one track has a big IP, a symptom of a big displacement from the reconstructed PV, and if at least one track has a $p_{\mathrm{T}} > 500\,\mathrm{MeV}/c$. HLT1 reduces the rate from 1 MHz to $50 - 110\,\mathrm{kHz}$. The execution order and specfic operations performed by HLT1 are visible in figure 3.21.

Events that pass HLT1 are passed to HLT2 as inputs. HLT2 performs a full event reconstruction. This is done by algorithms that are grouped into two categories called exclusive and inclusive trigger lines. Exclusive trigger lines select signature of specific decay channels. Inclusive trigger lines select $b-$hadron decays based on topological requirements. Inclusive trigger lines look for two track in the same event with a Distance Of Closest Approach (DOCA) $< 0.15\,\mathrm{mm}$, creating a 2-body object. Tracks are added sequentially to the object, imposing the same DOCA between each new track and the object at each step [128]. This process produces fully reconstructed events when it is not halted after a number of steps to obtain partially reconstructed events.

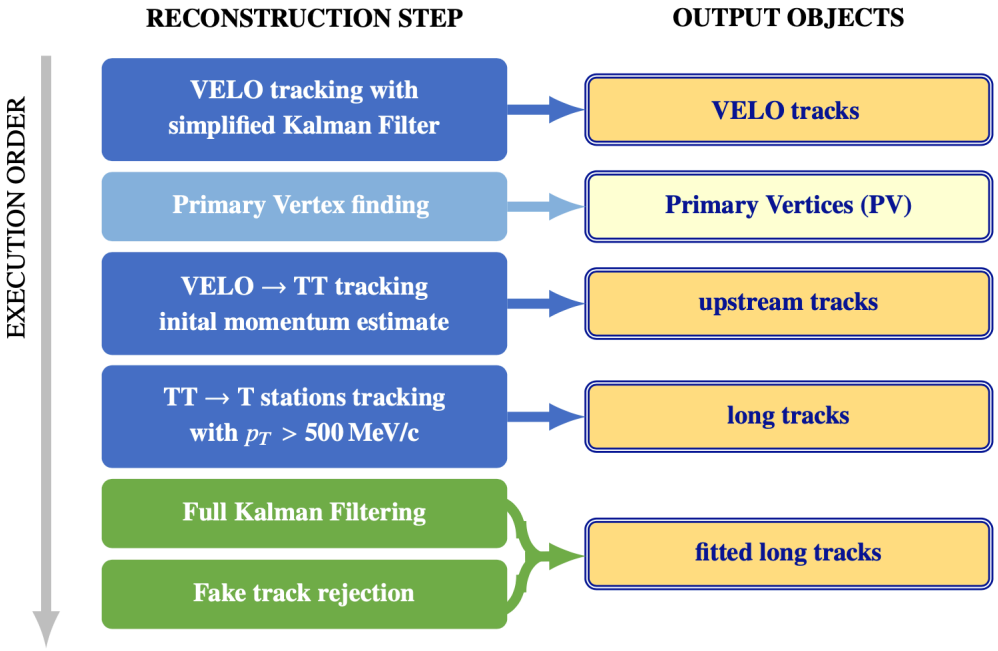

Figure 3.21: Chain of the reconstruction algorithms in HLT1 to filter data [126].

The HLT has been improved since its initial deployment in 2011, its evolution is shown in figure 3.22. Then, all its processes were synchronous with the L0 trigger, meaning that it was only active while LHCb was taking data. This meant that it was idle for 70% of the total time available in 2011. In 2012 a solution was found to make better use of this time. Roughly 20% of events that passed the L0 trigger were stored to disk and processed through the HLT during the L0 idle time. This improved the HLT processing rate by 25% and pushed towards a fully asynchronous HLT2 system for Run 2. In the new system, HLT1 is synchronous with L0, and all events that pass it are stored on a temporary buffer and passed to HLT2 when it is most convenient. This results in HLT2 making more nuanced decisions. It has also allowed the HLT2 reconstruction to be as efficient as the offline reconstruction, making the calculation of the trigger efficiency cleaner. Finally, an asynchronous HLT2 and a buffer allow to perform real time calibration of the LHCb detector which can then be used in the HLT2 trigger during Run 2.

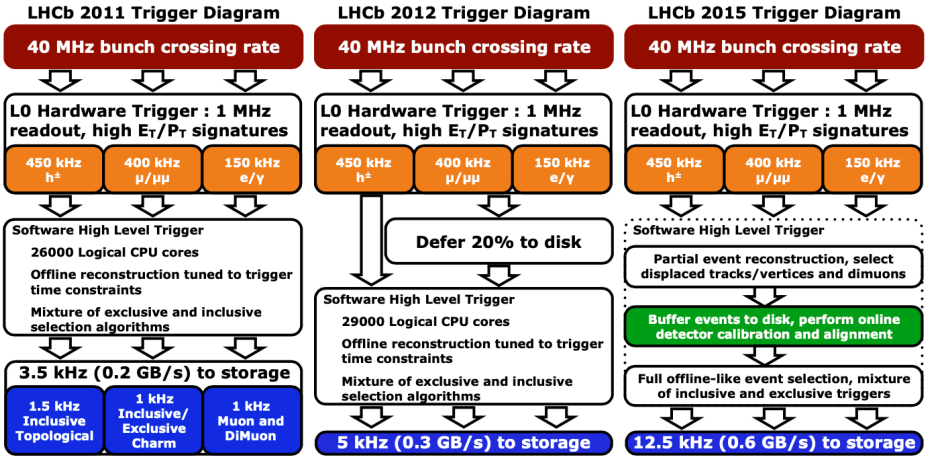

Figure 3.22: The evolution of the LHCb trigger system from its initial configuration in 2011 (left),through 2012 (middle) and to Run 2 data-taking in 2015 (right) [129]. Initially both HLT1 and HLT2 were synchronous with the L0 trigger. Then 20% of L0 events were deferred to disk to be passed to the HLT during idle time. Fianlly, HLT1 is synchronous with L0 and stores all its events to a temporary buffer. HLT2 performs full offline-like event reconstruction asynchronously to the rest of the trigger system.

3.6 The LHCb Upgrade

The LHCb experiment has been extremely successful in testing the SM in the quantum chromodynamics and the electroweak sectors as well as in direct searches and heavy ion sector. An upgrade of the LHCb detector has been designed and implemented to follow the experiment's success [130]. The motivation for the LHCb Upgrade is driven by several aspects. Firstly, the flavour anomalies detected in the electroweak sector with Run 1 and Run 2 data are not sufficient to declare that NP is present. The upgrade allows the collaboration to move from flavour exploration studies to precision studies. Furthermore, several precision measurements performed with Run 1 and Run 2 data have large uncertainties compared to their SM predictions. These include the branching fraction of the $B_s^0 \to \mu^+\mu^-$ decay, the CKM angle γ, and some charm CP violation searches. Finally, the increase in luminosity at the LHC has given the LHCb Collaboration the opportunity to go to a higher luminosity. This requires a redesign of the LHCb trigger system. The optimal trigger solution for the LHCb Upgrade is to forego the use of a hardware trigger, relying on a full software trigger instead. LHCb aims to collect 50fb^{-1} in Runs 3 and 4, and 300fb^{-1} in Runs 5 and 6. This is an increase of one and

two orders of magnitude respectively, compared to Runs 1 and 2. For Runs 3 and 4, this corresponds to an instantaneous luminosity of $2 \times 10^{33}\text{cm}^{-2}\,\text{s}^{-1}$ and an event readout rate of 30MHz by the High Level Trigger. The VELO was beyond its lifetime and at high risk of failure. Furthermore the shift to a full software trigger prompted the replacement of the VELO and of the tracking stations with their respective detector upgrades. The VELO Upgrade provides an improved IP resolution. The Upgraded Tracking System comprises a silicon-strip detector based Upstream Tracker placed upstream of the magnet, with finer granularity and detector elements closer to the beam. It also comprises Scintillating Fibre stations (SciFi) downstream of the magnet, to improve the overall tracking performance at LHCb. The LHCb Upgrade also includes Upgraded RICH detectors to maintain excellent Particle ID performance in harsher conditions. The LHCb Upgrade has been fully installed and operating since August 2022. It will not be discussed further as it is not relevant for this work .

Chapter 4

Analysis of the angular distribution of the $B^+ \to \pi^+\mu^+\mu^-$ decay

4.1 Analysis Strategy

The decay $B^+ \to \pi^+\mu^+\mu^-$ is a $b \to d$ flavour-changing neutral-current process, which is mediated by loop processes in the Standard Model of particle physics.[1] The decay was first observed by the LHCb collaboration in the experiment's 2011 data set [131]. A subsequent analysis using the full Run 1 data set has measured the differential branching fraction and *CP* asymmetry of the decay in bins of the dimuon mass squared, q^2 [132]. The angular distribution of the decay has not previously been studied. Work towards a first angular analysis is described in this chapter.

The work described in this chapter was developed in parallel with an updated branching fraction analysis and *CP* measurement that also makes use of the full Run 1 and 2 data set. The analysis strategy is heavily influenced by the Run 1 measurement of the differential branching fraction and *CP* asymmetry of the $B^+ \to \pi^+\mu^+\mu^-$ decay described in Ref. [132]. Changes between the Run 1 analysis and this analysis include improving the multivariate selection by increasing the number of variables used, re-optimising the training because of newer and better reconstruction and particle identification tools. The choice of the q^2 binning is also inherited from the Run 1 analysis [132].

[1] The inclusion of charge-conjugate processes is implied throughout this work, unless otherwise stated.

The angular analysis is performed in the q^2 ranges $[1.1 - 6.0]\,\mathrm{GeV}^2/c^4$ and $[15.0 - 22.0]\,\mathrm{GeV}^2/c^4$. Measurements are not performed in other q^2 regions, as the expected signal yield is too small. The analysis strategy is verified using the well known decay channels $B^+ \to J/\psi(\mu^+\mu^-)K^+$ and $B^+ \to J/\psi(\mu^+\mu^-)\pi^+$ as control modes in the q^2 range $[8.0 - 11.0]\,\mathrm{GeV}^2/c^4$. The aim of the angular analysis is to measure the observables A_{FB} and F_{H} in bins of dimuon invariant mass squared. These observables have physically allowed values in the ranges $[-\frac{1}{2}, +\frac{1}{2}]$ and $[0, 1]$, respectively. The distribution of the cosine of the helicity angle, θ_l, is a function of A_{FB} and F_{H}. The helicity angle in this work is defined as the angle between the positively charged muon direction and the pion direction in the dilepton rest-frame. The angular distribution of $\cos\theta_l$ is not positive definite unless the condition $A_{\mathrm{FB}} \leq \frac{1}{2}F_{\mathrm{H}}$ is satisfied. This introduces a complicated, triangular-shaped, allowed angular parameter space, with the Standard Model prediction sitting in the $(0, 0)$ corner. The parameter space is shown in figure 4.1. For this reason, the widely used software packages HESSE and MINOS [133] are not reliable when determining confidence intervals on A_{FB} and F_{H}. To perform a statistically sound analysis one typically resorts to the Feldman-Cousins approach [134] to determine confidence intervals.

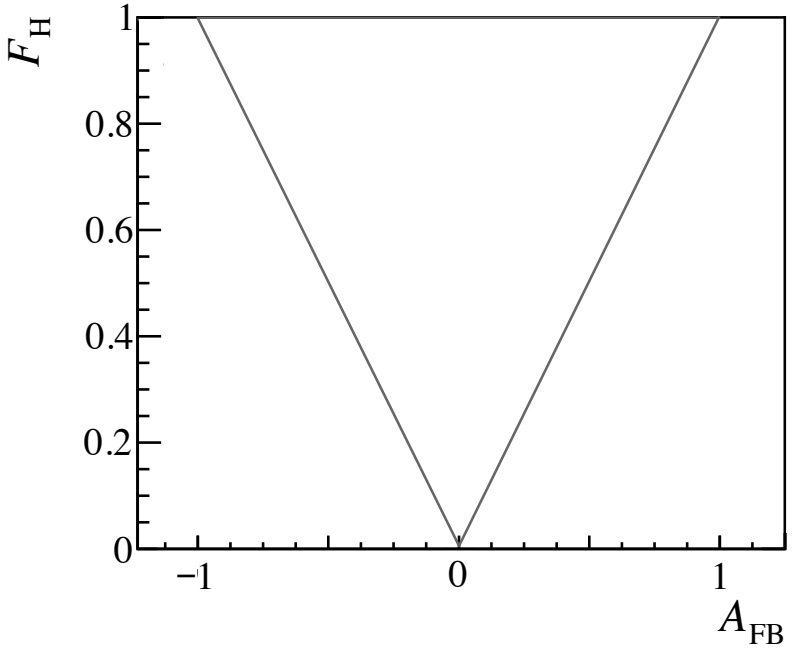

Figure 4.1: Allowed angular parameter space. The area in the triangle identifies the allowed region in the parameter space.

The analysis described in this work is designed to be performed blind, to be unblinded after it has been reviewed internally by the LHCb collaboration. Currently it is about to enter the internal review process within the LHCb collaboration so the results are still blind. The measurement is performed on pseudoexperiments to simulate the results of this study. A two-dimensional simultaneous fit to the invariant mass and helicity angle of candidate signal decays is performed to measure the angular distribution of the $B^+ \to \pi^+\mu^+\mu^-$. The fit model is validated on the $B^+ \to J/\psi K^+$ and $B^+ \to J/\psi \pi^+$ decays, which are much more abundant than the signal mode and topologically similar. To perform this analysis, all backgrounds to the signal and control modes must be identified. This is done in sections 4.2 and 4.7. Simulation datasets of the rare mode, control modes and the respective relevant backgrounds are used to characterise the probability distribution function used in the fits to the rare mode dataset and the control mode datasets. This is explained in detail in section 4.8. Furthermore, all efficiencies in collecting and selecting data must be calculated and accounted for. This is done largely by using simulation datasets of candidate decays from proton-proton collisions at LHCb also known as generator level samples, and simulation datasets of reconstructed candidate decays. The latter are obtained by performing the LHCb reconstruction on generator level samples. The efficiency calculation is explored in detail in section 4.5. Seeing the wide use of simulation samples in the different aspects of this analysis, it is imperative that the data-simulation agreement is good. This topic is explored in section 4.4. Finally, the sources of systematic uncertainties are identified in section 4.10.

4.2 Background sources

The data collected by the LHCb experiment contains signal $B^+ \to \pi^+\mu^+\mu^-$ decays and decays from many other sources. Some of these are similar to the signal in signature, and can therefore be confused with it. The signal must be distinguished from the background, and the latter must be rejected. The sources of background across the rare and control modes are summarised in table 4.1. They are classed into three categories: mis-identified background, mis-reconstructed background and combinatorial background. Decays that have one or more of the final products wrongly identified fall into the mis-identified background category, while decays that are only partly reconstructed fall in the mis-reconstructed group. Combinatorial background is formed from

randomly combined tracks that accidentally form a candidate that looks like signal.

The rare mode's background sources are $B^+ \to K^+\mu^+\mu^-$, $B^+ \to \overline{D}^0(K^+\mu^-\overline{\nu}_\mu)\mu^+\nu_\mu$, $B^+ \to \overline{D}^0(\pi^+\mu^-\overline{\nu}_\mu)\mu^+\nu_\mu$, $B_s^0 \to f_0\mu^+\mu^-$ and $B^+ \to \pi^+\pi^-\pi^+$ decays, as well as combinatorial background. The $B^+ \to K^+\mu^+\mu^-$ background is present because the kaon can be mis-identified as a pion. The decays $B^+ \to \overline{D}^0(K^+\mu^-\overline{\nu}_\mu)\mu^+\nu_\mu$, $B^+ \to \overline{D}^0(\pi^+\mu^-\overline{\nu}_\mu)\mu^+\nu_\mu$ and $B_s^0 \to f_0\mu^+\mu^-$ can be mis-reconstructed and look like the signal. In this work, the fit model for the rare mode includes the $B^+ \to K^+\mu^+\mu^-$ background and the combinatorial background only.

Similarly, the $B^+ \to J/\psi(\to \mu^+\mu^-)\pi^+$ control mode has background from mis-identified $B^+ \to J/\psi(\to \mu^+\mu^-)K^+$ decays and mis-reconstructed $B^+ \to J/\psi(\to \mu^+\mu^-)f_0$, $B^{+,0} \to J/\psi(\to \mu^+\mu^-)\rho^{+,0}$, and $B^{+,0} \to J/\psi(\to \mu^+\mu^-)K^{*,+,0}$ decays, as well as combinatorial background. The $B^+ \to J/\psi(\to \mu^+\mu^-)K^+$ control mode has background from mis-reconstructed $B^0 \to J/\psi(\to \mu^+\mu^-)K^*$ decays, as well as combinatorial background.

Table 4.1: Sources of background for the rare mode and the two control modes, $B^+ \to \pi^+\mu^+\mu^-$, $B^+ \to J/\psi(\to \mu^+\mu^-)\pi^+$ and $B^+ \to J/\psi(\to \mu^+\mu^-)K^+$ decays respectively.

background sources for the $B^+ \to \pi^+\mu^+\mu^-$ decay	background sources for the $B^+ \to J/\psi(\to \mu^+\mu^-)\pi^+$ decay	background sources for the $B^+ \to J/\psi(\to \mu^+\mu^-)K^+$ decay
$B^+ \to K^+\mu^+\mu^-$	$B^+ \to J/\psi(\to \mu^+\mu^-)K^+$	$B^0 \to J/\psi(\to \mu^+\mu^-)K^*$
$B^+ \to \overline{D}^0(K^+\mu^-\overline{\nu}_\mu)\mu^+\nu_\mu$	$B^+ \to J/\psi(\to \mu^+\mu^-)f_0$	
$B^+ \to \overline{D}^0(\pi^+\mu^-\overline{\nu}_\mu)\mu^+\nu_\mu$	$B^{+,0} \to J/\psi(\to \mu^+\mu^-)\rho^{+,0}$	
$B_s^0 \to f_0\mu^+\mu^-$	$B^{+,0} \to J/\psi(\to \mu^+\mu^-)K^{*,+,0}$	
$B^+ \to \pi^+\pi^-\pi^+$		
combinatorial background	combinatorial background	combinatorial background

While the data selection significantly reduces the amount of background, the background sources must be well understood. The $B^+ \to K^+\mu^+\mu^-$, $B^+ \to J/\psi(\to \mu^+\mu^-)K^+$ and $B^0 \to J/\psi(\to \mu^+\mu^-)K^*$ decays are included in the respective fit models of the $B^+ \to \pi^+\mu^+\mu^-$, $B^+ \to J/\psi(\to \mu^+\mu^-)\pi^+$ and $B^+ \to J/\psi(\to \mu^+\mu^-)K^+$ decays. The $B^{+,0} \to J/\psi(\to \mu^+\mu^-)\rho^{+,0}$, and $B^{+,0} \to J/\psi(\to \mu^+\mu^-)K^{*,+,0}$ decays are found not to affect the $B^+ \to J/\psi(\to \mu^+\mu^-)\pi^+$ fit. This is explained in section 4.8.1. Any background contribution not accounted for in the fit model for the rare mode is addressed in section 4.7. Furthermore, for each background excluded from the fit model for the rare mode, a systematic uncertainty is calculated. This is explained in detail in section 4.10.

4.3 Data and Selection

The data used in this analysis come from the Run 1 and Run 2 LHCb dataset. The data are centrally processed using LHCb software before it is released for analysis. This includes two stages described in paragraphs 4.3.1 and 4.3.2, respectively: a data selection performed on-line in the experiment's trigger and a second, off-line, stage called a stripping selection.

4.3.1 Trigger Selection

As described in chapter 3, the LHCb experiment only stores data that pass both L0 and HLT trigger steps. This translates in only keeping data which passes specific conditions, known as "trigger lines". The LHCb experiment subjects the data to many trigger lines for the numerous analyses undertaken by the collaboration. As a particle track causes a trigger line to fire, the flag for that trigger line is attached to the particle track in the data bookeeping system. The consequence of this is that the information regarding which particle candidates pass a given trigger line is available off-line. In most events many tracks cause the trigger to fire. It is therefore possible to select particle tracks based on their trigger flags. Each trigger line is named according to the specific conditions it enforces. Common flags used in LHCb analyses are `TOS` and TIS, which stand for Trigger On Signal and Trigger Independent of Signal. `TOS` identifies tracks that are reconstructed as part of the signal, so those tracks that trigger LHCb into storing their events as candidates. The `TIS` flag is attached to tracks that do not trigger LHCb, but are part of an event triggered upon by other tracks. Because events include more than one track, the same event can be triggered upon because of more than one track, and could include tracks that don't cause an LHCb trigger on their own. The selection for this work requires tracks to pass the `TOS` condition. Within the scope of this work, TIS occurs when the trigger is fired by particles from the other b-hadron candidate in the event. The L0 trigger requirement enforced in this selection is that events have hits in enough muon stations to account for at least one muon, with a high transverse momentum. At HLT1 level, the requirement used in this selection is that in each event either at least one good quality track is reconstructed with a high p_{T} and IP values, or at least one track can be reconstructed as a muon when relaxing slightly p_{T} condition for selection. The final trigger selection occurs in HLT2, and requires that events have the expected topology of a heavy b-hadron decay, with large p_{T} and

IP values of the final state particles and a displaced SV, or that a displaced dimuon pair exists in the event and that their reconstructed mass is larger than 1GeV.

4.3.2 Stripping Selection

The data is centrally processed using LHCb software before it is released for analysis. First a full event reconstruction is performed. The subsequent data stripping step. This has the two-fold effect of providing a more manageable datasets for off-line analysis and of providing a common starting point for similar analyses. Similar analyses will share broad characteristics, for example the presence of a dilepton pair in the final state. This work uses the data stream identified by the `B2XMuMu` stripping line. This line selects events with a b-hadron decaying into a final state corresponding to a dimuon pair and a hadron. The muons in the dimuon pair have opposite charges. Most LHCb $b \to s\mu^+\mu^-$ and $b \to d\mu^+\mu^-$ analyses share this stripping line as their first data selection requirement. The selected candidates have two well-reconstructed tracks of opposite charge, identified as muons, combined in a vertex with one other track, identified as a hadron.

Simulated data samples are created for each LHCb data sample studied in this analysis by using the LHCb simulation software. These comprise datasets per each LHCb data-taking year and magnet polarity for the decays

- $B^+ \to \pi^+\mu^+\mu^-$,
- $B^+ \to K^+\mu^+\mu^-$,
- $B^+ \to J/\psi(\to \mu^+\mu^-)\pi^+$,
- $B^+ \to J/\psi(\to \mu^+\mu^-)K^+$,
- $B^+ \to J/\psi(\to \mu^+\mu^-)K^*$,
- $B^+ \to J/\psi(\to \mu^+\mu^-)f_0$,
- $B^+ \to \mu^+\mu^- f_0$,
- $B^{+,0} \to J/\psi(\to \mu^+\mu^-)\rho^{+,0}$,
- $B^{+,0} \to J/\psi(\to \mu^+\mu^-)K^{*,+,0}$,
- $B^+ \to \pi^+\pi^-\pi^+$.

The LHCb simulated datasets are processed in the same way as the data after simulating the detector response for charged and neutral particles. The raw simulated samples are weighted to improve the agreement with the data, as described in Sec. 4.4.

4.3.3 Candidate Selection

The selection procedure for signal and control channels follows closely that developed for the measurement of the differential branching fraction and *CP*-asymmetry of $B^- \to \pi^-\mu^+\mu^-$ decay [1]. This consists in a the aforementioned trigger based selection and chosen stripping line, the use of a multivariate analysis, applying a fiducial cut and a particle identification selection. The multivariate analysis (MVA) is performed to reject combinatorial background. Candidates for the signal and control channels are selected first with a common loose preselection, which imposes "isMuonLoose" false and "InAccMuon" for pions and kaons, and $p_T > 300$MeV for all reconstructed particles.

The MVA is a boosted decision tree (BDT) trained under supervised learning, with ten-fold cross validation, used to reduce background. The combinatorial background sample chosen for training consists of $\pi^+\mu^+\mu^-$ data with an invariant mass > 550MeV and a mass veto for the B_c^+ and J/ψ modes. Without this veto the sample would otherwise be dominated by J/ψ decays with a pion from elsewhere, reconstructed as signal. The signal training sample is taken from LHCb simulation of $B^+ \to \pi^+\mu^+\mu^-$ decays. The PID information is deliberately not included in the MVA, so the MVA can be applied to kaon and pion modes alike. The variables used to train the BDT express characteristics of the B^+ candidate and characteristics of the pion and muon tracks. These comprise the angle between the momentum vector of the B^+ candidate and the direction vector between the PV and the SV; the $\pi^+\mu^+\mu^-$ candidate's flight distance, vertex quality and transverse momentum; and the transverse momentum, IP, and quality of the pion and muon tracks. In addition, the classifier uses the absolute difference in momentum between the two muon candidates and two isolation variables designed to reject backgrounds from combinations of tracks from two different b-hadron decays [135]. A separate MVA was trained for the Run I, 2016, 2017 and 2018 samples. Each MVA combines the samples from both magnet polarities. A fiducial cut is applied to the pion (kaon) and muons to only select those inside the momentum and pseudo-rapidity ranges $3 < p < 100\,\text{GeV}/c$ and $1.9 < \eta < 4.9$. These ranges correspond to the parameter space covered by the PID efficiency calculated using information from PIDCalib [136], and by the track calibration system [137]. This also corresponds to the range of coverage of the RICH detectors. Furthermore, only events with event track multiplicity < 300 tracks are selected.

Table 4.2: The particle identification criteria

	Run I & Run II
π	ProbNNpi > 0.2
	ProbNNk < 0.05
	IsMuon is false
K	ProbNNk > 0.4
	IsMuon is false
μ	ProbNNmu > 0.2
	IsMuon is true

Finally particle identification selections are made to separate the $B^+ \to \pi^+\mu^+\mu^-$ and $B^+ \to K^+\mu^+\mu^-$ decay modes. The latter is 25 times more abundant than the former. The PID criteria used in this analysis are given in Table 4.2. Posterior probabilities (ProbNN) for a particle to be a particular type are taken from the standard neutral networks trained to identify particular particle species [121]. To select a good quality dimuon pair, both muons are required to pass a selection known as "IsMuon" and to avoid contamination from kaons and pions both muons must satisfy a requirement on ProbNNmu. The IsMuon flag is assigned to tracks that are compatible with the hits registered in the LHCb muon stations [124]. To select the signal from the dominant mis-identified $B^+ \to K^+\mu^+\mu^-$, two particle identification cuts are made, one to select pions using ProbNNpi and one to veto kaons using ProbNNk. The decay candidates must also not satisfy the IsMuon criteria. To select the control mode a selection on ProbNNk is made. The decay candidates must also not satisfy the IsMuon criteria.

Due to the large amount of combinatorial background and mis-identified $B^+ \to K^+\mu^+\mu^-$ decays, the BDT response cut used to remove them are optimised simultaneously. The optimisation is done using fits to pseudo-experiments. Simplified toy datasets are produced with three components, signal, kaon background, and combinatorial background. The signal component is taken from simulated events according to the expected yield from the SM branching fraction. The $B^+ \to K^+\mu^+\mu^-$ yield is estimated similarly. The combinatorial background yield is taken from a fit to the uppermass sideband of the data.

A simplified fit model containing only three components is used. All of the shape parameters for the signal and mis-identified $B^+ \to K^+\mu^+\mu^-$ background are fixed to those obtained from a fit to simulated samples. The combinatorial background is modelled with an exponential, with all parameters free. One fit is performed with the signal yield free and one with the signal fixed to zero. A Figure of merit is taken to be the difference in the log likelihood at the best fit point, a measure of the signal significance using Wilks' theorem [138].

As this procedure requires PID calibration histograms for each selection, the optimisation is done on a grid with resolution 0.05 in each PID variable. For each point 1000 toy sets are generated to form a distribution from which the best selection is chosen.

The data and simulation samples are limited to the range in which the fit of the model to data is performed. This is enforced by requiring that all B candidates are in the mass range $[5180, 5600]\,\text{MeV}$. The lower bound of this range excludes many potential backgrounds from partially reconstructed B decays, while the upper bound gives a broad range that is dominated by combinatorial background and hence controls the contribution from this component in the invariant mass fit. All fits are performed within chosen q^2 ranges. The control mode fits to $B^+ \to J/\psi K^+$ and $B^+ \to J/\psi\pi^+$ are only performed on simulation and data that have a q^2 value within the interval $[8.0 - 11.0]\,\text{GeV}^2/c^4$. The data and simulation datasets for the rare modes, $B^+ \to K^+\mu^+\mu^-$ and $B^+ \to \pi^+\mu^+\mu^-$, are selected in a low q^2 bin or in a high q^2 bin. These q^2 bins correspond to the intervals: $[1.1 - 6.0]\,\text{GeV}^2/c^4$ and $[15.0 - 22.0]\,\text{GeV}^2/c^4$.

Finally the selection for the rare mode includes the rejection of any candidates that could come from a mis-identified J/ψ decay, where one of the muons could be mis-identified as a hadron. This is achieved by vetoing events that have a combined $h^+\mu^-$ invariant mass withn 100MeV of the J/ψ peak.

4.4 Simulation corrections

The simulated samples have several known deficiencies, in particular in their modelling of event occupancy and B^+ meson kinematics. Particle identification variables are also known to be poorly described. To ensure the angular efficiency is correctly determined, the discrepancies between data and simulation are tackled by correcting simulation samples using data-driven approaches.

Each simulated event is given a weight such that the distributions of the problematic variables match those of a clean data sample.

4.4.1 B^+ meson production

The data/simulation agreement is checked using $B^+ \to J/\psi K^+$ events in data. This sample can be selected cleanly and is large enough that the data can be binned finely in different variables. The preselection, PID and MVA selection requirements described in section 4.3 are not applied to either data or simulation in order to compare the datasets without biases. While most variable distributions of simulation and data are in good agreement, a minority are known to be in poor agreement. These include variables such as the transverse momentum of the particles in the $B^+ \to \pi^+\mu^+\mu^-$ decay, the number of tracks in the event and the number of tracks produced in the proton-proton interaction. The latter is also known as the number of degrees of freedom per PV. The simulation sample is corrected so that the discrepancy with data in the relevant variables is no longer present. The corrections are extrapolated from the $B^+ \to J/\psi K^+$ data sample.

Although the $B^+ \to J/\psi K^+$ data is one of the cleanest datasets available, it does contain some background, which must be removed before using the sample to compute corrections. The background is removed using the sPlot method [139], using weights from a fit to the $B^+ \to J/\psi K^+$ invariant mass distribution. The variable distributions in data are corrected by these weights to subtract the background. A set of kinematic weights is extracted from the comparison of the simulation and background-subtracted data distributions. The simulation dataset corrected using the kinematic weights is in good agreement with the data. Figure 4.2 shows the agreement for $B^+ \to J/\psi K^+$ data and simulation 2016 magnet polarity down datasets, and the effect of applying the kinematic weights.

PID efficiency Correction

It is known that the PID of raw LHCb simulated datasets is not a true replica of PID performance in LHCb data. The cause of this is a mismodelling of the occupancy. Due to the difference between data and simulation, the PID efficiency is obtained in a data-driven way using the PIDCalib software package [136, 140]. PIDCalib uses calibration samples obtained using kinematic information alone, without applying PID selection criteria. For the

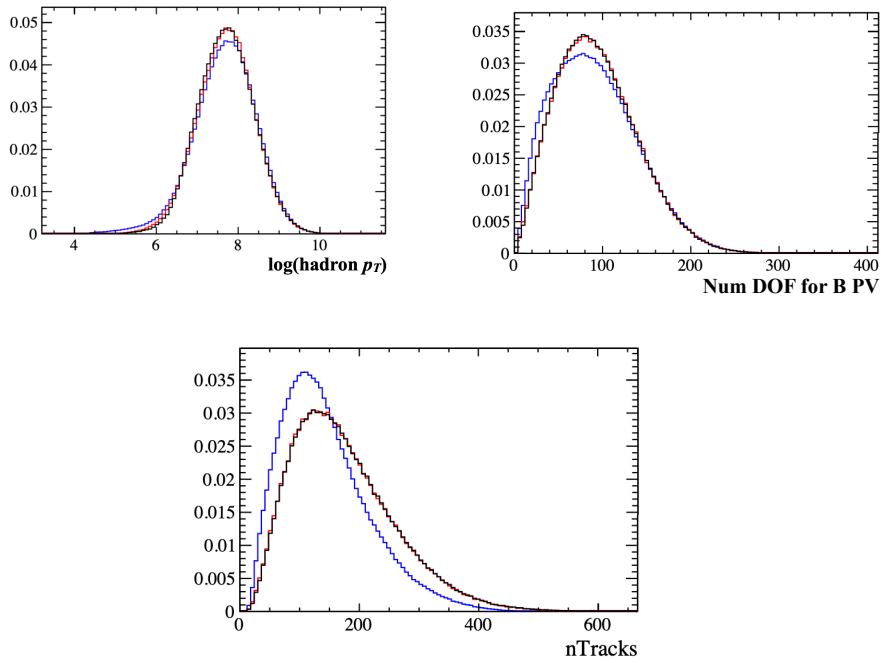

Figure 4.2: Correction of the simulation $B^+ \to J/\psi K^+$ 2016 magnet polarity down dataset to achieve good agreement with data. The kaon transverse momentum distribution, the number of degrees of freedom of the PV of the B^+ and the number of tracks distributions are shown respectively in the top left, top right and bottom plots. Background-subtracted data is in black, simulation is in blue and simulation corrected using kinematic weights is in red.

hadron PID efficiency, the calibration samples correspond to reconstructed $D^{*+} \to D^0(\to K^-\pi^+)\pi^+$ decays. For the muon PID efficiency, the calibration samples correspond to $J/\psi(\to \mu^+\mu^-)$ decays. PIDCalib provides PID efficiency histograms which depend on track momentum, p, pseudo-rapidity, η, and track multiplicity.

The efficiency of the PID selection criteria is accounted for by weighting the simulated candidates using the provided efficiency histograms. The PID efficiency histograms are calculated separately for each combination of year, magnet polarity and track charge. The same procedure is used to estimate probabilities that particles are incorrectly identified. Figure 4.4 shows example 2D projections of the PIDCalib histograms for muons, pions and kaons.

For reconstructed muons, the stripping line requires a loose muon PID selection. To account for the data-simulation differences associated with this loose selection, an additional correction is applied by weighting the

reconstructed muons with additional weights. These weights correspond to the ratio of the data and simulation efficiencies, depending on p, η, and track multiplicity. The efficiency in data is determined using the PIDCalib package and the efficiency in simulation is determined using $B^+ \to J/\psi(\to \mu^+\mu^-)K^+$ simulation samples, where the J/ψ candidates are reconstructed by imposing all the requirements of the `B2XMuMu` stripping line except the loose muon PID selection on the muon candidates. Figure 4.3 shows example 2D projections of the muon PID correction, obtained by averaging over the occupancy.

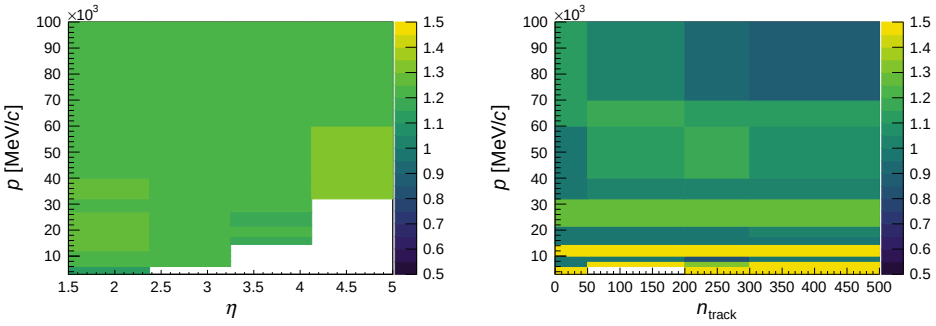

Figure 4.3: Two-dimensional projections of the muon ID correction histogram for data collected in 2016 with magnet polarity Up. On the left, the muon PID corrections as a function of pseudorapidity and momentum, on the right as a function of track multiplicity and momentum.

Tracking Efficiency Correction

The charged particle track reconstruction in simulation is corrected by using weights produced by the TrackCalib package [112]. The tracking efficiency in data is determined using a tag-and-probe approach with $J/\psi \to \mu^+\mu^-$ decays, where one of the muons is fully reconstructed and the other is reconstructed using only information from the muon system and the TT stations. The corrections are calculated separately for each combination of year, magnet polarity and track charge as a function of p and η. For the B-candidate, the weight corresponds to the product of the three weights corresponding to the three decay products. Example of tracking efficiency corrections are shown in Figure 4.5.

Trigger selection efficiency

The L0 trigger efficiency is determined in data and simulation from samples of $B^+ \to J/\psi(\to \mu^+\mu^-)\, K^+$ decays selected by the `B2XMuMu` stripping line,

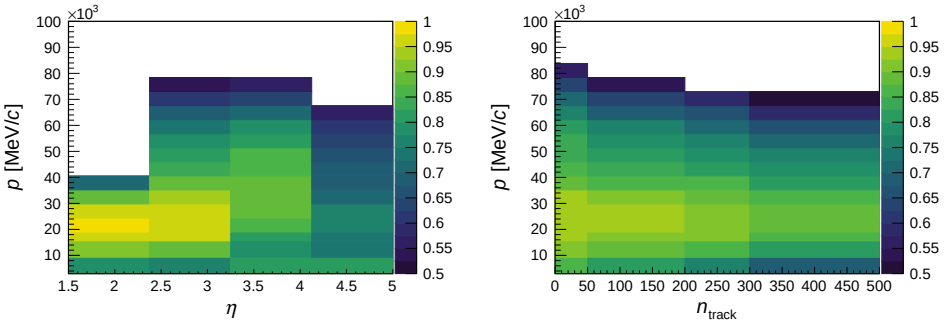

(a) Efficiency of π^+ PID for true pions

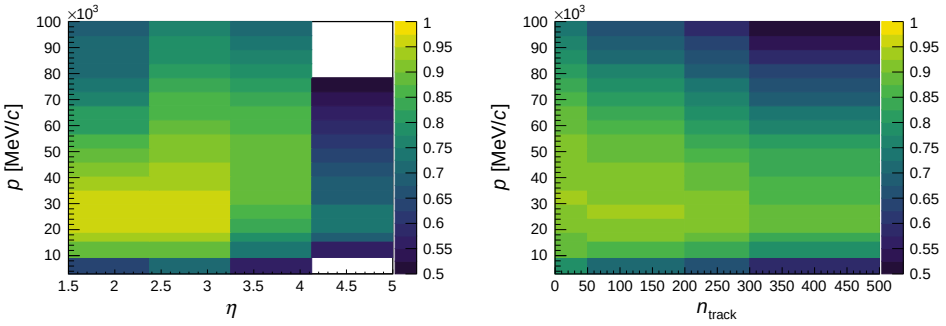

(b) K^+ selection for $B^+ \to K^+\mu^+\mu^-$ mode

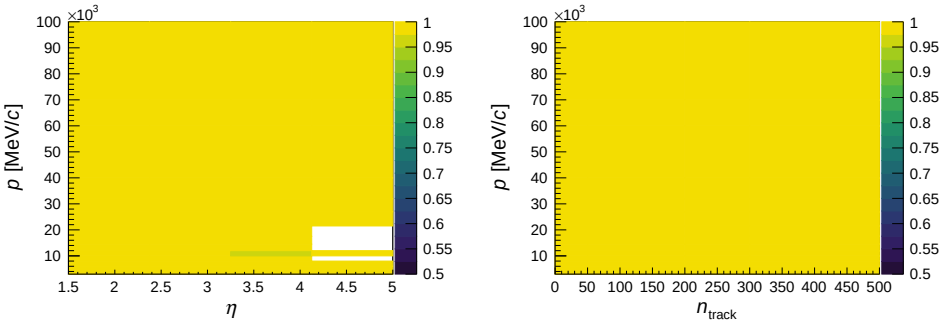

(c) μ^+ selection

Figure 4.4: Two-dimensional projections of PIDCalib efficiency histograms for data collected in 2016 with magnet polarity Up.

using the TISTOS method. The B candidates are required to be `TOS` at HLT1 (that is the μ or K candidate must be responsible for the trigger decision) and at HLT2. The J/ψ candidate is required to be `TIS` at L0. In addition, the K candidate is required to have `ProbNNk` > 0.1 to reject background from misidentified $B^- \to J/\psi(\to \mu^+\mu^-)\,\pi^-$ decays. The efficiency is then determined in bins of the transverse momentum p_{T} of the μ^+ and the μ^-.

In data, the efficiency is determined by fitting separately candidates that satisfy the `TIS` & `TOS` condition and candidates that satisfy the not-`TIS`

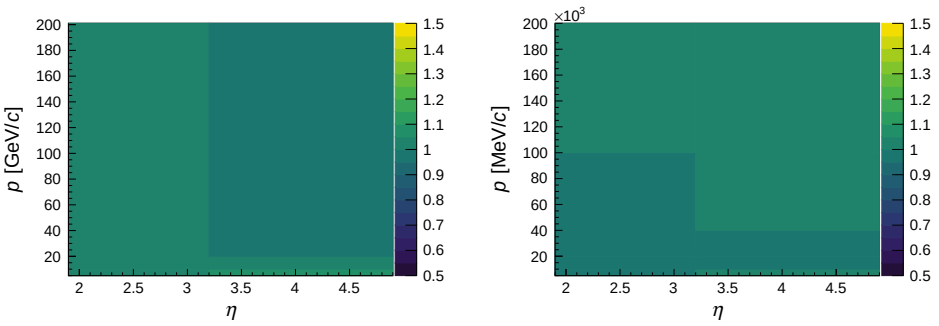

Figure 4.5: Tracking efficiency corrections for (left) 2012 and (right) 2016 data, both with magnet polarity Up.

& `TOS` condition. The resulting efficiency and uncertainty are given by

$$\varepsilon = \frac{N_{\mathrm{TOS}}}{N_{\mathrm{TOS}} + N_{\mathrm{NOT}}}, \quad \text{and} \quad \sigma_\varepsilon = \varepsilon \left(\left(\sigma_{\mathrm{TOS}} \cdot \frac{N_{\mathrm{NOT}}}{N_{\mathrm{TOS}}} \right)^2 + \sigma_{\mathrm{NOT}}^2 \right)^{\frac{1}{2}}, \quad (4.1)$$

where N_{TOS} is the yield of candidates that are `TIS` and `TOS`, and N_{NOT} is the yield of candidates that are `TIS` and not `TOS`. In the fits, the $B^+ \to J/\psi(\to \mu^+\mu^-)\, K^+$ signal shape is described by a Gaussian function with power-law tails. The tail parameters are fixed from fits to simulation datasets. The peak position and width of the shape are allowed to vary between p_{T} bins and are fixed from the combined `TIS` sample.The correction is calculated from the ratio between the efficiency in data and simulation. This is shown in figure 4.6.

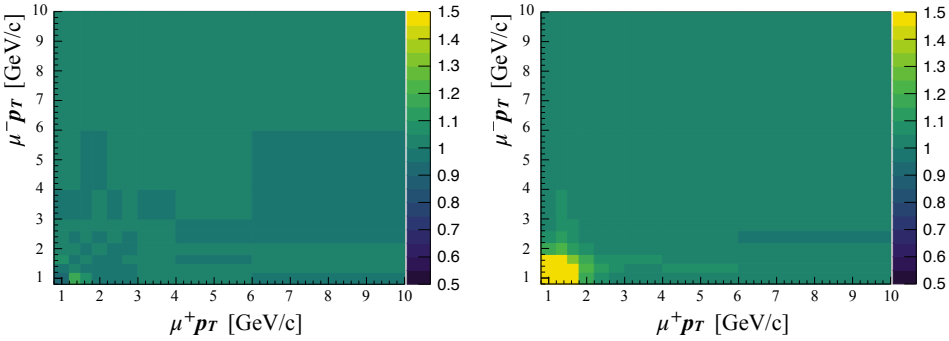

Figure 4.6: Ratio between `L0Muon` efficiency in data and simulation obtained with the TIS TOS method for (left) 2012 and (right) 2016 data with magnet polarity Up.

Kinematic selection correction

To account for data-simulation discrepancies in the occupancy and in the B kinematics, the simulation samples are corrected based on discrepancies in the distributions of n_{track} and p_{T}. To maintain correlations between these variables, an MVA is used to derive the weight for each event. The MVA is trained to separate simulated samples and real data, and a weight taken as the ratio of probabilities of an event to be data-like and simulation-like.

As in the previous cases, the data sample for calibration is $B^+ \to J/\psi(\to \mu^+\mu^-)K^+$, where the background is removed using the *sPlot* technique [139]. A simulation sample of $B^+ \to J/\psi(\to \mu^+\mu^-)K^+$ decays corrected for muon-PID, trigger and tracking efficiency is used to derive the weight which are then used to correct the simulation in the distributions of n_{track} and p_{T}.

Using the *sWeighted* data and the simulation corrected for muon-PID, trigger and tracking efficiency, a gradient boosted decision tree algorithm is trained as implemented in the hep_ml reweighting package [141].

The kinematic corrections described above are for fully reconstructed simulation samples. Some dedicated p_{T} correction histograms to correct raw simulation samples are also produced. These are needed to estimate the efficiencies for signal and control modes (see Sec. 4.5). For this, the normalized p_{T} histograms for the *sWeighted* data are devided by the full simulation corrected for muon-PID, trigger and tracking efficiency. The resulting ratio histogram is the source of the p_{T} weights for generator-level simulated B particles. Figure 4.7 shows example distributions of various kinematic observables for sWeighted data, raw simulation (with muon-PID, trigger and tracking efficiency corrections) and reweighted simulation (with all corrections).

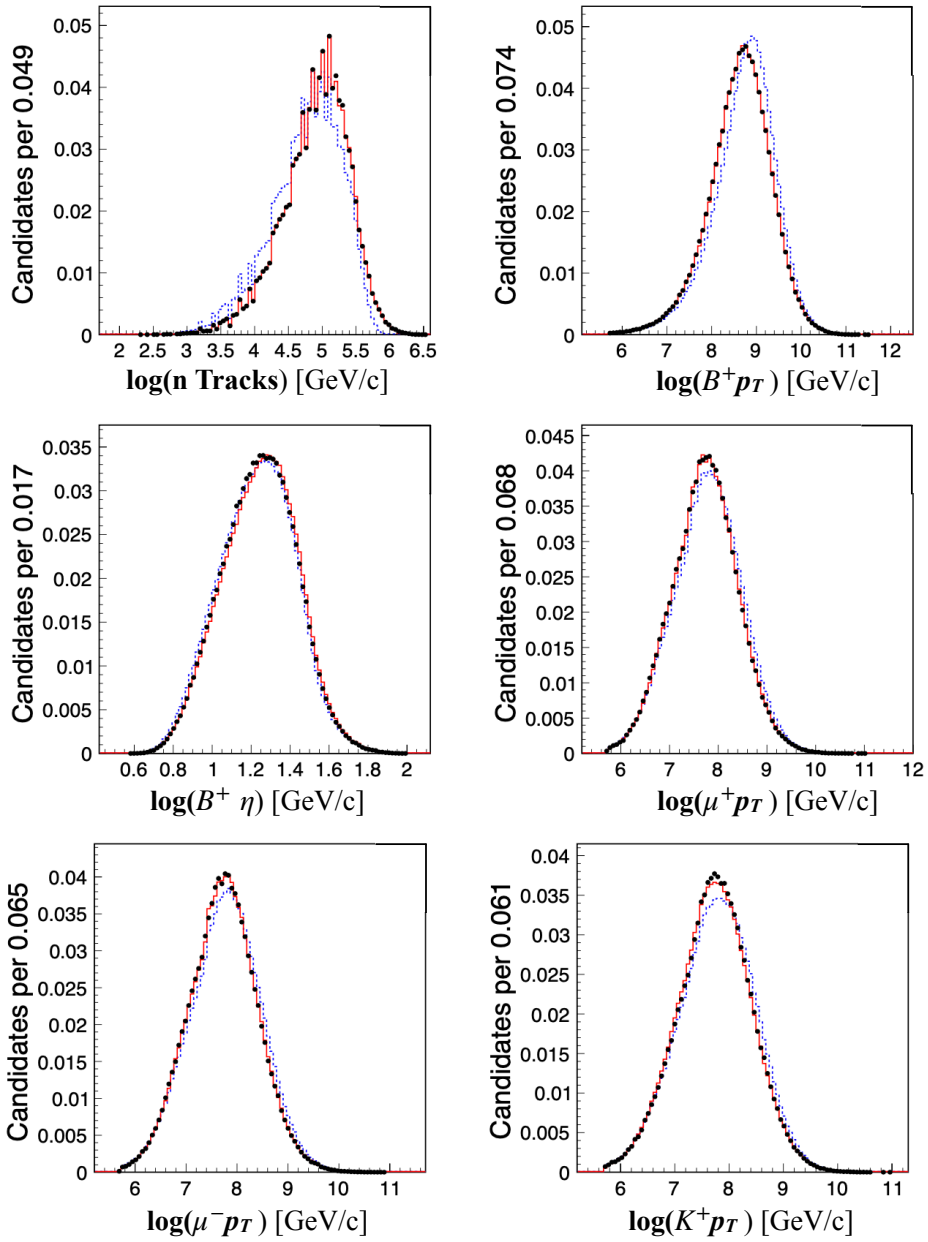

Figure 4.7: Distributions of kinematic observables for $B^+ \to J/\psi(\mu^+\mu^-)K^+$ candidates reconstructed in *sWeighted* data (black dots), partially corrected simulation (dashed blue line), fully corrected simulation (solid red line) for 2016 data with magnet polarity Up.

4.5 Efficiency studies

The efficiency of the LHCb detector to reconstruct and select $B^+ \to \pi^+\mu^+\mu^-$, $B^+ \to J/\psi(\mu^+\mu^-)\pi^+$ and $B^+ \to J/\psi(\mu^+\mu^-)K^+$ decays is a function of $\cos\theta_l$. It is necessary to account for this efficiency when determining the angular observables. The efficiency is calculated using simulation samples which are weighted as described in section 4.4 to remove data-simulation discrepancies. When studying the angular distribution of an individual data sample, as is the case for the control modes, the absolute normalisation of the efficiency is irrelevant. For a single data set the efficiency in a given bin of $\cos\theta_l$ is given by

$$\epsilon(\cos\theta_l) = N_{\text{sel.}}(\cos\theta_l)/N_{\text{gen.}}(\cos\theta_l), \tag{4.2}$$

where N_{sel} is the number of selected candidates in the bin of $\cos\theta_l$ and N_{gen} is the number of decays originally generated in that bin before any selection requirements. In principle, the selected and generated samples can be independent, so there is no requirement for N_{sel} to be a subset of N_{gen}. This is the case for the two control mode, where the control mode samples are not combined over years and polarities, so the absolute magnitude of the efficiencies is of no consequence. In this case, the relative efficiency distribution shape is sufficient. For this reason, the selection efficiencies for all years and polarities of the control modes' samples have been re-normalised to 1. These are illustrated in appendix A.

When there is the need to combine data samples from different years and polarities, the normalisation of the efficiency per sample is relevant. This is the case for the rare mode, where there is the need to combine the samples and average the efficiency to account for different data-taking conditions between the data-taking years. In this case, N_{sel} is a subset of N_{gen}. When the normalisation is needed, the efficiency in a given bin of $\cos\theta_l$ is given by

$$\epsilon(\cos\theta_l) = N_{\text{sel.}}(\cos\theta_l)/N_{\text{gen.}}(\cos\theta_l) \times \epsilon_{acc}(\cos\theta_l), \tag{4.3}$$

where N_{sel} is a subset of N_{gen} and $\epsilon_{acc}(\cos\theta_l)$ is the acceptance efficiency of the LHCb detector estimated on a separate sample.

The acceptance efficiency is the efficiency for the B^+ meson to be forward-going in the detector and for the pion/kaon and the two muons to be inside the nominal detector acceptance of 10–400 mrad. LHCb simulation

samples are often produced only in the acceptance to save resources as particles outside this range are not reconstructed. The acceptance efficiency is determined on an independent generator-level sample. The average efficiency calculation of the rare mode must take into account the particle acceptance efficiency per year as this is expected to vary across different data taking years. The acceptance efficiency of the rare mode for each year and polarity is determined as

$$\varepsilon_{\text{acc}} = \frac{N_{\text{InAcc}}}{N_{\text{gen}}}, \tag{4.4}$$

where N_{inacc} is the number of generated B-mesons whose children are in the acceptance region of the LHCb detector and N_{gen} is the number of generated signal B-mesons. N_{inacc} is a subset of N_{gen}. The acceptance requirement corresponds to a polar angle $\theta = \arccos(p_z/p)$ in the lab frame within the range $0.01 < \theta < 0.40\,\text{rad}$.

The rare mode's efficiency formula can be rearranged as

$$\epsilon(\cos\theta_l) = \epsilon_{sel}(\cos\theta_l) \times \epsilon_{acc}(\cos\theta_l), \tag{4.5}$$

Figure 4.8 shows the angular efficiency for the 2017 magnet polarity Up simulation sample, in the low and high q^2 regions.

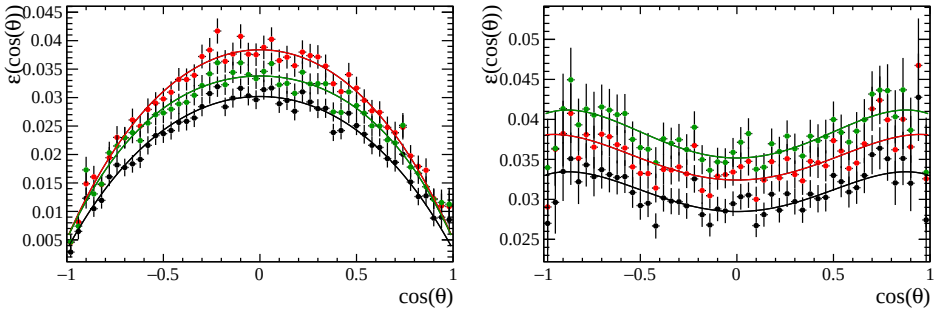

Figure 4.8: Selection efficiency of the $B^+ \to \pi^+\mu^+\mu^-$ decay in black, selection efficiency of the $B^+ \to \pi^+\mu^+\mu^-$ decay with no cut on the trigger in red, selection efficiency of the $B^+ \to \pi^+\mu^+\mu^-$ decay with no cut on PID in green. The distributions are fitted with a fourth order polynomial. Low q^2 range ($[1.1 - 6.0]$ GeV^2/c^4) on the left, high q^2 range ($[15.0 - 22.0]$ GeV^2/c^4) on the right. .

To estimate the statistical uncertainty on the efficiency, pseudo-data samples are generated by sampling from simulation samples (bootstrapping technique) [142]. For each pseudo-data sample, each reconstructed B-candidate gets a weight drawn from a Poisson distribution with expectation 1 [143].

Selection efficiency

The selection efficiency for each year and polarity is determined

$$\epsilon_{\text{sel}} = \frac{\sum_k^{N_{\text{sel}}} w^k_{\text{PID}} \cdot w^k_{\mu\text{ID}} \cdot w^k_{\text{trigger}} \cdot w^k_{\text{track}} \cdot w^k_{\text{kin}} \cdot}{N_{\text{gen}}}, \tag{4.6}$$

where w_{PID}, $w_{\mu\text{ID}}$, w_{trigger}, w_{track} and w_{kin} are the PID, muon ID, trigger, track reconstruction and kinematic weights detailed in Sec 4.4.1, N_{sel} is the number of selected candidates and N_{gen} is the number of generated signal B-mesons.

4.5.1 Efficiency distribution fit model

The efficiency distribution can be parametrised by a polynomial function. A sum of Legendre polynomial functions are preferred to an ordinary polynomial function because the individual terms in the expansion are orthogonal. The model is given by

$$\epsilon(\cos\theta_l) = N(1 + p_1 L_1(\cos\theta_l) + p_2 L_2(\cos\theta_l) + \tag{4.7}$$

$$p_3 L_3(\cos\theta_l) + p_4 L_4(\cos\theta_l)) \tag{4.8}$$

where L_i is a Legendre polynomial of order i. The normalisation parameter, N, can be absorbed in the overall normalisation parameter of the PDF used in the fit. In the nominal analysis, a symmetric function is used around $\cos\theta_l = 0$ fixing $p_1 = p_3 = 0$.

This model for the efficiency distribution was compared to an ordinary polynomial function and to a sum of Legendre polynomials that is not forced to be symmetric. This study was performed for both the $B^+ \to J/\psi(\mu^+\mu^-)\pi^+$ and $B^+ \to J/\psi(\mu^+\mu^-)K^+$ efficiency distributions.The efficiency distribution fit with the chosen and alternative models for $B^+ \to J/\psi(\mu^+\mu^-)\pi^+$ 2018 magnet polarity up samples is shown in figure 4.9. Appendix A contains plots for all data-taking years and polarities for both $B^+ \to J/\psi(\mu^+\mu^-)\pi^+$ and $B^+ \to J/\psi(\mu^+\mu^-)K^+$ samples. As expected, the ordinary polynomial PDF and the sum of Legendre polynomials PDF coincide after the fit to the distribution of the efficiency.

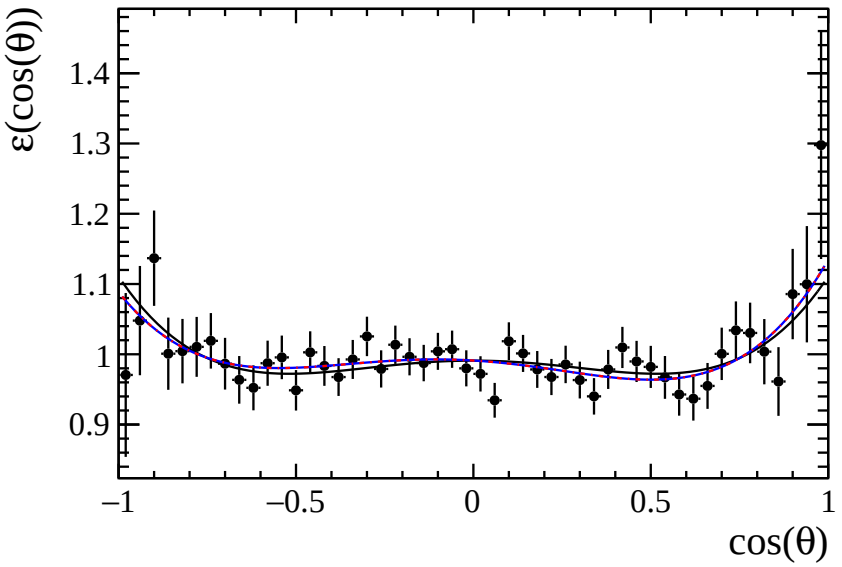

Figure 4.9: Efficiency distribution for the $B^+ \to J/\psi(\mu^+\mu^-)\pi^+$ 2018 magnet polarity up sample fitted with an ordinary polynomial (blue), a sum of Legendre polynomials (dotted red) and a symmetric sum of Legendre polynomials (black). .

4.5.2 Decay kinematics and the efficiency shape

The distribution of the acceptance over $\cos\theta_l$ changes shape with q^2. This reflects the particle kinematics in the decay. A few examples of extreme scenarios are given to illustrate how the $B^+ \to \pi^+\mu^+\mu^-$ kinematics vary over q^2 is shown in Fig. 4.10.

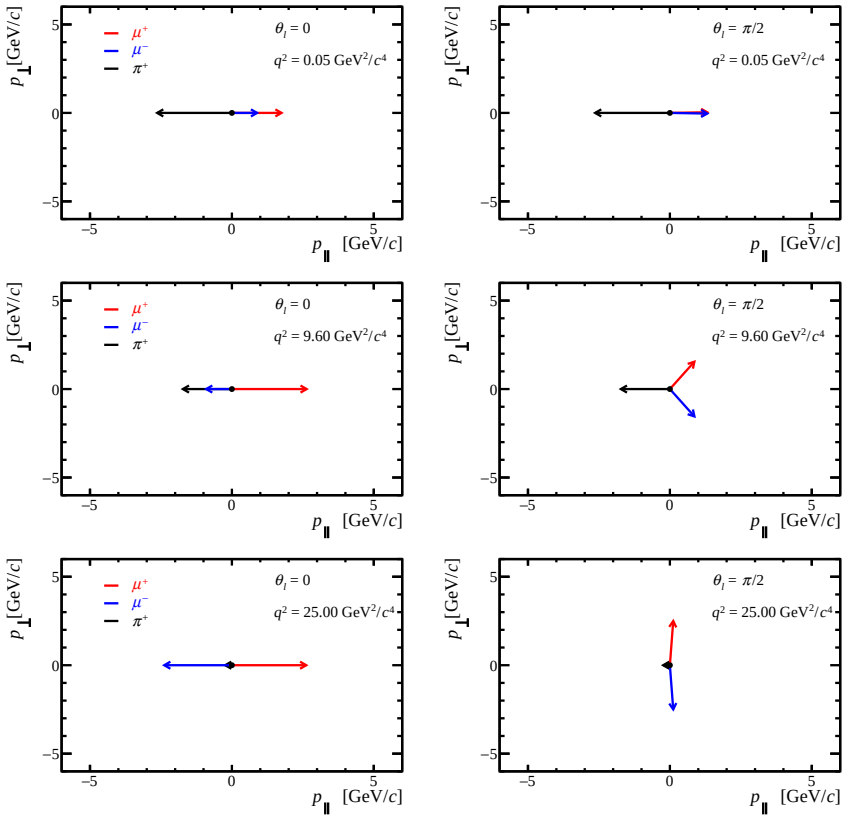

Figure 4.10: Illustration showing the particle momentum in the B^+ meson rest-frame for different values of q^2 and θ_l. The length of the arrow indicates the magnitude of the particle momentum. The momenta are drawn in the B^+ rest-frame using the plane of the decay of dilepton system, with $p_\parallel$ the momentum component parallel to the direction of the dilepton system in the B^+ meson rest-frame.

In the B^+ rest-frame, the hadron and the diplepton system are always produced back-to-back. When $q^2 = {q^2}_{\rm max} = (m_B - m_\pi)^2$, the dilepton system and the pion are at rest in the B^+ rest-frame. The dilepton system and B^+ frames coincide and the μ^+ and μ^- are back-to-back. When $q^2 = {q^2}_{\rm min} = 4m_l^2$, the two leptons are at rest in the dilepton rest-frame and are co-linear in the B^+ frame. The pion is also at its most energetic at ${q^2}_{\rm min}$. When θ_l is zero,

the μ^+ will always be aligned with the direction opposite that of the pion; at very low q^2 the μ^- is aligned with the direction of the μ^+ but at higher values it is aligned with the direction of the pion. To get to the laboratory frame the system needs to be boosted along the B^+ flight-direction. The direction of this boost is unrelated to any of the directions shown in the figure.

The variation of $B^+ \to \pi^+\mu^+\mu^-$ kinematics over the q^2 range is the source of the difference in the selection efficiency of the rare mode at low and high q^2 values. The main contributors to the inefficiency are the fact that muons need to have more than $3\,\text{GeV}/c$ of momentum to reach the muon system (to not be swept out by the magnetic field) and need to have more than $6\,\text{GeV}/c$ of momentum to penetrate the full muon system; that particles must have $\gtrsim 1.5\,\text{GeV}/c$ of momentum to be reconstructed as long tracks; and the requirement that at least one of the two muons must have $\gtrsim 1.5\,\text{GeV}/c^2$ of transverse momentum to satisfy the L0 trigger requirements. At low-q^2 the track and muon reconstruction requirements favour decays with θ_l away from zero and π, where one of the muon ends up being soft in the B^+ rest-frame. At intermediate and high-q^2, the L0 requirements favour events away from $\theta_l \sim \pi/2$, where the maximum muon momentum tends to be smaller. The variation in the efficiency shape in finer q^2 bins, of 1 GeV^2/c^4 width, is shown in Appendix B for the 2017 magnet-up polarity simulation.

The efficiency is expected to be symmetric in $\cos(\theta_l)$ because of the following considerations regarding the production asymmetry of B^+/B^-, detector asymmetries, and *CP* asymmetries in the $\pi^+\mu^+\mu^-$ and $\pi^-\mu^+\mu^-$ channels. The definition of $\cos\theta_l$ depends on μ^+ for B^+ decays, and on μ^- for B^- decays. For the efficiency to be non-symmetric when combining B^+ and B^- decays, either an efficiency difference for the differently charged muons is necessary, or an asymmetry in the $\pi^+\mu^+\mu^-$ and $\pi^-\mu^+\mu^-$ decays is necessary, or a combination of the tow. The measured B^+/B^- production asymmetry is consistent with 0, at $(-0.6 \pm 0.6)\%$, in a $B^0 - \overline{B^0}$ mixing analysis [144]. Any detector asymmetry is accounted for by the kinematic corrections applied to the data. Specifically, the asymmetries of the muon detection system cancel out since both decay channels include the $\mu^+\mu^-$ dilepton system. The kinematics of this dilepton system does not change between the two decay channels so no intrinsic detection asymmetry is expected to stem from the child dilepton system. The detection asymmetry of pions and antipions is caused by PID and tracking asymmetries and was measured for the two magnet polarities, respectively $\epsilon_{\pi^+}/\epsilon_{\pi^-} = 0.9914 \pm 0.0040$ and $\epsilon_{\pi^+}/\epsilon_{\pi^-} = 1.0045 \pm 0.0034$ for

magnet polarities up and down [145]. This asymmetry was also measured in bins of momentum, transverse momentum and azimuthal angle. It is known that the tracking efficiency depends on the azimuthal angle to a small degree and is flat in all other variables. This dependence disappears when averaging over magnet polarities. The PID asymmetry is corrected for by using PIDCalib PID efficiency histograms to reweight the PID variables in this analysis as described in section 4.4.

4.5.3 Efficiency averaging for the rare mode

The rare mode angular efficiency is calculated in two bins of q^2, $[1.1 - 6.0]\,\mathrm{GeV}^2/c^4$ and $[15.0 - 22.0]\,\mathrm{GeV}^2/c^4$. When averaging over years and polarities in each of the q^2 bins, the efficiency of the rare mode must be computed taking into account the fraction of data in each data-taking period (and magnetic polarity). To do this, each sample should be weighted so that the weighted number of events represents the number of B^+ mesons,

$$N_{B^+} = 2\mathcal{L} \cdot \sigma(pp \to b\bar{b}X) \cdot f_u \tag{4.9}$$

produced in that dataset. Here, $\mathcal{L}$ is the integrated luminosity of the data set, $\sigma(pp \to b\bar{b}X)$ the $b\bar{b}$ production cross-section in proton-proton collisions at the relevant centre-of-mass energy and f_u the B^+ production fraction, and the factor 2 accounts for the fact that B-mesons are produced in pairs from proton-proton collisions. Given the large uncertainty on the production cross-section, it is better to estimate the weight of each data set from the efficiency corrected yield of $B^+ \to J/\psi K^+$ decays in the data.

The statistical uncertainty on the average efficiency is estimated using a bootstrapping technique, where the efficiency is computed a number of times with each event assigned a weight chosen from a Poisson distribution with mean 1.0 in each iteration. The standard deviation of the resulting efficiency is assigned as the statistical uncertainty. This is carried in bins of $\cos\theta_l$ and the resulting distribution fitted to determine the efficiency model. The efficiency distribution including both statistical and systematic uncertainties, and the results of fits to the distributions, at low- and high-q^2 are shown in Fig. 4.11.

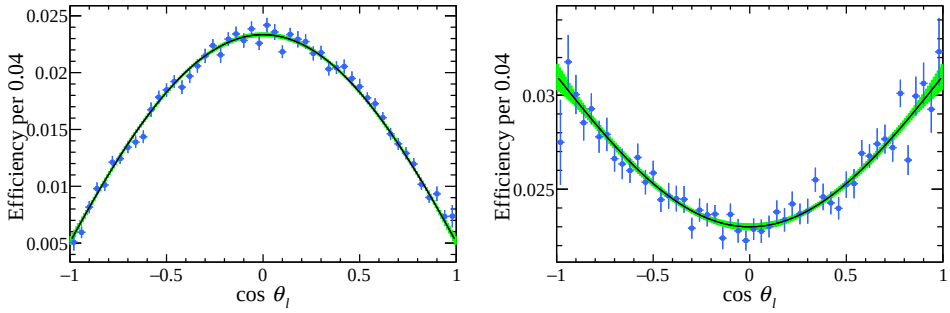

Figure 4.11: Efficiency averaged over the different data-taking periods for the $B^+ \to \pi^+\mu^+\mu^-$ (left) for 1.1–6.0 GeV/c^4 and (right) 15.0–22.0 GeV/c^4. The model is described by the sum of Legendre polynomials up-to and including order four.

4.6 Angular resolution

The angular resolution is measured using simulated $B^+ \to \pi^+\mu^+\mu^-$ decays by studying the difference between $\cos(\theta_l)$ at truth and reconstruction levels. The distribution of

$$\cos(\theta_l^{\text{true}}) - \cos(\theta_l^{\text{reco.}}) \tag{4.10}$$

for the 2018 magnet polarity up simulated dataset is shown in figure 4.12. The data are fitted with a Gaussian distribution to estimate the resolution. This model captures the behaviour of the core of the distribution but does not describe well the tails of the distribution. The widths of all of the Gaussian functions are smaller than 0.008. This is sufficiently small that the the resolution can be neglected in this analysis. The resolution will be considered as a source of systematic uncertainty.

4.7 Dangerous backgrounds

The candidate selection greatly enhances the signal to background ratio. Some of the background sources introduced in section 4.2 cannot be completely discredited yet though. Particles produced in J/ψ decays can be mis-identified by the LHCb detector: specifically, one muon is mis-identified as a hadron. This background is expected to be right in the signal region, so, to in investigate this, the combination of the mass of the reconstructed decay products, for each reconstructed event in the data, is calculated. This product was then compared to the reconstructed B mass of the event. The mass combinations are K^+K^-, $K^+\mu^-$, $K^+\pi^-$, $\pi^+\mu^-$ and $\pi^+\pi^-$. The distributions for the combined Run

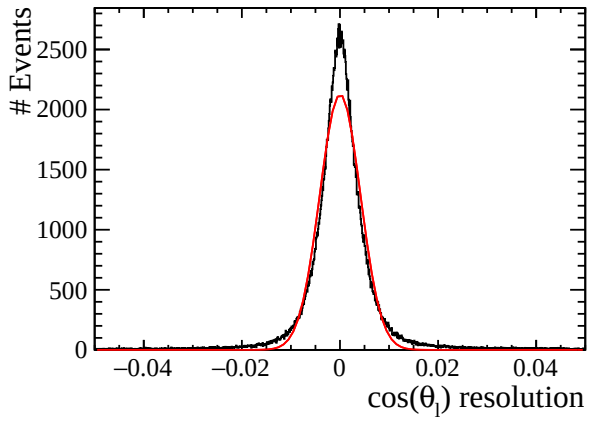

Figure 4.12: Gaussian PDF fit to the difference between simulated $\cos(\theta_l)$ at generator and reconstruction levels to extract the angular resolution of the LHCb detector, for 2018 magnet polarity up.

1 and Run 2 data in the low q^2 bin are shown as examples in figure 4.13. The J/ψ signature is clearly visible in the form of a horizontal band. This background is rejected by vetoing events that have a combined $h^+\mu^-$ invariant mass withn 100MeV of the J/ψ peak.

Another source of background consists in particles produced in $B^+ \to \overline{D}^0(K^+\mu^-\overline{\nu}_\mu)\mu^+\nu_\mu$ and $B^+ \to \overline{D}^0(\pi^+\mu^-\overline{\nu}_\mu)\mu^+\nu_\mu$ decays, which can also be mis-identified by the LHCb detector. One should note that these backgrounds are suppressed by an order of magnitude because of the lifetime of the charm meson. These have a different decay topology to the signal and a worse vertex fit quality. Nonetheless, when mis-identification of one of their decay products occurs, these backgrounds can form a shoulder close to the signal region. To investigate these backgrounds, for each reconstructed event in the data, the combination of the mass of the reconstructed decay products that could be a result of these backgrounds was calculated, as in the previous case. This product was then compared to the reconstructed B mass of the event to see how this background shoulder populates the fit range. The mass combinations are K^+K^-, $K^+\mu^-$, $\pi^+\pi^-$, $\pi^+\pi^-$, $\pi^+\mu^-$ and $K^+\pi^-$. The distributions for the combined Run 1 and Run 2 data in the low q^2 and high q^2 bins are shown respectively in figures 4.14 and 4.15. There is no evidence of this background in the rare data sample. The shoulder from this background sits below the minimum reconstructed B mass of the simultaneous two-dimensional mass and angle fit performed in this angular analysis, and is neglected in

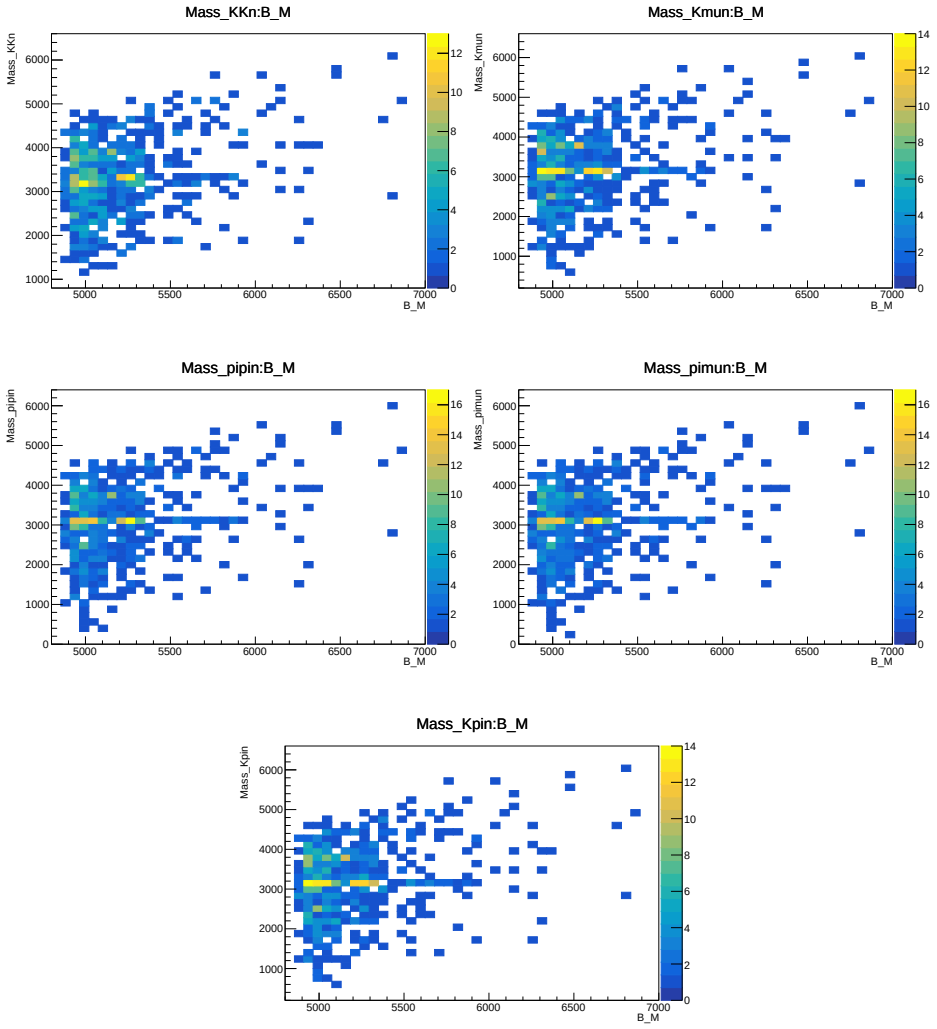

Figure 4.13: Scatter plot of the reconstructed invariant mass vs mass combinations K^+K^-, $K^+\mu^-$, $\pi^+\pi^-$, $\pi^+\mu^-$ and $K^+\pi^-$, from top to bottom, left to right, in the combined Run 1 and Run 2 data in the low q^2 bin.

the analysis. The data was also subjected to a further cut by requesting that the reconstructed B mass is within the interval $(5180, 5600)$MeV $/c^2$, which corresponds to this analysis's fit range. The 1D projection of the mass combinations K^+K^-, $K^+\pi^-$ and $\pi^+\pi^-$ with and without this reconstructed B mass constraint are shown in figures 4.16 and 4.17 for the low and high q^2 bins respectively.

Other sources of backgrounds include low-mass backgrounds from partially reconstructed b-hadron decays with one missing massive particle. Most dangerous backgrounds are from $B^0 \to \rho\mu^+\mu^-$ (or $B^+ \to \rho^+\mu^+\mu^-$)

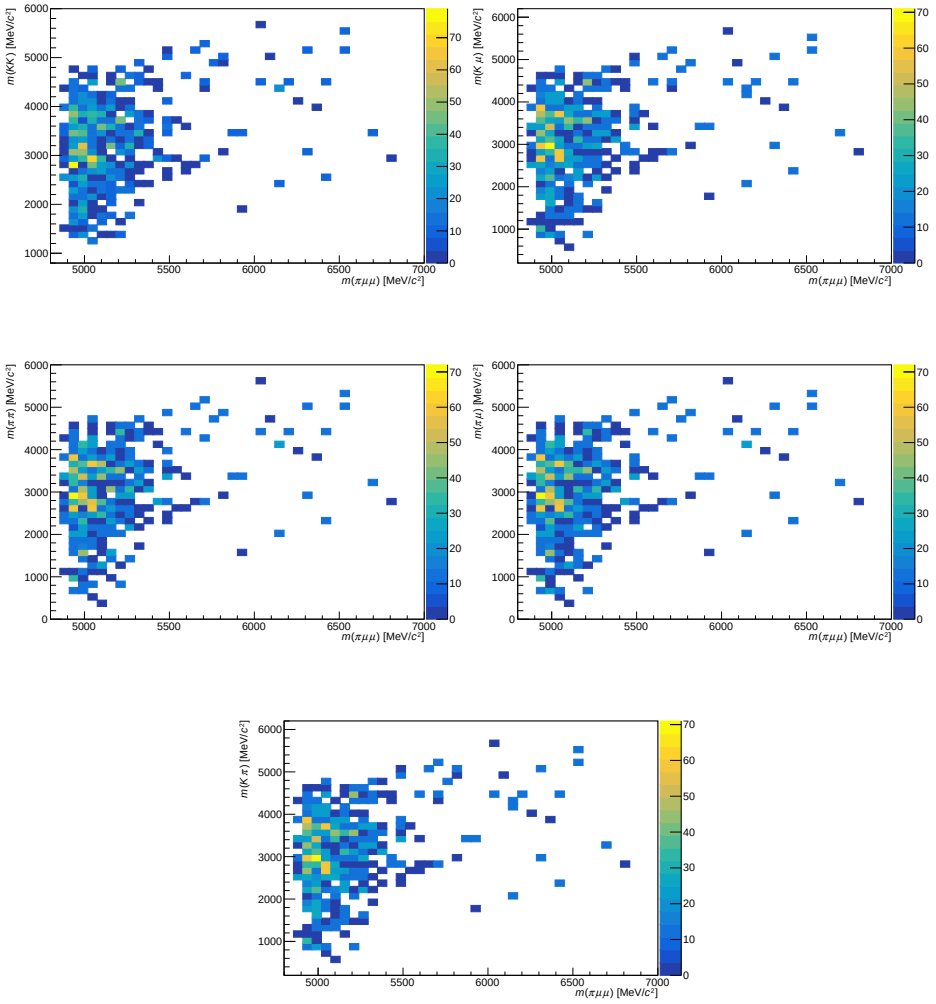

Figure 4.14: Scatter plot of the reconstructed invariant mass vs mass combinations K^+K^-, $K^+\mu^-$, $\pi^+\pi^-$, $\pi^+\pi^-$, $\pi^+\mu^-$ and $K^+\pi^-$, from top to bottom, left to right, in the combined Run 1 and Run 2 data in the low q^2 bin. The reconstructed kaon is a mis-identified true pion.

and $B_s^0 \to f_0\mu^+\mu^-$ where the ρ or f_0 decays to two pions and one pion is not reconstructed. A similar source of background are $B^0 \to K^{*0}\mu^+\mu^-$ and $B^+ \to K^{*+}(\to K^0\pi^+)\mu^+\mu^-$ decays, where the kaon is not reconstructed, or where a kaon is reconstructed as a pion and the other particle from the decay is not reconstructed. Decays with two (or more) missing particles constitute another source of background, but these will populate masses outside of our region of interest. Finally, fully hadronic decays, including $B^+ \to \overline{D}^0\pi^+$, $B^+ \to K^+\pi^+\pi^-$ and $B^+ \to \pi^+\pi^-\pi^+$ decays, with $\pi \to \mu$ or

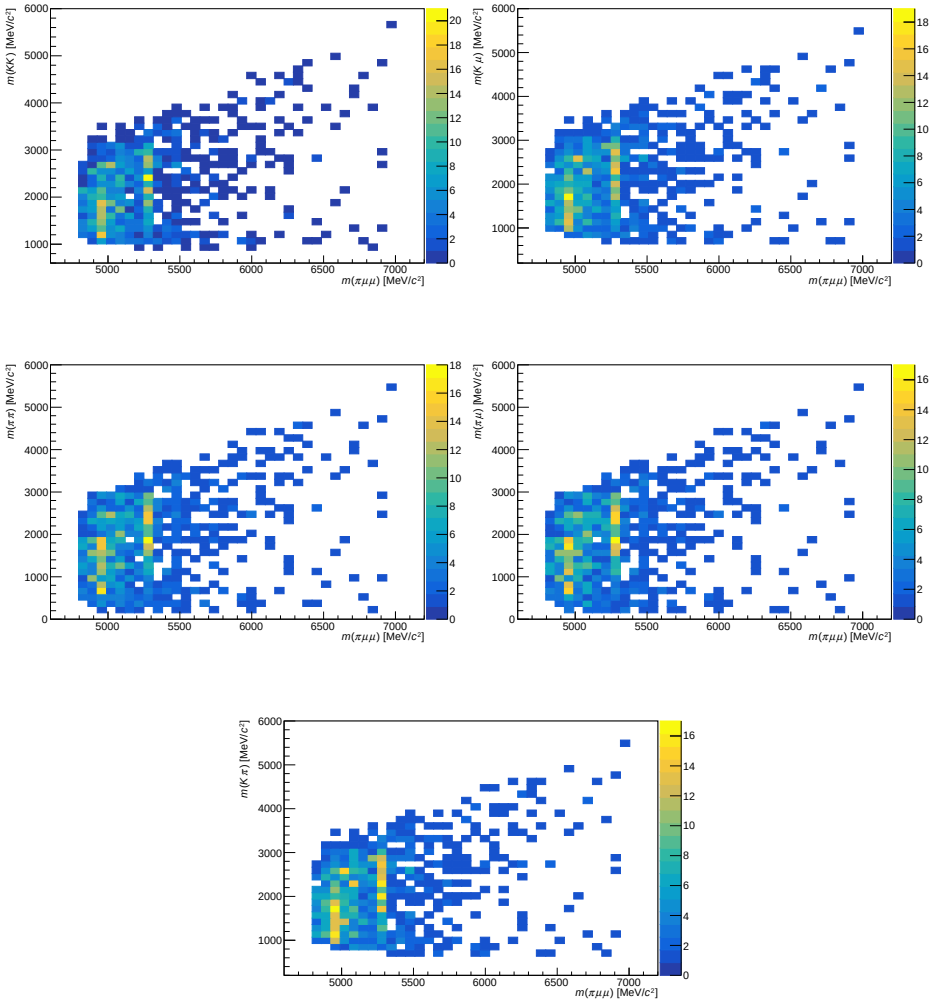

Figure 4.15: Scatter plot of the reconstructed invariant mass vs mass combinations K^+K^-, $K^+\mu^-$, $\pi^+\pi^-$, $\pi^+\pi^-$, $\pi^+\mu^-$ and $K^+\pi^-$, from top to bottom, left to right, in the combined Run 1 and Run 2 data in the high q^2 bin. The reconstructed kaon is a mis-identified true pion.

$K \to \mu$ misidentification are also a source of background.

The selection choices of requiring `IsMuon` and `ProbNNmu` > 0.2, result in a $\pi^\pm \to \mu^\pm$ ($K^\pm \to \mu^\pm$) a misidentification efficiency of 0.5% (0.4%). Using only `IsMuon`, the $K^\pm \to \mu^\pm$ misidentification probability would have been larger than that of $\pi^\pm \to \mu^\pm$ due to the increased likelihood for a kaon to decay in flight. The background from kaons can be further suppressed, without any appreciable loss of signal, using additional information from the RICH detectors. For example, requiring `DLLKpi` < 5 removes a further 60% of

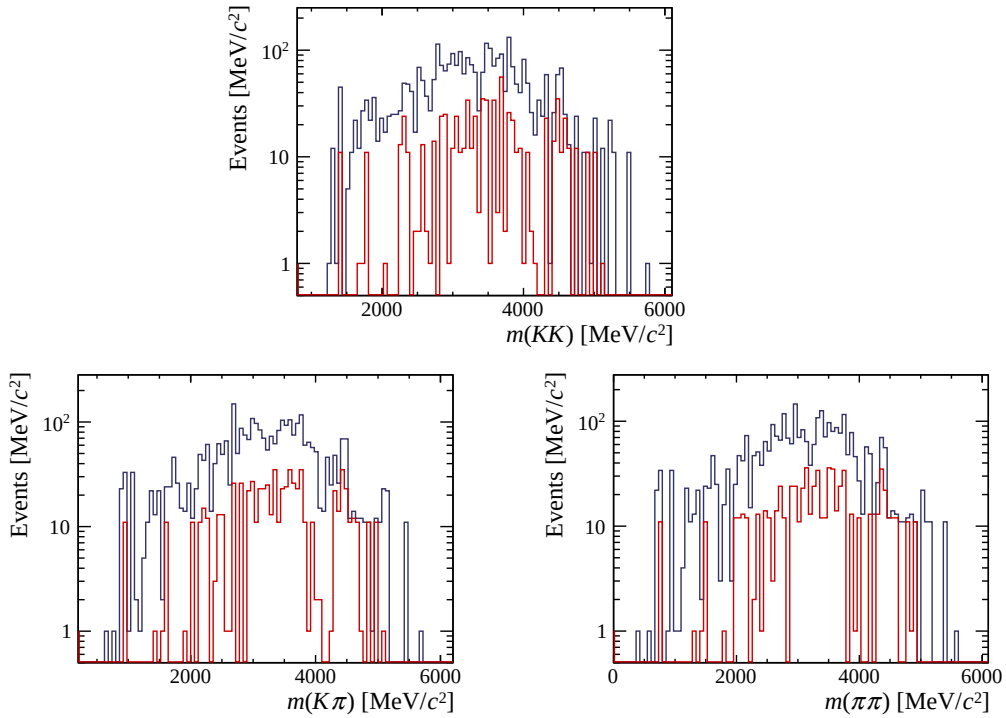

Figure 4.16: One-dimensional projection of the mass combinations K^+K^- (top left), $K^+\pi^-$ (top right) and $\pi^+\pi^-$ (bottom) in the combined Run 1 and Run 2 data in the low q^2 bin. The blue lines identify the data selected with no reconstructed B mass constraint. The red lines show the same data with a reconstructed B mass: 5180MeV $/c^2 < m(\pi\mu\mu) <$ 5600MeV $/c^2$.

$K^\pm \to \mu^\pm$ backgrounds but only 5% of the signal.

A list of sources of specific background and their branching fractions, taking into account all of the decays in the chain, are given in Table 4.3. Backgrounds with one-or-more missing pion or two missing neutrinos are not considered as these are sufficiently low in mass that they will not be present in the mass window used in this work. Backgrounds with a single missing neutrino form a broad background at low masses that is not easily separated from combinatorial background. Backgrounds with an intermediate charm meson that decays hardronically are searched for in the data in the $\pi^+\mu^-$ and $\mu^+\mu^-$ mass but are not identified.

Considering all of these aspects together, the most problematic backgrounds are from the decays $B^+ \to \pi^+\pi^+\pi^-$ and $B^+ \to K^+\pi^+\pi^-$. In the former, the are two possible ways to misidentify the final state as $\pi^+\mu^+\mu^-$. In the latter, only one of the combinations makes an appreciable contribution to the background rate; due to the strong $K^\pm \to \pi^\pm$ suppression used to

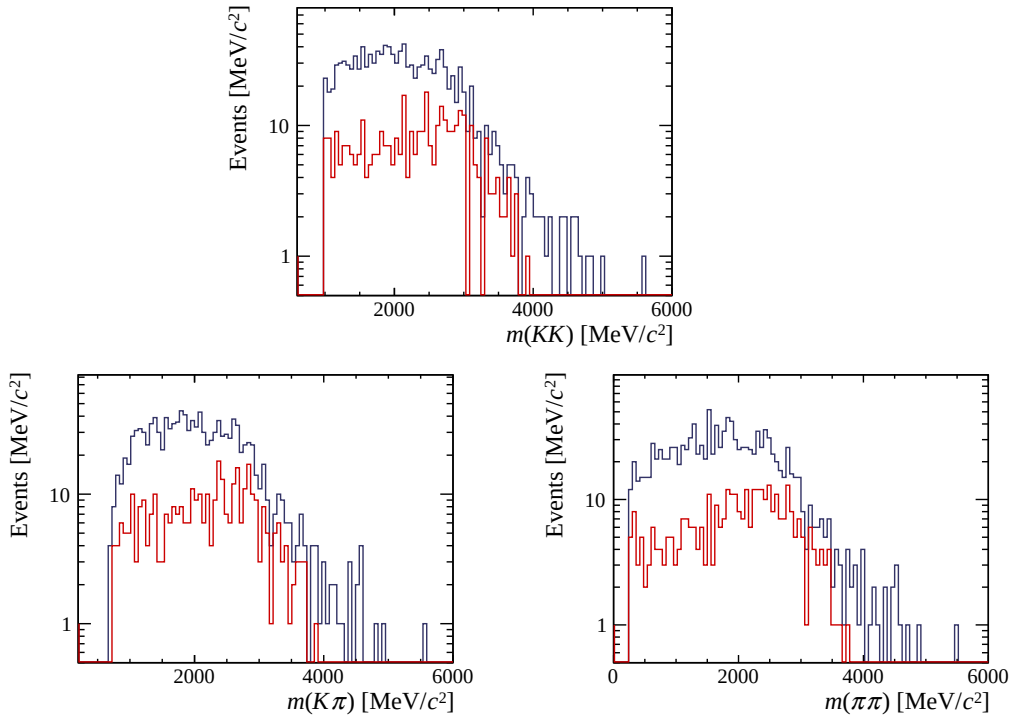

Figure 4.17: One-dimensional projection of the mass combinations K^+K^- (top left), $K^+\pi^-$ (top right) and $\pi^+\pi^-$ (bottom) in the combined Run 1 and Run 2 data in the high q^2 bin. 1D projection of the mass combinations K^+K^- (top left), $K^+\pi^-$ (top right) and $\pi^+\pi^-$ (bottom). The blue lines identify the data selected with no reconstructed B mass constraint. The red lines show the same data with a reconstructed B mass: 5180MeV $/c^2 < m(\pi\mu\mu) <$ 5600MeV $/c^2$.

Table 4.3: Sources of specific background for the $B^+ \to \pi^+\mu^+\mu^-$ decay.

Decay chain	Effective branching fraction
$B^+ \to \pi^+\pi^-\pi^+$	$(1.52 \pm 0.14) \times 10^{-5}$
$B^+ \to K^+\pi^-\pi^+$	$(5.10 \pm 0.29) \times 10^{-5}$
$B^+ \to K^+K^-\pi^+$	$(5.20 \pm 0.40) \times 10^{-6}$
$B^+ \to K^+K^-K^+$	$(3.40 \pm 0.15) \times 10^{-5}$
$B^+ \to \overline{D}^0(\to K^+\pi^-)\pi^+$	$(1.77 \pm 0.05) \times 10^{-4}$
$B^+ \to \overline{D}^0(\to \pi^+\pi^-)\pi^+$	$(6.50 \pm 0.21) \times 10^{-6}$
$B^+ \to \overline{D}^0(\to K^+K^-)\pi^+$	$(1.83 \pm 0.06) \times 10^{-5}$
$B^+ \to \overline{D}^0(\to K^-\mu^+\nu_\mu)\pi^+$	$(1.53 \pm 0.04) \times 10^{-4}$
$B^+ \to \overline{D}^0(\to \pi^-\mu^+\nu_\mu)\pi^+$	$(1.20 \pm 0.06) \times 10^{-5}$
$B^+ \to \overline{D}^0(\to K^+\pi^-)\pi^+$	$(1.77 \pm 0.05) \times 10^{-4}$
$B^+ \to \overline{D}^0(\to K^+\pi^-)\mu^+\nu_\mu$	$(9.08 \pm 0.36) \times 10^{-4}$
$B^+ \to \overline{D}^0(\to \pi^+\pi^-)\mu^+\nu_\mu$	$(3.33 \pm 0.14) \times 10^{-5}$
$B^+ \to \overline{D}^0(\to K^+\mu^-\overline{\nu}_\mu)\pi^+$	$(1.53 \pm 0.04) \times 10^{-4}$

reject $B^+ \to K^+\mu^+\mu^-$ decays in the analysis the contribution from decays with $K^+ \to \pi^+$ and $\pi^+ \to \mu^+$ is small. No events in simulation samples of one million $B^+ \to \pi^+\pi^+\pi^-$ decays survive the selections used in this analysis. To estimate the background level `RapidSim` [146] is used to produce samples of events that are weighted to have the correct Dalitz distributions using `Laura++` [147]. These samples are then weighted to account for the relative particle identification efficiency from `PIDCalib`. Using the $B^+ \to \pi^+\pi^+\pi^-$ and $B^+ \to K^+\pi^+\pi^-$ models from Refs. [148] and [149] the backgrounds are estimated to be at the level of $\sim 5\%$ (1.4%) and $\sim 6.2\%$ (3.4%) of the signal at low (high q^2), respectively. The $B^+ \to K^+\pi^+\pi^-$ decay is further reduced as noted above. The $B^+ \to \pi^+\pi^+\pi^-$ decay will peak under the signal in $\pi^+\mu^+\mu^-$ mass. The $B^+ \to K^+\pi^+\pi^-$ decay has a shape very similar to that of $B^+ \to K^+\mu^+\mu^-$.

The $\cos\theta_l$ distribution of the $B^+ \to \pi^+\pi^+\pi^-$ and $B^+ \to K^+\pi^+\pi^-$ decays of the Dalitz weighted `RapidSim` samples are shown in Fig. 4.18. The larger forward-background asymmetry arises from interference between spin-0 and spin-1 contributions to the amplitude of the decay. This is particularly dangerous for this analysis. Because usable fully reconstructed samples are not yet available for these backgrounds, they are currently considered as sources of systematic bias rather than as fit components.

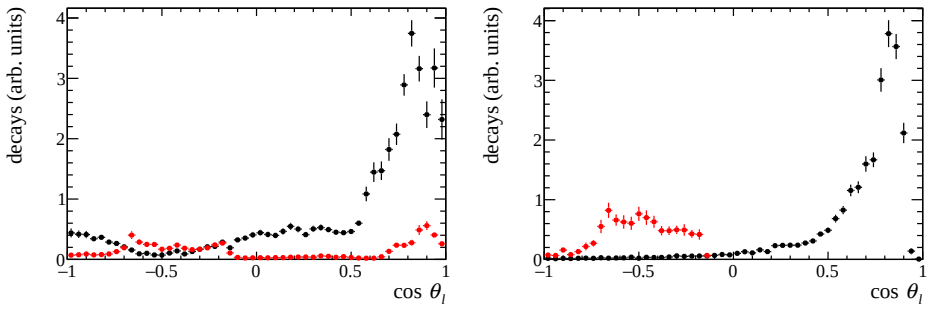

Figure 4.18: The angular distribution of simulated (left) $B^+ \to \pi^+\pi^-\pi^+$ decays where one of the π^+ and the π^- are misidentified as muons and (right) $B^+ \to K^+\pi^-\pi^+$ decays where the K^+ and the π^- are misidentified as muons. The distribution at low (high) q^2 is indicated by the black (red) markers.

4.8 Modelling the $B^+ \to \pi^+\mu^+\mu^-$ decay

The mass and angular model of the $B^+ \to \pi^+\mu^+\mu^-$ decay was fine-tuned and tested on the $B^+ \to J/\psi K^+$ and $B^+ \to J/\psi\pi^+$ decays. The final model for the fit to the $B^+ \to \pi^+\mu^+\mu^-$ decay was defined in stages. First fits to the invariant mass of $B^+ \to J/\psi K^+$ and $B^+ \to J/\psi\pi^+$ were performed to define an appropriate invariant mass distribution shape, as shown in section 4.8.1. Then two-dimensional fits to the invariant mass and helicity angle, $\cos(\theta_l)$ were performed on $B^+ \to J/\psi K^+$ and $B^+ \to J/\psi\pi^+$ to test the angular fitting strategy.

4.8.1 Fit strategy for the $\pi^+\mu^+\mu^-$ and $K^+\mu^+\mu^-$ invariant mass model

For each of the $B^+ \to \pi^+\mu^+\mu^-$, $B^+ \to J/\psi K^+$ and $B^+ \to J/\psi\pi^+$ decays, the signal mass distribution is described by the sum of a two-sided Crystal Ball function [150] and a Gaussian. The Crystal Ball shape has a Gaussian core and power-law tails on the left and right-hand side of the distribution. The left-hand tail receives contributions from final-state radiation from the pion/kaon and the two muons. Both tails are needed to describe non-Gaussian resolution effects. The Gaussian and Crystal Ball shapes share common peak positions but have different width parameters, labelled σ_1 and σ_2. Formally, the Crystal Ball shapes is defined as

$$s_m^{\mathrm{CB}}(m; m_0, \sigma_1, \alpha_{\mathrm{L}}, n_{\mathrm{L}}, \alpha_{\mathrm{R}}, n_{\mathrm{R}}) = \begin{cases} \exp\left(-\frac{1}{2}\left(\frac{m-m_0}{\sigma_1}\right)^2\right) & -\alpha_{\mathrm{L}} \leq \frac{m-m_0}{\sigma_1} \leq \alpha_{\mathrm{R}} \\ A_{\mathrm{L}}\left(B_{\mathrm{L}} - \left(\frac{m-m_0}{\sigma_1}\right)\right)^{-n_{\mathrm{L}}} & \frac{m-m_0}{\sigma_1} < -\alpha_{\mathrm{L}} \\ A_{\mathrm{R}}\left(B_{\mathrm{R}} - \left(\frac{m-m_0}{\sigma_1}\right)\right)^{-n_{\mathrm{R}}} & \frac{m-m_0}{\sigma_1} > +\alpha_{\mathrm{R}} \end{cases} \tag{4.11}$$

where

$$A_{\mathrm{L,R}} = \left(\frac{n_{\mathrm{L,R}}}{|\alpha_{\mathrm{L,R}}|}\right)^{n_{\mathrm{L,R}}} \cdot \exp\left(-\frac{|\alpha_{\mathrm{L,R}}|^2}{2}\right), \tag{4.12}$$

$$B_{\mathrm{L,R}} = \frac{n_{\mathrm{L,R}}}{|\alpha_{\mathrm{L,R}}|} - |\alpha_{\mathrm{L,R}}| \ . \tag{4.13}$$

If the two components are normalised

$$s_m(m) = f_{\mathrm{CB}} s_m^{\mathrm{CB}}(m) + (1 - f_{\mathrm{CB}}) s_m^{\mathrm{G}}(m) \tag{4.14}$$

where f_{CB} is the relative fraction of the Crystal Ball component and s_m^{G} is a Gaussian PDF.

In the case of each decay channel, the model is fit to simulation datasets to fix the fit function parameters, and then tested on data. When fitting data, the peak position is offset by Δm and the width scaled by δ_s. In order to establish this model, different shapes were tried on simulated samples. The potential distributions were: the sum of two one-sided crystal ball functions and a Gaussian function; the sum of two Gaussian functions and a one-sided crystal ball function; a single two-sided Crystal ball function; the sum of a two-sided Crystal ball function and a Gaussian function; and the sum of a two-sided Crystal ball function and two Gaussian functions. The chosen model is a two-sided Crystal ball function and a Gaussian function, shown in figure 4.19.

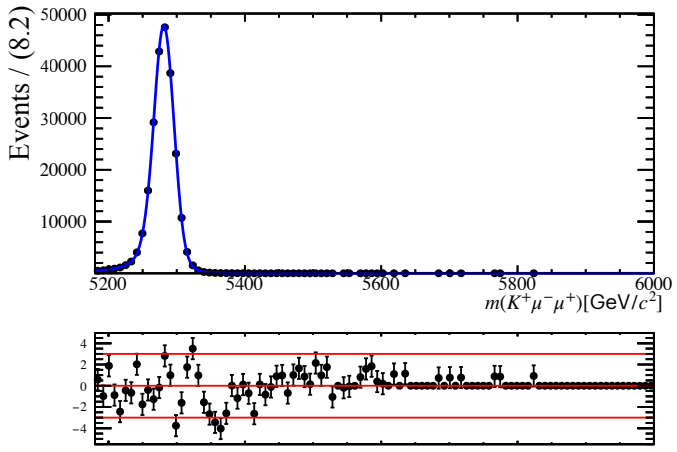

Figure 4.19: Mass distribution of simulated $B^+ \to J/\psi K^+$ decays fitted with the sum of a two-sided Crystal ball function and a Gaussian function.

The chosen model, or any of the discarder ones, is not able to fully describe the resolution in the peak region. This is expected as the mass resolution is momentum dependent and will vary candidate-to-candidate. For large data sets it is not possible to capture this behaviour without introducing a large number of model components with different mass resolutions. In practice, this small mis-modelling does not bias the signal estimate and is not a problem for the analysis. The chosen function provides the best balance between the number of fitted parameters and its ability to describe the simulated data set.

Table 4.4: Result of the fit to the $B^+ \to J/\psi K^+$ 2018 magnet-up data set.

Parameter	Value
Combinatorial slope	$(-5.97 \pm 0.44) \times 10^{-3}$
m_1	5280.81 ± 0.03
σ	25.87 ± 0.04
Combinatorial yield	$3\,007 \pm 319$
$B \to J/\psi K^*$ yield	$22\,387 \pm 215$
$B^+ \to J/\psi K^+$ yield	$434\,643 \pm 685$

$B^+ \to J/\psi K^+$ mass distribution

The $B^+ \to J/\psi K^+$ data set has the prominent signal and the best signal-to-background ratio. The data is described by three components, the signal, combinatorial background and background from partially reconstructed $B^+ \to J/\psi K^{*+}$ and $B^0 \to J/\psi K^{*0}$ decays. The partially reconstructed background is modelled using a Johnson SU function [151]. The parameters of the Johnson function were fixed from fits to simulated data sets of $B \to J/\psi K^*$ decays. This was done separately for each year and magnet polarity. In principle there can also be a small background from misidentified $B^+ \to J/\psi \pi^+$ decays but this background is small compared to the signal and has been neglected in the analysis of this mode. It is responsible for the poor fit performance in the 5300–5400 MeV/c^2 mass range. The result of the mass fit to the 2018 magnet polarity Up data set is shown in figure 4.20 and given in Table 4.4. Similar results are obtained for other years and polarities. Due to the momentum scale calibration of the detector the peak differs by ~ 5 MeV/c^2 between the Run 1 and 2 data set (it has been corrected in Run 2). The peak position shift and width scale factors determined from fitting the $B^+ \to J/\psi K^+$ data are used to correct the $B^+ \to J/\psi \pi^+$ and $B^+ \to \pi^+ \mu^+ \mu^-$ mass models.

$B^+ \to J/\psi \pi^+$ mass distribution

The $B^+ \to J/\psi \pi^+$ data set contains a much larger number of contributions from partially reconstructed decays. It is also essential to account for misidentified background from $B^+ \to J/\psi K^+$ as in this case the relevant CKM elements lead to a background after applying particle identification requirements that is still sizeable compared to the signal. Fitting in the range 5000–6000 MeV/c^2 it is necessary to include backgrounds $B_s^0 \to J/\psi(\mu^+\mu^-) f_0$, $B^{+,0} \to J/\psi(\mu^+\mu^-)\rho^{+,0}$,

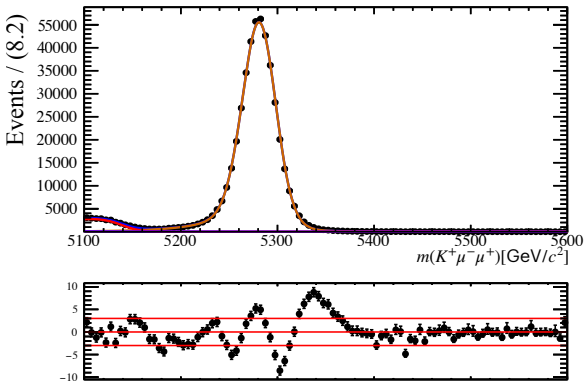

Figure 4.20: Reconstructed $K^+\mu^+\mu^-$ mass of $B^+ \to J/\psi(\mu^+\mu^-)K^+$ candidates in the 2018 magnet polarity Up data set. The result of (blue) a fit to the data set and the individual components from (orange) the signal (red) $B \to J/\psi K^*$ decays and (purple) combinatorial background are also shown.

Table 4.5: Result of the fit to the $B^+ \to J/\psi\pi^+$ 2018 magnet-up data set.

Parameter name	Value
Combinatorial slope 2018	-0.0013 ± 0.0001
Combinatorial yield	5106 ± 166
$B_s^0 \to J/\psi f_0$ yield	1054 ± 518
$B^+ \to J/\psi K^+$ yield	10004 ± 590
$B^+ \to J/\psi K^*$ yield	2124 ± 179
m DCB $\pi^+\mu^+\mu^-$ 2018	5278.4 ± 0.6
m1 DCB $K^+\mu^+\mu^-$ 2018	5231 ± 1
$B^{+,0} \to J/\psi\rho^{+,0}$ yield 2018	4679 ± 361
$\sigma_{\pi^+\mu^+\mu^-}$	27.0 ± 0.5
$\sigma_{K^+\mu^+\mu^-}$	23 ± 1
$B^+ \to J/\psi\pi^+$ yield	15389 ± 396

$B^+ \to J/\psi(\mu^+\mu^-)\rho^+$, and $B^{+,0} \to J/\psi(\mu^+\mu^-)K^{*+,0}$ decays. Each of these backgrounds is modelled by a Johnson SU function, whose parameters are fixed from dedicated simulated samples of the relevant decay. The yields of the components making up the cumulative PDF are left to vary in the fit to data. The shapes fitted to the LHCb simulated data sets can be seen in Fig. 4.21. The fit to the 2018 magnet-up data is also shown in figure 4.21 and the resulting parameter values are given in Table 4.5.

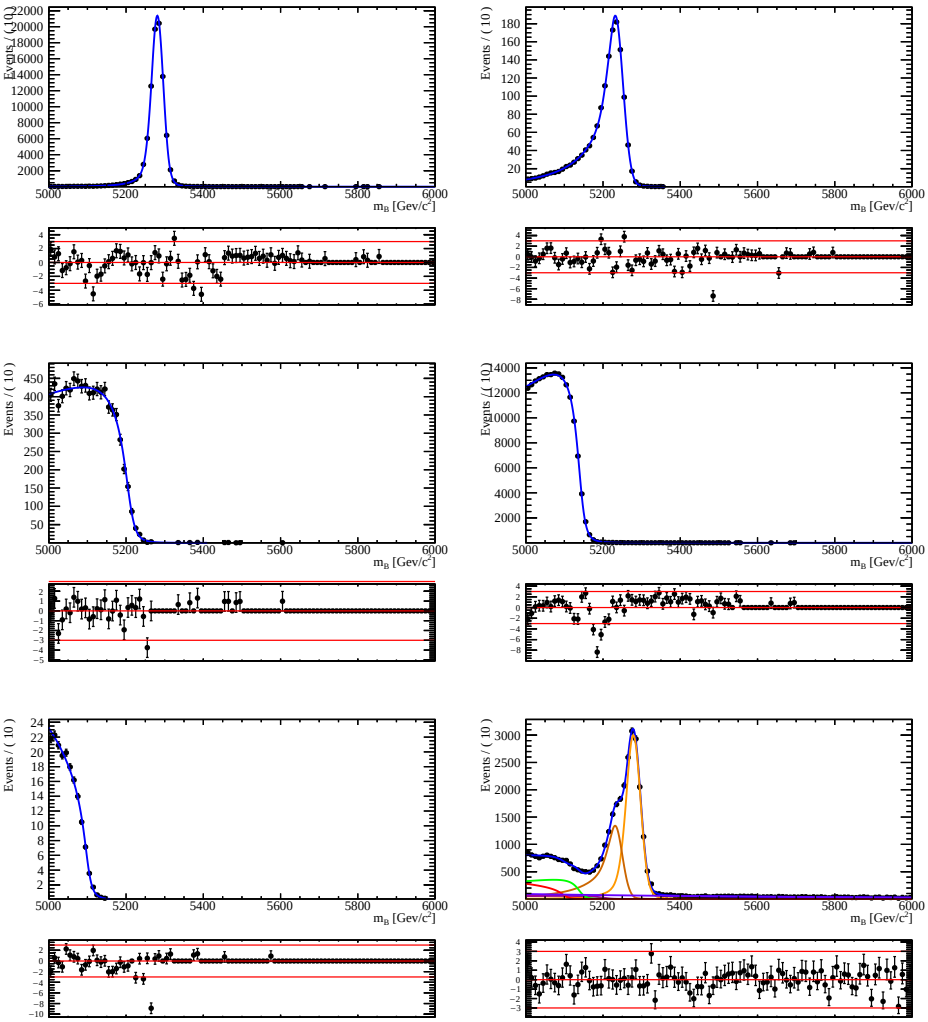

Figure 4.21: Reconstructed $\pi^+\mu^+\mu^-$ mass of simulated (top left) $B^+ \to J/\psi\pi^+$ decays, (top right) $B^+ \to J/\psi K^+$ decays, (middle left) $B_s^0 \to J/\psi f_0(980)$ decays, (middle right) $B^0 \to J/\psi\rho^0$ decays, (bottom left) $B^0 \to J/\psi K^{*0}$ decays, and of (bottom right) the $B^+ \to J/\psi\pi^+$ 2018 magnet-up data set. In the latter, the components shown are (blue) the full model, (orange) the signal, (brown) misidentified $B^+ \to J/\psi K^+$ decays, (green) $B^{+,0} \to J/\psi\rho^{+,0}$ decays (red) $B^{+,0} \to J/\psi K^{*+,0}$ decays and (purple) the combinatorial background.

$B^+ \to \pi^+\mu^+\mu^-$ decay

The measured event yield from the Run 1 measurement of the $B^+ \to \pi^+\mu^+\mu^-$ decay is of 92.7 ± 11.5 [131]. A larger number of events is necessary to perform this angular analysis and therefore the selected data taken during Runs 1 and 2, with magnet polarity Up and Down, are collected into one cumulative dataset. The fit of the model to data is performed to the cumulative dataset for the rare modes, contrary to how the control mode fits are performed. The consequence of this is that the simulation samples of the rare mode data must also be merged into cumulative datasets. Because of the differences between data-taking years, the proportion of simulated events per year and polarity have to match that of the data, when merging simulation data into one cumulative dataset. This is achieved by applying year-specific weights to the simulated events which also account for the different luminosity levels at LHCb.

The same sources of partially reconstructed background as in the $B^+ \to J/\psi\pi^+$ are present for the $B^+ \to \pi^+\mu^+\mu^-$ data set, with the exception that the J/ψ is replaced by the direct production of a dimuon pair in the rare B meson decay. To reduce the number of sources that need to be considered, the mass range is restricted to 5180–5600 MeV/c^2 mass range. In this range, the contribution from all of the decays other than the $B_s^0 \to f_0\mu^+\mu^-$ decay are negligible. The contribution from the $B_s^0 \to f_0\mu^+\mu^-$ decay is also expected to be small and will be considered as a source of systematic uncertainty. Hadronic backgrounds, *e.g.* from $B^+ \to \pi^+\pi^-\pi^+$ decays will also contribute at a very low level. These backgrounds are too small to include as fit components but will be considered as sources of systematic uncertainty. Hence, in the 5180–5600 MeV/c^2 mass range, the $B^+ \to \pi^+\mu^+\mu^-$ data can be described by only three components: the signal, combinatorial background and background from misidentified $B^+ \to K^+\mu^+\mu^-$ decays. The mass model PDF used to fit the cumulative simulated mis-identified $B^+ \to K^+\mu^+\mu^-$ decay sample is a Double Crystal Ball PDF. The model for the invariant mass for the signal mode is a Double Crystal Ball PDF. A one-dimensional fit of the invariant mass in $B^+ \to \pi^+\mu^+\mu^-$ data was not performed, in keeping with the choice of performing blind two-dimensional fits to the data in the rare decay mode. Therefore the model for the invariant mass distribution was fine tuned using simulation datasets only, results of which are provided in table 4.6 and figure 4.22. The results of the mass fits of the cumulative $B^+ \to K^+\mu^+\mu^-$ simulation dataset reconstructed as $B^+ \to K^+\mu^+\mu^-$ decays in the two q^2 bins are shown

in figure 4.23 and given in Table 4.7.

Table 4.6: Result of the fit to the $B^+ \to \pi^+\mu^+\mu^-$ cumulative simulation dataset, in bins of q^2.

Parameter name	Value at low q^2	Value at high q^2
a_{L}	-1.639 ± 0.002	-1.58 ± 0.02
a_{R}	2.222 ± 0.007	2.24 ± 0.03
invariant mass	5280.41 ± 0.05	5280.45 ± 0.04
n_{L}	1.82 ± 0.08	2.06 ± 0.07
n_{R}	2.8 ± 0.1	3.6 ± 0.1
σ $_{rmCB}$	16.32 ± 0.05	16.52 ± 0.04

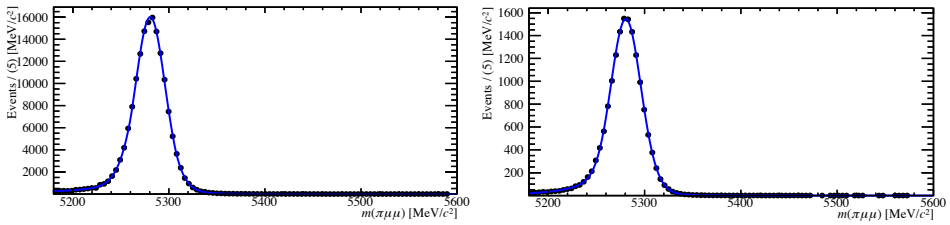

Figure 4.22: Studying the $B^+ \to \pi^+\mu^+\mu^-$ background in the two q^2 bins. Reconstructed $\pi^+\mu^+\mu^-$ mass of simulated $B^+ \to \pi^+\mu^+\mu^-$ decays at low (right) and high (left) q^2, fit with a double crystal ball PDF.

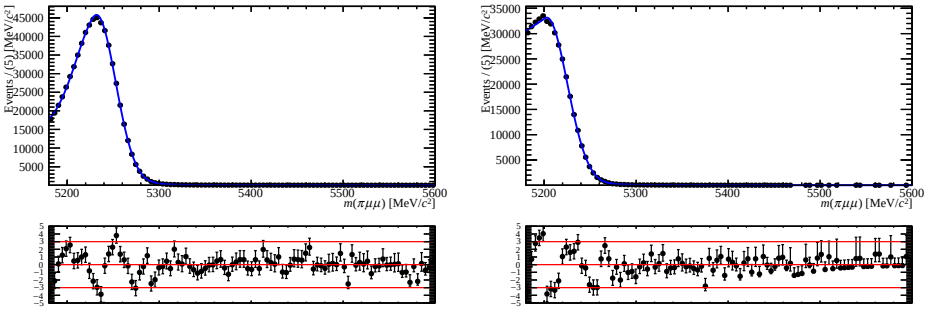

Figure 4.23: Studying the $B^+ \to K^+\mu^+\mu^-$ background in the two q^2 bins. Reconstructed $\pi^+\mu^+\mu^-$ mass of simulated $B^+ \to K^+\mu^+\mu^-$ decays at low (right) and high (left) q^2, fit with a tow-sided crystal ball PDF.

Table 4.7: Result of the fit to the $B^+ \to K^+\mu^+\mu^-$ cumulative simulation dataset, reconstructed as $B^+ \to \pi^+\mu^+\mu^-$, in bins of q^2.

Parameter name	Value at low q^2	Value at high q^2
$a_{\rm L}$	-0.480 ± 0.004	-0.084 ± 0.009
$a_{\rm R}$	2.75 ± 0.02	2.58 ± 0.02
invariant mass	5230.66 ± 0.08	5202.9 ± 0.2
$n_{\rm L}$	10.000 ± 0.002	10.0 ± 0.5
$n_{\rm R}$	1.56 ± 0.04	2.7 ± 0.1
$\sigma_{\rm CB}$	21.61 ± 0.06	22.3 ± 0.1

4.8.2 Fit strategy for the $\pi^+\mu^+\mu^-$ and $K^+\mu^+\mu^-$ invariant mass and helicity angle

For each of the $B^+ \to \pi^+\mu^+\mu^-$, $B^+ \to J/\psi K^+$ and $B^+ \to J/\psi\pi^+$ decay channels, a two-dimensional model is used to simultaneously describe $m(\pi^+\mu^+\mu^-)$ and $\cos\theta_l$ distributions of candidates in the B^+ candidate mass range $[5180, 5600]\text{GeV}/c^2$. The lower bound is chosen to remove background from partially reconstructed $B^0 \to J/\psi(\to \mu^+\mu^-)\rho^0$, $B^+ \to J/\psi(\to \mu^+\mu^-)\rho^+$ and $B \to J/\psi(\to \mu^+\mu^-)K^*$ decays. For each decay mode studied, the signal (s_m) and mis-identified background (b_m) mass shapes are modelled as described in section 4.8.1. The shape c_m is an exponential distribution that models the combinatorial background. The signal angular distribution, s_θ, is modelled by Eq. 2.40. To obtain a positive definite PDF for all values of $\cos\theta_l$, the angular observables must respect the condition $A_{\rm FB} \leq F_{\rm H}/2$. The detector efficiency as a function of $\cos\theta_l$ is accounted for by multiplying the signal angular PDF by the efficiency shape, $\varepsilon(\cos\theta_l)$ described in Sec. 4.5.1. The shape of the signal mass distributions is fixed from simulation and $B^+ \to J/\psi K^+$ data. The mis-identified and combinatorial background angular shapes (b_θ and c_θ) are accounted for by introducing a fourth order Chebychev polynomial model for each background, *e.g.*

$$c_\theta \propto 1 + p_1 T_1(\cos\theta_l) + p_2 T_2(\cos\theta_l) + p_3 T_3(\cos\theta_l) + p_4 T_4(\cos\theta_l), \qquad (4.15)$$

where $T_n(\cos\theta_l)$ is a Chebychev polynomial of order n. In the case of the mis-identified $B^+ \to J/\psi K^+$ background, the Chebychev polynomial is forced to be symmetric and p_1 and p_3 are fixed to 0 in the fit to data. The parameters of b_θ are fixed from samples of simulated $B^+ \to K^+\mu^+\mu^-$ decays.

The final PDF used to model the data is

$$\mathcal{P} = f_s s_m(m) s_\theta(\cos\theta_l)\varepsilon(\cos\theta_l) + f_b b_m(m) b_\theta(\cos\theta_l) + f_c c_m(m) c_\theta(\cos\theta_l) \ , \tag{4.16}$$

where f_s, f_b and f_c are the fractions of the $B^+ \to J/\psi\pi^+$, $B^+ \to J/\psi K^+$ and combinatorial background components in the fit. The signal angular PDF is normalised such that

$$\int_{-1}^{1} s_\theta(\cos\theta_l)\varepsilon(\cos\theta_l)\mathrm{d}\cos\theta_l = 1. \tag{4.17}$$

The other components are normalised over their allowed ranges.

The parameters A_{FB} and F_{H} are determined using an extended unbinned maximum-likelihood fit to the candidates, maximising the likelihood

$$L_{\mathrm{data}} = P(\mathrm{data}|N_s + N_b + N_c) \times \prod_i \mathcal{P}(m^i, \cos\theta_l^i) \tag{4.18}$$

where the sum is over the candidates in the data set. In this fit, the fractions are replaced by the yields of the components and $P(\mathrm{data}|N_s + N_b + N_c)$ is the Poisson probability to observe the number of candidates in the N_{data} given the fitted yields. In practice we minimise

$$\begin{aligned} -\log L_{\mathrm{data}} = -\sum_i \log\big(&N_s s_m(m^i) s_\theta(\cos\theta_l^i)\varepsilon(\cos\theta_l^i) + N_b b_m(m^i) b_\theta(\cos\theta_l^i) + \\ &N_c c_m(m^i) c_\theta(\cos\theta_l^i)\big) + N_s + N_b + N_c \ , \end{aligned} \tag{4.19}$$

The validation of this fitting strategy with pseudoexperiments is described in Section 4.8.4.

A_{FB} and F_{H} uncertainty extraction

For the control modes $B^+ \to J/\psi K^+$ and $B^+ \to J/\psi\pi^+$, the best fit points for each of the data-taking years and magnet polarities is expected to be in the vicinity of $A_{\mathrm{FB}} = 0$, $F_{\mathrm{H}} = 0$, which is in a corner of the allowed parameter space. Because the best fit point is on the boundary of the allowed parameter space, the uncertainty associated with the angular parameters cannot be extrapolated from the fit as the fits can have badly estimated covariance matrices. One attempt undertaken to solve this is to reparameterise $A_{\mathrm{FB}} = \frac{1}{2} F_{\mathrm{H}} A'_{\mathrm{FB}}$ where $A'_{\mathrm{FB}} \in [-1, +1]$ to solve this issue but this has its own issues in the fit as A'_{FB}

is undefined when F_{H} is zero.

In contrast to the signal channel, where the yields are small, for the two control channels the uncertainties on A_{FB} and F_{H} are estimated using the profile-likelihood method and Wilk's theorem. A likelihood scan of the angular parameter space is conducted. This comprises calculating $-2\log L_{\mathrm{data}}$ on a grid of A_{FB} and F_{H} points within the allowed triangle. One dimensional projections as a function of A_{FB} or F_{H} are obtained from the minimum value of $-2\log L_{\mathrm{data}}$ from the possible allowed values of the other variable. All remaining mass parameters of the PDF are fixed to the best fit result from the respective 2D mass and angle fit, illustrated in the previous paragraphs. The yields of the modelled modes and the background angular parameters are initially set to their respective best fit result and allowed to vary freely in the scan.

These scans have been performed for each year and polarity for the control modes. Figure 4.24 shows the likelihood scan for the $B^+ \to J/\psi(\mu^+\mu^-)\pi^+$ data taken in 2018 with magnet polarity Down. The extracted best fit values of A_{FB} and F_{H} are given in tables 4.8 and 4.9 for the control modes $B^+ \to J/\psi(\mu^+\mu^-)\pi^+$ and $B^+ \to J/\psi(\mu^+\mu^-)K^+$ respectively.

Table 4.8: Best fit value and intervals for the angular parameters A_{FB} and F_{H} extracted from the likelihood scan of the angular parameter space for all years and magnet polarities for the $B^+ \to J/\psi(\mu^+\mu^-)\pi^+$ decay.

Year	Magnet Polarity	F_{H}	Interval F_{H}	A_{FB}	Interval A_{FB}
2011	Up	0.006	$(0.000, 0.02)$	-0.002	$(-0.010, 0.005)$
2011	Down	0.000	$(0.000, 0.01)$	0.000	$(-0.008, 0.003)$
2012	Up	0.018	$(0.006, 0.03)$	0.009	$(0.002, 0.02)$
2012	Down	0.0100	$(0.0005, 0.02)$	0.0050	$(-0.0005, 0.01)$
2015	Up	0.024	$(0.000, 0.06)$	-0.012	$(-0.030, 0.001)$
2015	Down	0.018	$(0.000, 0.05)$	0.009	$(-0.005, 0.02)$
2016	Up	0.000	$(0.000, 0.005)$	0.000	$(-0.003, 0.003)$
2016	Down	0.004	$(0.000, 0.02)$	-0.002	$(-0.007, 0.004)$
2017	Up	0.008	$(0.000, 0.02)$	0.002	$(-0.004, 0.007)$
2017	Down	0.010	$(0.000, 0.02)$	-0.002	$(-0.008, 0.004)$
2018	Up	0.002	$(0.000, 0.009)$	-0.001	$(-0.005, 0.003)$
2018	Down	0.000	$(0.000, 0.008)$	0.000	$(-0.005, 0.002)$

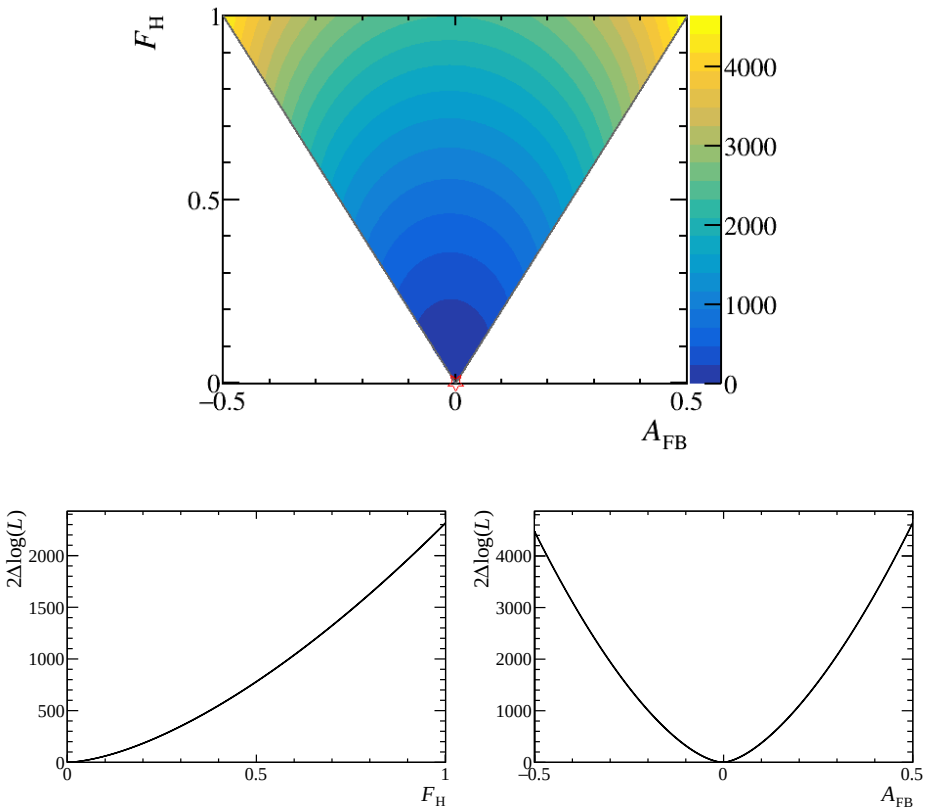

Figure 4.24: Top: Likelihood scan of the angular parameter space from the $B^+ \to J/\psi\pi^+$ decay for data-taking year 2018, magnet polarity Down. The best fit point is identified by the red star. Bottom: Profile of the likelihood over the angular parameter space as a function of F_H (left) and A_{FB} (right) for data-taking year 2018, magnet polarity Down.

$B^+ \to J/\psi K^+$ decay

The $B^+ \to J/\psi K^+$ decay can be cleanly selected and allows for precise check of the angular efficiency modelling. The mis-identified background from $B^+ \to J/\psi\pi^+$, after applying the kaon identification requirements, is tiny and no component is included in the fit to the data. A wider mass window of 5100-5600 MeV/c^2 is used when fitting the $B^+ \to J/\psi K^+$ candidates. A background from partially reconstructed $B^0 \to J/\psi K^{*0}$ decays is included at low mass. The parameters for the mass and angular shapes of this background are taken from simulation. The mass shape is parametrised by a Johnson function. Two additional parameters are also included when fitting the $B^+ \to J/\psi K^+$ sample: a signal shape resolution scale and a mass shift, which are respectively free to vary within the ranges $[0, 10]$ and $[m_{DCB} - 20\,\text{MeV}/c, m_{DCB} + 20\,\text{MeV}/c^2]$

Table 4.9: Best fit value and intervals for the angular parameters A_{FB} and F_{H} extracted from the likelihood scan of the angular parameter space for all years and magnet polarities for the $B^+ \to J/\psi(\mu^+\mu^-)K^+$ decay.

Year	Magnet Polarity	F_{H}	Interval F_{H}	A_{FB}	Interval A_{FB}
2011	Up	0.030	$(0.000, 0.02)$	0.000	$(-0.003, 0.003)$
2011	Down	0.033	$(0.000, 0.03)$	-0.001	$(-0.003, 0.001)$
2012	Up	0.070	$(0.000, 0.07)$	0.001	$(-0.002, 0.003)$
2012	Down	0.060	$(0.0005, 0.06)$	0.0020	$(-0.0005, 0.004)$
2015	Up	0.007	$(0.001, 0.01)$	-0.001	$(-0.004, 0.002)$
2015	Down	0.040	$(0.000, 0.04)$	0.000	$(-0.004, 0.002)$
2016	Up	0.074	$(0.000, 0.07)$	0.000	$(-0.003, 0.001)$
2016	Down	0.063	$(0.000, 0.06)$	-0.002	$(-0.004, 0.0005)$
2017	Up	0.069	$(0.000, 0.07)$	-0.001	$(-0.004, 0.0005)$
2017	Down	0.096	$(0.000, 0.01)$	0.000	$(-0.003, 0.001)$
2018	Up	0.050	$(0.005, 0.05)$	-0.001	$(-0.003, 0.0005)$
2018	Down	0.008	$(0.006, 0.009)$	-0.004	$(-0.006, 0.005)$

when performing the fit to data. The mass and angle projections of the 2D fit to the control mode $B^+ \to J/\psi(\mu^+\mu^-)K^+$ for 2018 magnet polarity up are shown as an example in figure 4.25. The extracted best fit values of A_{FB} and F_{H} have been given in table 4.9.

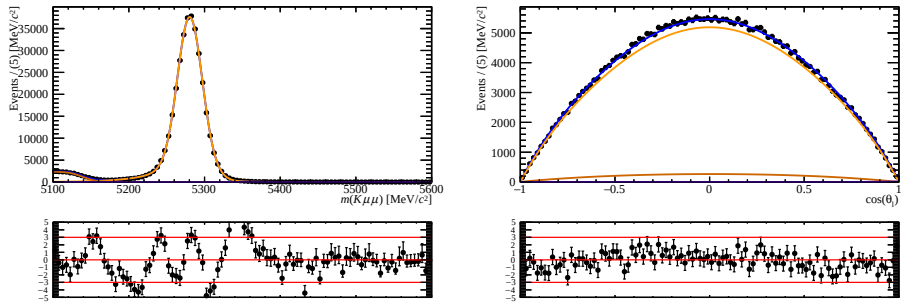

Figure 4.25: Mass and angle projections of the two-dimensional simultaneous fit to data for the $B^+ \to J/\psi K^+$ decay for data-taking year 2018, magnet polarity up. The fit model includes the a scaling factor for the resolution of the double crystal ball functions; and a shift in the peak position in the mass of the B meson. The signal component is in yellow, the mis-identified background component is in brown and the combinatorial background component is in purple. The pulls of the fit in the mass projection show that the signal component needs a more complicated fit model. The fit also suffers from disregarding the $B^+ \to J/\psi\pi^+$ background in the model function.

$B^+ \to J/\psi\pi^+$ decay

The $B^+ \to J/\psi\pi^+$ decay is similar to $B^+ \to J/\psi K^+$ in how it can be cleanly selected for good angular efficiency modelling. The chosen mass window of 5180-5600 MeV/c^2 removes all partially reconstructed backgrounds, so no components for these are included in the fit to the data. A background from mis-identified $B^0 \to J/\psi K^+$ decays is included at low mass. The parameters for the mass and angular shapes of this background are taken from simulation. The mass shape is parametrised by a Johnson function. The signal shape scaling factor in the mass and angle fit to $B^+ \to J/\psi\pi^+$ data is fixed to the best fit result from the fit to $B^+ \to J/\psi K^+$ data. This is because the resolution of the LHCb detector is expected to scale in the same way across the two control modes and the rare mode. The mass and angle projections of the 2D fit to the control mode $B^+ \to J/\psi(\mu^+\mu^-)\pi^+$ for 2018 magnet polarity up are shown as an example in figure 4.26. The extracted best fit values of $A_{\rm FB}$ and $F_{\rm H}$ have been given in table 4.8.

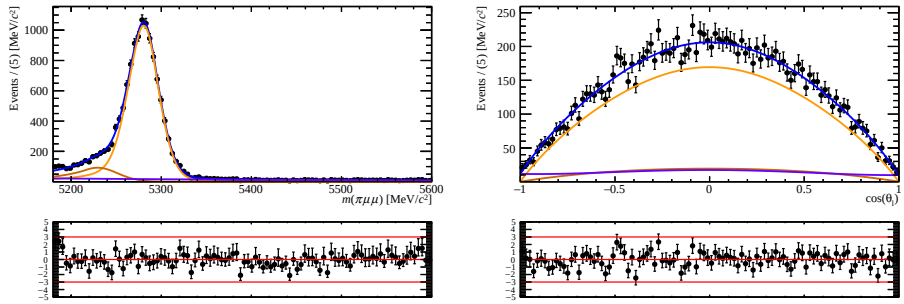

Figure 4.26: Mass and angle projections of the two-dimensional simultaneous fit to data for the $B^+ \to J/\psi\pi^+$ decay for data-taking year 2018, magnet polarity up. The fit model includes the a scaling factor for the resolution of the double crystal ball functions; and a shift in the peak position in the mass of the B meson. The signal component is in yellow, the mis-identified background component is in brown and the combinatorial background component is in purple.

$B^+ \to \pi^+\mu^+\mu^-$ decay

The model for the invariant mass and angle two-dimensional study for the rare mode is fine tuned on $B^+ \to \pi^+\mu^+\mu^-$ and mis-identified $B^+ \to K^+\mu^+\mu^-$ simulation datasets in the two q^2 bins. The results of the mass fits of the cumulative $B^+ \to \pi^+\mu^+\mu^-$ simulation dataset in the two q^2 bins are shown in figure 4.22 and given in Table 4.6. The signal component of the angular

model is fit to the $B^+ \to \pi^+\mu^+\mu^-$ simulation, shown in figure 4.27.The results of the mass fits of the cumulative mis-identified $B^+ \to K^+\mu^+\mu^-$ simulation dataset in the two q^2 bins are shown in figure 4.23 and given in Table 4.7. The mis-identifed background component of the angular model is fit to the $B^+ \to K^+\mu^+\mu^-$ simulation, shown in figure 4.28 and given in Table 4.10.

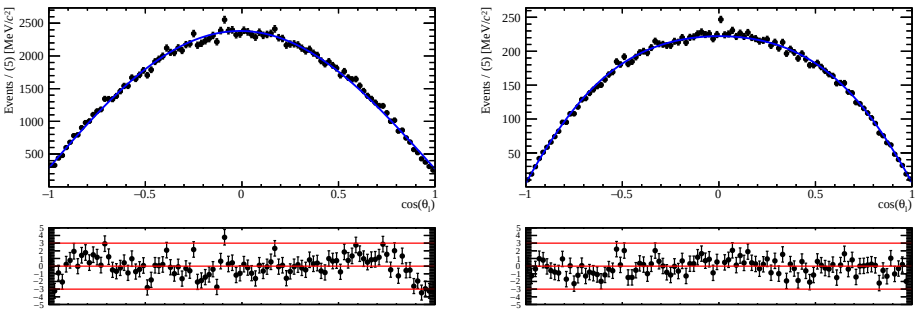

Figure 4.27: Studying the $B^+ \to \pi^+\mu^+\mu^-$ background in the two q^2 bins. Simulated $B^+ \to \pi^+\mu^+\mu^-$ decays at low (right) and high (left) q^2, fit with the angular distribution model in equation 2.40.

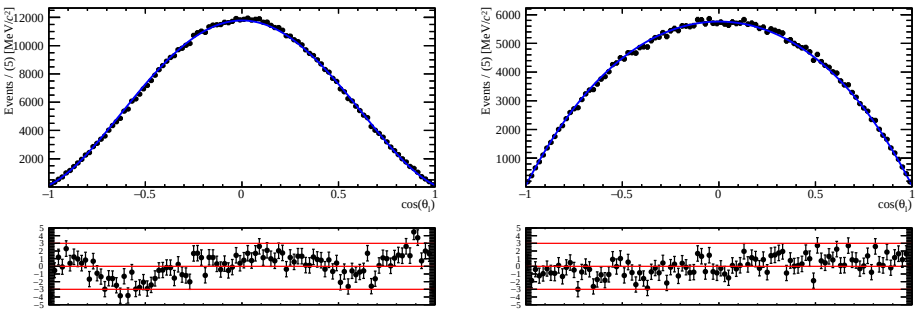

Figure 4.28: Studying the $B^+ \to K^+\mu^+\mu^-$ background in the two q^2 bins. Reconstructed as $B^+ \to K^+\mu^+\mu^-$ decays, simulated $B^+ \to K^+\mu^+\mu^-$ decays at low (right) and high (left) q^2, fit with the fourth order Chebyshev polynomial PDF.

The selection criteria that rejects mis-identified J/ψ decay, where one muon is mis-identified as a hadron, cuts out part of the rare mode signal in a narrow range of $\cos\theta_l$ at a fixed q^2 value. The signal events cut out from the selection cause a dip in the angular distribution. This is not included in the efficiency model as it cannot easily be described by a polynomial function. In the fit to data this effect is modelled as an angular efficiency, ϵ_{veto}. This efficiency is a distribution in $\cos(\theta_l)$, calculated by taking the ratio

Table 4.10: Result of the fit to the $B^+ \to K^+\mu^+\mu^-$ simulation dataset, reconstructed as $B^+ \to \pi^+\mu^+\mu^-$, in bins of q^2, when combining datasets from all the years and magnet polarities.

Parameter name	Value at low q^2	Value at high q^2
p_2	-1.192 ± 0.002	-0.951 ± 0.002
p_4	$+0.204 \pm 0.003$	$+0.031 \pm 0.003$

of simulation datasets with and without the rejection of mis-identified J/ψ decay events:

$$\epsilon_{\text{veto}} = \frac{N_{\text{veto}}(\cos\theta_l)}{N_{\text{total}}(\cos\theta_l)}. \tag{4.20}$$

The effect of the J/ψ veto in different q^2 bins for the rare modes $B^+ \to K^+\mu^+\mu^-$ and $B^+ \to \pi^+\mu^+\mu^-$ is shown respectively in figures 4.29, 4.30. The statistical fluctuations present in ϵ_{veto} are smoothed in the fit to data.

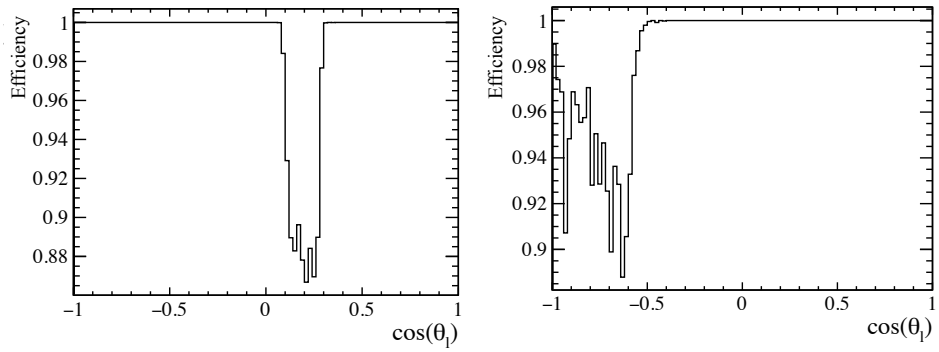

Figure 4.29: Effect of the J/ψ veto applied to the $B^+ \to K^+\mu^+\mu^-$ decays in the low (right) and high (left) q^2 bins.

Table 4.11: Expected component yields in the $B^+ \to \pi^+\mu^+\mu^-$ decay study for the combined Run 1 and Run 2 data

Component	Yield at low q^2	Yield at high q^2
Combinatorial background	190.9	232.9
$B^+ \to \pi^+\mu^+\mu^-$	116.9 ± 8.8	109.6 ± 7.7
$B^+ \to K^+\mu^+\mu^-$ misID	1.44 ± 0.04	1.15 ± 0.02

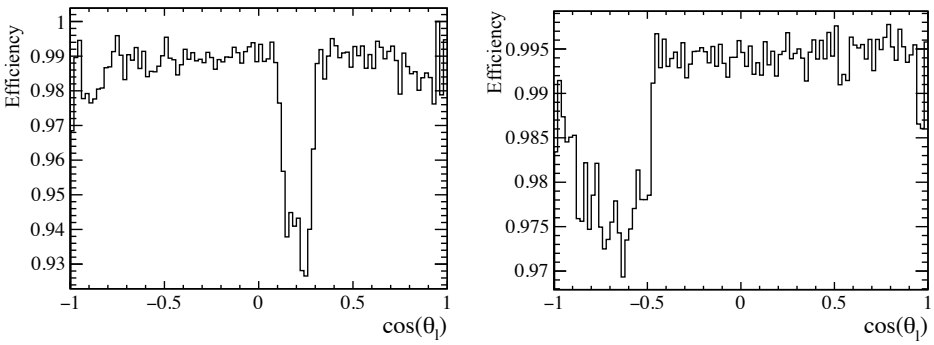

Figure 4.30: Effect of the J/ψ veto applied to the $B^+ \to \pi^+\mu^+\mu^-$ decays in the low (right) and high (left) q^2 bins.

4.8.3 Expected yields

The final model of the two-dimensional simultaneous fit of the invariant mass and angle of the $B^+ \to \pi^+\mu^+\mu^-$ decay is tested on toy experiments described in section 4.8.4. Realistic values for the yields related to the model components are necessary as starting point values to run the toy experiments. The model components comprise the signal, combinatorial background and background from misidentified $B^+ \to K^+\mu^+\mu^-$ decays.

The expected yields for the three components from the combined Run 1 and Run 2 data are reported in table 4.11. The $B^+ \to \pi^+\mu^+\mu^-$ yield in each q^2 bin is calculated in the following way:

$$N_{B\to\pi\mu\mu} = \frac{\mathcal{B}(B^+ \to \pi^+\mu^-\mu^+)}{\mathcal{B}(B^+ \to J/\psi K^+)} \frac{\epsilon_{\pi\mu^+\mu^-}(q^2)}{\epsilon_{J/\psi K}(q^2)} N_{B^+\to J/\psi K^+}, \tag{4.21}$$

where $\mathcal{B}(B^+ \to \pi^+\mu^-\mu^+)$ is measured by the previous analysis, [131], $\mathcal{B}(B^+ \to J/\psi K^+)$ is from the PDG [152], $\epsilon_{\pi\mu^+\mu^-}$ and $\epsilon_{J/\psi K}$ are efficiencies calculated from simulation samples, and $N_{B^+\to J/\psi K^+}$ is the yield of the $B^+ \to J/\psi K^+$ decay, taken from the fit to the mass of $B^+ \to J/\psi K^+$.

The yield of the misidentified $B^+ \to K^+\mu^+\mu^-$ decay is calculated using the similar formula:

$$N_{B\to K\mu^+\mu^-} = \frac{\mathcal{B}(B^+ \to K^+\mu^+\mu^-)}{\mathcal{B}(B^+ \to \pi^+\mu^+\mu^-)} \frac{\epsilon^{\text{mis-ID}}_{K^+\mu^+\mu^-}(q^2)}{\epsilon_{\pi^+\mu^+\mu^-}(q^2)} N_{B^+\to\pi^+\mu^+\mu^-}, \tag{4.22}$$

where $\mathcal{B}(B^+ \to K^+\mu^+\mu^-)/\mathcal{B}(B^+ \to \pi^+\mu^+\mu^-)$ is taken from the previous analysis in Ref. [131].

The combinatorial background yield over the fit range is extrapolated from the combinatorial background yield present in the upper sideband, $[5400, 6000]\text{MeV}/c^2$, of the mass projection of the cumulative $B^+ \to \pi^+\mu^+\mu^-$ data. The combinatorial background yield in this range was extracted by fitting an exponential PDF to the data, shown in figure 4.31. The upper sideband combinatorial yield is extrapolated to the fit mass window, $[5180, 5600]\text{MeV}/c^2$, and reported in table 4.11 for both q^2 modes.

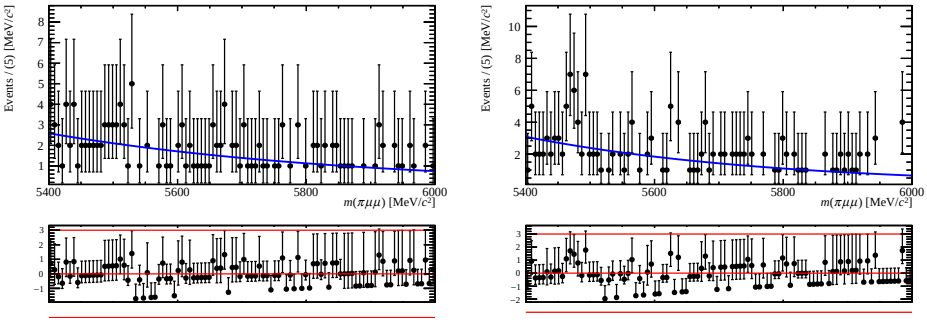

Figure 4.31: Fit of an exponential PDF to the upper sideband of the reconstructed B mass from the cumulative $B^+ \to \pi^+\mu^+\mu^-$ data in different q^2 bins. The low q^2 data is on the left, the high q^2 data is on the right.

4.8.4 Pseudo-experiments

Simulated pseudo-experiments were used to assess the ability to determine the parameters A_{FB} and F_{H}. Each pseudo-experiment simulates the $B \to \pi^+\mu^+\mu^-$ decay signal, the angular efficiency and the mis-reconstructed background from the $B \to K^+\mu^+\mu^-$. Figure 4.32 shows the mass and angle distributions for a pseudo-experiment, fit with the model PDF. The dataset in the pseudo-experiment was generated using the low q^2 conditions. SM-like starting values of $A_{\text{FB}} = 0.0$, $F_{\text{H}} = 0.1$ were used to generate the pseudo-experiment's dataset. One should note that in the low q^2 case the mis-identified background component is present but not visible because it is very small. This is consistent with the expected yield of this component (see tab. 4.11). The effect of the veto of the J/ψ background is visible in the angular distribution. This was repeated in the case of high q^2 conditions, as can be seen in figure 4.33. In this case, the mis-identified background experiences an upward fluctuation from the expected yield.

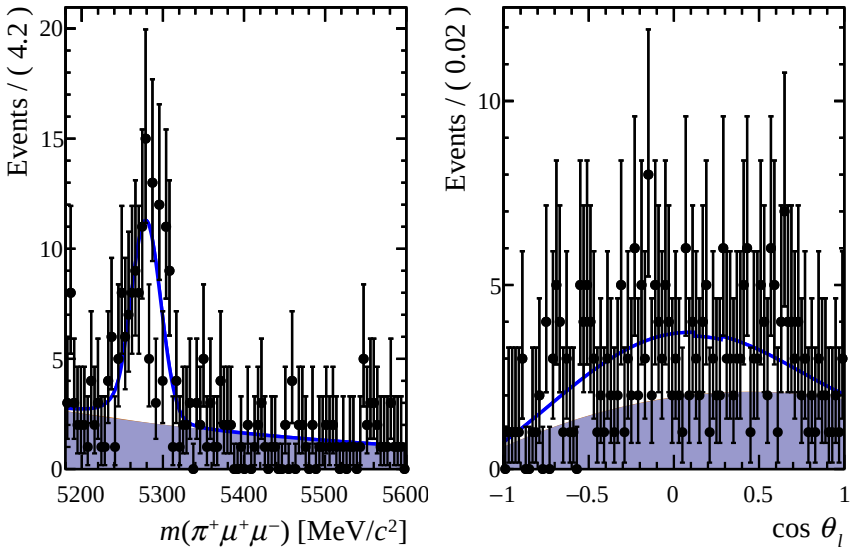

Figure 4.32: Mass and angle distributions from one pseudo-experiment, fit with the model PDF. The dataset in the pseudo-experiment was generated using the low q^2 conditions, with the initial values $A_{\rm FB} = 0.0$, $F_{\rm H} = 0.1$. Combinatorial background is shaded in purple, the mis-identified component is shaded is orange.

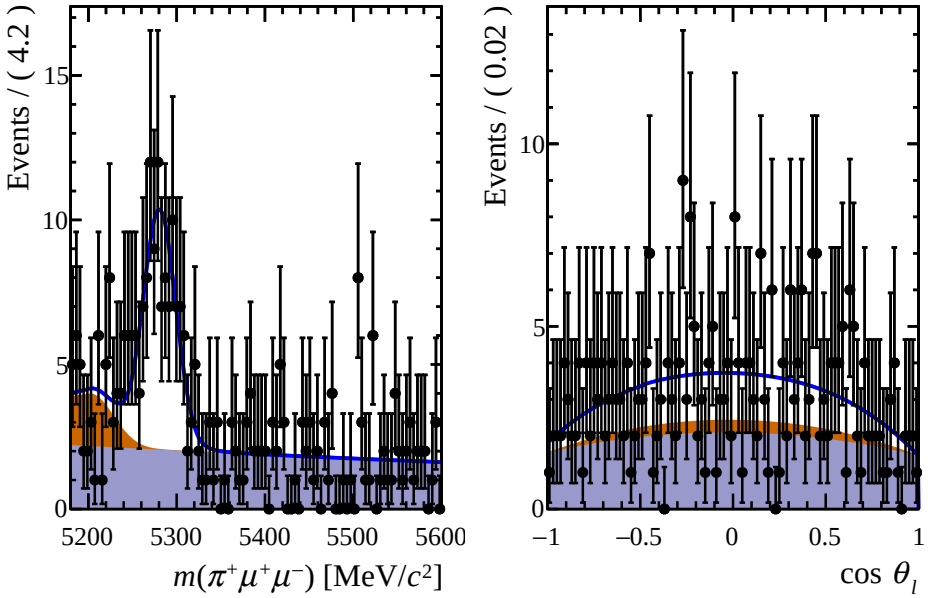

Figure 4.33: Mass and angle distributions from one pseudo-experiment, fit with the model PDF. The dataset in the pseudo-experiment was generated using the high q^2 conditions, with the initial values $A_{\rm FB} = 0.0$, $F_{\rm H} = 0.1$. Combinatorial background is shaded in purple, the mis-identified component is shaded is orange.

For each pseudo-experiment, a likelihood scan is performed, shown in figure 4.34, and one dimensional projections of the likelihood as a function of F_{H} and A_{FB} are minimised to extract and determine the values of the angular observables. As an example, figure 4.35 shows the 1-dimensional likelihood projections in the high q^2 bin.

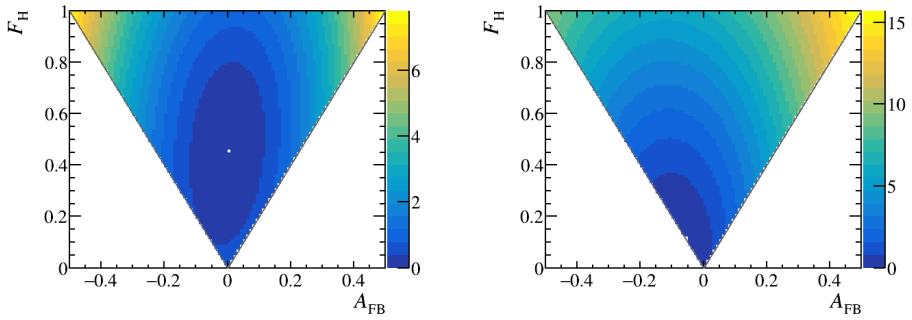

Figure 4.34: Likelihood scans of the angular parameter space for two individual pseudo-experiments, fit with the model PDF. The dataset in the first pseudo-experiment was generated using the low q^2 conditions, with the initial values $A_{\mathrm{FB}} = 0.0$, $F_{\mathrm{H}} = 0.1$, and produced the left-hand-side scan. The scan on the right-hand side is of the second pseudo-experiment, generated using the high q^2 conditions, also with initial values $A_{\mathrm{FB}} = 0.0$, $F_{\mathrm{H}} = 0.1$

Pseudo-experiments were also performed with non SM-like stating points for the angular parameters as a proof of concept for this method. The two toy datasets were generated with starting values of $A_{\mathrm{FB}} = 0.2$, $F_{\mathrm{H}} = 0.5$, and fit with the model to extract the angular observables.

An ensemble of 1000 pseudo-experiments is generated from the initial A_{FB} and F_{H} values of 0.0 and 0.1 respectively for each q^2 bin. These ensembles are used to check for biases in the measurement of the angular observables, and to check the coverage of the confidence intervals. The distributions of A_{FB} and F_{H} in the low and high q^2 bins are shown in figures 4.36 and 4.37, along with their respective pull distributions. The observable A_{FB} looks Gaussian, but does not have the correct coverage. On the other hand, F_{H} is strongly affected by the parameter space and is non-Gaussian. These are the reasons behind the need for the Feldman-Cousins method. The differences between the angular observables' distributions in the two q^2 ranges is due to the difference in the shape of the efficiency distribution of the two q^2 bins.

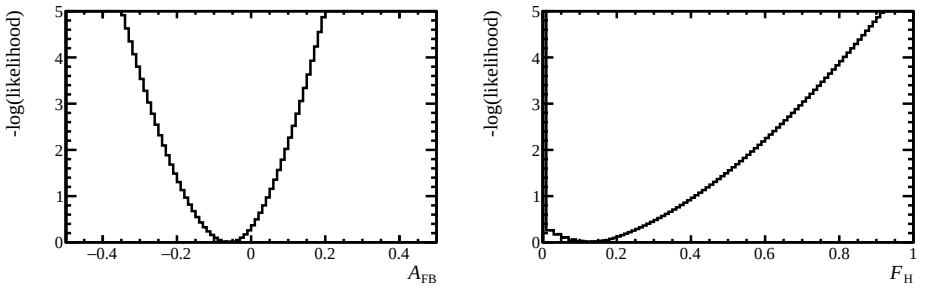

Figure 4.35: Likelihood profile as a function of F_H (left) and A_{FB} (right) extracted from the likelihood scan of the angular parameter space for a pseudo-experiment experiment, generated using the high q^2 conditions, with the initial values $A_{FB} = 0.0$ and $F_H = 0.1$.

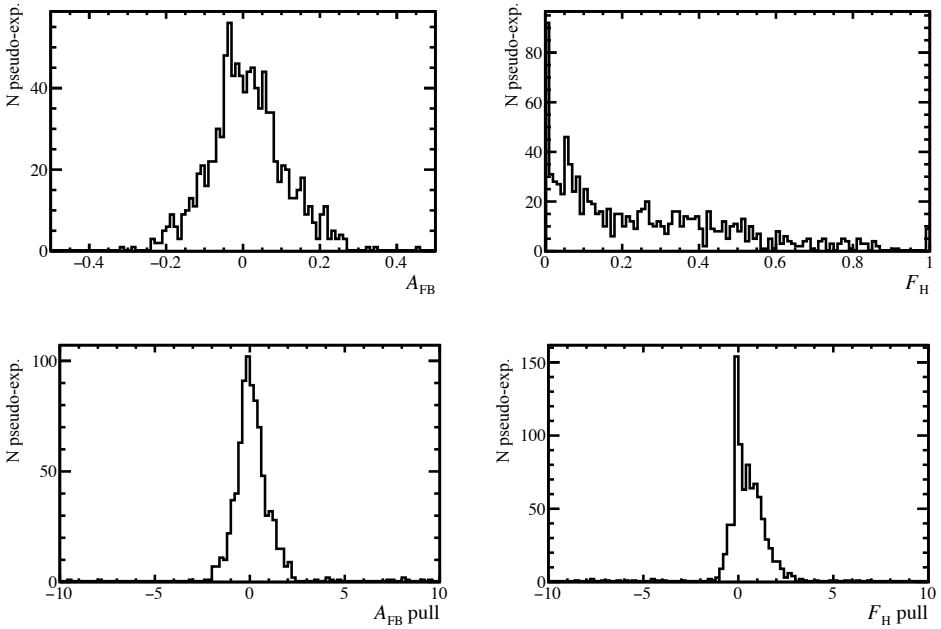

Figure 4.36: Top: Distributions of A_{FB} (left) and F_H (right) extracted from an ensemble of 1000 pseudo-experiments, generated using the low q^2 conditions, with the initial values $A_{FB} = 0.0$, $F_H = 0.1$.
Bottom: Respective pull distributions of the above angular distributions.

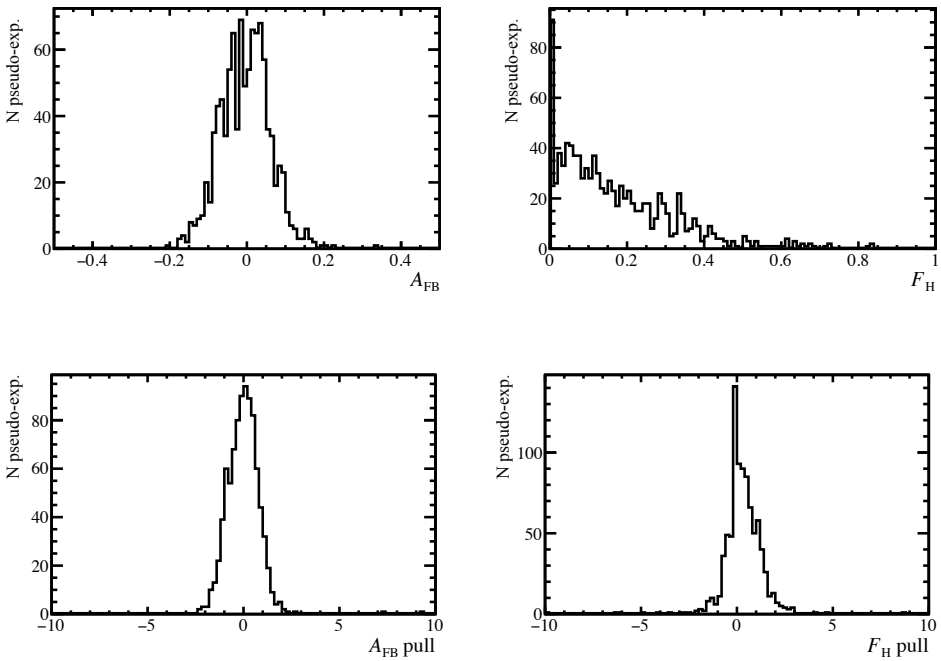

Figure 4.37: Top: Distributions of A_{FB} (left) and F_H (right) extracted from an ensemble of 1000 pseudoexperiments, generated using the high q^2 conditions, with the initial values $A_{\mathrm{FB}} = 0.0$, $F_{\mathrm{H}} = 0.1$.
Bottom: Respective pull distributions of the above angular distributions.

4.9 Estimating confidence intervals

Due to the boundary issues seen in the pseudo-experiments and the small signal yields, it is not possible to determine confidence intervals on $A_{\rm FB}$ and $F_{\rm H}$ with the correct coverage from the software packages HESSE or MINOS. Instead, confidence intervals will be determined using the Feldman-Cousins approach [134]. This is a Neyman construction with the likelihood ratio (or log-likelihood difference) as an ordering principle. Confidence intervals are determined in one- and two-dimensions:

- At each point in $A_{\rm FB}$ and $F_{\rm H}$, a fit is performed to the data set with $A_{\rm FB}$ and $F_{\rm H}$ fixed. The log-likelihood difference at this point $\Delta_{\rm data} = -(\log L_{\rm data} - \log L^{\rm best}_{\rm data})$, where $L^{\rm best}$ is the maximum likelihood achieved with $A_{\rm FB}$ and $F_{\rm H}$ allowed to freely vary.

- An ensemble of pseudoexperiments is then generated at the current $A_{\rm FB}$ and $F_{\rm H}$ point. In the pseudoexperiment generation, the values of the nuisance parameters (e.g. the background shape parameters) are set to the values obtained from the fit returning $L_{\rm data}$. This is the so-called plug-in method [153].

- Each pseudoexperiment is fit twice, once with all parameters allowed (yielding $L^{\rm best}_{\rm toy}$) to vary in the fit and once with $A_{\rm FB}$ and $F_{\rm H}$ fixed to the current point ($L_{\rm toy}$).

- The confidence level for the given $A_{\rm FB}$ and $F_{\rm H}$ point is determined from the probability that $\Delta_{\rm toy}$ is larger that $\Delta_{\rm data}$.

Figure 4.38 is an example of the result of using the Feldman-Cousins method [134] to extract the confidence intervals for the angular observables of the rare decay in the low q^2 bin from a fit to a pseudo-experiment. The confidence level is 1.0 at the best fit point. The 1σ interval corresponds to confidence levels above 0.32.

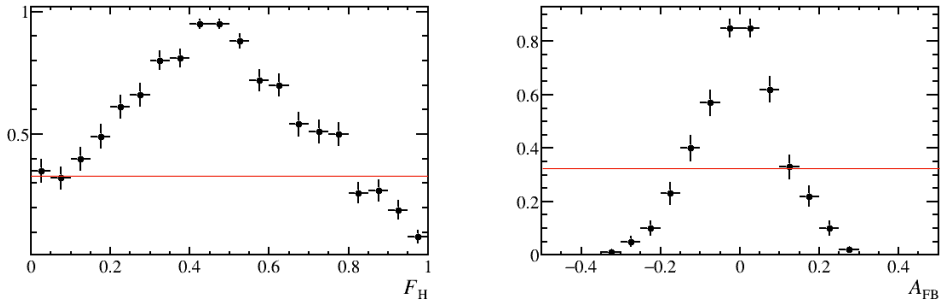

Figure 4.38: Confidence level for F_H and A_{FB} extracted using the Feldman-Cousins method [134] for the rare mode in the low q^2 bin. The 1σ boundary is marked by the red line.

4.10 Systematic Studies

The sources of systematic uncertainty on A_{FB} and F_H are considered if they would either bias the signal angular distribution or bias the estimated signal contribution, *e.g.* due to the presence of backgrounds that are neglected in the analysis. The different sources of uncertainty are described in detail below. A summary of the different sources of systematic uncertainty on A_{FB} and F_H is provided in Tables 4.12 and 4.13. The background from the $B^+ \to \pi^+\pi^-\pi^+$ decays is problematic, especially for the measurement of A_{FB}, as it peaks under the signal, as discussed in section 4.7 (see fig. 4.18), and has a large A_{FB}.

4.10.1 Simulation sample size

To estimate the uncertainty due to the finite size of the simulated sample, the parameters that come from fitting the efficiency distribution are varied within their uncertainties according to the covariance matrix on the parameters. For each variation of the efficiency parameters, a large pseudo-experiment with 100k signal decays is generated. The yields of the combinatorial and misidentified background are scaled to maintain their proportion relative to the signal. Each pseudoexperiment is then fit assuming the nominal efficiency model. The standard deviation of the distribution of the biases on A_{FB} and F_H, from 100 pseudoexperiments, is assigned as the uncertainty due to the simulation sample size.

Source	$[1.1, 6.0]$ GeV$^2/c^4$	$[15.0, 22.0]$ GeV$^2/c^4$
Simulation sample size	0.006	0.004
Data-simulation corrections (hadron ID)	0.004	0.002
Data-simulation corrections (muon ID)	0.005	0.003
Data-simulation corrections (tracking eff.)	0.005	0.002
Data-simulation corrections (trigger eff.)	0.007	0.005
Data-simulation corrections (kinematics)	0.005	0.005
Data-simulation corrections ($p_{\rm T}$)	0.007	0.005
Efficiency model order	0.004	0.004
Truth matching criteria	0.005	0.005
Signal angular resolution	0.006	0.003
Signal mass model	0.007	0.004
Combinatorial background model order	0.005	0.003
Factorisation of mass/angles for $B^+ \to K^+\mu^+\mu^-$	0.006	0.003
Background from $B^+ \to K^+\pi^+\pi^-$	0.009	0.005
Background from $B^+ \to \pi^+\pi^-\pi^+$	0.017	0.010

Table 4.12: Summary of the sources of different systematic uncertainty on the $A_{\rm FB}$ measurement in the two q^2 bins. The sources are described in the text.

Source	$[1.1, 6.0]$ GeV$^2/c^4$	$[15.0, 22.0]$ GeV$^2/c^4$
Simulation sample size	0.004	0.008
Data-simulation corrections (hadron ID)	0.002	0.005
Data-simulation corrections (muon ID)	0.003	0.005
Data-simulation corrections (tracking eff.)	0.002	0.004
Data-simulation corrections (trigger eff.)	0.005	0.009
Data-simulation corrections (kinematics)	0.005	0.008
Data-simulation corrections ($p_{\rm T}$)	0.007	0.010
Efficiency model order	0.003	0.007
Truth matching criteria	0.005	0.008
Signal angular resolution	0.003	0.013
Signal mass model	0.015	0.011
Combinatorial background model order	0.003	0.009
Factorisation of mass/angles for $B^+ \to K^+\mu^+\mu^-$	0.003	0.008
Background from $B^+ \to K^+\pi^+\pi^-$	0.005	0.018
Background from $B^+ \to \pi^+\pi^-\pi^+$	0.161	0.025

Table 4.13: Summary of the sources of different systematic uncertainty on the $F_{\rm H}$ measurement in the two q^2 bins. The sources are described in the text.

4.10.2 Data-simulation corrections

The corrections applied to the simulation are described in Sec. 4.4. They comprise corrections for hadron identification, muon identification, tracking efficiency, trigger efficiency, kinematic and generator-level p_{T} distributions. Two kinds of variations of the corrections are performed to assess the systematic error associated with them. First, a systematic uncertainty is estimated due to some of the choices made when determining the efficiency model: the choice of the binning of the trigger and p_{T} correction histograms and the choice of the inputs of the kinematic correction BDT. New efficiency models are calculated by making variations of these choices. For the trigger and p_{T} correction histograms, the binning is varied by increasing the number of bins by two in each axis. For the kinematic correction BDT, an alternative BDT is trained. It receives as input B^+ χ^2_{vtx}/ndof together with the default inputs (p_{T} and n_{tracks}). For each new efficiency model, a large pseudoexperiment of 100k signal decays is generated. The pseudoexperiments are then fit with the nominal model. The square-root of the bias and error on the bias are added in quadrature and assigned as an uncertainty. Second, a systematic uncertainty is estimated due to the statistical uncertainty on the correction histograms. For this, each histogram is varied within its uncertainty 100 times by varying the content of each bin following a Gaussian distribution. The Gaussian mean and width correspond to the central value and width of the respective bin in the nominal histogram. The varied histograms are used to estimate a new efficiency model. Pseudo-experiments are produced from a varied model and fit with the default model. The standard deviation of the distribution of the biases on A_{FB} and F_{H}, from 100 pseudoexperiments, is assigned as an uncertainty.

4.10.3 Truth matching criteria

In simulation datasets a small signal contribution ($\sim 1\%$ of the total) is seen from a group of candidate decays where one or more tracks have associated signals in the LHCb detector but are not related to any one particle in reality. This component is not included in the truth matching criteria used in the analysis because this component is not easily distinguishable from a significant background component. A systematic efficiency associated with the truth matching criteria is calculated by including the candidate decays where one or more particles is classified as a ghost. To estimate the bias from neglecting this

group of candidate decays, a large pseudoexperiment with 100k signal decays is generated from an efficiency model that includes this group of candidate decays. The pseudoexperiment is then fit with the nominal efficiency model, *i.e.* neglecting this group of candidate decays. The square-root of the bias and error on the bias added in quadrature is assigned as for uncertainty related to the truth matching.

4.10.4 Signal mass model

A systematic uncertainty associated with the choice of the signal mass model is determined from a large pseudo-experiment with 100k candidates. The candidates are generated according to an alternative mass model, a Hypathia function [154]. The pseudo-experiment is then fit with the nominal, sum of crystal ball shapes, model. The square-root of the bias and error on the bias added in quadrature is assigned as for uncertainty related to the mass modelling.

4.10.5 Efficiency model order

The nominal efficiency model is a fourth order polynomial expansion, with odd terms removed. To asses the impact of the chosen model for the angular efficiency, two alternatives are tested: using a model that includes odd ordered terms; and using a sixth order polynomial with only even order terms. In both cases the size of the bias is estimated using a large pseudo-experiment with 100k candidates. The pseudo-experiments are generated from the modified efficiency models and are then fit with the nominal model. In each case the square-root of the bias and error on the bias is added in quadrature. The largest of the two values is assigned as the systematic uncertainty on the efficiency model.

4.10.6 Signal angular resolution

The angular resolution of the $B^+ \to \pi^+\mu^+\mu^-$ decays is neglected in the analysis. To estimate the bias introduced by neglecting the resolution, a large pseudo-experiment of 100k candidates is generated. The pseudo-experiment is generated according to the nominal model. The signal decays in the toy generation are then smeared in θ_l by the angular resolution determined from simulation in section 4.6. The sample is then fit back by the nominal model.

The square-root of the bias and error on the bias added in quadrature is assigned as for uncertainty related to the angular resolution.

4.10.7 Factorisation of mass and angles for the $B^+ \to K^+\mu^+\mu^-$ decay

The assumption that the mass and angular distribution of the $B^+ \to K^+\mu^+\mu^-$ decay factorises is not completely valid because of the $K^+ \to \pi^+$ mass assignment. Under the pion hypothesis the angular variables are calculated under a false assumption about the B^+ boost. The size of this bias is estimated using a large pseudoexperiment with 100k candidates. Rather than generating the $B^+ \to K^+\mu^+\mu^-$ decay from the nominal model, events are chosen instead from fully simulated $B^+ \to K^+\mu^+\mu^-$ events and introduced into the data set. The sample is then fit with the nominal model. The square-root of the bias and error on the bias added in quadrature is assigned as for uncertainty related to the modelling.

4.10.8 Combinatorial background angular distribution

The combinatorial background is modelled by a fourth order polynomial with both even and odd terms. To estimate the uncertainty associated with this choice, the BDT cut is removed and the background in the upper mass sideband is fit with a sixth order polynomial. A large pseudoexperiment with 100k candidates is then generated using the sixth order background model. The sample is then fit using the nominal model, *i.e.* with a fourth order polynomial. The square-root of the bias and error on the bias added in quadrature is assigned as for uncertainty related to the angular modelling.

4.10.9 Residual background from hadronic B^+ meson decays

The biases from neglecting the small residual background from $B^+ \to \pi^+\pi^-\pi^+$ and $B \to DX$ decays are estimated in the same manner as the bias from $B^0_s \to f_0\mu^+\mu^-$ decays. For each mode, a large pseudoexperiment of 100k candidates is generated from the nominal model. The expected level of $B^+ \to \pi^+\pi^-\pi^+$ (or $B \to DX$) decays is introduced from fully simulated MC. The simulation dataset is weighted to ensure that it has the correct Dalitz distribution using `Laura++` based on the measured distributions in Ref. [148, 155]. The sample is then fit with the nominal model, *i.e.* neglecting

this background. The uncertainty from neglecting this background is taken as the square-root of the bias and error on the bias added in quadrature.

4.10.10 Discussion about systematic uncertainties

The most significant systematic uncertainty sources come from the neglecting the backgrounds from the $B^+ \to \pi^+\pi^-\pi^+$ $B^+ \to K^+\pi^-\pi^+$ decays. This is consistent with their estimated level compared to the signal, introduced in section 4.7. Furthermore, the former peaks under the signal and the latter has a tail that reaches under the signal peak, and any variation to the distribution in these regions alters the measurement. The systematic uncertainties from data-simulation corrections all suffer from the statistical limitation of the data samples used to produce these corrections with the PIDCalib and TrackCalib packages. The same is true for the uncertainty introduced by the efficiency model, which is calibrated on control mode datasets. These contributions to the uncertainty could be reduced by using larger samples.

At the time of writing this work, some systematic uncertainties from remaining sources of systematic uncertainties are still being calculated. A description of how each of these is being evaluated follows.

Signal angular model

The signal angular model is able to describe the effects of all short-distance operators in the SM operator basis. It can also include effects from scalar, pseudoscalar, tensor or axialtensor operators that can appear in extensions of the SM. No systematic uncertainty needs to be considered to account for these effects. It is, however, known that QED effects can modify the angular distribution of the decay [156]. To estimate the size of this effect, the values of $A_{\rm FB}$ and $F_{\rm H}$ obtained from a fit to generator level decays are compared to those obtained from a sample produced without final-state-radiation from the package PHOTOS.

$B^+ \to K^+\mu^+\mu^-$ mass distribution

To assess the impact of the chosen PDF to model the mass distribution of the $B^+ \to K^+\mu^+\mu^-$ decays, a large pseudoexperiment, containing 100k candidates, is used. The candidates are generated from an alternative mass PDF, a Hypathia function [154], for the $B^+ \to K^+\mu^+\mu^-$ decay. The pseudoexperiment is then fit with the nominal model. The square-root of the bias and error on

the bias added in quadrature is assigned as for uncertainty related to the mass model.

$B^+ \to K^+\mu^+\mu^-$ angular distribution

The angular model for the $B^+ \to K^+\mu^+\mu^-$ background is taken from fully simulation events that have been corrected for data-simulation discrepancies. The simulation is based on a SM assumption for the angular structure. To test the impact of this assumption, the simulation is reweighted to have $A_{\rm FB}$ and $F_{\rm H}$ values compatible with those measured in Ref. [157]. A large pseudoexperiment of 100k candidates is then generated from the modified model. The pseudoexperiment is then fit with the nominal model, *i.e.* with the angular distribution model from simulation. The square-root of the bias and error on the bias added in quadrature is assigned as for uncertainty related to the $B^+ \to K^+\mu^+\mu^-$ angular modelling.

Residual background from $B_s^0 \to f_0\mu^+\mu^-$

The background from $B_s^0 \to f_0\mu^+\mu^-$ decays, where $f_0 \to \pi^+\pi^-$, is expected to be small and is neglected in the analysis. To estimate the bias introduced by this assumption, a large pseudoexperiment of 100k candidates is generated. The expected level of $B_s^0 \to f_0\mu^+\mu^-$ decays is then introduced from fully simulated MC. Given that the f_0 meson is a scalar, the angular distribution is expected to be very similar to that of the signal. In the correct helicity frame, the angular distribution would have no forward-backward asymmetry. However, because one of the pions from the f_0 is not reconstructed, the wrong frame is used when computing θ_l. The sample is then fit with the nominal model, *i.e.* neglecting this background. The uncertainty from neglecting this background is taken as the square-root of the bias and error on the bias added in quadrature.

4.11 Concluding remarks on the state of the analysis of the angular distribution of the $B^+ \to \pi^+\mu^+\mu^-$ decay

The chosen path for the analysis of the angular distribution of the $B^+ \to \pi^+\mu^+\mu^-$ decay using Run I and Run II LHCb data is influenced by the Run I measurement of the differential branching fraction and *CP* asymmetry of

the same decay (Ref. [132]). Firstly, the choice of binning in dilepton mass squared is based on the differential branching fraction and *CP* asymmetry analysis. Secondly, the candidate selection criteria is the same in this work as in the previous investigations. The multivariate selection used to identify the combinatorial background in the previous analysis was optimised to improve the PID by colleagues performing the updated differential branching fraction measurement using Run I and Run II data. The method chosen to perform the analysis of the angular distribution of the $B^+ \to \pi^+\mu^+\mu^-$ decay was successfully validated on the control channels $B^+ \to J/\psi(\mu^+\mu^-)K^+$ and $B^+ \to J/\psi(\mu^+\mu^-)\pi^+$.

During the development of this work it became apparent that the backgrounds from the $B^+ \to \pi^+\pi^-\pi^+$ and $B^+ \to K^+\pi^-\pi^+$ decays must be treated differently than in the previous analysis, where they were not considered relevant. In the case of this angular analysis, neglecting both sources of background introduces the largest and second-largest sources of systematic uncertainties on the measurement of $A_{\rm FB}$ and $F_{\rm H}$. Furthermore, these particular systematic uncertainties are $5\% - 17\%$ for the latter observable and $5\% - 25\%$ for the former. The values of these systematic uncertainties point to the fact that the background from these decays should not be neglected.

The next step in this analysis is to include two extra fit components to account for the backgrounds from the $B^+ \to \pi^+\pi^-\pi^+$ and $B^+ \to K^+\pi^-\pi^+$ decays. As with the backgrounds already accounted for, the models for these backgrounds will be extracted by performing separate mass and angle fits to LHCb simulation samples.

The analysis will be put forward for internal review to the LHCb Rare Decays Working Group, which will assess whether the work is ready for unblinding. Unless any modifications are requested in the internal review process, the candidate selection, the treatment of efficiencies, the list of sources of systematic uncertainties presented in this work are final.

Chapter 5

TORCH Detector R&D

5.1 Aim of the TORCH detector

The Time Of internally Reflected CHerenkov light (TORCH) detector is a large-area, Time Of Flight (TOF) detector designed for charged particle identification (PID) in the 2-20 GeV/c momentum range [158]. It is proposed for the LHCb Upgrade 2 [130], during the High-Luminosity LHC era, to complement the LHCb RICH detectors, introduced in Chapter 3, which have poor particle identification performance at low momentum. Currently charged hadrons with momentum below $\sim$10 GeV/c cannot be separated into pions, kaons and protons by the RICH detectors. Furthermore, below $\sim$25 GeV/c, kaons and protons are not distinguishable. Above this threshold kaons emit Cherenkov radiation, contrary to protons. In addition to these limitations of kaon identification, proton-kaon discrimination is inefficient for particles with momentum below 20 GeV/c [102]. Figures 3.15, 3.18 and 3.19 show respectively, the reconstructed Cherenkov angle as a function of track momentum of charged particles traversing the RICH C4F10 radiator, and the efficiency of kaon and proton identification of LHCb in Run2 as a function of momentum, where these limitations at low momentum can be seen.

The TORCH detector exploits the production of Cherenkov radiation as charged hadrons traverse it to measure their TOF. The Cherenkov radiation provides a prompt timing signal, needed for the TOF measurement. The proposed VELO detector upgrade for the next LHCb Upgrade is a timing detector, which will provide the start time of the charged hadrons' TOF [130]. The TOF is calculated from the VELO and TORCH timing signals. The TOF measurement is used to identify the hadronic species of the charged particle.

5.2 Principles of the TORCH detector

5.2.1 Particle Identification

A charged hadron's mass, m, and momentum, p, follow the relationship

$$m = \frac{p}{c\beta\gamma}, \tag{5.1}$$

where c is the speed of light in vacuum, β is the hadron's velocity relative to c and γ is the Lorentz factor, $\gamma = 1/\sqrt{1-\beta^2}$. One relevant consequence of this relation is that given a measured momentum and a measured velocity one can infer the mass, and therefore the hadronic species, of a charged particle. TORCH is designed to receive momentum information from tracking and to measure the TOF of the charged hadron from its production to detection in TORCH. The path of the charged hadron's track, of length L, is bracketed by a tracking station at the start, and the TORCH detector at the end. The tracking stations provide a time stamp corresponding to the production time i.e. to the start time of the TOF used by TORCH to measure the TOF. The TOF difference for particles of different species, with masses m_1 and m_2, with the same momentum follows the equation

$$\Delta t_{\mathrm{TOF}} = |t_{\mathrm{TOF1}} - t_{\mathrm{TOF2}}| = \left| \frac{L}{\beta_1 c} - \frac{L}{\beta_2 c} \right| = \frac{L}{c} \left| \sqrt{1 + \frac{m_1^2 c^2}{p^2}} - \sqrt{1 + \frac{m_2^2 c^2}{p^2}} \right|. \tag{5.2}$$

Figure 5.1 shows the TOF difference for pions, kaons and protons as a function of momentum within 2-10 GeV/c for a flight path of 9.5 m.

In order to perform PID, the species separation power of the detector must be statistically significant. The number of Gaussian standard deviations of the TOF as a function of momentum and TOF resolution, σ_{TOF}, is given by

$$N_{\sigma\mathrm{TOF}} = \frac{|t_{\mathrm{TOF1}} - t_{\mathrm{TOF2}}|}{\sigma_{\mathrm{TOF}}} \approx \frac{Lc}{2p^2 \sigma_{\mathrm{TOF}}} |m_1^2 - m_2^2|. \tag{5.3}$$

One can immediately notice that $N_{\sigma\mathrm{TOF}}$ goes to 0 for very large momenta. For momentum values in the 2-20 GeV/c range, one can maximise the particle path trajectory length, L, and minimise the TOF resolution of the detector to obtain a $N_{\sigma\mathrm{TOF}} \geq 3$.

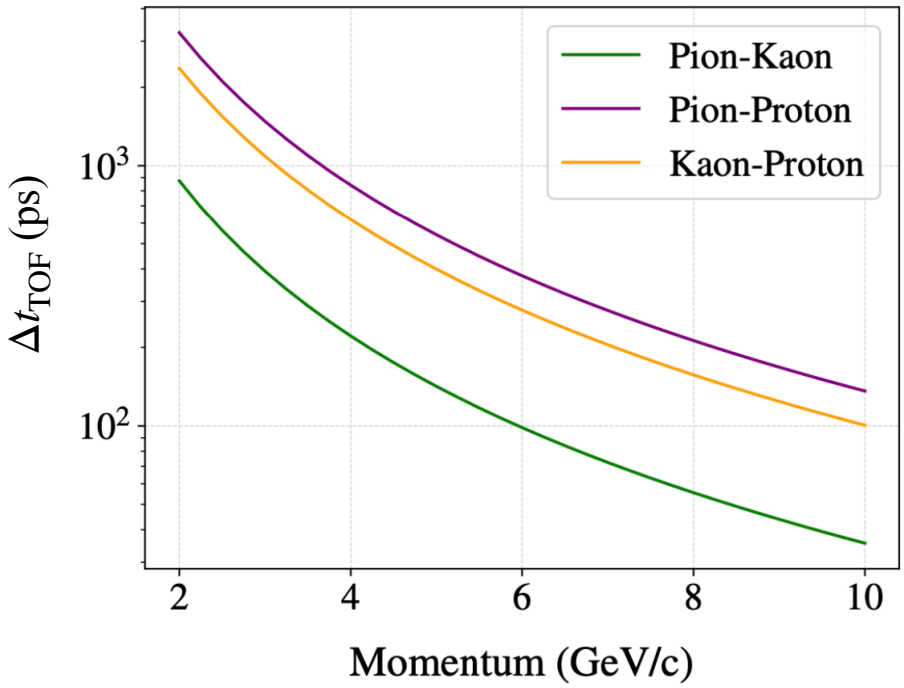

Figure 5.1: Time Of Flight difference as a function of momentum for pions, kaons and protons flying over a 9.5 m path. [159].

The TOF resolution depends on the resolution of the tracking station which measures the start time, and on the time resolution of the TORCH detector. A description of the design of the TORCH detector, which follows in section 5.3, shows how charged hadrons are detected through the detection of their Cherenkov radiation (illustrated in section 5.2.2) via the use of fast-photon detectors. The TORCH time resolution receives contributions from the photon detector time resolution, the readout electronics noise, and the resolution of the particle path. The individual contributions to the TORCH time resolution are explored further in section 5.9.

The time resolution per track needed to achieve a 3σ separation of pions and kaons over a 9.5 m flight path, at low momentum, is 13 ps. About ~ 30 Cherenkov photons are detected per charged particle, so the TORCH time resolution per photon for the same 3σ separation is 70 ps. The TORCH single photon time resolution is the result of three components, as explained in detail in section 5.8.

5.2.2 Cherenkov Radiation

The TORCH detector exploits the prompt Cherenkov radiation emitted when charged hadrons traverse a dielectric radiator plate to perform PID. As the charged particle traverses a dielectric, it electrically polarises the molecules along its path in it. If the charged particle travels at a speed which is less than the phase velocity of light in the dielectric, the medium molecules transition back to their ground state at a speed greater than the particle's. However, if the charged particle's speed is greater than that of the phase velocity of light in the dielectric, the charged particle interacts with the polarised medium molecules, exciting them, before they can relax back to their ground state. As the polarised molecules transition to their ground state a photon is emitted. The photons are emitted in a spherical wave-front originating from the charged particle. Because the source of the spherical wave is moving in a straight line, the electromagnetic radiation waves interfere constructively to form a cone of light. This constitutes Cherenkov radiation [160, 161] and this process can be compared to a plane travelling at a speed greater than the speed of sound and generating a supersonic boom. An illustration of the Cherenkov radiation wavefronts is shown in figure 5.2.

The angle, θ_C, between the charged particle track and the emitted Cherenkov photons depends on the medium's refractive index, following the relationship

$$\cos(\theta_C) = \frac{1}{n\beta}, \tag{5.4}$$

where n is the phase refractive index of the medium and β is the ratio between the speed of the charged particle and the speed of light in vacuum.

Cherenkov photons are emitted across a continuous spectrum of wavelengths. This leads to two considerations which significantly informed the TORCH detector design. Firstly, a medium's refractive index depends on the wavelength of the electromagnetic radiation. This causes the Cherenkov photons with different wavelengths resulting from the same charged particle interaction to experience chromatic dispersion since their Cherenkov angles differ and to travel at different group velocities. Secondly, the medium absorbs part of the radiation, being transparent to the photons in the optical region only. The number of emitted photons per charged particle can be expressed

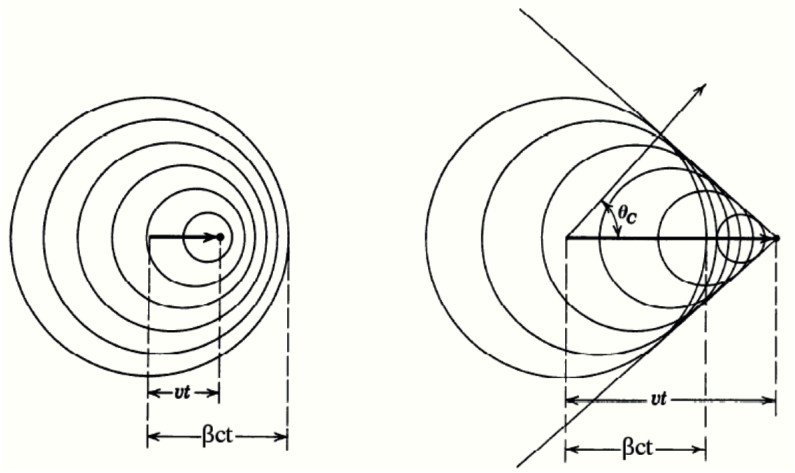

Figure 5.2: Cherenkov radiation emission by charged particles travelling through a dielectric medium at a smaller velocity than the phase velocity of light (left) and for charged particles traversing the dielectric at a greater speed than the phase velocity of light (right). The second case results in a coherent wavefront of Cherenkov photons travelling at an angle θ_C from the charged particle's trajectory [162].

as a function of the Cherenkov angle using the Frank-Tamm equation [163],

$$\frac{d^2N}{dEdx} = \frac{\alpha}{\hbar c} Z^2 \left(1 - \frac{1}{n(E)^2\beta^2}\right), \tag{5.5}$$

where N is the number of emitted photons per charged particle, E is the energy of the photons, Z is the electrical charge of the particle, x is the distance travelled by the charged particle in the medium, $\hbar$ is the reduced Plank constant and α is the fine structure constant. Substituting equation 5.4 and integrating over the distance travelled by the charged particle, one obtains the differential number of photons emitted per charged particle as a function of the Cherenkov angle:

$$\frac{dN}{dE} = \frac{\alpha}{\hbar c} Z^2 L \sin^2\theta_C, \tag{5.6}$$

where L is the total distance travelled by the charged particle in the dielectric medium.

5.3 The design of the TORCH detector

The TORCH detector is designed to exploit the Cherenkov radiation described in the previous section to perform particle identification of pions, protons and kaons which have a momentum within the 2-20 GeV/c range [164]. It was inspired by the BaBar DIRC [165] and the Belle II TOP [166, 167] detectors. The dielectric medium chosen for the TORCH detector is quartz. Cherenkov photons are propagated to the periphery of the radiator by total internal reflection, where they enter the focussing block. This too is made of quartz and focusses the photons on to an array of 11 micro-channel plate photomultiplier tubes (MCP-PMTs) via the use of a cylindrical-mirrored surface. This constitutes a so-called TORCH module, an illustration of which can be seen in figure 5.3.

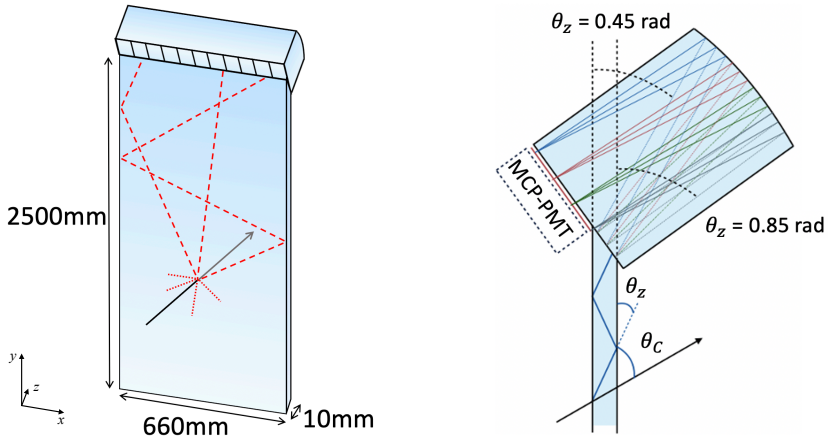

Figure 5.3: Illustration of a single TORCH module. Charged hadrons traversing the quartz plate emit Cherenkov photons, which are propagated to the edge of the detector via total internal reflection. The photons are focused by a cylindrical mirror onto a detector plane comprising 11 MCP-PMTs. The position of a photon along the MCP-PMT is used to infer the photon Cherenkov angle. Photons with the same Cherenkov angle are focused in the same spatial position on the MCP-PMT local $y - axis$. This coupled with chromatic dispersion results in one charged particle producing many duplicate images on the sensitive area. This is shown using the possible photon paths, represented by coloured lines, on the figure on the right.

The focus geometry is such that photons with the same Cherenkov angle are focused in the same position on the MCP-PMT's local $y - axis$, regardless of their y coordinate when entering the focusing block or when being emitted as Cherenkov radiation in the first place. This coupled with the chromatic dispersion of Cherenkov radiation results in one charged particle producing many duplicate images on the sensitive area. The value of θ_C can be used to correct the final image for chromatic dispersion and improve the detector's resolution. The photon's arrival position on the MCP-PMTs is used to reconstruct the photon angle in the y-z plane (defined in figure 5.3). The photon angle in the x-z plane is determined geometrically from the charged hadron's track information. Combining the knowledge of these two angles, the Cherenkov angle can be determined. From this the charged hadron entry point and time can be reconstructed. To do so, the hadron's momentum is used to reconstruct the chromatic dispersion for a given mass hypothesis. The time of photon propagation in the TORCH module can be corrected for chromatic dispersion. The corrected time of propagation is subtracted from the time of arrival of the Cherenkov photons to obtain the time of flight of the charged particle, which coincides with the time the hadron entered the TORCH detector.

5.3.1 TORCH Optics

The TORCH detector aims to cover a 6 m × 5 m area, which corresponds to the angular acceptance of the LHCb detector (±300 mrad horizontally, ±250 mrad vertically) at a 9.5 m distance from the interaction point. This is achieved by combining many optical elements. Specifically, the detector is split into independent modules [168] which are constructed and mounted separately. The radiator bar in each module consists of two sheets of fused silica, each 10 mm × 660 mm × 1250 mm (thick × width × length), joined to produce a 2500 mm long radiator bar. The focusing element is manufactured separately from the radiator bar, and consists in a fused silica parallelepiped with a mirrored black spherical surface on the far side, to reflect and focus the photons on the sensitive area. One of the fused silica sheets has a 36° bevel along the edge in contact with the focusing block. All the quartz components are connected through the use of a glue with optimum UV transmission [169] since Cherenkov light peaks in the UV region of the spectrum.

5.3.2 TORCH Multichannel photomultiplier tubes

The TORCH Multichannel photomultiplier tubes (MCP-PMTs) detect Cherenkov radiation. These devices are ideal because they provide a fast response to a single-photon signal, can endure strong magnetic fields, and can provide a high spatial resolution [170–172]. MCP-PMTs exploit the photoelectric effect [173] to detect photons. For this process to take place, MCP-PMTs comprise a quartz window with a photocathode and an anode in a vacuum tight case. The final component of the MCP-PMTs is an electron multiplier, which gives an avalanche gain of $(\mathcal{O})(1\text{M})$.

The photons interact with the photocathode via the photoelectric effect and produce photoelectrons, according to the quantum efficiency of the device. The photoelectrons are accelerated by an electric field onto an electron multiplier, which consists in two planes of microchannel plates arranged in a "chevron-like" manner. When a photoelectron hits a plate, it triggers a charge avalanche of secondary photoelectrons. Because of the presence of a uniform electric field across the MCP-PMT, these can also hit plates and trigger further avalanches. For every photoelectron, the electron multiplier produces a large number of electrons in the avalanche, which are collected by the anode. In the TORCH MCPs, anode pins are embedded in a dielectric layer and connected to each other at the base and to a circuit board by an anisotropic connective film. The cross-section of an MCP-PMT is illustrated in figure 5.4. The compact design of the MCP-PMT, with a narrow gap between the photocathode and the anode, results in a fast response which is of the order of tens of picoseconds.

Three key requirements, specifically identified for the TORCH MCP-PMTs, were used in a development program undertaken in collaboration with Photek UK (Ltd.) [172, 175]. The tubes must endure an accumulated anode charge greater than $5\,\mathrm{C\,cm^{-2}}$ without significant changes in sensitivity; allow for close linear packing with a large active area (88%) along the x axis; achieve a spatial granularity of 6 mm and 0.4 mm respectively in the x and y coordinates local to the MCP-PMT. The latter requirement corresponds to a respective spatial resolution of $6/\sqrt{12}$ mm and $0.4/\sqrt{12}$ mm.

The development program was planned to produce three tubes in three consecutive phases. Phase I yielded a tube meeting the first requirement, Phase II culminated in the production of a tube that meets the spatial resolution requirement, and Phase III saw the completion of a tube that meets all three key requirements.

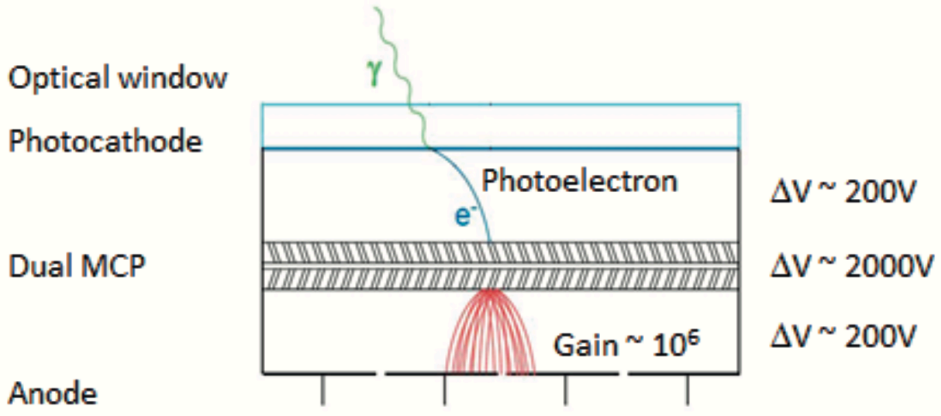

Figure 5.4: Illustration of the crossection of a typical MCP-PMT with a dual microchannel plate [174].

The Phase III tubes (fig. 5.5) employ chervon micro channel plates to maximise the instrument's lifetime by minimising the damage to the photocathode caused by ions liberated from the MCP pores on the tube body as secondary electrons also avalanche. Another source of ions is any residual gas which can be present in the vacuum or gas which is released from the sides of the surfaces in the tube. The ions are accelerated by the electric field towards the photocathode, reducing its quantum efficiency and gradually reducing the lifetime of the tube. The secondary electrons hit the bottom of the MCP, and since this is deployed in a chevron pattern, there is no direct path for the ions produced in this manner from their production point to the photocathode. The chevron pattern eliminates the largest cause of damage to the photocathode [176].

To further increase the tube's lifetime, the MCP is treated with Atomic Layer Deposition (ALD). This process consists in coating the surface of the MCP with layers of single-atom thickness of Al_2O_3. This enhances the production of secondary electrons, achieving the same gain at a lower voltage and therefore lower secondary electron production energies. The lower secondary electron production energy causes fewer ions to be liberated from the MCP pores. Furthermore, the presence of the ALD layer acts as sealant for the MCP pores, further suppressing the presence of damaging ions [177].

The required granularity was achieved by developing a design which in some aspects resembles a charge-sharing imaging device. A distinctive characteristic of the design is the collection of the charge from the avalanches received by all the anodes on a single resistive ink layer. Because of this indirect coupling, charge is spread across several pads. Charge sharing allows for a finer granularity than that with the same number of pads and no charge sharing [172]. The high granularity achieved via charge sharing requires a high density of connections between the anode and the readout electronics. This is carried out with the use of Anisotropic Conductive Film (ACF) to connect the tube to a Printed Circuit Board (PCB). ACF is a thin ($\sim 100\,\mu m$) film with wires embedded in its surface. The wires share the same pitch, and conduct in one direction.

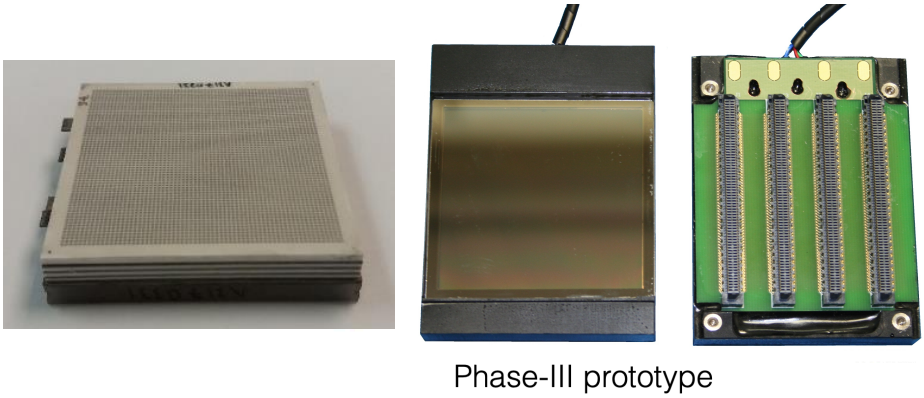

Figure 5.5: TORCH Phase-III MCP-PMT.

The Phase III tubes have an active area of $53 \times 53\,mm^2$, over a physical area of $59 \times 59\,mm^2$. The tubes are produced with 64×64 pads, but since the TORCH requires a coarser granularity along the x axis, sets of neighbouring pads are ganged together, in groups of eight, on the PCB [172]. Charge sharing is employed to double the granularity along the y axis. This results in an 8×128 effective pixel arrangement.

5.3.3 TORCH Readout Electronics and Data acquisition

A custom system was designed to readout the signal from the Phase III MCP-PMTs, shown in figures 5.6 and 5.7. The system comprises a readout board, an ultrafast front-end preamplifier-discriminator board using a NINO chipset, two High Performance Time To Digital Conversion (HPTDC) boards

and a backplane board [172, 178–180]. The MCP-PMT pixels are mapped to corresponding NINO channels. The NINO amplifies the signal and provides a Time Over Threshold (TOT) measurement of the amplified signal [181, 182]. Figure 5.8 illustrates how the signal is discriminated by the NINO chip. The TOT measurement provides information to a cluster-algorithm. The amplitude of the signal input to the NINO chip is correlated to the amount of charge deposited in the MCP-PMT pixel, to the duration of the signal in time, and to when the leading edge of the signal is logged in time. Larger charge deposits produce signals with larger amplitudes, which remain above threshold for longer. Longer signals also pass the threshold earlier than smaller charge deposits. The output of the NINO board is digitized by the HPTDC board, which mounts two HPTDC chips [183, 184]. The HPTDC time stamps the leading and trailing edges of the signal. Each HPTDC chip has 32 channels. An FPGA chip on the HPTDC board stores the leading and trailing edges of the signal from the HPTDC chip into buffer [180]. The HPTDC chips can be operated in high or very high resolution mode, corresponding respectively to 100 ps and 25 ps time bin precision per channel. The current channel mapping design introduces a limitation when operating the HPTDC in very high resolution mode. Only one in every 4 channels of the HPTDC is accessible in this configuration. The next iteration of the development of the readout electronics is expected not to suffer from this limitation. Furthermore, it is well known that the HPTDC introduces an integrated non-linearity (INL) in the signal they process [185]. This is because the spacing in time of the digitisation bins is not as precise as the rest of the electronic components comprised in the readout electronics. This effect is corrected for, as explained in 5.9.2. The HPTDC boards are connected to the readout board via the backplane, and the signal is transmitted to a data-acquisition system from the readout board.

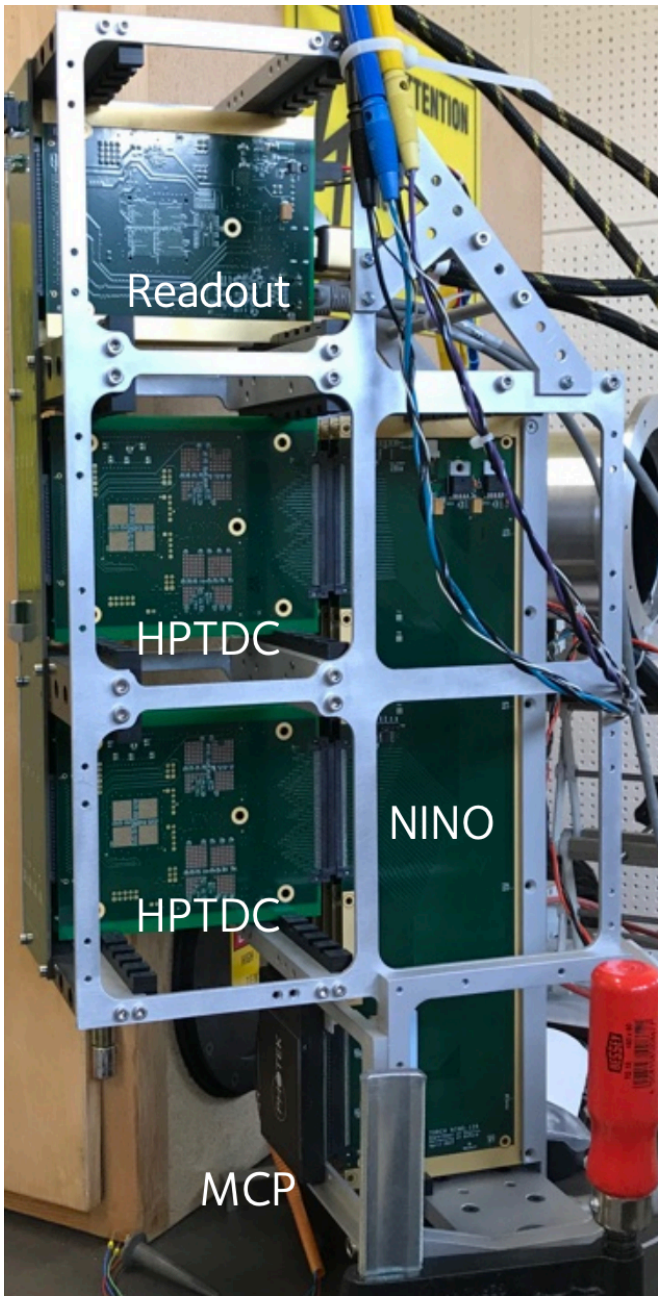

Figure 5.6: Custom readout electronics for the Phase III MCP-PMTs, comprising a NINO board, two HPTDC boards, a readout board and a backplane board.

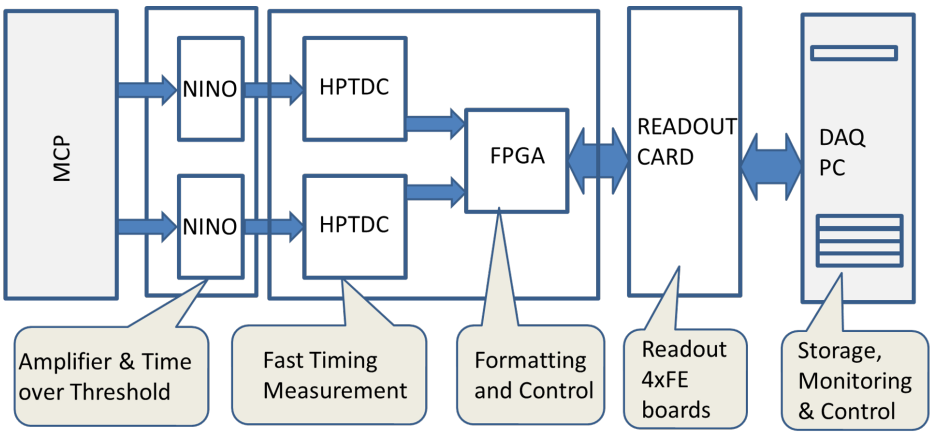

Figure 5.7: Illustration of the custom readout electronics for the Phase III MCP-PMTs, comprising a NINO board, two HPTDC boards, a readout board and a backplane.

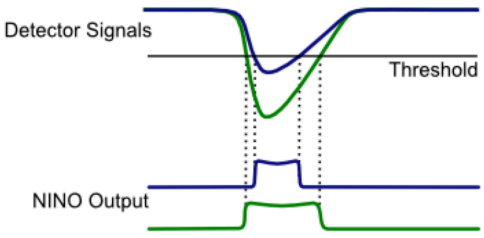

Figure 5.8: Illustration of the input and output NINO signals. Only those signals that pass the NINO threshold produce an output signal.

5.4 TORCH as an LHCb sub-detector

The TORCH detector has been proposed for PID at low momentum in the LHCb Upgrade II experiment [130]. TORCH comprises 18 modules, arranged with 9 optically separated modules above and 9 below the beamline. An illustration of the front view taken from upstram of the TORCH detector in LHCb is shown in figure 5.9. The envisioned placement for TORCH in LHCb is in front of the RICH2 detector (fig. 5.10) because of the good trade-off between maximising the distance from the interaction point and minimising the amount of material in front of the TORCH. In this position the hadrons fly over 9.5 m before traversing the TORCH, resulting in a measurable TOF difference between hadronic species.

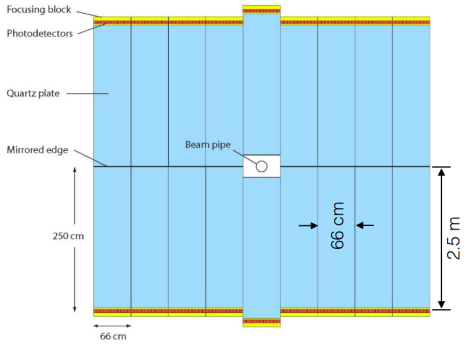

Figure 5.9: Illustration of the TORCH detector as seen from upstream in LHCb.

The charged particle flux traversing each module depends on the position of the module. The central modules are closer to the beampipe so they receive the highest number of particles, and the largest photon fluxes. On the other had, the modules at the periphery are the least densely traversed because of their distance from the beampipe. This is visible in figure 5.11 which shows a simulation of the track positions resulting from pp collisions in LHCb Upgrade II conditions superimposed on the TORCH detector.

The predicted PID performance of the TORCH detector as a part of the LHCb experiment was assessed by simulating the 18 TORCH modules in GEANT4 simulation. The detector geometry description, encompassing its detector volumes, surfaces and materials, is encoded in an xml format within the LHCb detector geometry description. This is then passed as input to the LHCb simulation software, Gauss [186]. Gauss simulates proton-proton collisions using the Pythia software [187], and the passage of the particles through the detector material using Geant4 software [188]. The simulation

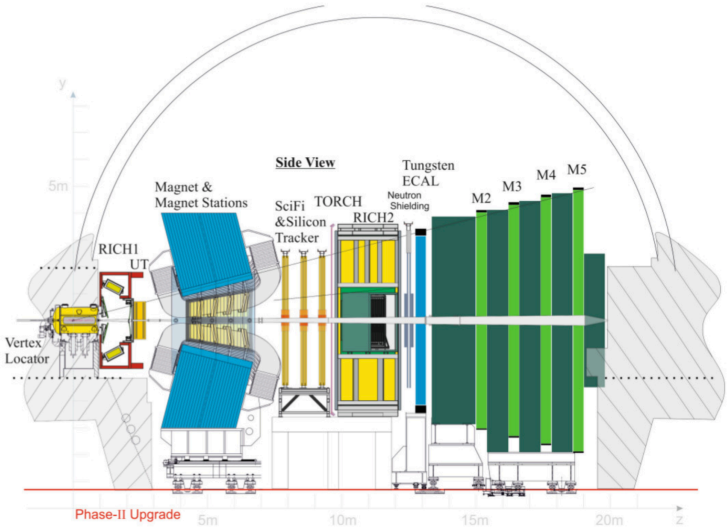

Figure 5.10: Side view of the LHCb detector, including the TORCH subdetector. [130].

includes Cherenkov process, energy loss due to scattering of the charged particles and surface effects, for example quartz surface roughness of 0.5 nm. The simulated TORCH detector is illustrated in figure 5.12.

In the simulated geometry, each module comprises the quartz radiator bar, quartz focusing block, a cylindrical focusing mirror mounted in the focusing block and an array of 11 MCP-PMTs mounted on the focal plane of the focusing block. Each module is then surrounded by air. The total internal reflection of the Cherenkov photons is simulated at the quartz-air boundary. The sensitive end of a simulated module is illustrated in figure 5.13.

The likelihood calculation is modelled on the reconstruction software used for the RICH detectors in LHCb, where PID for a given track is achieved by performing a hypothesis test based on likelihood ratios. The photon pattern caused by the track is tested against the likelihood of each hadron species hypothesis and the best PID is assigned to the charged particle [189]. More detail regarding the likelihood calculation are given in section 5.6. TORCH events are simulated by generating a pattern of photon hits for each incident charged hadron and for each hadron species hypothesis. Each photon pattern is used to produce a corresponding probability density function which is used to calculate the $\Delta log(\mathcal{L})$ with respect to the reconstructed photon pattern. The PID hypothesis that maximises the $\Delta log(\mathcal{L})$ is selected [159]. High-luminosity LHC conditions were simulated. These correspond to $\mathcal{L} = 1.4 \times 10^{34}\,\mathrm{cm}^{-2}\mathrm{s}^{-1}$

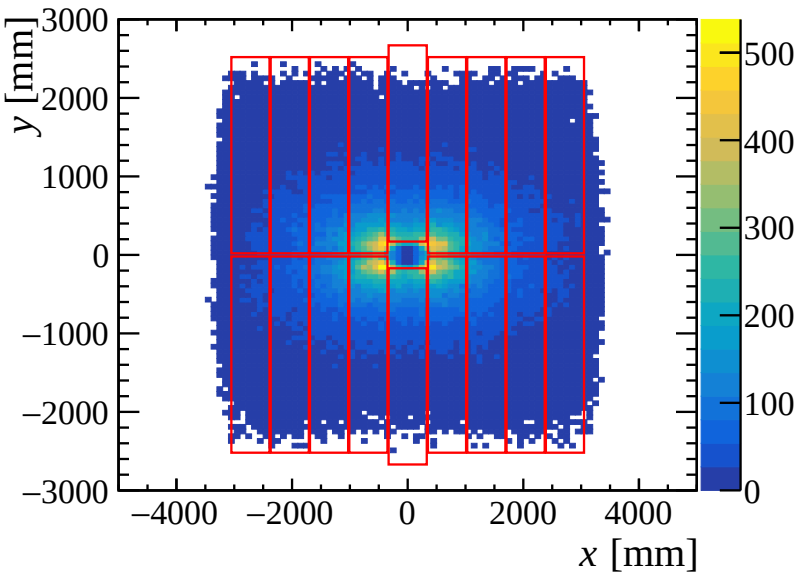

Figure 5.11: Simulation of charged hadrons traversing the TORCH as a subdetector in lhcb in Run3 conditions, which correspond to a beam energy of 7 TeV and a luminosity of $2 \times 10^{33} \mathrm{cm}^{-2}\,\mathrm{s}^{-1}$. The TORCH modules are represented by the red lines, positioned in a 2×9 grid around the beampipe, situated at $(0, 0)$. The two central modules are shifted by 260 mm in the y direction to make room for the beampipe.

and to a TORCH MCP-PMT effective pixel granularity of 128×32 and of 128×8, for the central and peripheral modules, respectively [130]. Figure 5.14 illustrates the TORCH kaon-pion (proton-kaon) separation power achievable. There is good separation between $\pi/K/p$ in the target range of 2–10 GeV. Overall as particle momentum increases the particle identification efficiency drops and the misidentification rate increases. This is because their ToF difference decreases and eventually, at around 20 GeV/c drops below the time resolution of the detector. Particles with a momentum below 2 GeV/c experience larger multiple scattering in the quartz radiator. This degrades TORCH's PID performance, as can be seen from the first bins of both plots of figure 5.14. The simulated TORCH performance in the LHCb experiment in High Luminosity LHC (HL-LHC) conditions shows that TORCH can improve the overall LHCb detector particle identification (PID) performance.

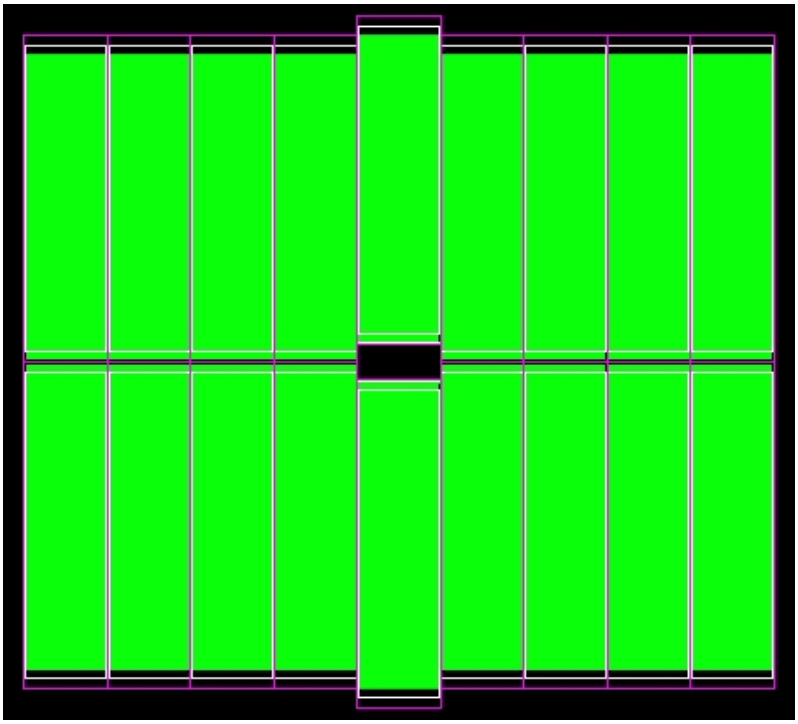

Figure 5.12: Visual representation of the simulated TORCH detector in the LHCb simulation software.

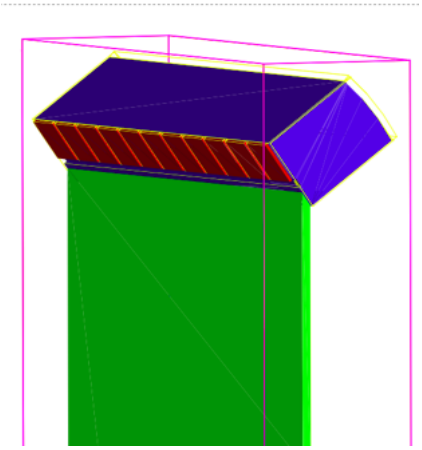

Figure 5.13: View of the sensitive end of the simulated module. The quartz bar is in green, the focusing block in blue, the focusing mirror mounted on the curve side of the block and outlined in yellow, the array of 11 MCP-PMTs in red, the aluminium box around each module outlined in pink.

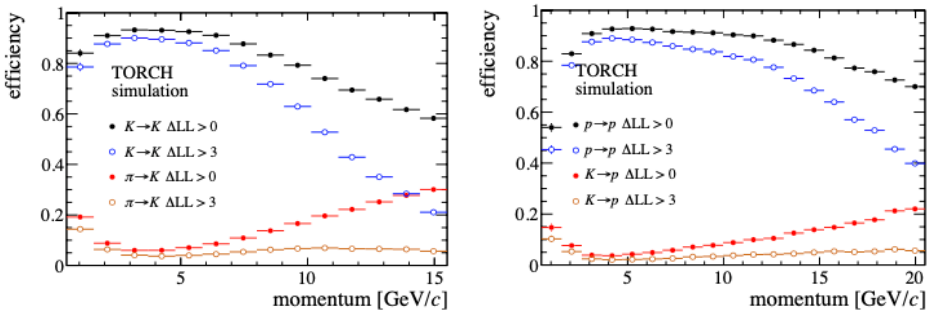

Figure 5.14: TORCH PID performance in LHCb in HL-LHC data taking conditions. Two different likelihood requirements are shown for kaon-pion separation efficiency (left) and for proton-kaon separation efficiency (right) [130].

5.5 Simulation of TORCH for alternative designs

The design of the TORCH detector is still under consideration. While the presence of key elements such as a quartz radiator bar and focusing block are firm decisions by now, aspects such as the number, size and relative position of the TORCH modules and module components could yet change. The reasons for this include the need of minimizing the MCP-PMT occupancy at high luminosity levels, and increasing the cost-effectiveness of the TORCH detector. The first point is investigated by changing some geometry parameters that affect where the Cherenkov photons land on the plane of the sensitive area. This is detailed in paragraph 5.5.1. A solution to spread the cost consists in designing the so called Staged TORCH. The Staged TORCH design consists in initially mounting only four wider TORCH modules in the next LHCb Upgrade, and in adding further modules only during subsequent LHCb Upgrades. While the Staged TORCH design has been developed and its performance simulated, it is currently not the chosen design.

5.5.1 Alternative TORCH geometries to reduce MCP-PMT occupancy levels

TORCH simulation and data from TORCH prototypes (for details see section 5.7) show that with the current designs, the majority of Cherenkov photons produced in the central modules land on the bottom half of the MCP-PMTs. A plot of the distribution of the hits on the MCP-PMT's vertical coordinate from TORCH simulated in the LHCb geometry is shown in figure 5.15. Furthermore,

the photon arrival time is peaking, as shown in figure 5.16. This causes the occupancy in the central modules under High Luminosity LHC conditions to be too high for the TORCH detector to operate correctly. Several solutions have been proposed to spread the hits over the whole MCP-PMT area, to decrease the occupancy per pixel, and to make use of the sensitive area in its entirety.

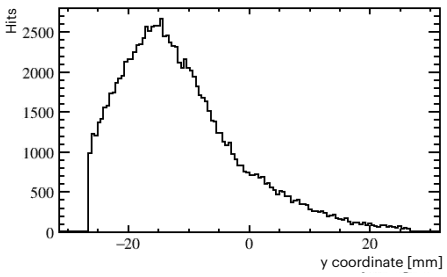

Figure 5.15: Distribution of hits on the MCP-PMT along the vertical axis of the tube, where y=0 is at the centre of the active area. The majority of the hits are registered in the bottom half of the tube.

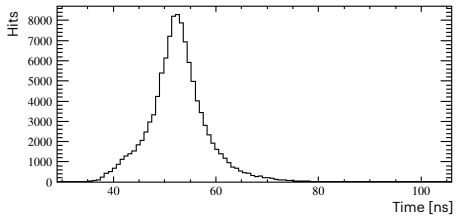

Figure 5.16: Distribution of hits on the MCP-PMT in time.

The proposed changes in design that should be explored are:

1. Tilt the TORCH detector with respect to the hadron beam. This will change the angle of the trajectory of the Cherenkov photons within the TORCH, and potentially shift the densely populated region towards the top of the sensitive area.

2. Shift the centre of curvature of the mirrored surface of the focussing block. This will shift the point where the photons are focused towards.

3. Change the radius of curvature of the mirrored surface of the focusing block in conjunction with a change in focal plane position, to keep the image in focus. A change in the radius of curvature enlarges or reduces the image, and a change in focal plane position effectively translates to changing the length of the focusing block. This also has the effect of enlarging or reducing the image made by the focused Cherenkov photons.

4. Change the angle between the radiator bar and the focusing block by rotating the block. The focusing block maps the angle to the y coordinate so this change will shift the image. Consequentially, the angular acceptance is affected.

When changing radius of curvature and focal plane position, the focal plane should be placed at $\sim 1/2$ the radius of curvature away from the curved mirror for the image to remain in focus. With this in mind, the first study to be performed was to increase the radius of curvature to 150% of the nominal one, from 260 mm to 390 mm. The effect this has on where the photons land on the sensitive area is shown in figure 5.17. As expected, increasing the radius of curvature spread the image over a larger area, covering the entirety of the tube along the vertical direction. Also expected is the poor PID performance of this design because the image is not in focus, having changed the radius of curvature while keeping the focal plane position constant. The next step in this study is to increase the distance between the mirror and the focal plane to 150% of the nominal value to obtain a focused image that spans the full height of the sensitive area. This work is ongoing and part of the current R&D TORCH simulation studies. Studies on the remaining points that could change the local occupancy of the MCP-PMT pixels are planned for future simulation work.

5.6 TORCH reconstruction studies

The TORCH reconstruction software achieves particle separation by using a likelihood calculation for different hadron hypotheses, h:

$$ln(\mathcal{L}_h) = \sum_{\text{hits}} ln(P(x_{\text{hit}}, t_{\text{hit}}, h). \tag{5.7}$$

The probability density function, $P(x_{\text{hit}}, t_{\text{hit}}, h)$, depends on the hit coordinates in space and time $(x_{\text{hit}}, t_{hit})$ and of the hadron hypothesis. There are

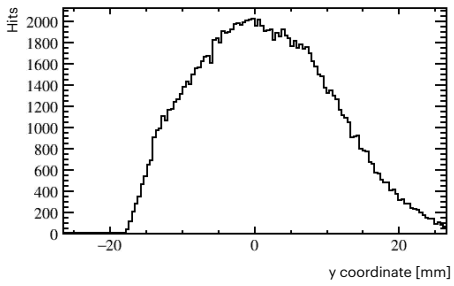

Figure 5.17: Simulation of hits in the alternative design of the focusing block, where the radius of curvature is increased to 150% of the nominal value. Distribution of hits on the MCP-PMT along the vertical axis of the tube (left), where y=0 is at the centre of the active area, and in time (right). The majority of the hits are spread over the entirety of the sensitive area along the vertical direction.

two algorithms to calculate the probability of a hadron track producing the observed hits in space and time under a given mass hypothesis, known as local and global algorithm. The local algorithm calculates the probability of a given track as

$$P^h_{\text{track}} = \prod_{\text{hits}} P^h_{\text{hit}}(x_{\text{hit}}, t_{\text{hit}}) \tag{5.8}$$

$$= \prod_{\text{hits}} [f^{\text{sig}} P^{\text{sig}}_{\text{hit}}(x_{\text{hit}}, t_{\text{hit}}|h) + f^{\text{bkg}} P^{\text{bkg}}_{\text{hit}}(x_{\text{hit}}, t_{\text{hit}}|h)], \tag{5.9}$$

where the functions f^{sig} and f^{bkg} are the fraction of signal and background, connected by the condition $f^{\text{sig}} + f^{\text{bkg}} = 1$. The probability of the hit to be signal or background, $P^{\text{sig}}_{\text{hit}}$ and $P^{\text{bkg}}_{\text{hit}}$ respectively, are templates. For each track mass hypothesis, 1M photons are generated and propagated through the optics to estimate the $P^{\text{sig}}_{\text{hit}}$ template. The template for the $P^{\text{bkg}}_{\text{hit}}$ come from summing over all events to simulate a random background PDF. The mass hypothesis test consists in a Likelihood ratio. The global algorithm was developed to assess all tracks in an event simultaneously. This is done by calculating the $log\mathcal{L}$ for each track as

$$\log \mathcal{L} = \sum_{\text{hits}} \log[\sum_{j \neq t} \frac{N_j}{N_{\text{tot}}} P_j(x_i, t_i|h^{\text{best}}_j) + \frac{N_t}{N_{tot}} P_t(x_i, t_i|h_t) + \frac{N_{\text{bkg}}}{N_{\text{tot}}} P_{\text{bkg}}(x_i, t_i)], \tag{5.10}$$

where $f^{\text{sig}} = \frac{N_t}{N_{tot}}$, $f^j = \sum_{j \neq t} \frac{N_j}{N_{\text{tot}}}$ and $f^{\text{bkg}} = \frac{N_{\text{bkg}}}{N_{\text{tot}}}$ are respectively the fraction of signal, other tracks and background; $P_j(x_i, t_i | h_j^{\text{best}})$ is the PDF for the hypothesis assignment for the other tracks, $P_t(x_i, t_i | h_t)$ is the PDF for the considered track, and $P_{\text{bkg}}(x_i, t_i)$ is the PDF for the background distribution, assumed flat. For each track probability, this approach separates the background hits into hits coming from other reconstructed tracks in the same event and hits from other sources of background. The track assignment of the best mass hypothesis is achieved through iteration by flipping the track hypothesis for each track and each background track. Tracks are initially assigned the pion hypothesis. In the n^{th} iteration, they assign the best hypothesis from the $(n-1)^{th}$ step. The yields of each component are estimated from N_j as $N_{\text{bkg}} = N_{\text{tot}} - \sum_j N_j$. N_j is estimated by forward propagating 1000 photons through the optics of the focusing block and the radiator bar. The PDF for a given track and hypothesis combination is determined by reconstructing the Cherenkov angle θ_{C} from the hits. Via θ_{C} the hits are mapped through the focusing block and down the radiator bar to the emission point, where their coordinates are transformed from the emission space to the detection space in the following way:

$$P(x, t | h) = |J| P(E_\gamma, \theta_{\text{C}}, t_0), \tag{5.11}$$

where J is the Jacobian of the transformation:

$$J = \left| \frac{\delta y_{\text{d}}}{\delta E_\gamma} \frac{\delta x_{\text{d}}}{\delta \theta_{\text{C}}} - \frac{\delta x_{\text{d}}}{\delta E_\gamma} \frac{\delta y_{\text{d}}}{\delta \theta_{\text{C}}} \right|, \tag{5.12}$$

x_{d} and y_{d} are the detection coordinates in space, and E_γ is the photon energy. This is done for every photon hit, mass hypothesis and track. In principle the global algorithm is optimal because of the better background treatment. In practice there is little difference between the outputs of the two algorithms because of the background comprising photons without associated hadron tracks, such as those produces by γ conversion. The TORCH reconstruction alternates between using the global and local algorithms.

The photon hit time is related to the hadron detected time, which is defined as:

$$t_d = t_0 + \frac{r_{\text{track}}}{\beta c} + \frac{r_\gamma}{v_g}, \tag{5.13}$$

where t_0 is the hadron production time, r_{track} is the track path length from

production to TORCH, βc depend on the hadron mass hypothesis, r_γ is the Cherenkov photon path length within TORCH, and v_g is the photon group velocity. For a fixed hadron production time and track path length, one can separate between mass hypotheses by comparing $-log(\mathcal{L})$ values.

5.6.1 Vertex time reconstruction

The time, t_0 of the Primary Vertex (PV) can be extrapolated from TORCH data. Within the LHCb experiment this would add an off-line constraint to the PV t_0 calculated by using the readout from the next LHCb Upgrade, improving the precision. While in the TORCH particle identification the t_0 is known from an external source, for the vertex time reconstruction t_0 is allowed to vary and extrapolated from the data.

Because of the high momentum, one can assume that all particles are saturated and perform a likelihood calculation treating them as pions. An example of t_0 reconstruction for tracks from the same PV is shown in figure 5.18. A PV likelihood is calculated from the individual tracks that make each PV. Outlier reconstructed tracks are excluded from the PV t_0 likelihood calculation of the reconstructed PVs. Reconstructed tracks are classified as outliers if

$$| - log(\mathcal{L}_{track}(t_{\text{min}})) + log(\mathcal{L}_{track}(t_{\text{PVmin}}))| > 2, \tag{5.14}$$

where t_{PVmin} is the time which minimises $-log(\mathcal{L}_{\text{PV}}(t))$. The likelihoods of outlier tracks are re-evaluated under the kaon and proton hypothesis to assess whether they are more compatible with the PV before being excluded for the PV t_0 reconstruction. Tracks that qualify as outliers under the pion hypothesis but become compatible with the PV under either the kaon or proton have their hypothesis reassigned to the most compatible one and are not excluded from the measurement.

The TORCH reconstruction software is tested using a dataset composed of simulated inclusive b hadron events in LHCb Upgrade Ib environment with an instantaneous luminosity of $2 \times 10^{33}\text{cm}^{-2}\,\text{s}^{-1}$. As can be seen in figure 5.19, the reconstruction algorithm results in a PV time resolution of 17.7 ps, measured by fitting a Gaussian function to the reconstructed PV t_0 of the simulated data in a window centred around the peak. This window was chosen to exclude the long tails present in the distribution which are not representative of the PV t_0 resolution. The causes of these long tails are

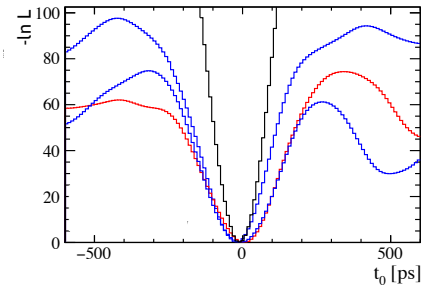

Figure 5.18: An example of the reconstructed PV t_0 from three tracks which share the same PV. The tracks are from two true pions, which have reconstructed PV t_0 values at the minimum of the blue curves, and one true kaon, which has a reconstructed PV t_0 value at the minimum of the red curve. All tracks are reconstructed as pions for this study. The reconstructed PV t_0 from the combination of the three tracks is at the minimum of the black curve. The negative log-lokelihood distribution of the combination of tracks is more precise than the individual track negative log-lokelihood distributions.

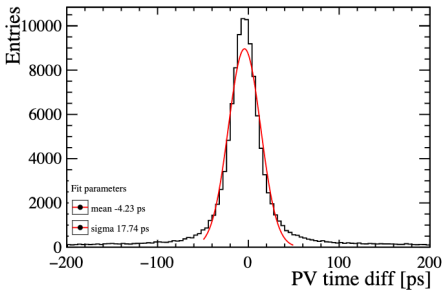

Figure 5.19: Plot of the PV t_0 resolution from reconstruction for a large sample of simulated $b\bar{b}$ events using the reconstruction algorithm described in section 5.6.1. The distribution is fitted with a Gaussian function to extract the time resolution.

addressed in the next paragraph.

The distribution of the time resolution of the PV in figure 5.21 presents some long tails. To understand the source of the tails, the resolution measurement was performed in two alternative ways. The first new method consists in reconstructing simulated events, and using the truth information for the hadron hypotheses in the likelihood minimization to extract the time of the PV. The second alternative method takes this one step further, by using truth information to identify the correct PV as well as the correct hadron hypothesis to separate any overlapping PVs that might be present. The output of these studies is shown in figure 5.20, from which it is clear that the origin of the long tails lies in assigning tracks to the wrong reconstructed PV, and

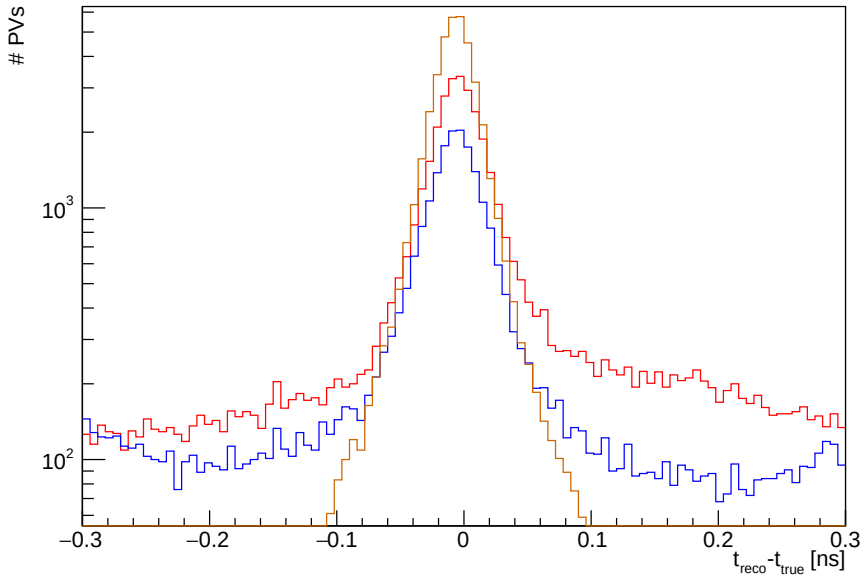

Figure 5.20: The PV t_0 resolution from the method described in this section. The red curve results from the nominal t_0 PV resolution calculation. The blue curve results from the nominal calculation, where the truth information is used to assign the correct hadron hypothesis to each track. The yellow curve results from the nominal procedure with truth information used to assign the correct hadron species to the track, and to exclude tracks from other PVs.

in giving the tracks the wrong hadron mass hypothesis. The results of this study suggest that the input of external tracking information in the TORCH reconstruction algorithm would be beneficial for the PV t_0 resolution. In particular, the planned LHCb VELO Upgrade would provide timing as well as spatial information, resulting in fewer tracks assigned to the wrong PV. The PV t_0 resolution is expected to be $\propto 1/\sqrt{N_{\text{tracks}}}$, therefore how the number of reconstructed tracks per PV affects the resolution of the reconstructed t_0 of the PV is investigated. The distribution of the PV time resolution is calculated first for PVs with more than 8 tracks, and then for PVs with 8 tracks or fewer. These were compared to the nominal result, and the comparison is shown in figure 5.21. The narrowest distribution is that from PVs with a high number of tracks, as expected.

Figure 5.22 shows the average track t_0 resolution as a function of the number of detected Cherenkov photons. The latter is expected to follow a $1/\sqrt{N_{\text{photons}}}$ dependence, where N_{photons} is the number of photons per track. Evidently, it does not. The presence of background photons, typically

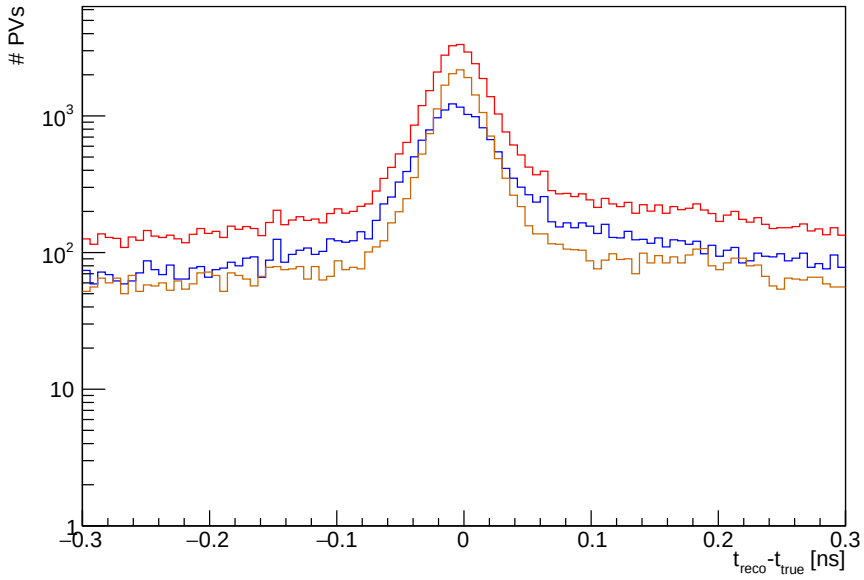

Figure 5.21: The the PV t_0 resolution distribution from all PVs in red, from PVs with more than 8 tracks in blue, and from PVs with 8 tracks or less in yellow.

Cherenkov radiation produced by other particles, causes this deviation to occur. The same study is performed using truth information to exclude photons emitted by other particles, results of which are shown in figure 5.23. This dependence is modelled by the function $p_0 + \frac{p_1}{\sqrt{N}}$, where N is the number of photons. This is proof of the role of background photons towards the degradation of the track and PV time resolution. The parameters p_0 and p_1 from the fit correspond to (3.4 ± 0.5)ps and (78 ± 2)ps, respectively. The parameter p_1 corresponds to the single photon time resolution. This is slightly greater than the TORCH goal single photon time resolution (70 ps). The cause of this difference is the combination of a finite pixel size and the long path lengths of most Cherenkov photons. The majority of the Cherenkov photons are produced close to the beam and far from the photo detector plane in TORCH within LHCb. The finite pixel size introduces an uncertainty on the Cherenkov angle, which grows with the path length. As a consequence, photons with large path lengths have larger uncertainties on the reconstructed photon energy, and on the reconstructed group velocity. This effect is also observed in beam test campaigns of TORCH prototypes [190].

The PV t_0 reconstruction studies show that TORCH is capable of performing said reconstruction, and highlight the limitations related to the

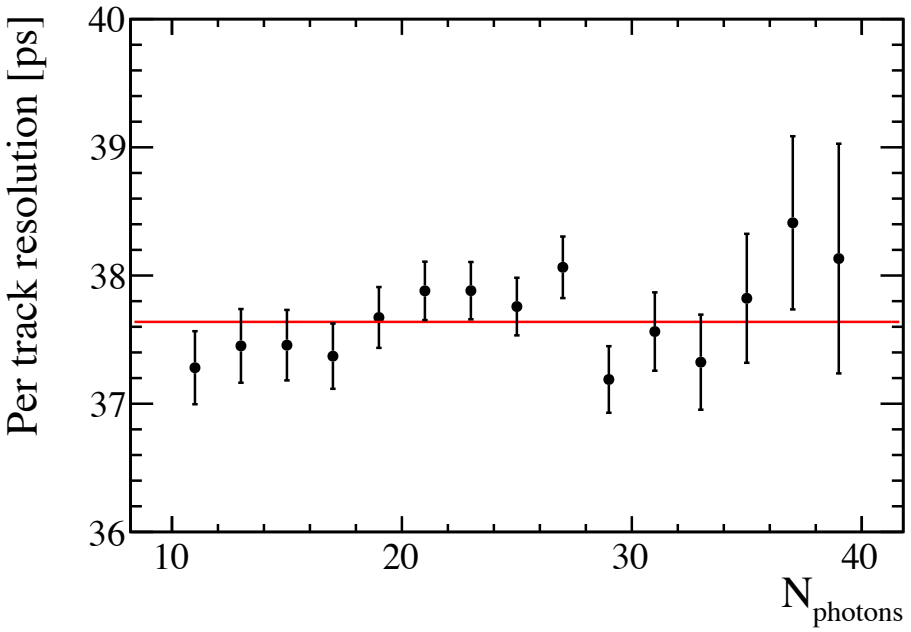

Figure 5.22: The average per-track resolution as a function of number of reconstructed photons. The best fit function to the data points appears to be independent of the number of Cherenkov photons.

mass hypothesis assignation, to the grouping of tracks by reconstructed PV, and to the presence of background photons. Background photons are produced by charged particles interacting with material present in TORCH and LHCb. The photon production processes comprise by pair production in the quartz, and electromagnetic or hadronic interactions in the Fibre Tracker.

Background photons degrade the time resolution of the TORCH detector. Simulations of shielding the TORCH within the LHCb detector were carried out to identify a way of reducing the photon background. Adding material around the detector can stop particles produced outside the TORCH box, but new particles might be produced in it and enter the detector. Simulations of the TORCH detector with modules shielded by aluminium or carbon fibre were performed. These materials were chosen because of their light weight, and because they don't shield energetic hadrons. The thickness and the shielding material were investigated to identify which combination results in a reduction of background photons in the TORCH detected signal. These simulations show that while aluminium stops a greater number of background photons

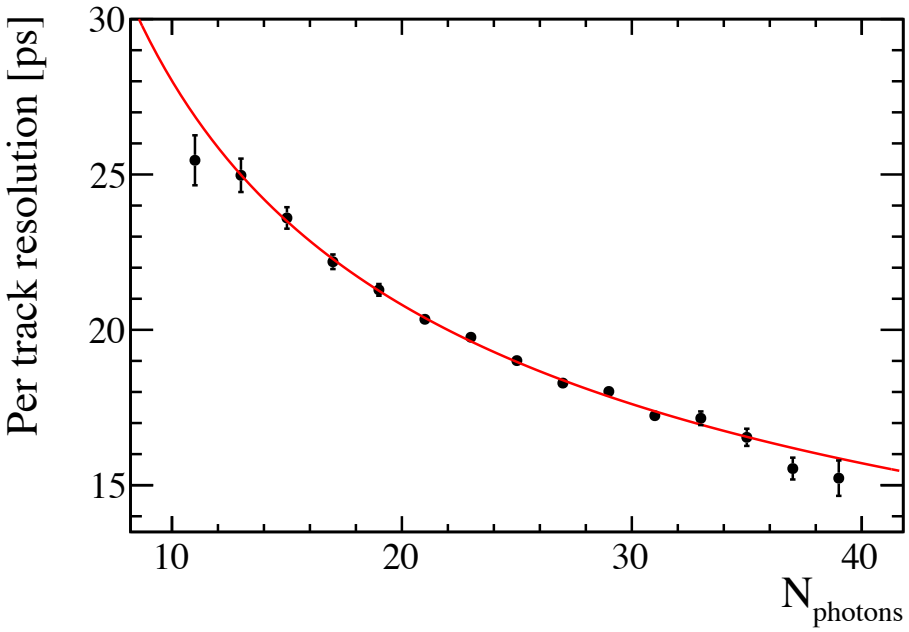

Figure 5.23: The average per-track time resolution as a function of number of reconstructed photons, excluding background photons using truth information. The best fit function to the data points is the distribution: $p_0 + \frac{p_1}{\sqrt{N_{\text{photons}}}}$, where N_{photons} is the number of photons.

from reaching the TORCH sensitive area compared to carbon fibre, it also introduces more background photons than carbon fibre does. Furthermore, the simulations show that these shielding methods do not reduce the photon background in the TORCH signal. The amount of background photons and how to reduce it remains an ongoing study within the TORCH R&D program.

5.7 TORCH prototypes and Test-Beam Results

Several test beam campaigns were carried out to test the properties of the TORCH detector. Two TORCH prototypes were built and tested in a hadron beam, "Mini-TORCH" and subsequently the larger "Proto-TORCH", in figure 5.24. One of the aims of each test beam campaign was to measure the single-photon time resolution of the TORCH prototype. The second aim of the test beam campaigns was to asses the photon counting efficiency of the prototype by comparing the number of detected photon clusters to the number of photon

clusters expected from simulation.

Figure 5.24: Photo of Proto-TORCH.

In the most recent test beam campaigns the setup, visible in figure 5.25, comprised two threshold Cherenkov counters, two scintillator and time-reference stations, and a pixel telescope from EUDET/AIDA [191]. The latter was used to measure the beam profile. The time reference stations comprise borosilicate bars from which Cherenkov light is detected using single channel MCP-PMTs. The stations were placed 10 m upstream and 1 m downstream of proto-TORCH. The threshold Cherenkov counters independently identify the particles in the beam. The HPTDC chips in proto-TORCH were operated in high resolution mode.

5.7.1 TORCH Prototypes

For the November 2017 and June 2018 test beam campaigns a TORCH prototype called Mini-Torch was built. It is a small-scale TORCH module demonstrator, with a quartz radiator bar of dimensions $120 \times 350 \times 10\text{mm}^3$. While this prototype has space to accommodate two MCP-PMTs, only one was mounted, in the top left corner of the module when looking at its front face. The beam used in both campaigns comprised protons and pions from the CERN PS. The best single photon time resolution for pions measured during each of the two aforementioned test beam campaigns is 104.3 ± 1.4ps

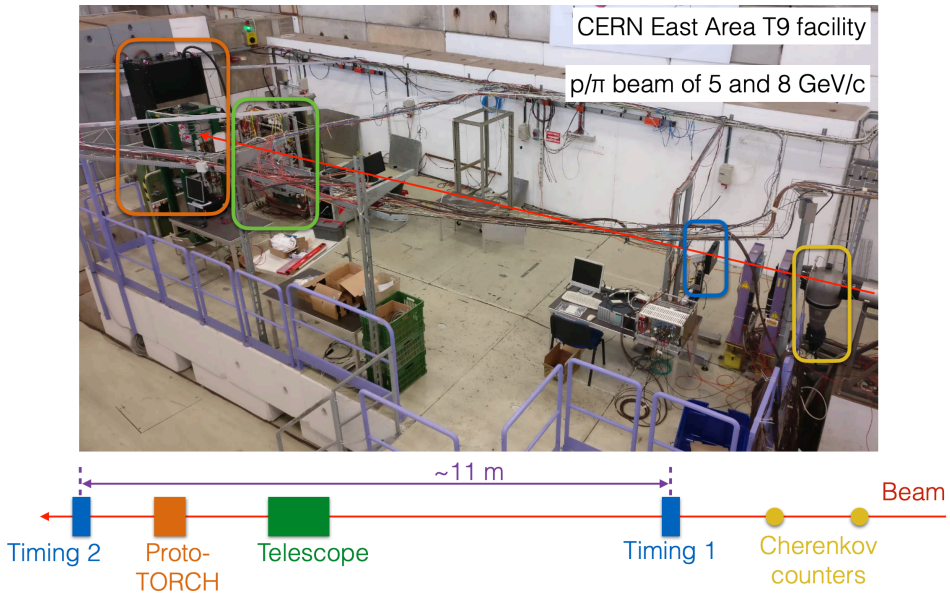

Figure 5.25: Photo of the latest Proto-TORCH test beam set up. Proto-torch is highlighted by the orange box, the Cherenkov counters by the yellow box. Only one of the timing stations is in the shot, highlighted by the blue box. The second timing station is off camera to the left.

and 83.8 ± 1.3ps, respectively. The improvement from the November 2017 to the June 2018 campaign can be attributed to an improved reconstruction, and in an small amount to a change in granularity of the x axis of the MCP-PMT. The reconstruction improvements include a better time-walk correction and better signal extraction compared to simulation. The same measurement for protons can only be performed on data taken during the June 2018 campaign, and corresponds to 87.5 ± 1.4ps. The uncertainties on the single photon time resolution measurements are purely statistical [159, 192]. The ratio of counted photons in data and simulation of Mini-TORCH measured in the two test beam campaigns corresponds to $90.8\% \pm 0.5\%$ and $67.0\% \pm 0.5\%$. The difference is due to a tube with a lower quantum efficiency being used in the second measurement [192].

The latest TORCH prototype (proto-TORCH) comprises a half height (125cm), full width (66cm) TORCH module, instrumented with two MCP-PMTs (Tube A and Tube B). The two tubes are located in the top left corner of the module when looking at its front face. Proto-TORCH underwent a

test beam in October-November 2018 at the CERN PS East Hall T9 facility, with an 8GeV/c beam. The single photon time resolution measurement was performed using data from tube B because of tube A's lower quantum efficiency. The measurement varies as a function of the beam entry position in the radiator. The measured single photon time resolution was better for beam entry positions closer to the MCP-PMT plane. Chromatic dispersion experienced by Chrenkov radiation degrades images from photons emitted further from the MCP-PMT plane more than images from Cherenkov photons produced closer to the plane. The measurement for pion and proton candidates varies in the ranges [63ps, 112ps] and [65ps, 109ps], respectively. More details regarding this measurement are given in reference [190].

Ratio of photons counted in data and simulation for Proto-TORCH is measured by only including reconstructed photon tracks that travel to the MCP-PMT with one near-side reflection or less in the comparison. The measured ratio of photons counted is of order 90% [190]. The ongoing development of the tubes will result in a higher quantum efficiency, so more photons will be detected.

5.8 TORCH Single photon time resolution contributions

The design goal for the TORCH single photon time resolution is of 70 ps. This can be factorised into components that can be attributed to the propagation of the photons in quartz, to the readout electronics and to the MCP-PMT. The single photon time resolution can be expressed as

$$\sigma^2_{\mathrm{TORCH}} = \sigma^2_{\mathrm{prop}}(t_{\mathrm{p}}) + \sigma^2_{\mathrm{RO}}(\sqrt{N_{\mathrm{hits}}}) + \sigma^2_{\mathrm{MCP-PMT}} \ , \tag{5.15}$$

where $\sigma_{\mathrm{prop}}(t_{\mathrm{prop}})$ is the time resolution on the measurement of the photon propagation time in the quartz, t_{prop}, where $\sigma_{\mathrm{MCP-PMT}}$ is the MCP-PMT's intrinsic time resolution, and $\sigma_{\mathrm{RO}}(\sqrt{N_{\mathrm{hits}}})$ is time resolution associated with the readout electronics. The latter scales by $\sqrt{N_{\mathrm{hits}}}$, the number of pixels hit by a single photon. The time resolution component related to the photon propagation time in the quartz is expected to grow linearly with the propagation time due to the fixed pixel size. The contribution of the MCP-PMT intrinsic time resolution and the readout electronics time resolution, $\sigma^2_{\mathrm{RO}}(\sqrt{N_{\mathrm{hits}}}) + \sigma^2_{\mathrm{MCP-PMT}}$, is expected to be ~ 50 ps.

The laboratory studies of one of the Phase III MCP-PMTs described in section 5.9 aim to measure the single photon time resolution of the Phase III MCP-PMT coupled to the custom readout electronics, $\sigma^2_{\mathrm{RO}}(\sqrt{N_{\mathrm{hits}}}) + \sigma^2_{\mathrm{MCP-PMT}}$.

5.9 Laboratory characterisation of the TORCH PCM-PMTs

5.9.1 Laboratory test stand set up

A laboratory test-stand was set up to characterise the Phase III MCP-PMT and the TORCH readout electronics, of which figure 5.26 is an illustration. The MCP-PMT was placed in a light-tight box and illuminated with a fast-pulsed blue laser source. The laser emits a trigger signal, synchronously with the light pulses, which has a twofold purpose. On one hand it is fed as input to a pulse generator which produces a delayed pulse that is input to the trigger unit. The delay used for diffused light measurements, described in section 5.9.2 corresponds to 275 ns, while that used for collimated light measurements, described in section 5.9.4, is of 300 ns. The laser's trigger signal is sent to the backboard and stored as a time reference in four of each TDC's channels. For this reason, these four channels per TDC are not connected to the corresponding MCP-PMT pixels. The MCP-PMT output is captured by a data acquisition computer via the readout electronics, already illustrated in paragraph 5.3.3. The test stand can be operated in two configurations: the laser light can be focused to a spot with a diameter of $\sim 20\,\mu$m; or the laser light can be diffused with delrin disks of varying thickness to illuminate the entire tube for HPTDC calibration studies and for homogeneity studies. The trigger of the readout electronics is synchronised with the laser pulses. When the laser light is focused, it is attenuated via a digital attenuator to reproduce the single photon conditions that the MCP-PMT experiences when used in a TORCH module. In the collimated laser light configuration, the light is delivered through an optical fibre, and the end of the optical fibre is mounted on a translation stage so that the light spot position on the tube can be changed. The translation stage is controlled externally and can centre the light spot on any of the tube's pixels.

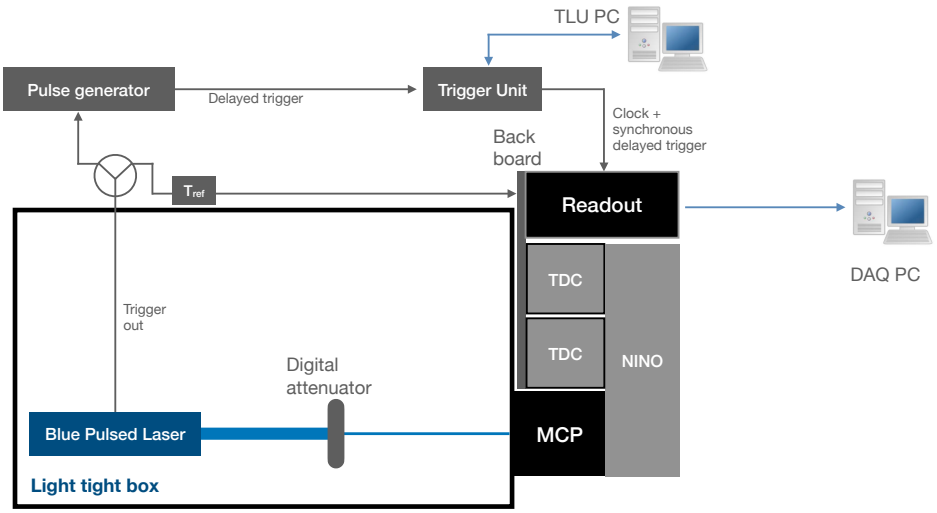

Figure 5.26: Illustration of the laboratory test stand set-up. The Phase III MCP-PMT is paced in a light-tight box and stimulated using a blue pulsed laser beam. The laser beam is attenuated using a digital attenuator to reproduce the single photon conditions of the TORCH detector. The laser also outputs a trigger synchronously with the light pulse, this is split and serves as input to the readout's 8 time reference channels and to a pulse generator. The pule generator emits a delayed trigger which is received by the trigger unit. A trigger unit counter controls the latter to give a clock signal to the readout board and to store a user-defined number of triggers via the DAQ computer which receives the readout signal.

5.9.2 Diffused light measurements

Diffused light measurements have a twofold purpose: to produce calibrations samples to account for the HPTDC's integrated non-linearity in its response; and to probe the homogeneity of the Phase III MCP-PMT response.

The laser rate was set to 100 hertz. A 2 mm delrin disk was inserted between the laser light beam and the tube, at a 20 mm distance from the end of the optical cable. The laser light was fed through a splitter, with 96% of the total light reaching the diffusing disk. The delayed pulse emitted from the pulse generator to the trigger unit was set to 275 ns. Over time, because of temperature variations of the laser, the laser pulses and the data-taking window following the trigger tend to drift out of sync. This choice in delay

allows the entirety of the signal, from leading to trailing edge to remain within the time window even while it experiences a drift.

The diffused light data is visible in figure 5.27. A clear non uniformity in the MCP-PMT is present, as the centre of the tube presents a drop in response compared to the sides. This behaviour could be caused by a drop in quantum efficiency, by a drop in gain or by a combination of the two. To investigate this non uniformity in more detail, a scan of the tube using the focused light set-up was planned. More detail regarding this is found in section 5.9.3.

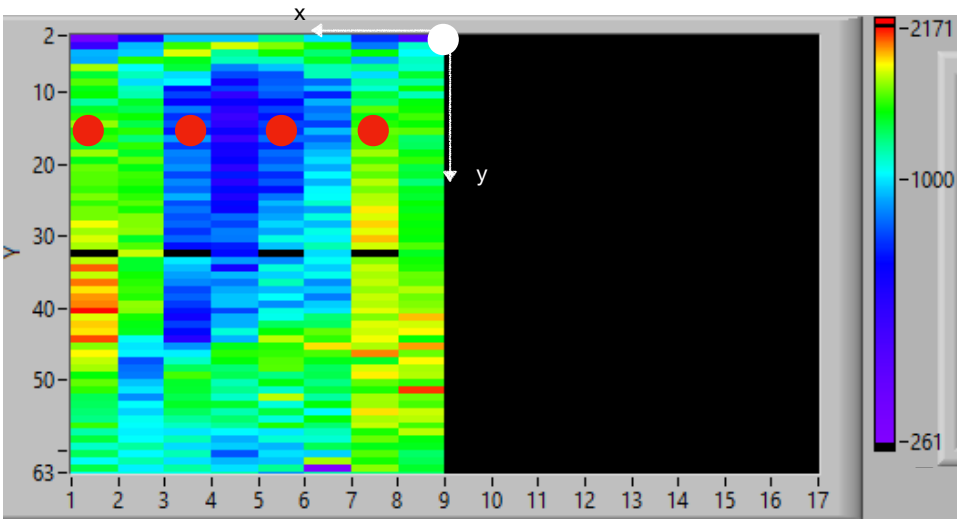

Figure 5.27: Data taken by the MCP-PMT, processed by the HPTDC during a diffused light run with the HPTDC operating in high resolution mode. A non uniform response is visible, with less sensitivity at the centre of the tube. The four bins in black are not accessible since the time reference is mapped to their corresponding NINO channels. The red circles identify the pixels selected for a horizontal scan of the MCP-PMT with the focused light set up of the test stand, described in section 5.9.3. The chosen pixels have coordinates (48.4, 14.9), (35.2, 14.9), (21.9, 14.9) and (8.7, 14.9), from left to right.

The signal collected from the time reference channels originates directly from the trigger output of the pulsed laser. It should consequently be constant for all recorded triggers. Because of the INL introduced by the HPTDC, the

signal from the time reference channels is not constant and reveals the effect the INL has on any dataset. From the time reference signal it is possible to isolate and observe the INL. An INL correction is generated for all channels using a code density test [193]. This is performed by calculating the Differential Non-Linearity ($\mathrm{DNL_i}$) per time bin, which corresponds to the number of hits in each bin collected during a diffused light run to the expected number of hits for a uniform distribution of bins in time:

$$\mathrm{DNL_i} = \frac{\mathrm{P_i} - \mathrm{P_{exp}}}{\mathrm{P_{exp}}} \ , \tag{5.16}$$

where P_i is the number of hits in each bin, and P_{exp} is the number of expected hits from a uniform distribution in time of bins. The DNL is a measure of the shift the centre of each bin experiences in time, compared to its ideal timing in a uniform distribution. The INL correction for each bin is the sum of the DNL of all preceding bins:

$$\mathrm{INL_i} = \sum_{\mathrm{j=0}}^{\mathrm{i}} \mathrm{DNL_j} \ . \tag{5.17}$$

An example of a set of INL corrections is shown in figure 5.28. Corrections extracted from the time reference channels are shown as well as those calculated for channel 204 as an example. Previous studies have shown that the minimum number of events needed in the calibration sample to calculate INL corrections is $\mathcal{O}(10^6)$. Smaller samples produce corrections that, when applied to a time resolution measurement, significantly degrade the time resolution [159, 194]. Two calibration samples containing 20 million events each were taken in this configuration, with the HPTDC chip operating in the high resolution mode first and in the very high resolution mode for the second. The MCP-PMT was operated at a gain of $\mathcal{O}(10^6)$.

The long nature of the diffused light data taking runs necessary to correct the INL of HPTDC is unfortunately unavoidable. Reducing the level of attenuation applied to the laser light to increase the number of hits, which corresponds to collecting the same amount of data in less time, is not a good alternative. This is because of the intrinsic difference between the two data taking scenarios. While the first corresponds to a single photon per hit situation, this assumption probably does not hold any longer for a smaller laser light attenuation value. No work around the duration of the INL calibration runs was found.

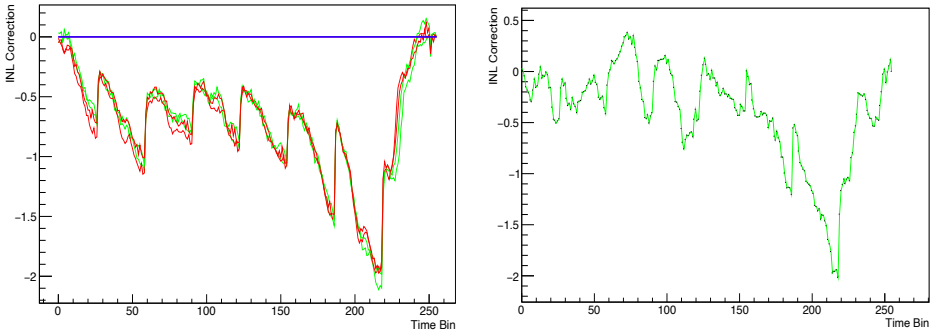

Figure 5.28: Example of integrated non-linearity corrections as a function of time bin for the time reference channels on the left, and for channel 204 of the MCP-PMT on the right. For the specific case of this plot, data were taken using one HPTDC chip only, resulting in calculating INL corrections for those four time reference channels specific to the active HPTDC only. These are visible in green and red. The INL corrections for the time reference channels relevant to the inactive HPTDC were not calculated in this specific instance and set automatically to 0, in blue.

5.9.3 Scan of the MCP-PMT to investigate inhomogeneous response

The diffused light measurement shows a drop in performance at the centre of the tube. This prompted an investigation in the form of a horizontal scan of the MCP-PMT using the focused laser light setup of the test stand. The scan consists in taking high-resolution and very-high-resolution HPTDC mode data in four points across the MCP-PMT, precisely at (48.4, 14.9), (35.2, 14.9), (21.9, 14.9) and (8.7, 14.9), from left to right. The points are indicated in figure 5.27. At each point selected for the scan, a dataset was recorded by sampling one million triggers, with the HPTDC operated in high-resolution mode. It is not possible to investigate the drop in performance while operating the HPTDC in very-high-resolution mode because only one every two NINO channels is accessible in this configuration. The hits registered by the disabled channels are lost, so it is not possible to determine the registered hits as a percentage of the total number of triggers.

Comparing the data collected across the tube in the high-resolution mode, one notices a drop in the number of hits registered as a percentage of the total number of triggers. The number of hits registered across the horizontal scan corresponds to $\sim 14\%$, $\sim 9\%$ and $\sim 8\%$, $\sim 14\%$ of the total number of triggers respective to the four chosen light spot positions. Furthermore, there is a non-conservation of the qualitative shape of the cluster across the

illuminated MCP-PMT pixels. The first point suggests a localised drop in quantum efficiency, while the second highlights the possibility of a gain decrease. Figure 5.29 shows the hits registered by the MCP-PMT pixels illuminated by the light spot, across the points chosen for the scan. This analysis was the motivation for further quantum efficiency and gain measurements of the tube. Subsequent studies undertaken by the TORCH collaboration have shown that the quantum efficiency is uniform across the MCP-PMT with a variation of quantum efficiency between different positions of $\sim 3\%$.

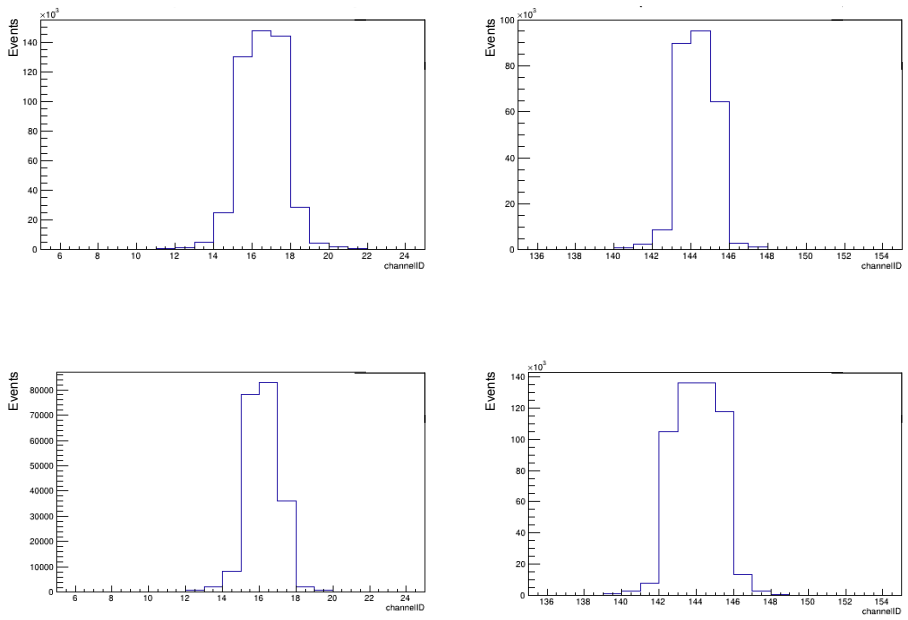

Figure 5.29: Hits registered by the MCP-PMT pixels in the vicinity of where the focused light spot is placed. The light spot spreads over four pixels and was centred on the coordinates (48.410, 14.904) (top left), (35.162, 14.904) (top right), (21.914, 14.904) (bottom left) and (8.666, 14.904) (bottom right), where the origin is a the top right corner of the tube. The data was processed by the HPTDC operating in high-resolution mode.

5.9.4 Single photon time resolution of a Phase III MCP-PMT coupled to the readout electronics

The measurement of the single photon time resolution of the MCP-PMT coupled to the readout electronics is performed by using the test stand in the collimated laser light configuration. The laser spot has a diameter of 20µm, and it can be centred on a specific MCP-PMT pixel using the translation stage. This measurement was first performed on the pixel at coordinates (48.4,14.9), where the (0,0) point is at the top right corner of the tube. One million events were taken with a pulsed laser light frequency of 2 kHz and an attenuation of 20 dB, the MCP-PMT operating at a gain of $\mathcal{O}(10^6)$, and the HPTDC operating in high-resolution mode. The raw data was corrected for INL effects, with corrections extrapolated from the diffused light calibration sample of 20 million events described in paragraph 5.9.2. The leading edge distributions of the raw data events and of the INL corrected events were fitted with Gaussian functions, as illustrated in figure 5.30, to estimate the single photon time resolution. The functions have standard deviations of (121.0 ± 0.005) ps and(104.0 ± 0.005) ps, respectively. The fit range does not cover the tail of the distribution as it is skewed by the relaxation pulse of the laser and by electron back-scattering from the MCP-PMT input face.

Triggered events with constant time-over-threshold values are assumed to have constant amplitude to first order, and were selected to eliminate time-walk effects from the measurement of the single photon time resolution. The leading edge distribution of the events was fitted with a Gaussian function, as illustrated in figure 5.30, to estimate the single photon time resolution. The function has a standard deviation of (78.0 ± 0.01) ps, which approaches the 50 ps goal for the TORCH detector.

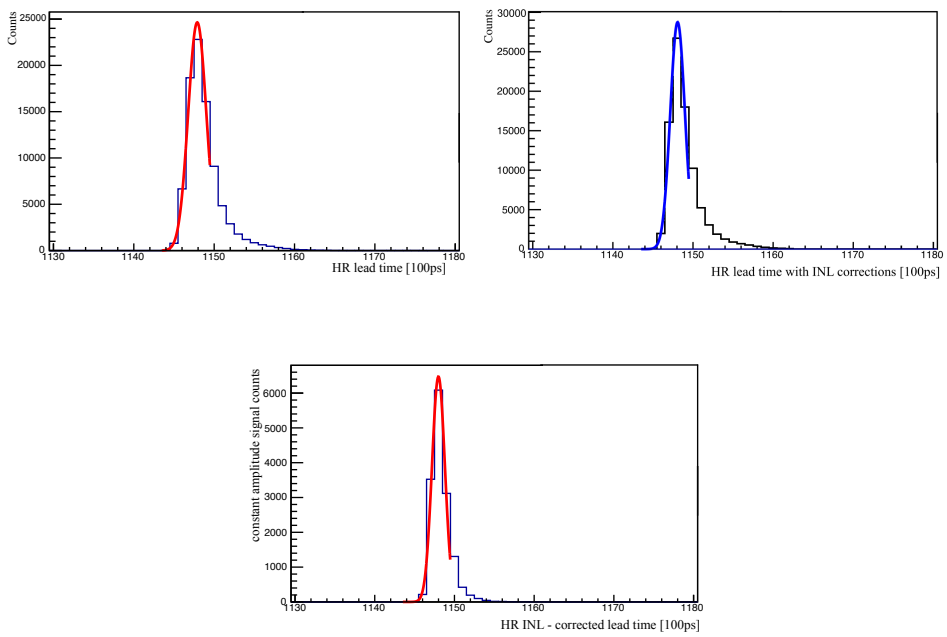

Figure 5.30: Distribution of the leading edge of raw data (left), INL corrected data (right) and constant amplitude signals selected from INL corrected data (bottom), taken with the HPTDC operating in high-resolution mode. The distributions are fitted with a Gaussian PDF, as described in section 5.9.4, to extract the single photon time resolution of the MCP-PMT coupled to the readout electronics.

The same procedure was repeated with the HPTDC operating in very-high-resolution mode. In this case, the INL corrections were calculated from a diffused light sample also collected in very-high-resolution mode. This improves the accuracy of the INL corrections. A dataset containing 10 million events was collected in the focused light setup of the test stand, with the laser light pointing at the same pixel as the one used for the previous study, (48.4,14.9). The measured resolutions from the fit of a Gaussian PDF to the raw, INL-corrected, and constant amplitude INL-corrected samples are respectively (108.750 ± 0.005) ps, (63.25 ± 0.01) ps and (47.50 ± 0.03) ps. The latter measurement is below the TORCH goal of 50 ps. The Gaussian fits to the INL-corrected data and to constant amplitude signals selected from INL corrected data are shown in figure 5.31.

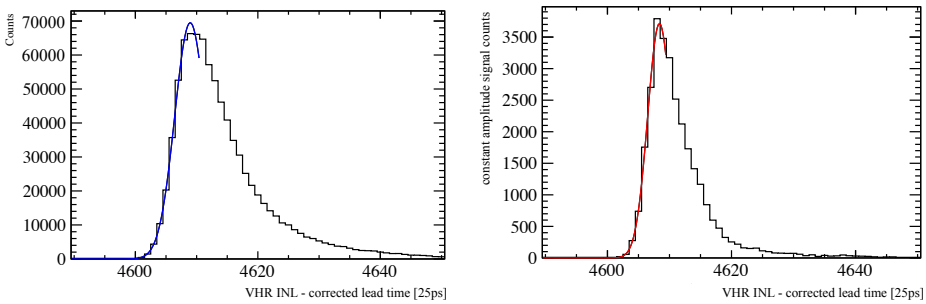

Figure 5.31: Distribution of the leading edge of INL-corrected data (left) and of constant amplitude signals selected from INL corrected data (right), taken with the HPTDC operating in very-high-resolution mode. The distributions are fitted with a Gaussian PDF, as described in section 5.9.4, to extract the single photon time resolution of the MCP-PMT coupled to the readout electronics.

5.9.5 Single photon time resolution of a Phase III MCP-PMT

The single photon time resolution of the Phase III MCP-PMT A2170504 was also measured using the test stand. It was mounted with the analogue breakout board instead of the readout electronics described in section 5.3.3, a fast amplifier, a Constant Fraction Discriminator (CFD), a Time to Amplitude Converter (TAC) and a Multi-Channel Buffer (MCB). The breakout board reads the four vertically adjacent MCP-PMT channels illuminated by the 20 µm laser light spot. The MCP-PMT signal is amplified by the fast amplifier and passed to the CFD. The TAC receives a trigger signal from the laser and a stop signal from the CFD. The TAC'S output signal is sent to the MCB and then to a DAQ PC, as visible in figure 5.32. A photo of the breakout board is visible in figure 5.33. The TAC can be operated with the a time difference between the start and stop signals within the ranges 200 ns, 100 ns and 50 ns, which correspond respectively to TAC time resolutions of 25 ps, 12.5 ps and 6.5 ps. The first TAC time range is comparable to the HPTDC's very-high-resolution mode. The second TAC time range is comparable to the picoTDC [195], the chip identified for future TORCH readout electronics developments, when used in 12 ps bin mode. The CFD corrects signals for amplitude variation, eliminating time-walk effects. This ensures that the comparison between the single photon time resolution measured in section 5.9.4 and the one measured this the set-up described here is sensible.

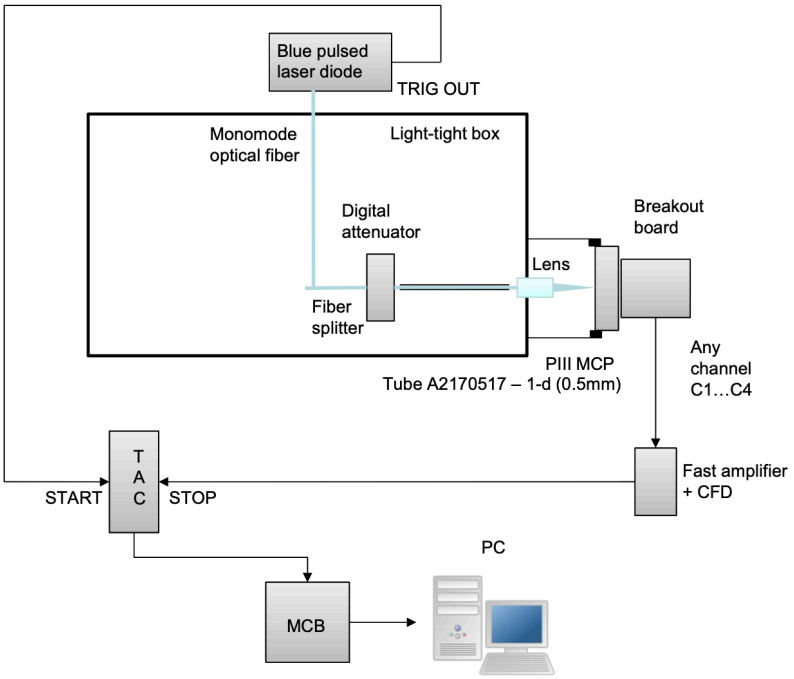

Figure 5.32: Illustration of the test stand configuration when taking analogue time resolution measurements. In this configuration a breakout board carries the signal from four vertically adjacent MCP-PMT channels to a Constant Fraction Discriminator (CFD), whose output corresponds to the stop signal of a Time to Analogue Converter (TAC) that takes the laser trigger as a start signal.

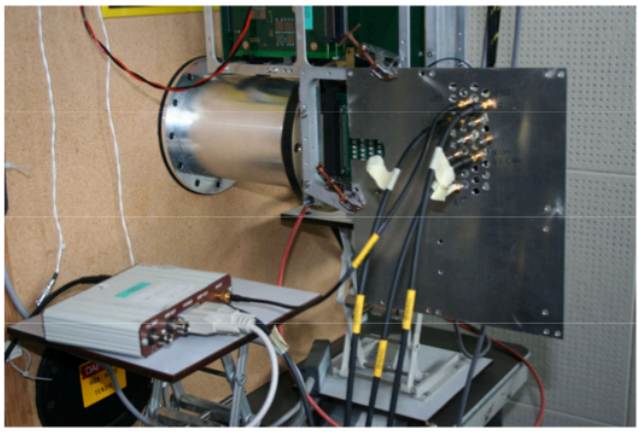

Figure 5.33: Photo of the analogue breakout board connected to the MCP-PMT output.

Data was taken with the light spot centred at coordinates (48.4, 14.9), with a laser light attenuation of 20 dB and the three TAC time ranges of 200 ns, 100 ns and 50 ns. For the three datasets, the data taken from each of the four vertically adjacent MCP-PMT channels shows three features: the primary peak which stems from the time jitter corresponding to the resolution of the set-up, a tail due to the laser relaxation pulse, and a tail caused by backscattering. Each primary peak was fitted with a Gaussian to extract the single photon time resolution. Figure 5.34 is provided as an example to show the fit to data taken with the TAC time range 50 ns. The extracted time resolution per channel, per TAC setting, is available in table 5.1. It is below the TORCH goal of 50 ps in all cases, and compatible with the test stand measurement of the MCP-PMT coupled to the readout electronics reported in section 5.9.4 when the HPTCP is operated in the very-high-resolution mode. One should note that the single photon time resolution of the central pixels is $\mathcal{O}(30\,\text{ps})$, which is the same order of magnitude as the MCP-PMT's intrinsic single photon time resolution. This set-up measures values approaching the minimum possible single photon time resolution of the system.

Table 5.1: Single photon time resolutions extracted for four vertically adjacent MCP-PMT channels using the analogue breakout board, for different TAC time ranges, with the light spot centred at coordinates (48.410, 14.904), with a laser light attenuation of 20 dB, an MCP-PMT HV of 3.0 kV.

	TAC range = 200 ns	TAC range = 100 ns	TAC range = 50 ns
Ch1	49.5 ± 0.5 ps	45.7 ± 0.6 ps	42.8 ± 0.6 ps
Ch2	44.93 ± 0.5 ps	32.9 ± 0.5 ps	35.6 ± 0.4 ps
Ch3	34.2 ± 0.3 ps	34.2 ± 0.4 ps	33.3 ± 0.4 ps
Ch4	48.7 ± 0.8 ps	48.7 ± 0.8 ps	47.6 ± 0.9 ps

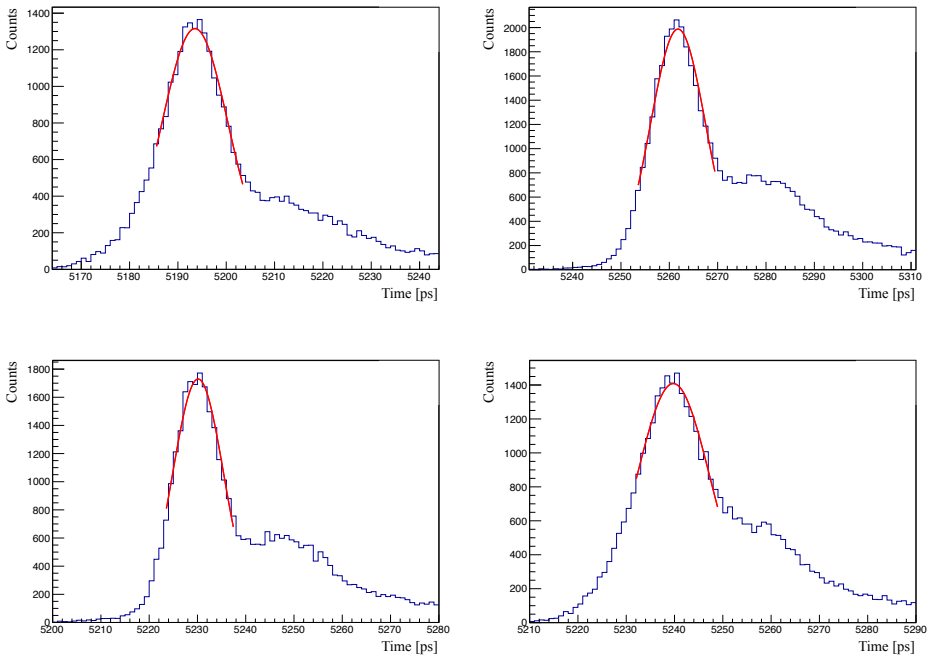

Figure 5.34: From left to right, top to bottom, data from channels 1-4 with light spot centred at coordinates (48.4, 14.9) for single photon analogue measurement described in section 5.9.5. The TAC time range was set to 50 ns, with a time resolution comparable to the picoTDC chip planned for future TORCH readout electronics when operated in 12 ps time bin mode. Channels 1 and 4 are peripheral, channels 2 and 3 are central. The data in all channels presents a primary peak, a laser relaxation pulse, and a backscattering tail. The primary peak was fitted with a Gaussian function to extract the single-photon time resolution.

5.9.6 Gain measurement of a Phase III MCP-PMT

The gain of the Phase III MCP-PMT was measured by connecting the analogue breakout board to a digital oscilloscope. The test stand configuration for the measurement of the gain of the tube is shown in figure 5.35. A screen-shot of the display of the oscilloscope during data-taking is available in figure 5.36.

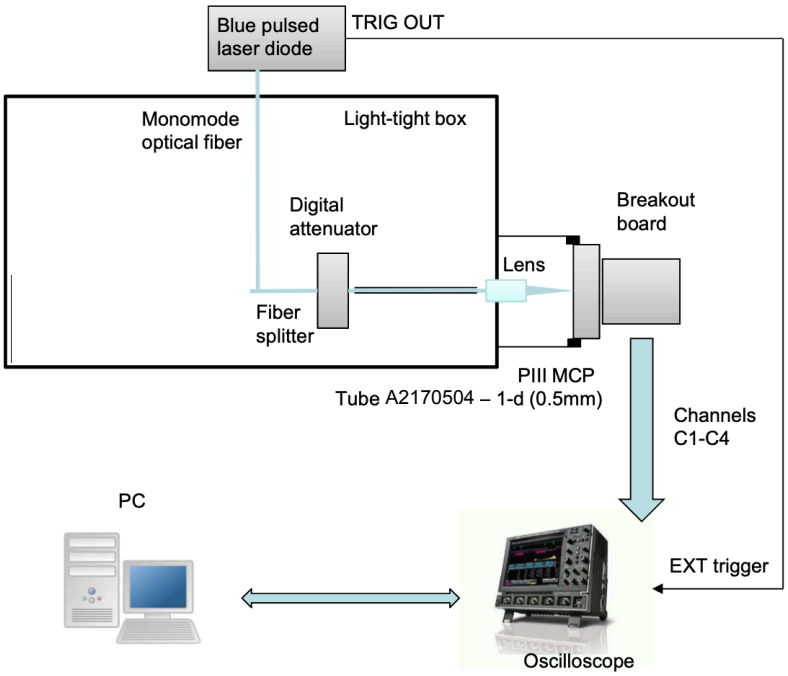

Figure 5.35: Illustration of the test stand configuration when taking analogue gain measurements. In this configuration a breakout board carries the signal from four adjacent MCP-PMT channels to a digital oscilloscope.

Data was taken at coordinate (8.7, 14.9) for two different MCP-PMT HV settings: 2.95 kV and 3 kV; and for three different levels of laser light attenuation: 11 dB, 14 dB and 17 dB. The data collected in each configuration was fitted with a PDF defined as:

$$PDF = \frac{e^{-\mu}}{\sqrt{2\pi}} \sum_{i=0}^{2} \left(\frac{\mu^i}{i!\sigma_i} e^{\frac{-(x-x_i)^2}{2\sigma_i^2}} \right) , \tag{5.18}$$

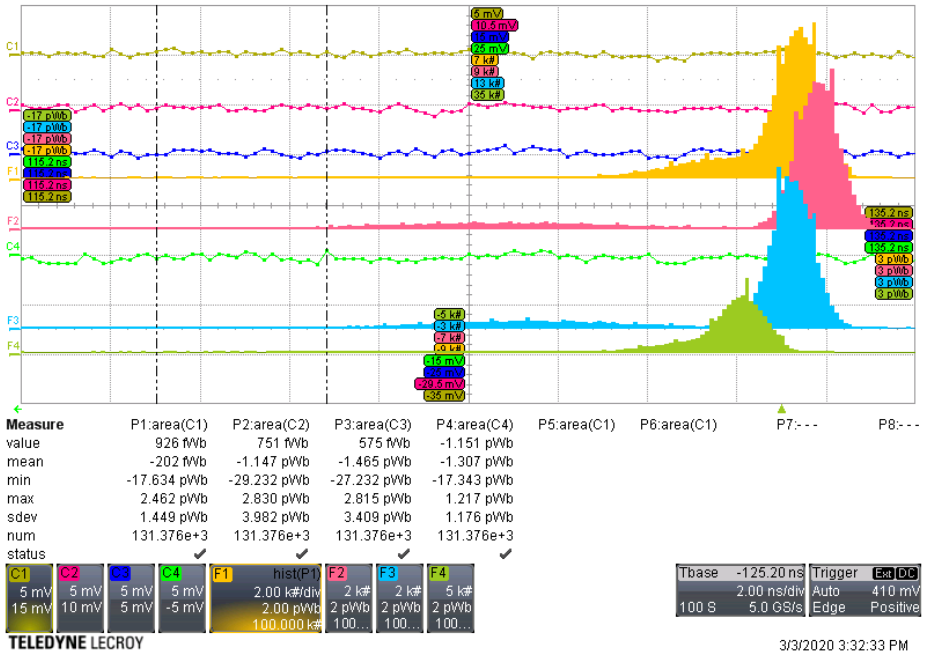

Figure 5.36: A screen-shot of the oscilloscope display while taking MCP-PMT data using the focused laser light configuration. The laser light experiences a 17 dB attenuation. The MCP-PMT is set at a high voltage of 3 kV. The data points C1-C4 are the signals received from the breakout board taken by four vertically adjacent pixels. C1 and C4 are the two peripheral pixels, while C2 and C3 are the central pixels. The distributions F1-F4 are the accumulated charges per pixel over time.

where the following dependencies hold:

$$\sigma_1 = k\sigma_0, \quad \sigma_2 = \sqrt{2}\sigma_1, \quad \sigma_3 = \sqrt{3}\sigma_1,$$
$$x_1 = x_0 + \Delta x, \quad x_2 = x_0 + 2(x_1 - x_0),$$
$$x_3 = x_0 + 3(x_1 - x_0),$$

and k is a proportionality constant greater than 1. This models the Poissonian nature of the photoelectron conversion. In the PDF, each photoelectron is modelled as a Gaussian distribution to account for resolution effects. The PDF models the pedestal and the first two photoelectron peaks. As an example, the fits to data from four channels, with settings 3 kV, 17 dB, is shown in figure 5.37. The integrated charge and the Poissonian mean per channel are extrapolated. The charge is a function of the difference along the x axis of the pedestal and photoelectron peaks' positions (Δx), and of the terminator

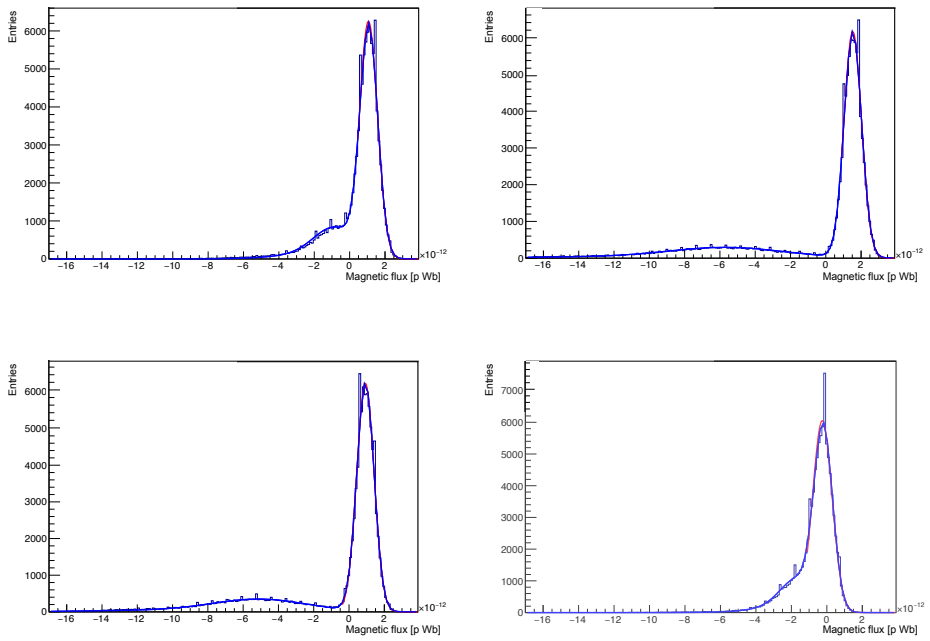

Figure 5.37: Magnetic flux measured by the oscilloscope of signal from four vertically adjacent MCP-PMT pixels, fit with the function described in equation 5.18. Each plot presents the pedestal peak at values $\sim 2\,\text{pWb}$, which is followed but the photoelectron peaks as the flux decreases. Due to a binning effect, the oscilloscope introduces artefacts periodically in the datasets. To first approximation these do not affect the fit.

resistance on the oscilloscope, $Q = \Delta x/50\Omega$. The charges deposited in each channel from a set of four are summed to obtain the total charge deposited by the laser pulse. The Poissonian mean per channel is averaged across the set of four channels to obtain the average Poissonian mean. These are used to extract the gain of the Phase III MCP-PMT for the different laser light attenuations and for different HV values. The results are shown in tables 5.2 and 5.3. In single photon data-taking conditions, at 17 dB laser light attenuation, the measured gain corresponds to 2.06 $\times 10^6$ and 1.68×10^6 at 3.00 kV and 2.95 kV respectively. Ideally the TORCH needs a gain of order 1.0×10^6, so the MCP-PMT HV can be lowered to 2.95 kV or beyond for future operations.

Table 5.2: Total charge and average gain for MCP-PMT opertated at HV = 2.95 kV

Attenuation	Average μ	Total charge	Average Gain
11 dB	0.74	278.8 fC	1.74×10^6
14 dB	0.53	272.4 fC	1.70×10^6
17 dB	0.27	269.4 fC	1.68×10^6

Table 5.3: Total charge and average gain for MCP-PMT opertated at HV = 3.00 kV

Attenuation	Average μ	Total charge	Average Gain
11 dB	1.17	353.0 fC	2.20×10^6
14 dB	0.61	336.2 fC	2.10×10^6
17 dB	0.31	328.9 fC	2.06×10^6

5.10 Concluding remarks regarding the R&D of the TORCH detector

The TORCH project is at an advanced stage to deliver a TORCH detector. This will be used as a sub-detector in LHCb Upgrade 2 to improve the PID of the LHCb detector. Two prototypes have been built and tested in a test beam multiple times. A stand-alone TORCH simulation has been developed, as well as reconstruction software. The R%D of the TORCH detector presented in this work ranges from simulation studies, to reconstruction efforts, to hardware characterization.

Existing limitations of the current status of the project are addressed. In particular alternative detector geometries are proposed to address the too-high occupancy per MCP-PMT pixel in LHCb Upgrade 2 conditions. It is clear that a focussing block with a larger radius of curvature and a larger focal distance than the nominal ones will enlarge the image, exploiting the whole MCP-PMT area, and reducing the occupancy per pixel. Future work in this direction is needed and will be undertaken by the TORCH collaboration.

An alternative use of the TORCH detector within LHCb is presented and explored: given PID information on charged particles across the 2-100 GeV/c momentum range, TORCH can reconstruct PV timing information. Simulation studies of this scenario result in a PV time resolution of 17.7 ps. Two issues came to light during this simulation study, namely the background introduced by other PVs in the time reconstruction of one PV, and the presence of background photons. The background from other PVs will be reduced by using timing information from the VELO in Upgrade 2. On the other

hand, the presence of background photons prompted an investigation into the possibility of shielding the detector, which was unsuccessful. As long as there is background from photons which are unrelated to the charged track traversing TORCH, the per-track resolution will not improve as the number of Cherenkov photons per track rises.

The work conducted in the TORCH laboratory consists in the characterisation of one of the MCP-PMT prototypes produced for TORCH, and of the custom readout electronics. These studies were carried out after performing the October-November 2018 beam test on the torch prototype proto-TORCH, which measured a single photon time resolution of pion and proton candidates in the ranges [63ps, 112ps] and [65ps, 109ps], respectively. The single photon time resolution components that can be attributed to the MCP-PMT and the readout electronics were measured cumulatively in this work. The cumulative time resolution MCP-PMT and the readout electronics components for INL-corrected, and constant amplitude INL-corrected data samples taken with the HPTDC operating in VHR mode are respectively (63.25 ± 0.01) ps and (47.50 ± 0.03) ps. The former measurement is below the TORCH time resolution measured from beam test data, as expected, and latter measurement is below the TORCH goal of 50 ps. The single photon time resolution of the TORCH MCP-PMT only was also measured to identify a lower limit for the single photon time resolution measurements, which is set by current photon sensor choice. This corresponds to about 35 ps.

While performing the single photon time resolution studies, an inhomogeneity of the MCP-PMT was detected. This was then characterised with diffused light studies. This analysis motivated further quantum efficiency and gain measurements of the tube. In particular, in this work the MCP-PMT's gain was measured as a function of the high voltage. The results of this study are reason to lower the high voltage working point of the TORCH MCP-PMT to increase the device's longevity.

The future of the TORCH project lies in different directions. Firstly, the TORCH simulation software will be improved by adding better modelling of the front end electronics. Secondly, a new time resolution analysis will be performed on the data collected during the November 2022 test beam campaign. This analysis will benefit from the improvements to the calibrations of the readout electronics. Furthermore, more MCP-PMTs will be characterised in the TORCH laboratory by studying their single photon time resolution, gain and quantum efficiency. Looking further in the future, the TROCH

collaboration plans to design a new version of the readout electronics which will include the picoTDC chip to improve the single photon time resolution. This will happen in parallel with the construction of a full-sized TORCH module which will be subjected to beam tests.

Chapter 6

Conclusion

The TORCH detector is a large area time-of-flight detector aiming to provide charged particle separation in the 2–20 GeV/c momentum range over a 10 m flight path, proposed as a future LHCb upgrade. The test beam and laboratory studies of the TORCH time resolution demonstrate good performance which is approaching the TORCH design goals. A full-width, half-height, partially instrumented TORCH prototype module underwent a successful test beam in 2018; a single-photon time resolution that approaches the design goal of 70 ps required to obtain a $10 - 15$ ps per-track timing resolution, was measured. Laboratory studies of the time resolution of the TORCH MCP-PMT and readout electronics complement the test beam results. A measured time resolution of (47.5 ± 0.7) ps shows that TORCH time resolution design goals are achievable. A measurement of the gain as a function of the high voltage of the TORCH MCP-PMT performed in this work is the first calibration-like study of the gain performed by the collaboration. To maximise the lifetime of the MCP-PMTs in TORCH, these should be operated at a gain of $\mathcal{O}(10^6)$. Therefore, this study is essential to find the optimal working point for the TORCH collaboration. The overall characterization of the TORCH MCP-PMT performed in this work is essential to understand the detector, inform design choices and simulation. Simulation studies of the TORCH detector in the LHCb experiment show that TORCH can significantly add to the LHCb physics program by providing efficient pion-kaon and kaon-proton separation in the 2–10 GeV/c and 2–20 GeV/c momentum ranges, respectively. As more data becomes available, more and more analyses of rare decays involving pions can be performed. For these, correct pion and kaon identification is crucial, so the role of the TORCH detector in LHCb will grow in relevance.

An analysis of the angular distribution of the $B^+ \to \pi^+\mu^+\mu^-$ decay performed with LHCb Run 1 and 2 datasets, in the q^2 ranges $[1.1-6.0]\,\mathrm{GeV}^2/c^4$ and $[15.0-22.0]\,\mathrm{GeV}^2/c^4$, is also presented and at an advanced stage. This is the first angular analysis of a $b \to d$ flavour changing neutral current process and will provide interesting constraints of new physics model. All the sources of systematic uncertainties have been identified, and most effects have been evaluated, including those from the most important systematic uncertainty sources. The study of the sources of systematic uncertainty presented in this thesis suggest it would be beneficial to include the background from $B^+ \to \pi^+\pi^-\pi^+$ decays in the two-dimensional simultaneous invariant mass and helicity angle fit. The simulation samples needed to achieve this are currently being produced. It is expected that a paper regarding this analysis will be submitted for publication early next year.

Appendix A

Modelling the efficiency distribution

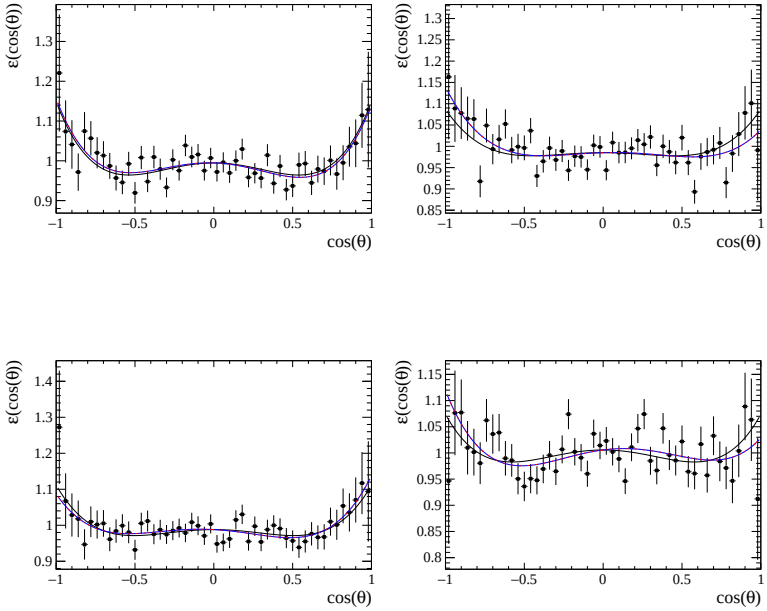

Figure A.1: Efficiency distribution for the $B^+ \to J/\psi(\mu^+\mu^-)K^+$ samples fitted with an ordinary polynomial (blue), a sum of Legendre polynomials (dotted red) and a symmetric sum of Legendre polynomials (black). From left to right: down and up magnet polarities, from top to bottom, 2011 and 2012 data-taking years. .

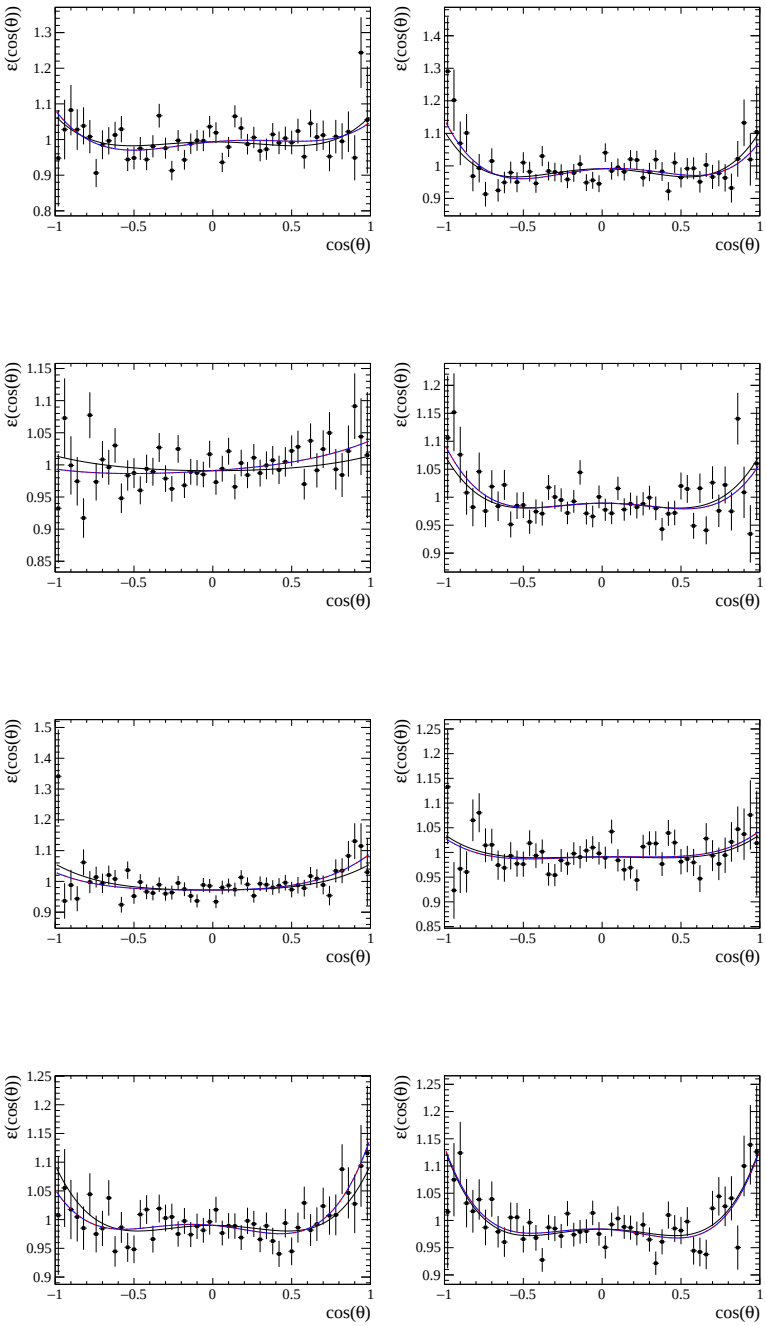

Figure A.2: Efficiency distribution for the $B^+ \to J/\psi(\mu^+\mu^-)K^+$ samples fitted with an ordinary polynomial (blue), a sum of Legendre polynomials (dotted red) and a symmetric sum of Legendre polynomials (black). From left to right: down and up magnet polarities, from top to bottom, 2015, 2016, 2017, 2018 data-taking years. .

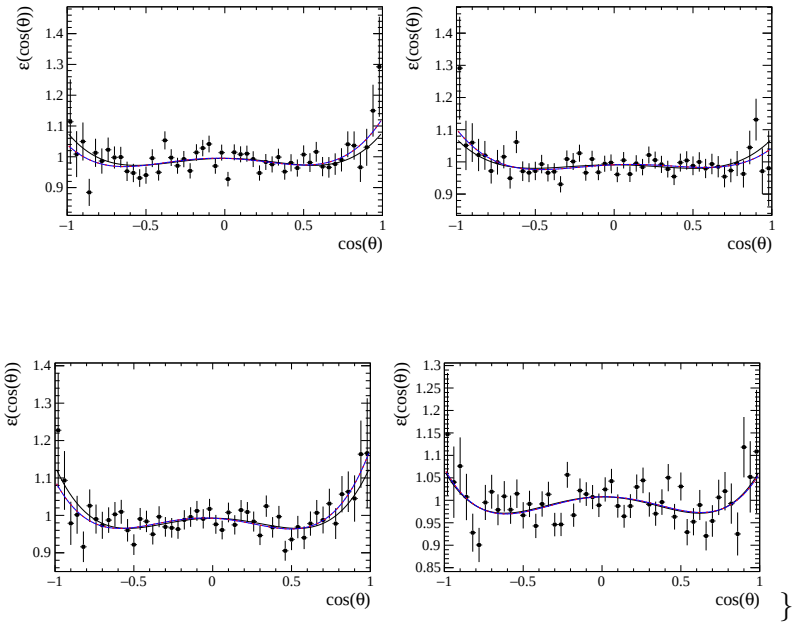

Figure A.3: Efficiency distribution for the $B^+ \to J/\psi(\mu^+\mu^-)\pi^+$ samples fitted with an ordinary polynomial (blue), a sum of Legendre polynomials (dotted red) and a symmetric sum of Legendre polynomials (black). From left to right: down and up magnet polarities, from top to bottom, 2011 and 2012 data-taking years. .

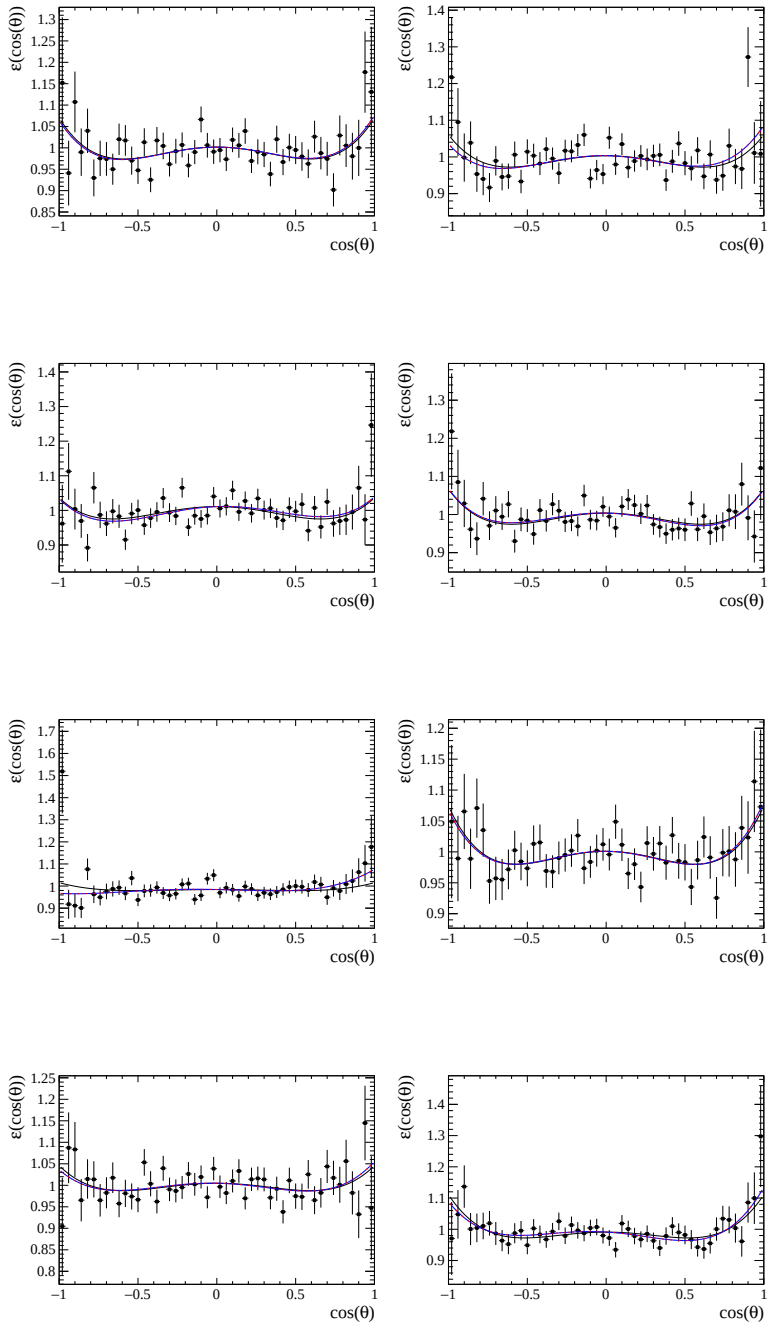

Figure A.4: Efficiency distribution for the $B^+ \to J/\psi(\mu^+\mu^-)\pi^+$ samples fitted with an ordinary polynomial (blue), a sum of Legendre polynomials (dotted red) and a symmetric sum of Legendre polynomials (black). From left to right: down and up magnet polarities, from top to bottom, 2015, 2016, 2017, 2018 data-taking years. .

Appendix B

Efficiency distribution in finer q^2 bins

The variation in the efficiency shape in finer q^2 bins, of 1 GeV^2/c^4 width, is shown in Figs. B.1 and B.2 for the 2017 magnet-up polarity simulation.

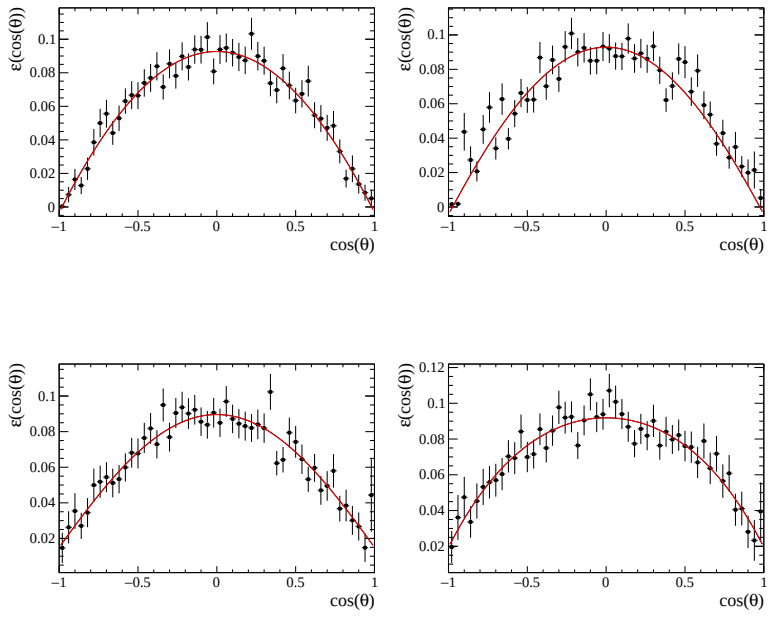

Figure B.1: Selection efficiency from the simulation of the $B^+ \to \pi^+\mu^+\mu^-$ decays for the 2017 magnet polarity Up sample calculated in fine bins of q^2 in the low q^2 region. The efficiency is fitted with a fourth order Legendre polynomial function. From left to right, top to bottom, the q^2 bins are $[1.1 - 2.1]$ GeV^2/c^4, $[2.1 - 3.1]$ GeV^2/c^4, $[3.1 - 4.1]$ GeV^2/c^4 and $[4.1 - 5.1]$ GeV^2/c^4.

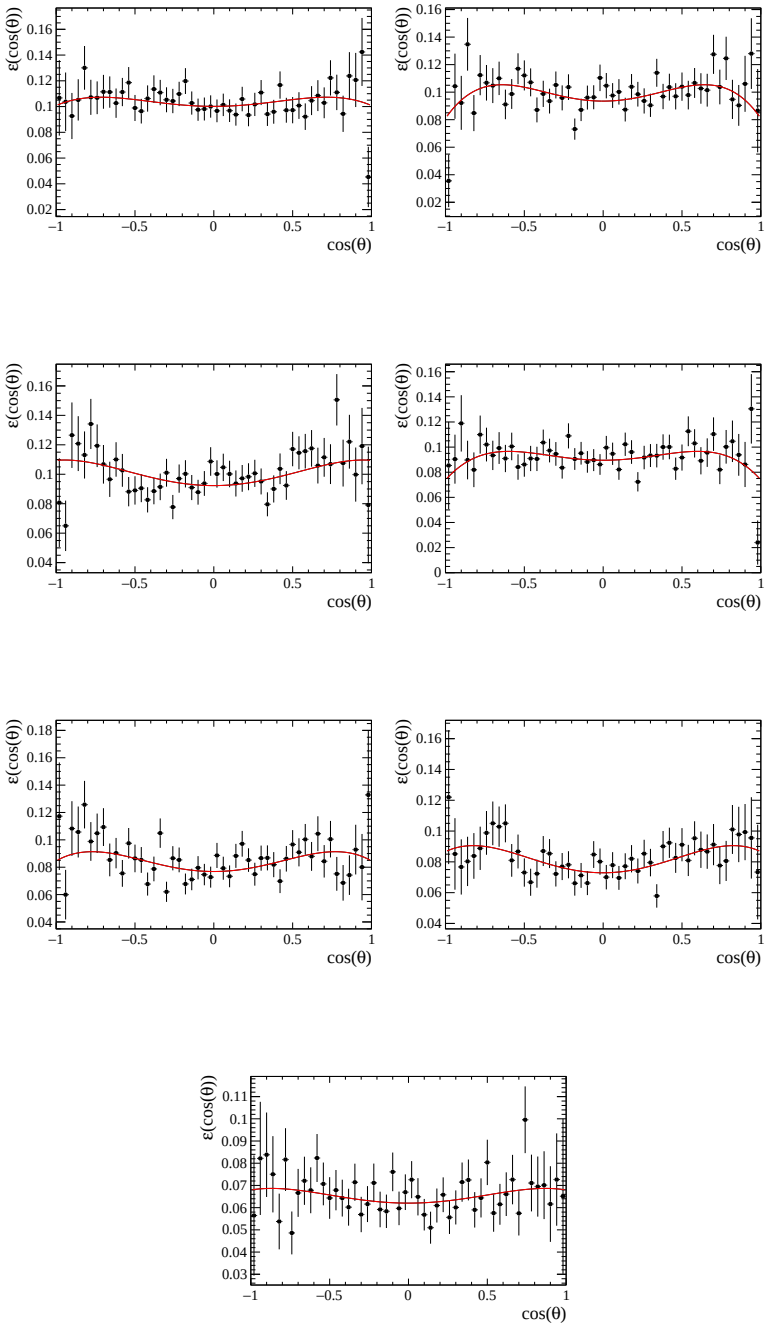

Figure B.2: Selection efficiency from the simulation of the $B^+ \to \pi^+\mu^+\mu^-$ decays for the 2017 magnet polarity Up sample calculated in fine bins of q^2 in the high q^2 region. The efficiency is fitted with a fourth order Legendre polynomial function. From left to right, top to bottom, the q^2 bins are $[15.0 - 16.0]$ GeV^2/c^4, $[16.0 - 17.0]$ GeV^2/c^4, $[17.0 - 18.0]$ GeV^2/c^4, $[18.0 - 19.0]$ GeV^2/c^4, $[19.0 - 20.0]$ GeV^2/c^4, $[20.0 - 21.0]$ GeV^2/c^4 and $[21.0 - 22.0]$ GeV^2/c^4.

Bibliography

[1] LHCb collaboration, R. Aaij *et al.*, *First measurement of the differential branching fraction and CP asymmetry of the* $B^{\pm} \to \pi^{\pm}\mu^{+}\mu^{-}$, J. High Energ. Phys. (2015) 34.

[2] Wikipedia contributors, *Standard model of elementary particles — Wikipedia, the free encyclopedia*, `https://en.wikipedia.org/w/index.php?title=Plagiarism&oldid=5139350`, 2021. [Online; accessed 10/03/2022].

[3] R. P. Feynman and M. Gell-Mann, *Theory of Fermi interaction*, Phys. Rev. **109** (1958) 193.

[4] LHCb collaboration, R. Aaij *et al.*, *Observation of the resonant character of the* $Z(4430)^{-}$ *state*, Phys. Rev. Lett. **112** (2014) 222002, `arXiv:1404.1903`.

[5] LHCb collaboration, R. Aaij *et al.*, *Observation of* $J/\psi p$ *Resonances Consistent with Pentaquark States in* $\Lambda_b^0 \to J/\psi K^{-} p$ *Decays*, Phys. Rev. Lett. **115** (2015) 072001, `arXiv:1507.03414`.

[6] F. Halzen and A. D. Martin, *, Quark & Leptons: An Introductory Course In Modern Particle Physics*, John Wiley and Sons, 1991.

[7] S. L. Glashow, *Partial-symmetries of weak interactions*, Nuclear Physics **22** (1961) 579.

[8] S. Weinberg, *A model of leptons*, Phys. Rev. Lett. **19** (1967) 1264.

[9] A. Salam, *Weak and Electromagnetic Interactions*, Conf. Proc. C **680519** (1968) 367.

[10] P. W. Higgs, *Broken symmetries and the masses of gauge bosons*, Phys. Rev. Lett. **13** (1964) 508.

[11] F. Englert and R. Brout, *Broken symmetry and the mass of gauge vector mesons*, Phys. Rev. Lett. **13** (1964) 321.

[12] G. S. Guralnik, C. R. Hagen, and T. W. B. Kibble, *Global conservation laws and massless particles*, Phys. Rev. Lett. **13** (1964) 585.

[13] D. J. Griffiths, *Introduction to elementary particles*, Wiley-VCH, 2020.

[14] C. S. Wu *et al.*, *Experimental test of parity conservation in beta decay*, Phys. Rev. **105** (1957) 1413.

[15] J. H. Christenson, J. W. Cronin, V. L. Fitch, and R. Turlay, *Evidence for the* 2π *Decay of the* K_2^0 *Meson*, Phys. Rev. Lett. **13** (1964) 138.

[16] Particle Data Group, M. Tanabashi *et al.*, *Review of particle physics*, Phys. Rev. D **98** (2018) 030001.

[17] HFLAV collaboration, Y. S. Amhis *et al.*, *Averages of b-hadron, c-hadron, and* τ*-lepton properties as of 2018*, Eur. Phys. J. C **81** (2021) 226, `arXiv:1909.12524`.

[18] BABAR Collaboration, B. Aubert *et al.*, *Observation of CP violation in the* B^0 *meson system*, Phys. Rev. Lett. **87** (2001) 091801.

[19] Belle Collaboration, K. Abe *et al.*, *Observation of large CP violation in the neutral B meson system*, Phys. Rev. Lett. **87** (2001) 091802.

[20] LHCb collaboration, R. Aaij *et al.*, *Observation of CP Violation in Charm Decays*, Phys. Rev. Lett. **122** (2019) 211803, `arXiv:1903.08726`.

[21] Particle Data Group, P. A. Zyla *et al.*, *Review of Particle Physics*, PTEP **2020** (2020) 083C01.

[22] *Precision electroweak measurements on the z resonance*, Physics Reports **427** (2006) 257.

[23] *Electroweak measurements in electron–positron collisions at w-boson-pair energies at lep*, Physics Reports **532** (2013) 119, Electroweak Measurements in Electron-Positron Collisions at W-Boson-Pair Energies at LEP.

[24] PIENU Collaboration, A. Aguilar-Arevalo *et al.*, *Improved measurement of the* $\pi \to e\nu$ *branching ratio*, Phys. Rev. Lett. **115** (2015) 071801.

[25] C. Lazzeroni, A. Romano *et al.*, *Precision measurement of the ratio of the charged kaon leptonic decay rates*, Physics Letters B **719** (2013) 326.

[26] KEDR collaboration, V. M. Aulchenko *et al.*, *Measurement of the ratio of the leptonic widths* $\Gamma_{ee}/\Gamma_{\mu\mu}$ *for the* J/ψ *meson*, Phys. Lett. B **731** (2014) 227, arXiv:1311.5005.

[27] P. W. Higgs, *Broken symmetries, massless particles and gauge fields*, Phys. Lett. **12** (1964) 132.

[28] P. W. Higgs, *Broken Symmetries and the Masses of Gauge Bosons*, Phys. Rev. Lett. **13** (1964) 508.

[29] G. S. Guralnik, C. R. Hagen, and T. W. B. Kibble, *Global Conservation Laws and Massless Particles*, Phys. Rev. Lett. **13** (1964) 585.

[30] J. Ellis, M. K. Gaillard, and D. V. Nanopoulos, in *A Historical Profile of the Higgs Boson*, L. Maiani and L. Rolandi, eds., pp. 255–274, 2016. arXiv:1504.07217.

[31] Y. Sofue and V. Rubin, *Rotation curves of spiral galaxies*, Ann. Rev. Astron. Astrophys. **39** (2001) 137, arXiv:astro-ph/0010594.

[32] R. Massey, T. Kitching, and J. Richard, *The dark matter of gravitational lensing*, Reports on Progress in Physics **73** (2010) 086901.

[33] SNO Collaboration, Q. R. Ahmad *et al.*, *Direct evidence for neutrino flavor transformation from neutral-current interactions in the sudbury neutrino observatory*, Phys. Rev. Lett. **89** (2002) 011301.

[34] K. Zuber, *Neutrino physics: Second edition*, CRC Press, Taylor et Franics Group, 2020.

[35] A. D. Sakharov, *Violation of CP Invariance, C asymmetry, and baryon asymmetry of the universe*, Pisma Zh. Eksp. Teor. Fiz. **5** (1967) 32.

[36] L. Canetti, M. Drewes, and M. Shaposhnikov, *Matter and antimatter in the universe*, New Journal of Physics **14** (2012) 095012.

[37] C. A. Baker *et al.*, *An Improved experimental limit on the electric dipole moment of the neutron*, Phys. Rev. Lett. **97** (2006) 131801, arXiv:hep-ex/0602020.

[38] C. Csáki and P. Tanedo, *Beyond the Standard Model*, in *2013 European School of High-Energy Physics*, 169–268, 2015, arXiv:1602.04228.

[39] A. Ereditato, T. Kajita, and A. Masiero, *Focus on particle physics at the TeV scale*, New Journal of Physics **9** (2007) .

[40] M. Kobayashi and T. Maskawa, *CP Violation in the Renormalizable Theory of Weak Interaction*, Prog. Theor. Phys. **49** (1973) 652.

[41] N. Cabibbo, *Unitary Symmetry and Leptonic Decays*, Phys. Rev. Lett. **10** (1963) 531.

[42] L.-L. Chau and W.-Y. Keung, *Comments on the Parametrization of the Kobayashi-Maskawa Matrix*, Phys. Rev. Lett. **53** (1984) 1802.

[43] A. Buras, *Gauge Theory of Weak Decays*, Cambridge University Press, 2020.

[44] Particle Data Group, C. Patrignani *et al.*, *Review of particle physics*, Chin. Phys. **C40** (2016) 100001.

[45] CKMfitter Group, J. Charles *et al.*, *CP violation and the CKM matrix: Assessing the impact of the asymmetric B factories*, Eur. Phys. J. C **41** (2005) 1, arXiv:hep-ph/0406184.

[46] S. L. Glashow, J. Iliopoulos, and L. Maiani, *Weak Interactions with Lepton-Hadron Symmetry*, Phys. Rev. D **2** (1970) 1285.

[47] S. L. Glashow, J. Iliopoulos, and L. Maiani, *Weak interactions with lepton-hadron symmetry*, Phys. Rev. D **2** (1970) 1285.

[48] LHCb collaboration, R. Aaij *et al.*, *First observation of the decay $B^+ \to \pi^+\mu^+\mu^-$*, JHEP **12** (2012) 125, arXiv:1210.2645.

[49] Particle Data Group, R. L. Workman, *Review of Particle Physics*, PTEP **2022** (2022) 083C01.

[50] H. Georgi, *Effective field theory*, Annual Review of Nuclear and Particle Science **43** (1993) 209, arXiv:https://doi.org/10.1146/annurev.ns.43.120193.001233.

[51] T. Blake *et al.*, *Rare b hadron decays at the LHC*, Annu. Rev. Nucl. Part. Sci. **65** (2015) 113.

[52] R. Alonso, B. Grinstein, and J. Martin Camalich, *$SU(2) \times U(1)$ gauge invariance and the shape of new physics in rare B decays*, Phys. Rev. Lett. **113** (2014) 241802, arXiv:1407.7044.

[53] G. Hiller and M. Schmaltz, *R_K and future $b \to s\ell\ell$ physics beyond the standard model opportunities*, Phys. Rev. D **90** (2014) 054014, arXiv:1408.1627.

[54] P. J. Fox *et al.*, *Deciphering top flavor violation at the LHC with B factories*, Phys. Rev. D **78** (2008) 054008, arXiv:0704.1482.

[55] M. Beneke, T. Feldmann, and D. Seidel, *Systematic approach to exclusive $B \to Vl^+l^-$, $V\gamma$ decays*, Nucl. Phys. B **612** (2001) 25, arXiv:hep-ph/0106067.

[56] B. Grinstein and D. Pirjol, *Exclusive rare $B \to K^*\ell^+\ell^-$ decays at low recoil: Controlling the long-distance effects*, Phys. Rev. D **70** (2004) 114005, arXiv:hep-ph/0404250.

[57] C. Bobeth, G. Hiller, and G. Piranishvili, *Angular distributions of $\bar{B} \to \bar{K}\ell^+\ell^-$ decays*, JHEP **12** (2007) 040, arXiv:0709.4174.

[58] A. Ali, P. Ball, L. T. Handoko, and G. Hiller, *A Comparative study of the decays $B \to (K, K^*)\ell^+\ell^-$ in standard model and supersymmetric theories*, Phys. Rev. D **61** (2000) 074024, arXiv:hep-ph/9910221.

[59] C. Bobeth, G. Hiller, and D. van Dyk, *General analysis of $\bar{B} \to \bar{K}^{(*)}\ell^+\ell^-$ decays at low recoil*, Phys. Rev. D **87** (2013) 034016, arXiv:1212.2321.

[60] G. Kumar and N. Mahajan, *$B \to K^*l^+l^-$: Zeroes of angular observables as test of standard model*, Phys. Rev. D **93** (2016) 054041, arXiv:1412.2955.

[61] F. Beaujean, C. Bobeth, and S. Jahn, *Constraints on tensor and scalar couplings from $B \to K\bar{\mu}\mu$ and $B_s \to \bar{\mu}\mu$*, Eur. Phys. J. C **75** (2015) 456, arXiv:1508.01526.

[62] S. Descotes-Genon, J. Matias, M. Ramon, and J. Virto, *Implications from clean observables for the binned analysis of $B \to K^*\mu^+\mu^-$ at large recoil*, JHEP **01** (2013) 048, arXiv:1207.2753.

[63] M. Beneke, C. Bobeth, and R. Szafron, *Power-enhanced leading-logarithmic QED corrections to $B_q \to \mu^+\mu^-$*, JHEP **10** (2019) 232, arXiv:1908.07011.

[64] ATLAS collaboration, M. Aaboud *et al.*, *Study of the rare decays of B_s^0 and B^0 mesons into muon pairs using data collected during 2015 and 2016 with the ATLAS detector*, JHEP **04** (2019) 098, arXiv:1812.03017.

[65] CMS collaboration, A. M. Sirunyan *et al.*, *Measurement of properties of $B_{\mathrm{s}}^0 \to \mu^+\mu^-$ decays and search for $B^0 \to \mu^+\mu^-$ with the CMS experiment*, JHEP **04** (2020) 188, arXiv:1910.12127.

[66] LHCb collaboration, R. Aaij *et al.*, *Measurement of the $B_s^0 \to \mu^+\mu^-$ branching fraction and effective lifetime and search for $B^0 \to \mu^+\mu^-$ decays*, Phys. Rev. Lett. **118** (2017) 191801, arXiv:1703.05747.

[67] ATLAS collaboration, *Combination of the ATLAS, CMS and LHCb results on the $B_{(s)}^0 \to \mu^+\mu^-$ decays*, .

[68] LHCb collaboration, R. Aaij *et al.*, *Analysis of Neutral B-Meson Decays into Two Muons*, Phys. Rev. Lett. **128** (2022) 041801, arXiv:2108.09284.

[69] LHCb collaboration, R. Aaij *et al.*, *Measurement of the $B_s^0 \to \mu^+\mu^-$ decay properties and search for the $B^0 \to \mu^+\mu^-$ and $B_s^0 \to \mu^+\mu^-\gamma$ decays*, Phys. Rev. D **105** (2022) 012010, arXiv:2108.09283.

[70] LHCb collaboration, R. Aaij *et al.*, *Differential branching fractions and isospin asymmetries of $B \to K^{(*)}\mu^+\mu^-$ decays*, JHEP **06** (2014) 133, arXiv:1403.8044.

[71] LHCb collaboration, R. Aaij *et al.*, *Differential branching fraction and angular analysis of the decay $B^0 \to K^{*0}\mu^+\mu^-$*, Phys. Rev. Lett. **108** (2012) 181806, arXiv:1112.3515.

[72] CMS collaboration, S. Chatrchyan *et al.*, *Angular Analysis and Branching Fraction Measurement of the Decay $B^0 \to K^{*0}\mu^+\mu^-$*, Phys. Lett. B **727** (2013) 77, arXiv:1308.3409.

[73] LHCb collaboration, R. Aaij *et al.*, *Angular analysis and differential branching fraction of the decay $B_s^0 \to \phi\mu^+\mu^-$*, JHEP **09** (2015) 179, arXiv:1506.08777.

[74] CDF collaboration, T. Aaltonen *et al.*, *Observation of the Baryonic Flavor-Changing Neutral Current Decay* $\Lambda_b \to \Lambda\mu^+\mu^-$, Phys. Rev. Lett. **107** (2011) 201802, arXiv:1107.3753.

[75] LHCb collaboration, R. Aaij *et al.*, *Measurement of the differential branching fraction of the decay* $\Lambda_b^0 \to \Lambda\mu^+\mu^-$, Phys. Lett. B **725** (2013) 25, arXiv:1306.2577.

[76] S. Descotes-Genon, L. Hofer, J. Matias, and J. Virto, *Global analysis of* $b \to s\ell\ell$ *anomalies*, JHEP **06** (2016) 092, arXiv:1510.04239.

[77] M. Bordone, G. Isidori, and A. Pattori, *On the Standard Model predictions for* R_K *and* R_{K^*}, Eur. Phys. J. C **76** (2016) 440, arXiv:1605.07633.

[78] B. Capdevila, S. Descotes-Genon, J. Matias, and J. Virto, *Assessing lepton-flavour non-universality from* $B \to K^*\ell\ell$ *angular analyses*, JHEP **10** (2016) 075, arXiv:1605.03156.

[79] A. Bharucha, D. M. Straub, and R. Zwicky, $B \to V\ell^+\ell^-$ *in the Standard Model from light-cone sum rules*, JHEP **08** (2016) 098, arXiv:1503.05534.

[80] W. Altmannshofer, C. Niehoff, P. Stangl, and D. M. Straub, *Status of the* $B \to K^*\mu^+\mu^-$ *anomaly after Moriond 2017*, Eur. Phys. J. C **77** (2017) 377, arXiv:1703.09189.

[81] S. Jäger and J. Martin Camalich, *Reassessing the discovery potential of the* $B \to K^*\ell^+\ell^-$ *decays in the large-recoil region: SM challenges and BSM opportunities*, Phys. Rev. D **93** (2016) 014028, arXiv:1412.3183.

[82] LHCb collaboration, R. Aaij *et al.*, *Test of lepton universality in beauty-quark decays*, Nature Phys. **18** (2022) 277, arXiv:2103.11769.

[83] LHCb collaboration, R. Aaij *et al.*, *Test of lepton universality with* $B^0 \to K^{*0}\ell^+\ell^-$ *decays*, JHEP **08** (2017) 055, arXiv:1705.05802.

[84] W. Altmannshofer and P. Stangl, *New physics in rare B decays after Moriond 2021*, Eur. Phys. J. C **81** (2021) 952, arXiv:2103.13370.

[85] HFLAV collaboration, Y. Amhis *et al.*, *Averages of b-hadron, c-hadron, and* τ*-lepton properties as of 2021*, arXiv:2206.07501.

[86] LHCb collaboration, R. Aaij *et al.*, *Angular Analysis of the $B^+ \to K^{*+}\mu^+\mu^-$ Decay*, Phys. Rev. Lett. **126** (2021) 161802, arXiv:2012.13241.

[87] W. Altmannshofer and P. Stangl, *New physics in rare B decays after Moriond 2021*, Eur. Phys. J. C **81** (2021) 952, arXiv:2103.13370.

[88] J. Aebischer, J. Kumar, P. Stangl, and D. M. Straub, *A Global Likelihood for Precision Constraints and Flavour Anomalies*, Eur. Phys. J. C **79** (2019) 509, arXiv:1810.07698.

[89] M. Algueró *et al.*, *Emerging patterns of New Physics with and without Lepton Flavour Universal contributions*, Eur. Phys. J. C **79** (2019) 714, arXiv:1903.09578, [Addendum: Eur.Phys.J.C 80, 511 (2020)].

[90] M. Algueró *et al.*, *$b \to s\ell^+\ell^-$ global fits after R_{K_S} and $R_{K^{*+}}$*, Eur. Phys. J. C **82** (2022) 326, arXiv:2104.08921.

[91] M. Ciuchini *et al.*, *Lessons from the $B^{0,+} \to K^{*0,+}\mu^+\mu^-$ angular analyses*, Phys. Rev. D **103** (2021) 015030, arXiv:2011.01212.

[92] J. Aebischer *et al.*, *B-decay discrepancies after Moriond 2019*, Eur. Phys. J. C **80** (2020) 252, arXiv:1903.10434.

[93] A. Arbey *et al.*, *Update on the b→s anomalies*, Phys. Rev. D **100** (2019) 015045, arXiv:1904.08399.

[94] M. Ciuchini *et al.*, *New Physics in $b \to s\ell^+\ell^-$ confronts new data on Lepton Universality*, Eur. Phys. J. C **79** (2019) 719, arXiv:1903.09632.

[95] K. Kowalska, D. Kumar, and E. M. Sessolo, *Implications for new physics in $b \to s\mu\mu$ transitions after recent measurements by Belle and LHCb*, Eur. Phys. J. C **79** (2019) 840, arXiv:1903.10932.

[96] C. Hati, J. Kriewald, J. Orloff, and A. M. Teixeira, *The fate of $\mathbf{V_1}$ vector leptoquarks: the impact of future flavour data*, Eur. Phys. J. C **81** (2021) 1066, arXiv:2012.05883.

[97] ATLAS collaboration, G. Aad *et al.*, *Search for pair production of third-generation scalar leptoquarks decaying into a top quark and a τ-lepton in pp collisions at $\sqrt{s}$ = 13 TeV with the ATLAS detector*, JHEP **06** (2021) 179, arXiv:2101.11582.

[98] CMS collaboration, A. M. Sirunyan *et al.*, *Search for leptoquarks coupled to third-generation quarks in proton-proton collisions at* $\sqrt{s} = 13$ *TeV*, Phys. Rev. Lett. **121** (2018) 241802, arXiv:1809.05558.

[99] O. Bruning, H. Burkhardt, and S. Myers, *The Large Hadron Collider*, Prog. Part. Nucl. Phys. **67** (2012) 705.

[100] T. Taylor and D. Treille, *The Large Electron Positron Collider (LEP): Probing the Standard Model*, Adv. Ser. Direct. High Energy Phys. **27** (2017) 217.

[101] E. Mobs, *The CERN accelerator complex - August 2018. Complexe des accélérateurs du CERN - Août 2018*, arXiv:http://cds.cern.ch/record/2636343, General Photo.

[102] *LHC Machine*, JINST **3** (2008) S08001.

[103] W. Herr and B. Muratori, *Concept of luminosity*, doi: 10.5170/CERN-2006-002.361.

[104] LHCb collaboration, R. Aaij *et al.*, *LHCb detector performance*, Int. J. Mod. Phys. **A30** (2015) 1530022, arXiv:1412.6352.

[105] L. collaboration, *Lhcb material for presentations*, https://lhcb.web.cern.ch/lhcb/speakersbureau/html/Material_for_Presentations.html. Accessed: 8/09/2022.

[106] E. Norrbin and T. Sjostrand, *Production and hadronization of heavy quarks*, Eur. Phys. J. C **17** (2000) 137, arXiv:hep-ph/0005110.

[107] A. D. Martin, W. J. Stirling, R. S. Thorne, and G. Watt, *Parton distributions for the LHC*, Eur. Phys. J. C **63** (2009) 189, arXiv:0901.0002.

[108] E. J. Millard, *Studies of the rare decays* $B^0(B_s^0) \to \pi^+\pi^-\mu^+\mu^-$ *with the LHCb experiment*, PhD thesis, Warwick U., 2020.

[109] LHCb collaboration, R. Aaij *et al.*, *Measurement of* $\sigma(pp \to b\bar{b}X)$ *at* $\sqrt{s} = 7$ *TeV in the forward region*, Phys. Lett. **B694** (2010) 209, arXiv:1009.2731.

[110] LHCb collaboration, C. Elsässer, $\bar{b}b$ *production angle plots*, https://lhcb.web.cern.ch/lhcb/speakersbureau/html/bb_ProductionAngles.html. Accessed: 03/03/2022.

[111] LHCb collaboration, A. A. Alves Jr. *et al.*, *The LHCb detector at the LHC*, JINST **3** (2008) S08005.

[112] LHCb collaboration, R. Aaij *et al.*, *Measurement of the track reconstruction efficiency at LHCb*, JINST **10** (2015) P02007, arXiv:1408.1251.

[113] LHCb collaboration, P. R. Barbosa-Marinho *et al.*, *Vertex locator technical design report*, CERN-PH-EP (2001) arXiv:http://cdsweb.cern.ch/record/504321.

[114] M. Alexander *et al.*, *Mapping the material in the LHCb vertex locator using secondary hadronic interactions*, JINST **13** (2018) P06008, arXiv:1803.07466.

[115] R. Aaij *et al.*, *Design and performance of the LHCb trigger and full real-time reconstruction in run 2 of the LHC*, Journal of Instrumentation **14** (2019) P04013.

[116] M. Adinolfi, others, and T. L. R. Collaboration, *Performance of the lhcb rich detector at the lhc*, The European Physical Journal C **73** (2013) 2431.

[117] A. Papanestis and C. D'Ambrosio, *Performance of the lhcb rich detectors during the lhc run ii*, Nuclear Instruments and Methods in Physics Research Section A: Accelerators, Spectrometers, Detectors and Associated Equipment **876** (2017) 221, The 9th international workshop on Ring Imaging Cherenkov Detectors (RICH2016).

[118] LHCb collaboration, R. Aaij *et al.*, *The LHCb Detector at the LHC*, Institute of Physics Publishing and SISSA **The CERN Large Hadron Collider: Accelerator and Experiments** (2008).

[119] Y. Guz, *The LHCb calorimeter system: design, performance and upgrade*, Journal of Instrumentation **12** (2017) C07024.

[120] A. A. Alves *et al.*, *Performance of the LHCb muon system*, Journal of Instrumentation **8** (2013) P02022.

[121] LHCb collaboration, R. Aaij *et al.*, *LHCb Detector Performance*, Int. J. Mod. Phys. A **30** (2015) 1530022, arXiv:1412.6352.

[122] LHCb Collaboration, *Global PID performance for charged particles*, arXiv:https://cds.cern.ch/record/2718739.

[123] LHCb collaboration, A. Seuthe, *PID performance in Run 2 at LHCb*, PoS **LHCP2020** (2021) 047.

[124] F. Archilli *et al.*, *Performance of the Muon Identification at LHCb*, JINST **8** (2013) P10020, arXiv:1306.0249.

[125] R. Aaij *et al.*, *The LHCb Trigger and its Performance in 2011*, JINST **8** (2013) P04022, arXiv:1211.3055.

[126] LHCb collaboration, R. Aaij *et al.*, *Design and performance of the LHCb trigger and full real-time reconstruction in Run 2 of the LHC*, JINST **14** (2019) P04013, arXiv:1812.10790.

[127] R. Aaij *et al.*, *The LHCb trigger and its performance in 2011*, Journal of Instrumentation **8** (2013) P04022.

[128] M. Williams *et al.*, *The HLT2 Topological Lines* , CERN, Geneva, 2011.

[129] LHCb collaboration, B. Sciascia, *LHCb Run 2 trigger performance*, PoS **BEAUTY2016** (2016) 029.

[130] LHCb Collaboration, *Framework TDR for the LHCb Upgrade II - Opportunities in flavour physics, and beyond, in the HL-LHC era* , http://cds.cern.ch/record/2776420, 2021.

[131] LHCb collaboration, R. Aaij *et al.*, *First observation of the decay $B^+ \to \pi^+\mu^+\mu^-$*, JHEP **12** (2012) 125, arXiv:1210.2645.

[132] LHCb collaboration, R. Aaij *et al.*, *First measurement of the differential branching fraction and CP asymmetry of the $B^+ \to \pi^+\mu^+\mu^-$ decay*, JHEP **10** (2015) 034, arXiv:1509.00414.

[133] F. James, *MINUIT Function Minimization and Error Analysis: Reference Manual Version 94.1*, .

[134] G. J. Feldman and R. D. Cousins, *A Unified approach to the classical statistical analysis of small signals*, Phys. Rev. D **57** (1998) 3873, arXiv:physics/9711021.

[135] LHCb collaboration, G. Wormser, *Measurement of the ratio of branching fractions $\mathcal{B}(B^0 \to D^{*-}\tau^+\nu_\tau)/\mathcal{B}(B^0 \to D^{*-}\mu^+\nu_\mu)$ with τ three-prong decays*, in *52nd Rencontres de Moriond on EW Interactions and Unified Theories*, 203–210, 2017.

[136] L. Anderlini *et al.*, *The PIDCalib package*, .

[137] LHCb collaboration, R. Aaij *et al.*, *Measurement of the track reconstruction efficiency at LHCb*, JINST **10** (2015) P02007, arXiv:1408.1251.

[138] S. S. Wilks, *The large-sample distribution of the likelihood ratio for testing composite hypotheses*, Ann. Math. Stat. **9** (1938) 60.

[139] M. Pivk and F. R. Le Diberder, *sPlot: A statistical tool to unfold data distributions*, Nucl. Instrum. Meth. **A555** (2005) 356, arXiv:physics/0402083.

[140] R. Aaij *et al.*, *Selection and processing of calibration samples to measure the particle identification performance of the LHCb experiment in Run 2*, Eur. Phys. J. Tech. Instr. **6** (2018) 1, arXiv:1803.00824.

[141] A. Rogozhnikov, *Reweighting with Boosted Decision Trees*, J. Phys. Conf. Ser. **762** (2016) 012036, arXiv:1608.05806, https://github.com/arogozhnikov/hep_ml.

[142] B. Efron, *Bootstrap Methods: Another Look at the Jackknife*, Annals Statist. **7** (1979) 1.

[143] J. A. Hanley and B. MacGibbon, *Creating non-parametric bootstrap samples using poisson frequencies*, Computer Methods and Programs in Biomedicine **83** (2006) 57.

[144] LHCb collaboration, R. Aaij *et al.*, *Measurement of the semileptonic CP asymmetry in B^0–$\overline{B}^0$ mixing*, Phys. Rev. Lett. **114** (2015) 041601, arXiv:1409.8586.

[145] LHCb collaboration, R. Aaij *et al.*, *Measurement of the D_s^+– D_s^- production asymmetry in 7 TeVpp collisions*, Phys. Lett. **B713** (2012) 186, arXiv:1205.0897.

[146] G. A. Cowan, D. C. Craik, and M. D. Needham, *RapidSim: an application for the fast simulation of heavy-quark hadron decays*, Comput. Phys. Commun. **214** (2017) 239, arXiv:1612.07489.

[147] J. Back *et al.*, LAURA^{++}*: A Dalitz plot fitter*, Comput. Phys. Commun. **231** (2018) 198, arXiv:1711.09854.

[148] LHCb collaboration, R. Aaij *et al.*, *Amplitude analysis of the $B^+ \to \pi^+\pi^+\pi^-$ decay*, Phys. Rev. **D101** (2020) 012006, arXiv:1909.05211.

[149] BaBar collaboration, B. Aubert *et al.*, *Evidence for Direct CP Violation from Dalitz-plot analysis of $B^\pm \to K^\pm\pi^\mp\pi^\pm$*, Phys. Rev. D **78** (2008) 012004, arXiv:0803.4451.

[150] T. Skwarnicki, *A study of the radiative cascade transitions between the Upsilon-prime and Upsilon resonances*, PhD thesis, Institute of Nuclear Physics, Krakow, 1986, DESY-F31-86-02.

[151] N. L. Johnson, *Systems of frequency curves generated by methods of translation*, Biometrika **36** (1949) 149.

[152] Particle Data Group, P. A. Zyla *et al.*, *Review of particle physics*, Prog. Theor. Exp. Phys. **2020** (2020) 083C01.

[153] S. Bodhisattva, M. Walker, and M. Woodroofe, *On the Unified Method with Nuisance Parameters*, Statist. Sinica **19** (2009) 301.

[154] D. Martínez Santos and F. Dupertuis, *Mass distributions marginalized over per-event errors*, Nucl. Instrum. Meth. A **764** (2014) 150, arXiv:1312.5000.

[155] LHCb collaboration, R. Aaij *et al.*, *Observation of several sources of CP violation in $B^+ \to \pi^+\pi^+\pi^-$ decays*, Phys. Rev. Lett. **124** (2020) 031801, arXiv:1909.05211.

[156] G. Isidori, S. Nabeebaccus, and R. Zwicky, *QED corrections in $\overline{B} \to \overline{K}\ell^+\ell^-$ at the double-differential level*, JHEP **12** (2020) 104, arXiv:2009.00929.

[157] LHCb collaboration, R. Aaij *et al.*, *Angular analysis of charged and neutral $B \to K\mu^+\mu^-$ decays*, JHEP **05** (2014) 082, arXiv:1403.8045.

[158] N. Brook *et al.*, *Testbeam studies of a TORCH prototype detector*, Nucl. Instrum. Meth. A **908** (2018) 256, arXiv:1805.04849.

[159] T. H. Hancock, *Searches for $B \to \mu^+\mu^-$ decays and test-beam studies of TORCH detector prototypes*, PhD thesis, Oxford U., 2020.

[160] P. A. Cherenkov, *Visible luminescence of pure liquids under the influence of γ-radiation*, Dokl. Akad. Nauk SSSR **2** (1934) 451.

[161] P. A. Cherenkov, *Influence of magnetic field on the observed luminescenceof fluids induced by γ rays*, 1936.

[162] J. D. Jackson, *Classical Electrodynamics*, Wiley, 1998.

[163] I. M. Frank and I. E. Tamm, *Coherent visible radiation of fast electrons passing through matter*, Compt. Rend. Acad. Sci. URSS **14** (1937) 109.

[164] LHCb collaboration, M. J. Charles and R. Forty, *TORCH: Time of Flight Identification with Cherenkov Radiation*, Nucl. Instrum. Meth. A **639** (2011) 173, arXiv:1009.3793.

[165] Belle-II collaboration, T. Abe *et al.*, *Belle II Technical Design Report*, arXiv:1011.0352.

[166] BaBar DIRC collaboration, I. Adam *et al.*, *The DIRC particle identification system for the BaBar experiment*, Nucl. Instrum. Meth. A **538** (2005) 281.

[167] Belle-II Barrel Particle Identification Group, J. Fast, *The Belle II imaging Time-of-Propagation (iTOP) detector*, Nucl. Instrum. Meth. A **876** (2017) 145.

[168] LHCb collaboration, *Letter of Intent for the LHCb Upgrade*, .

[169] L. Castillo Garcia, *Study of a prototype module of a precision time-of-flight detector for particle identification at low momentum*, PhD thesis, Ecole Polytechnique, Lausanne, 2016, doi: 10.5075/epfl-thesis-7027.

[170] J. L. Wiza, *Microchannel plate detectors*, Nucl. Instrum. Meth. **162** (1979) 587.

[171] G. W. Frazer *et al.*, *Enhanced soft X-ray detection efficiencies for imaging microchannel plate detectors*, Nature **300** (1982) 509.

[172] T. M. Conneely *et al.*, *The TORCH PMT: a close packing, multi-anode, long life MCP-PMT for Cherenkov applications*, JINST **10** (2015) C05003.

[173] A. Einstein, *Concerning an heuristic point of view toward the emission and transformation of light*, Annalen Phys. **17** (1905) 132.

[174] S. Korpar, P. Krizan, and R. Pestotnik, *Timing and cross-talk properties of BURLE multi-channel MCP PMTs*, PoS **PD07** (2006) 021.

[175] J. S. Milnes *et al.*, *The TORCH PMT, a close packing, multi-anode, long life MCP–PMT for Cherenkov applications*, Nucl. Instrum. Meth. A **766** (2014) 183.

[176] T. M. Conneely *et al.*, *Extended lifetime MCP-PMTs: Characterisation and lifetime measurements of ALD coated microchannel plates, in a sealed photomultiplier tube*, Nucl. Instrum. Meth. A **A** (2013) 388.

[177] T. Gys *et al.*, *Performance and lifetime of micro-channel plate tubes for the TORCH detector*, Nucl. Instrum. Meth. A **766** (2014) 171.

[178] R. Gao *et al.*, *Development of precision Time-Of-Flight electronics for LHCb TORCH*, JINST **9** (2014) C02025.

[179] R. Gao *et al.*, *Development of scalable electronics for the TORCH time-of-flight detector*, JINST **10** (2015) C02028.

[180] R. Gao *et al.*, *Development of TORCH readout electronics for customised MCPs*, JINST **11** (2016) C04012.

[181] F. Anghinolfi *et al.*, *NINO: An ultrafast low-power front-end amplifier discriminator for the time-of-flight detector in the ALICE experiment*, IEEE Trans. Nucl. Sci. **51** (2004) 1974.

[182] F. Anghinolfi *et al.*, *NINO, an ultra-fast, low-power, front-end amplifier discriminator for the Time-Of-Flight detector in ALICE experiment*, Nuclear Science Symposium Conference Record, 2003 IEEE **1** (2003) 375.

[183] M. Mota *et al.*, *A flexible multi-channel high-resolution time-to-digitalconverter ASIC* , Nuclear Science Symposium Conference Record, 2000 IEEE **2** (2000) 9/155.

[184] A. N. Akindinov *et al.*, *Design aspects and prototype test of a very precise TDC system implemented for the multigap RPC of the ALICE-TOF*, Nucl. Instrum. Meth. A **533** (2004) 178.

[185] J. Christiansen, *HPTDC High Performance Time to Digital Converter* , CERN, Geneva, 2004. Version 2.2 for HPTDC version 1.3.

[186] LHCb collaboration, M. Clemencic *et al.*, *The LHCb simulation application, Gauss: Design, evolution and experience*, J. Phys. Conf. Ser. **331** (2011) 032023.

[187] T. Sjöstrand, S. Mrenna, and P. Skands, *PYTHIA 6.4 physics and manual*, JHEP **05** (2006) 026, arXiv:hep-ph/0603175.

[188] GEANT4 collaboration, S. Agostinelli *et al.*, *GEANT4–a simulation toolkit*, Nucl. Instrum. Meth. A **506** (2003) 250.

[189] R. W. Forty and O. Schneider, *RICH pattern recognition*, .

[190] J. C. Smallwood *et al.*, *Test-beam demonstration of a TORCH prototype module*, in *International Conference on Technology and Instrumentation in Particle Physics*, 2021, arXiv:2111.04627.

[191] I. Rubinskiy and H. Perrey, *An eudet/aida pixel beam telescope for detector development*, Proc. of Science **213** (2014) 122.

[192] S. Bhasin *et al.*, *Test-beam studies of a small-scale TORCH time-of-flight demonstrator*, Nucl. Instrum. Meth. A **961** (2020) 163671, arXiv:2002.07632.

[193] S. Liu *et al.*, *Lut-based non-linearity compensation for bes iii tof's time measurement*, , Nuclear Science and Techniques **21** (2010) 49.

[194] M. Van Dijk, *Design of the TORCH detector: A Cherenkov based Time-of-Flight system for particle identification*, PhD thesis, Bristol U., 2016.

[195] M. Horstmann *et al.*, *picoTDC: a 3 ps bin size 64 channel TDC for HEP experiments*, https://indico.cern.ch/event/799025/contributions/3486148/attachments/1902032/3140087/picoTDC_TWEPP_2019.pdf, 2019. presented at TWEPP 2019 Topical Workshop on Electronics for Particle Physics, Santiago de Compostela, Spain, 3 September.